Uniwersytet Mikołaja Kopernika w Toruniu

Szkoła Doktorska Nauk Ścisłych i Przyrodniczych
Academia Scientiarum Thoruniensis

Wydział Chemii

Interdyscyplinarne Centrum Nowoczesnych Technologii

Mgr Oleksandra Pryshchepa

Rozprawa doktorska

Badanie molekularnych mechanizmów wiązania metali z białkami

Praca wykonana pod kierunkiem

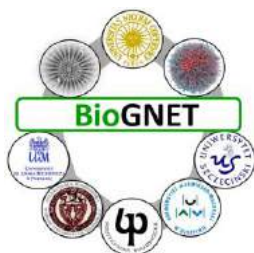dr hab. Pawła Pomastowskiego, prof. UMK

w Interdyscyplinarnym Centrum Nowoczesnych Technologii

Toruń 2023

Study on molecular mechanisms of metal-protein binding

Spis Treści

Wykaz skrótów

AgNPs	Nanocząstki srebra (ang. *Silver Nanoparticles*)
bLTF	Laktoferyna bydlęca (ang. *Bovine Lactoferrine*)
BAL	Biuro Ekonomiki Rolnictwa i Studiów Wiejskich, Niemcy (niem. *Büro für Agrarsoziologie und Landwirtschaft*)
CE-ICP-MS	Elektroforeza kapilarna łączona z spektrometrią mas sprzężoną z plazmą wzbudzaną indukcyjnie (ang. *Capillary Electrophoresis − Inductively Coupled Plasma Mass Spectrometry*)
DFT	Teoria funkcjonału gęstości (ang. *Dencity Functional Theory*)
DMT-1	Transporter dwuwartościowych jonów metali-1 (ang. *Divalent Metal Transporter 1*)
FTIR	Spektroskopia w podczerwieni z transformacją Fouriera (ang. *Fourier Transform InfraRed spectroscopy*)
HSAB	Teoria miękkich i twardych zasad i kwasów Lewisa (ang. *Hard and Soft Acids and Bases*)
hLTF	Laktoferyna ludzka (ang. *human Lactoferrine*)
IDA	Niedokrwistość z niedoboru żelaza (ang. *Iron Deficiency Anemia*)
ICP-MS	Spektrometria mas sprzężona z plazmą wzbudzaną indukcyjnie (ang. *Inductively Coupled Plasma Mass Spectrometry*)
LTF	Laktoferyna (ang. *Lactoferrine*)
LRP-1	Białko 1 związane z receptorem lipoproteiny o niskiej gęstości (ang. *Low Dencity Lipoprotein Receptor Related Protein-1*)
MALDI-TOF-MS	Spektrometria mas z laserową jonizacją/desorpcją próbki wspomagana matrycą z tandemowym analizatorem czasu przelotu (ang. *Matrix-Assisted Laserd Desorption/Ionization coupled to Time-Of-Flight Mass Spectrometry*)
MD	Dynamika molekularna (ang. *Molecular Dynamics*)
MIB server	Serwer wiązania jonów metali (ang. *Metal Ion-Binding server*)
MIC	Minimalne stężenie hamujące (ang. *Minimum Inhibitory Concentration*)
NALDI	Laserowa jonizacja/desorpcja próbki wspomagana nanostrukturami (ang. *Nanostrure-Assisted Laser Desorption/Ionization*)
NPs	Nanocząstki (ang. *Nanoparticles*)
PDB	Bank danych białek (ang. *Protein Data Bank*)

SDS-PAGE Elektroforeza w denaturującym żelu poliakryloamidowym (ang. *Sodium Dodecyl Sulfate – Polyacrylamide Gel Electrophoresis*)

SERS Powierzchniowo wzmocniona spektroskopia Ramana (ang. *Surface Enhanced Raman Spectroscopy*)

1. Wprowadzenie

Współczesne rynki mleczarskie, farmaceutyczne i kosmetyczne charakteryzują się wysokim ryzykiem i niepewnością, podlegają też ciągłym zmianom. Preferencje konsumentów oraz agresywna konkurencja ze strony przedsiębiorstw mają szczególny wpływ na dynamikę zmian w tych kluczowych obszarach [1]. Firmy, które chcą pozostać konkurencyjne, rozwijać się i być ekspansywnym na rynku krajowym i globalnym są zobligowane do wdrażania innowacji objętych programem zrównoważonego rozwoju [2]. Aby móc konkurować w dynamicznym otoczeniu, przedsiębiorstwa mleczarskie, farmaceutyczne i kosmetyczne muszą oceniać swoje produkty z perspektywy konsumentów, jak i konkurentów. Wdrażając wytyczne dotyczące zrównoważonego rozwoju, powinny stale monitorować swoje oferty i doskonalić je poprzez wdrażanie nowych, innowacyjnych technologii, które poprawiają właściwości produktów.

Światowa produkcja mleka wzrasta i jest stymulowana wzrostem popytu, jak i zmianami dietetycznymi. Koncerny farmaceutyczne udoskonalają leki, a przemysł kosmetyczny zgodnie z ekologicznymi trendami, wprowadza naturalne preparaty kosmetyczne o ulepszonym działaniu. Jednak stosunkowo wysoki koszt produkcji mleka oraz ograniczenia w kształtowaniu cen produktów mleczarskich powodują ciągłe poszukiwanie przez przetwórców mleka nowych produktów o wysokiej wartości dodanej. Badania przeprowadzone przez BAL (Biuro Ekonomiki Rolnictwa i Studiów Wiejskich, Niemcy) wykazały, iż koszt produkcji mleka w państwach Unii Europejskiej jest średnio o 23% wyższy niż cena jego skupu [3]. Zatem możliwość pozyskiwania nowych substancji biologicznie czynnych na bazie białek mleka jest atrakcyjna z finansowego punktu widzenia. Produkcja udoskonalonych artykułów spożywczych, w szczególności o cechach funkcjonalnych, leków nowej generacji i naturalnych kosmetyków na ich bazie staje się niewątpliwie szansą zaistnienia na rynku, jak również w kierunku rozwoju potencjału naukowo-badawczego prowadzącego między innymi do stworzenia i wprowadzenia do gospodarki nowego produktu. Wpisuję się to też w trendy współczesnego świata skierowanego na produkcję bezodpadową oraz poszukiwanie nowych ekologicznych materiałów opartych na surowcach odnawialnych (Gospodarka 4.0).

Mleko jest cennym źródłem biologicznie aktywnych składników, między innymi, tłuszczy, węglowodanów, witamin, białek i ich peptydów [4]. Zarówno białka mleka, jak i ich peptydy wykazują szereg unikatowych właściwości prozdrowotnych, takich jak właściwości przeciwbakteryjne, przeciwwirusowe, przeciwnowotworowe, regenerujące i in. [5,6]. Białka mleka składają się z dwóch głównych grup, a mianowicie kazeiny i białek serwatkowych, których zawartość w mleku krowim wynosi odpowiednio ok. 80% i 20% [4,5]. Białka serwatkowe nazywane zostały dlatego, że w większości pozostają w serwatce przy produkcji

sera, twarogów lub kazein. Serwatka jest największym produktem ubocznym przemysłu mleczarskiego. W 2020 r. w Europie wyprodukowano 148 mln mleka, z czego prawie 50% wykorzystano do produkcji sera w wyniku czego powstało ok. 54.8 mln ton płynnej serwatki [7]. W warunkach przemysłowych serwatka jest w zasadzie niekorzystnym ekologicznie odpadem, uzyskiwanym w ogromnych, zazwyczaj niemożliwych do efektywnego zagospodarowania, ilościach. Zawiera ona jednak najbardziej cenne białka mleka, dlatego też może stanowić surowiec do ich pozyskania. Do najważniejszych białek serwatkowych zaliczamy β-laktoglobulinę (40-55%), α-laktoglobulinę (11-20%), immunoglobuliny (8-11%), albuminę surowicy bydlęcej (4-12%), laktoferynę (LTF, bLTF) (1%) i laktoperoksydazę (1%) [4,7].

Warto zaznaczyć, że LTF uważana jest za jedno z najbardziej cennych białek serwatkowych [8]. Białko to jest glikoproteiną o szerokim zakresie funkcji biologicznych, gdzie za najważniejsze można uznać regulację układu odpornościowego, funkcję regenerującą oraz wspieranie absorpcji i prawidłowej dystrybucji mikroelementów [9]. LTF po raz pierwszy została zidentyfikowana i pozyskana z mleka krowiego w 1939 roku. Od tego czasu były przeprowadzone liczne badania wskazujące na korzystne działania LTF na organizm ludzki, co spowodowało, że w 1985 r. belgijska firma Oleofina Company jako pierwsza opatentowała metodę produkcji LTF na skalę przemysłową [10]. Już od 1986 roku LTF bydlęca była dopuszczona w Japonii do stosowania w preparatach początkowego żywienia niemowląt. Ponadto, od 2001 r. amerykańska Agencja Żywności i Leków (FDA) zaczęła nadawać status GRAS (Generally Recognized as Safe) izolatom LTF do wykorzystania w żywności [11]. Spowodowało to wprowadzenie na rynek szerokiej gamy produktów fortyfikowanych LTF. Na rynku polskim można zakupić preparaty dla niemowląt takie jak Laktowit Premium Laktoferyna+MFGM (Geo-Poland sp. z o.o., Polska) lub też Mleko Początkowe Dla Niemowląt Kendamil (Kendal Nutricare, Wielka Brytania). Dużo więcej jest rodzajów suplementów z LTF w formie kapsułek, tabletek i kropli, w tym w mieszaninie z innymi komponentami prozdrowotnymi takimi jak mikroelementy, witaminy, bakterie probiotyczne i in.: Laktoviryna, kapsułki z cynkiem (Natur Produkt Pharma sp. z o.o., Polska), Symbiosys Alflorex, kapsułki z *Bifidobacterium infantis* (Biocodex sp. z o.o., Polska), Laktoferyna IgG, tabletki do ssania z kolostrum i witaminą D3 (Pharmabest sp. z o.o., Polska).

LTF jest biologicznie aktywna w stanie natywnym. Ogólnie, pojęcie „aktywność biologiczna" można zdefiniować jako każde bezpośrednie działanie (pozytywne lub negatywne) substancji na komórki organizmów żywych, w szczególności człowieka i zwierząt, ale także i mikroorganizmów [12]. W przypadku LTF jest ona związana ze stopniem glikozylacji, wysyceniem jonami żelaza oraz ilością zdegradowanego bądź zdenaturowanego białka [9,13,14].

Stopień i rodzaj glikozylacji związany jest głównie ze źródłem, z którego pozyskiwana jest LTF [13]. Poziom wysycenia jonami żelaza może być w większym stopniu kontrolowany poprzez odpowiednie procesy technologiczne. Natomiast stopień degradacji i denaturacji białka jest niepożądanym skutkiem ubocznym stosowanych procesów technologicznych. Literatura fachowa dotycząca otrzymywania i oczyszczania LTF w skali przemysłowej wskazuje kolumnową chromatografię kationowymienną jako najbardziej rozpowszechnioną technikę [14,15]. Wpływ poszczególnych procesów technologicznych na strukturę LTF, w korelacji z aktywnością biologiczną białka, został opisany w pracy I. Franko i in. [16]. Do głównych czynników mających wpływ na zmiany w strukturze białka zalicza się: temperaturę (≥70°C), bardzo wysokie ciśnienie używane między innymi do sterylizacji (≥400MPa), fermentację spowodowaną bakteriami, zbyt niskie pH (≤4,0), dostępność tlenu oraz czas ekspozycji na każdy z tych czynników. Połączenie kilku tych czynników przyspiesza proces denaturacji i degradacji białka, które mogą sięgać 50%, a w skrajnych przypadkach może zachodzić całkowita denaturacja.

Mianem aktywności biologicznej LTF, wspominanej w literaturze [14], jest suma wartości A i C, z których A określa procent wysycenia żelazem, z kolei C - zdolność wiązania żelaza. W patencie US 2021/0388058 A1 [14] opublikowane zostały wyniki badań czterech komercyjnie dostępnych preparatów LTF w porównaniu do białka otrzymanego według procedury opisanej w tym patencie. Przebadane produkty charakteryzowały się wartością A na poziomie 4,6-11,7% i C 34,4-52,1% oraz sumą tych wartości 39,0-60,3%. Dlatego też ważnym i aktualnym aspektem badawczym jest poszukiwanie możliwości „ulepszenia" układów białkowych, zarówno pod względem potencjalnego zastosowania przemysłowego, przekładającego się na cechy użytkowe, konkurencyjnych pod względem właściwości prozdrowotnych. Jednym z takich sposobów może być modyfikacja jonami metali o znaczeniu biologicznym, takimi jak kationy: cynku, żelaza, magnezu, selenu czy też srebra. Takie kompleksy jonów metali na bazie białek mają wysoki potencjał aplikacyjny jako nowe substancje aktywne w preparatach farmaceutycznych lub suplementach diety [17–19]. Niezbędnym etapem w opracowaniu formulacji tego rodzaju substancji chemicznych jest przeprowadzenie badań opisujące ich właściwości fizyko-chemiczne i biologiczne. Ponadto, z naukowego punktu widzenia ważny jest również opis mechanizmów wiązania metal-białko.

Biorąc pod uwagę przytoczone dane, w ramach niniejszej rozprawy doktorskiej zostały podjęte próby opisania procesów i zmian strukturalnych zachodzących w czasie oddziaływania LTF z jonami srebra, żelaza(III) i cynku. Podejście interdyscyplinarne z wykorzystaniem metod instrumentalnych zostało uzupełnione komplementarnymi wynikami uzyskanymi za pomocą

chemii obliczeniowej. Dane te pozwoliły na opis mechanizmu oddziaływania jonów (układów) cynku z LTF oraz na wyodrębnię poszczególnych etapów takich oddziaływań. Ponadto, opisane zostały procesy, które z dużą wiarygodnością odbywają się w czasie wiązania jonów metali na białku. Dla kompleksów jonów żelaza(III) z LTF wykazano możliwość tworzenia się nowych miejsc wiązania w układzie Fe-LTF. Na koniec za pomocą metod biologii komórkowej oraz mikrobiologii została zbadana aktywność biologiczna kompleksów, mianowicie cytotoksyczność oraz działanie przeciwdrobnoustrojowe wobec wybranych bakterii. Opracowane metody syntezy bogatych w jony metali kompleksów białkowych otwierają drogę do ich zastosowania w przemyśle farmaceutycznym, gdzie nanokompozyty srebra na bazie LTF mogą być wykorzystane jak aktywna substancja w preparatach antybakteryjnych. Z kolei, kompleksy żelaza i cynku mogą być zastosowane w leczeniu stanów chorobowych z niedoborem tych mikroelementów, między innymi anemii, leukopenii, zaburzeniach procesów przemiany materii i in.

Dysertacja oparta jest na pięciu publikacjach naukowych opublikowanych w recenzowanych czasopismach międzynarodowych o sumarycznym współczynniku oddziaływania (*impact factor*, IF) ponad 34 i 750 punktów ministerialnych:

1. **O. Pryshchepa**, P. Pomastowski, B. Buszewski, *"Silver nanoparticles: synthesis, investigation techniques, and properties"*, Advances in Colloid and Interface Science, 284, 2020: 102246, https://doi.org/10.1016/j.cis.2020.102246; (**IF=15,190, MEiN = 200**)

2. **O. Pryshchepa**, P. Pomastowski, K. Rafińska, A. Gołębiowski, A. Rogowska, M Monedeiro-Milanowski, G. Sagandykova, B. Michalke, P. Schmitt-Kopplin, M. Gloc, R. Dobrucka, K. Kurzydłowski, B. Buszewski, *"Synthesis, physicochemical characterization and antibacterial performance of silver-lactoferrin complexes"*, International Journal of Molecular Sciences, 23 (13), 2022: 7112, https://doi.org/10.3390/ijms23137112 (**IF = 6,028, MEiN = 140**);

3. **O. Pryshchepa**, K. Rafińska, A. Gołębiowski, M. Sugajski, G. Sagandykova, P. Madajski,B. Buszewski, P. Pomastowski, *"Synthesis and physicochemical characterization of bovine lactoferrin supersaturated complex with iron (III) ions"*, Scientific Reports, 12 (1), 2022: 12695, https://doi.org/10.1038/s41598-022-15814-2 (**IF = 4,996, MEiN = 140**);

4. **O. Pryshchepa**, G. Sagandykova, J. Rudnicka, P. Pomastowski, S. Sprynskyy, B. Buszewski *"Synthesis and physicochemical characterization of zinc-lactoferrin complexes"*, Journal of Dairy Science, 3 (105), 2022: 1940-1958, https://doi.org/10.3168/jds.2021-20538 (**IF = 4,225, MEiN = 200**);

5. A. Rogowska, **O. Pryshchepa**, Som N. Narayan, P. Śpiewak, A. Gołębiowski, K. Rafińska, K. Kurzydłowscki, B. Buszewski, P. Pomastowski, *"Study on the zinc ions binding to*

human   lactoferrin",   Journal   of   Molecular   Structure,   1282,   2023:   135149, https://doi.org/10.1016/j.molstruc.2023.135149 (**IF = 3,841, MEiN = 70**).

2. Obiekt badawczy

2.1 Występowanie LTF

LTF należy do grupy niehemowych białek wiążących żelazo, z rodziny transferryn. Białka z tej rodziny pełnią swoje funkcje biologiczne regulując poziom wolnego żelaza w płynach ustrojowych zwierząt i człowieka, biorą udział w transporcie żelaza w osoczu i pobieraniu żelaza przez błonę śluzową jelit. Są one potrzebne do solubilizacji oraz sekwestracji żelaza, gdyż w warunkach fizjologicznych preferowaną formą żelaza jest Fe^{3+}, która jest podatna na szybką hydrolizę z utworzeniem nierozpuszczalnych wodorotlenków [20]. Warto zauważyć, że LTF jest białkiem, które ulega ekspresji tylko u ssaków i jest znana głównie jako białko serwatkowe z mleka. LTF wydzielana jest do mleka poprzez komórki nabłonkowe gruczołu mlekowego. Stężenie LTF w mleku zmienia się w okresie laktacji. Jego stężenie w siarze (colostrum) jest znacznie wyższe niż w mleku. U człowieka stężenie tego białka w dojrzałym mleku wynosi 1-2 mg/ml i 10 mg/ml w siarze. Z kolei u bydła, zawartość LTF wynosi <0,2 mg/ml w dojrzałym mleku i <1,5 mg/ml w siarze [9]. Zwiększenie zawartości LTF w mleku nie związane z etapami laktacji spowodowane jest przede wszystkim zapaleniem gruczołu mlekowego, ale też może być skutkiem zakażenia innych narządów, w tym z infekcjami wirusowymi. Dodatkowo, wykazano także wzrost zawartości LTF w mleku u zdrowych kobiet z chorymi niemowlętami [21]. Takie zmiany spowodowane są z zwiększoną ekspresją i uwalnianiem LTF z granul neutrofili polimorfojądrowych, które są drugim najważniejszym źródłem LTF w organizmie ssaków. Podczas infekcji poziom LTF we krwi może wzrosnąć nawet 500-krotnie [9]. Oprócz mleka i krwi, LTF występuję niemal we wszystkich płynach ustrojowych, między innymi: w łzach, plazmie nasienia, śluzie z pochwy, płynie owodniowym, płynie rdzeniowo-mózgowym i in., gdzie prawdopodobnie pełni funkcję ochronną [22]. Dlatego też sugeruję się, że LTF może ulegać ekspresji w innych komórkach, takich jak mikroglej [23] czy też doczesnej (przerosła błona śluzowa macicy) [22].

2.2 Struktura LTF

LTF zbudowana jest z jednego łańcucha polipeptydowego zawierającego ok. 700 aminokwasów, w tym dojrzała LTF ludzka (hLTF) składa się z 692 aminokwasów, natomiast bydlęca (bLTF) ma 689 reszt aminokwasowych. Trójwymiarową strukturę obu LTF przedstawiono na **Rycinie 1.A,C**. LTF wykazuję wysoką homologię i konserwatywność sekwencji łańcucha polipeptydowego międzygatunkową i podobieństwo do innych białek z rodziny transferryn (wśród ssaków jest w zakresie 61-78%) [20]. W zależności od źródeł pozyskiwania, stopnia glikozylacji i zastosowanej techniki instrumentalnej, masy molekularne LTF zostały wyznaczone w zakresie od 75 do nawet 84 kDa [22,24]. W **Rozdziałach 6.4 oraz**

6.5 niniejszej pracy przedstawiono wyniki oznaczania masy molekularnej dla LTF bLTF oraz rekombinowanej hLTF, których masy wyniosły odpowiednio 83,2 i 78,5 kDa. W tym celu wykorzystano spektrometrię mas z laserową jonizacją/desorpcją próbki wspomaganej matrycą z tandemowym analizatorem czasu przelotu (ang. *Matrix-Assisted Laserd Desorption/Ionization coupled to Time-Of-Flight Mass Spectrometry, MALDI-TOF-MS*). Łańcuch polipeptydowy tak dużej molekuły LTF ułożony jest w mniejsze jednostki strukturalne. Białko utworzone jest z płatów N i C z jednym miejscem wiążącym Fe^{3+} każdy, które wykazują podobny do siebie wzorzec fałdowania polipeptydu. Miejsce wiążące jony metalu jest zbudowane z dwóch tyrozyn (Tyr), kwasu asparaginowego (Asp) i histydyny (His) (**Ryc. 1.B**). Dodatkowo, w wiązaniu bierze udział jon węglanowy, którego ładunek jest neutralizowany poprzez argininę. Procent homologii obu płatów mieści się w zakresie od 33 do 41%. Płaty te są połączone tzw. regionem zawiasowym ułożonym w strukturę α-helisy, który nadaje molekule białka elastyczność. W przypadku hLTF oraz bLTF region ten mieści się pomiędzy aminokwasami 333 i 343 oraz 327 i 340 odpowiednio. Z kolei, płat N łańcucha polipeptydowego hLTF zbudowany jest z aminokwasów od 1 do 332, natomiast płat C z aminokwasów od 345 do 692. Dla bLTF odpowiednio są to aminokwasy od 1 do 327 oraz 341 i 689. Łańcuch polipeptydowy każdego z płatów ma w swojej strukturze zarówno α-helisy jak i β-harmonijki, które tworzą dwie subdomeny. Taka złożona struktura przyczynia się do unikatowej zdolności silnego wiązania jonów żelaza(III) [9].
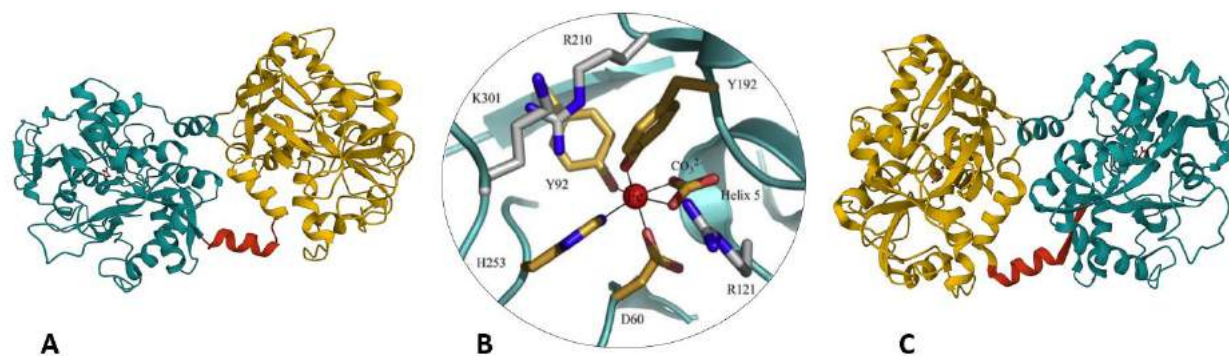
Rycina 1. Struktura **A.** molekuły laktoferyny bydlęcej (PDB 1BLF[25]), **B.** miejsca wiążącego żelazo w N-płacie transferryn [26]**, C.** molekuły laktoferyny ludzkiej (PDB 1LFG[27]), gdzie N i C płaty są w kolorach żółtym i patyny, a region zawiasowy - czerwony.

2.3 Glikozylacja LTF

Ważnym aspektem strukturalnym LTF jest glikozylacja. W LTF występuję N-glikozylacja, która polega na przyłączeniu reszt cukrowych do azotu łańcuchów bocznych asparaginy [28,29]. N-glikany można podzielić na trzy główne grupy: wielomannozowe, kompleksowe i hybrydowe N-glikany [30]. W zależności od gatunku LTF może mieć od jednego

do pięciu miejsc N-glikozylacji. hLTF ma trzy potencjalne miejsca N-glikozylacju, przy czym w 85% jest ona glikozylowana w dwóch miejscach (Asn138 i Asn479), w 9% w trzech miejscach (Asn138, Asn479 i Asn624), a w 5% w jednym miejscu (Asn479) [28]. Z kolei bLTF ma cztery miejsca, które są zawsze glikozylowane (Asn233, Asn368, Asn476 i Asn545) oraz jedno (Asn281), które jest glikozylowane tylko w 15-30% (**Ryc. 2**). Większy stopień glikozylacji dla hLTF i bLTF jest obserwowany w colostrum [28,31]. Glikozylacja określa nie tylko masę cząsteczkową, ale także inne właściwości fizykochemiczne i biologiczne białek, między innymi, punkt izoelektryczny, stabilność przeciwko proteazom, właściwości przeciwbakteryjne i in. [29–32].
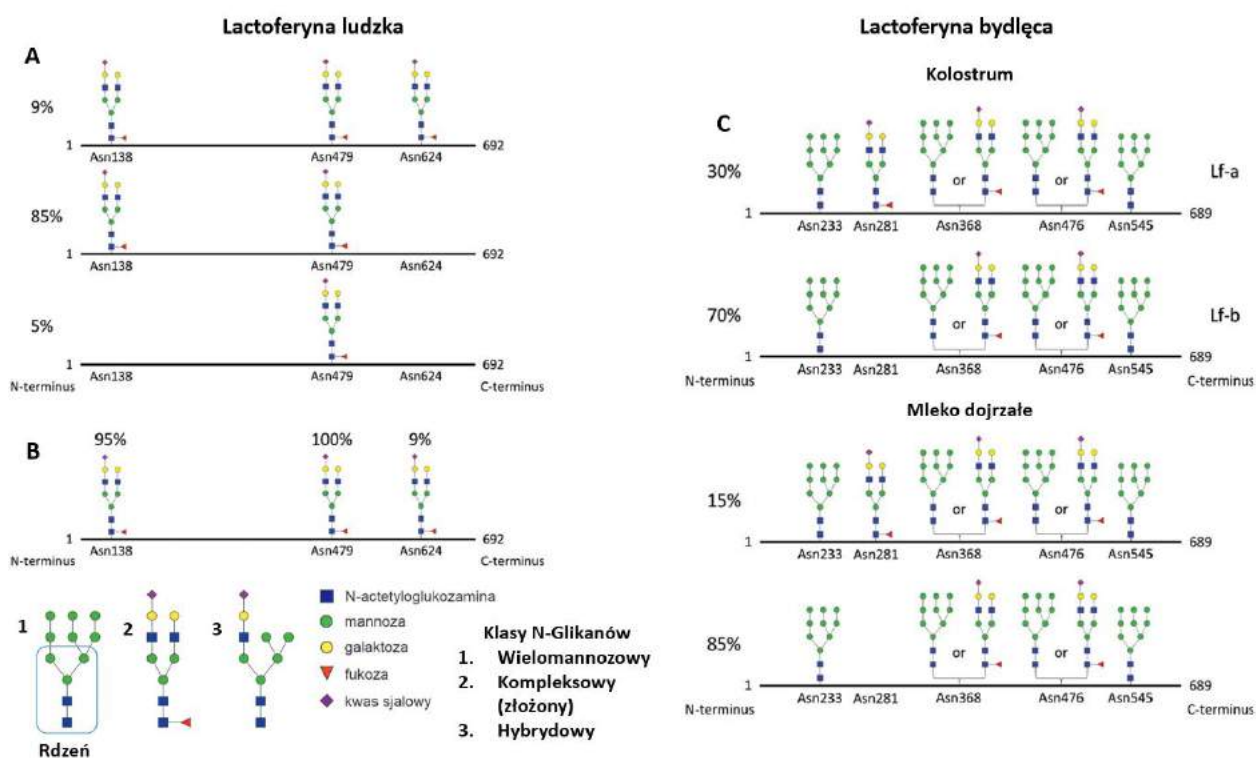
Rycina 2. Przedstawiono struktury N-glikanów LTF **A i B** ludzkiej oraz **C** bydlęcej (dostosowano wg [28]).

Składnik glikanowy bLTF stanowi od 6,7 do 11,2 % całkowitej masy białka [29]. Łańcuch polipeptydowy bLTF ma masę 77 kDa. Wówczas masa dwóch występujących naturalnie glikozylowanych wariantów białka z pięcioma i czterema N-glikanami (LTF-a oraz LTF-b) wynosi ok. 84 oraz 80 kDa odpowiednio [29,33]. Podstawowymi cukrami wchodzącymi w skład N-glikanów LTF, jak i dla innych białek, są N-acetyloglukozamina, N-acetylgalaktozamina, mannoza, galaktoza, fukoza oraz kwas sjalowy (kwasy N-acetyloneuraminowy oraz N-gluconyloneuraminowy). Wyróżniającym bLTF jest obecność fukozylacji rdzenia, terminalna sjalizacja oraz obecność struktur takich jak N-acetylolaktozaminy (Gal-β-(1→4)-GlcNAc, LacNAc), N',N''-diacetylolaktozaminy (GalNAc-β-

(1→4)-GlcNAc, LacdiNAc) oraz Gal-α-(1→3)-Gal [29]. Ponadto, dla bLTF charakterystyczna jest obecność glikanów wielomannozowych, które nie zostały zidentyfikowane dla naturalnego hLTF [28,31,34]. W sumie w bLTF wykryto 76% obojętnych, 9% mono-sjalilowanych i 15% di-sjalilowanych struktur glikanu, przy czym 8,5% wykrytego kwasu sjalowego występuję w formie kwasu N-gluconyloneuraminowego. Szczególnie istotne jest to, że zawartość kwasu sjalowego określa ładunek związany z łańcuchem oligosacharydowym. Jest to mocny kwas o pKa 2,6 i przy fizjologicznym pH występuje w postaci zdeprotonowanej. Zawartość tego kwasu wpływa na zdolność bLTF do wiązania jonów metali, między innymi Ca^{2+}, co jest kluczowe dla stabilizacji struktury białka, ale także może być związane z właściwościami przeciwdrobnoustrojowymi LTF [29]. Z kolei, stopień glikozylacji i jej wpływ na właściwości białka często są pomijane w badaniach, w tym związanych z oddziaływaniami z metalami czy też innymi związkami niskocząsteczkowymi.

Ze względu na ilość potencjalnych miejsc glikozylacji w hLTF składnik glikanowy jest znacznie mniejszy niż w bLTF, zwykle nie przekracza 5,9% [34,35]. Jak dotąd dla naturalnego hLTF zidentyfikowano tylko kompleksowe struktury N-glikanów, na ogół znane są co najmniej 20 różnych struktur [28,31,34]. Ekspresja hLTF w organizmie krów transgenicznych pozwalała na uzyskanie tego białka z wielomannozowymi N-glikanami, jednak w znacznie niższym stopniu niż dla bLTF. Ogólnie, dla rekombinowanego hLTF rodzaj glikanów zależy od układu, w którym została przeprowadzana ekspresja i związana jest z obecnością odpowiednich enzymów. Dla rekombinowanej hLTF wyprodukowanej z wykorzystaniem komórek roślinnych, takich jak kukurydza czy też roślina tabaki, charakterystyczna jest obecność krótkich glikanów mannozowych [28]. Nie jest wyjątkiem także hLTF rekombinowany w ryżu, gdzie wykazano cukry zawierające od 5 do 7 reszt oraz terminalne reszty mannozowe [36]. Badania dla hLTF wykazały też różnice pomiędzy glikanami dla hLTF izolowanymi z mleka oraz leukocytów. Badania przeprowadzone przez francuskich naukowców wykazały brak α-1,3 oraz α-1,6 połączonych reszt fukozy, co jest charakterystyczne dla hLTF mleka. Dodatkowo, wykazano, że hLTF leukocytarna zawiera dwa glikany posiadające dwuantenową strukturę typu disjalilowanej N-acetylo-laktozaminy, która jest identyczna z glikanami ludzkiej transferryny w surowicy. Autorzy zasugerowali, że związane jest to z obecnością lub brakiem odpowiednich enzymów [35]. Różnica w strukturach glikanów jest także zależna od stadium laktacji. Dla hLTF wykazano zmniejszenie różnorodności z czasem oraz zwiększenie ilości fukozylacji [31].

2.4 Wybrane właściwości fizyko-chemiczne

2.4.1 Punkt izoelektryczny

Z chemicznego punktu widzenia roztwory białek są układami koloidalnymi. Łańcuch polipeptydowy ułożony w strukturę globularną tworzy rdzeń cząsteczki koloidu z wystającymi na powierzchni grupami funkcyjnymi reszt aminokwasów, które w zależności od pH roztworu posiadają ładunek ujemny lub też dodatni [37]. Sumaryczny ładunek wszystkich grup funkcyjnych wyznacza ładunek całej molekuły. Manipulując pH roztworu można stworzyć warunki, w których ładunek białka będzie wynosić zero – punkt izoelektryczny (pI) [38]. LTF należy do białek wysoce zasadowych (polikationy), które w warunkach fizjologicznych przeważnie posiadają ładunek dodatni. Związane jest to z przewagą zawartości aminokwasów, które posiadają ładunek dodatni (histydyna, lizyna oraz arginina) nad aminokwasami o ładunku ujemnym (kwas glutaminowy i kwas asparaginowy). Sumarycznie bLTF i hLTF posiada 102 i 98 odpowiednio aminokwasy o charakterze dodatnim oraz dla obu tych białek tylko 65 aminokwasów o charakterze ujemnym [39]. Z kolei, inne białka serwatkowe, takie jak laktoalbumina i β-laktoglobulina odpowiednio posiadają 17 i 20 aminokwasów o charakterze dodatnim oraz 20 i 26 aminokwasów ujemnych (obliczenia przeprowadzone na podstawie sekwencji przedstawionych w bazie danych białek www.uniprot.org).

Większość publikacji wskazuje, że pI LTF jest w zakresie od 8,0 do nawet 9,3, gdzie najczęściej został on oznaczany poprzez ogniskowanie izoelektryczne [40,41]. Jednak K.-I. Shimazaki i wsp. przebadali liczne prace naukowe w poszukiwaniu właściwych znaczeń pI dla hLTF oraz bLTF [42]. Opracowane wyniki metaanalizy wskazują, że wartość ta nie jest jednoznaczna i może być w zakresie od 4,8 do nawet 10,0 dla bLTF oraz od 5,2 do 10,0 dla hLTF w zależności od źródła jej pozyskiwania i użytej metody analitycznej. Autorzy też przeprowadzili własne badania, w których wykazali, że dla bLTF ustalone pI za pomocą ogniskowania izoelektrycznego i chromatograficznego (ang. *chromatofocusing*) wyniosło odpowiednio 8,8 oraz 8,2-8,9. Dla hLTF uzyskane wyniki były bardziej rozbieżne 8,7 oraz 6,8-8,0 odpowiednio. Również w niniejszej pracy w **Rozdziałach 6.4** oraz **6.5** przedstawiono wyniki oznaczania pI dla bLTF oraz rekombinowanej hLTF, które wynoszą odpowiednio 7,4 oraz 6,6. Do oznaczania użyto pomiar ζ-potencjału względem zmiany pH w 0,09 % roztworze chlorku sodu. Doniesienia literaturowe także wskazują, że pI może różnić się w zależności od stopnia wysycenia żelazem. W przeprowadzonych badaniach przez H. Bokhima i wsp. pI dla bLTF wyznaczono za pomocą pomiaru ζ-potencjału względem pH roztworu [43]. Dla apo-bLTF oraz holo-bLTF znaczenie pI było w zakresie 5,5-6,5 oraz 8,0-9,0 odpowiednio. Ponadto, na pI białka będzie miał wpływ skład glikanów, mianowicie ilość reszt kwasu sjalowego. Ładunek białka jest

ważny ze względu na zdolność jego oddziaływania z cząsteczkami posiadającymi ładunek, między innymi, lipopolisacharydami, białkiem CD14, heparyną, lizosomami, proteoglikanami oraz DNA. Wszystko to może wskazywać na funkcję i właściwości biologiczne LTF. Właśnie z obecnością silnie zasadowych sekwencji w LTF wiążą jeden z możliwych mechanizmów jej działania przeciwbakteryjnego. Są one zlokalizowane na wystającym elastycznym N-końcu białka (reszty 1-7) oraz zewnętrznym obszarze pierwszej helisy (reszty 13-30) subdomeny N1. Te ostatnie stanowią główną część peptydu laktoferycyny o silnym działaniu przeciwbakteryjnym [9]. Ogólny ładunek białka też ma wpływ na oddziaływania z jonami metali, gdyż siły elektrostatycznego odpychania będą miały wpływ na zdolność wiązania przeciw-jonów przekładającą się na siłę wiązań [44].

2.4.2 Zdolność wiązania metali

Właściwości wiązania jonów metali, w szczególności jonów żelaza(III) przez laktoferynę wynikają ze stałej trwałości kompleksu Fe^{3+}-LTF wynoszącej $K \approx 10^{22}$ M^{-1} [9]. Dla innych transferryn wartość ta jest nieco niższa i wynosi około $K \approx 10^{20} - 10^{21}$ M^{-1} [45]. Pomimo tego, że wszystkie transferryny mają podobne miejsca wiążące jony żelaza, powinowactwo hLTF oraz bLTF do jonów żelaza jest wyższe 260- oraz 30-krotnie niż odpowiednie im transferyny surowicy krwi. Skutkiem jest wyższa stabilność tych dwóch kompleksów w obniżonym pH. Dla ludzkiej transferyny w surowicy uwalnianie jonów żelaza zaczyna się już przy pH 6,0 i kończy się przy pH 4,0. Z kolei hLTF uwalnia jony żelaza w zakresie pH 4,0-2,5 [9]. Wolne od jonów żelaza(III) białko określane jest mianem apo-LTF, z kolei białko, w którym oba miejsca wiążące jony żelaza są zajęte nazywane jest holo-LTF. W **Rozdziałach 6.4** oraz **6.5** przedstawiono wyniki oznaczania zawartości żelaza(III) w bLTF oraz rekombinowanej hLTF wykorzystanych w badaniach. Do oznaczania użyto spektrometrię mas sprzężoną z plazmą wzbudzaną indukcyjnie (ang. *Inductively Coupled Plasma Mass Spectrometry, ICP-MS*). Wyniki wykazały, że użyte w badaniach standardy LTF zawierały po dwa Fe^{3+} na jedną molekułę białka, a to znaczy, że były w holo-formie. W literaturze holo-LTF określane jest jak białko „wysycone żelazem". Wykazano jednak, że bLTF może wiązać znacznie więcej żelaza niż można by przewidywać na podstawie jego struktury. Kawakami H. i wsp. stwierdzili, że bLTF i jej peptydy zdolne są do zwiększenia rozpuszczalności (solubilizacji) Fe^{3+}, gdzie każda molekuła białka może utrzymywać w roztworze ponad 70 atomów żelaza. Dla fosfopeptydu kazeinowego zdolność ta była 10-krotnie niższa [46]. Z kolei, Nagasako i wsp. wykazali, że w obecności bLTF roztwór zawierający 10 000 µg/ml jonów żelaza(II) pozostawał klarowny przez nawet 7 dni. W tym samym czasie, w roztworze siarczanu żelaza(II) jon metalu ulegał utlenianiu i wytrącał się osad. Co więcej, albumina surowicy bydlęcej oraz hydrolizaty

kazeiny nie wykazują zdolności hamowania strącania się żelaza(II) [47]. Wszystko to wskazuje na obecność innych miejsc wiążących jony metali (w tym żelaza), jednak o mniejszym powinowactwie chemicznym. **Rozdział 6.3** przedstawia wyniki badań, w których po raz pierwszy zsyntetyzowano kompleks bLTF o wysokiej zawartości Fe^{3+}. Oznaczanie zawartości Fe^{3+} z wykorzystaniem ICP-MS wykazało, że w otrzymanym kompleksie każda molekuła białka była związana z ok. 50 atomami żelaza.

Warto jednak zaznaczyć, że dane literaturowe wskazują, że zdolność transferyn do wiązania jonów żelazo(II) jest dużo niższa w porównaniu do żelaza(III). Stała trwałości Fe^{2+} dla transferyny surowicy wynosi tylko $4 \cdot 10^7$ M^{-1} i jest prawie dwukrotnie mniejsza niż stała trwałości dla wiązania Zn^{2+} ($7,45 \cdot 10^7$ M^{-1}) [45]. Oprócz dolności wiązania jonów żelaza(III) dla apo-LTF wykazano zdolność wiązania innych jonów metali takich jak miedź(II), cynk(II), glin(III), wapń(II) i in. [9,29,48–50]. Jony wapnia wiążą się głównie do grup karboksylowych reszt sjalowych skutkiem czego jest stabilizacja struktury białka [29]. Dane literaturowe pokazują, iż 40 różnych jonów metali może wiązać się do białek z rodziny transferyn [45]. Interesującym jest to, że w mleku ludzkim hLTF występuję z luźno związanym cynkiem(II), gdzie stosunek cynku do białka jest taki sam jak stosunek żelaza(III) do białka. Wskazuję to na możliwą rolę LTF w stabilizacji i absorpcji tego mikroelementu w organizmie [48]. W **Rozdziałach 6.1, 6.4** oraz **6.5** niniejszej pracy wykazano także, że Zn^{2+} oraz Ag^+ mogą tworzyć stabilne kompleksy z holo-LTF.

2.5 Biologiczna aktywność LTF.

2.5.1 Homeostaza mikroelementów

Funkcje fizjologiczne LTF, jak i transferyn, były określane względem ich zdolności wiązania jonów metali, przede wszystkim jonów żelaza(III), w kontekście ich absorbcji z jelit i prawidłowej dystrybucji w organizmie. Co ciekawe, gatunki, które mają wysokie stężenie LTF w mleku, mają zwykle bardzo niskie stężenie transferyny w mleku i odwrotnie. Sugeruje to, że większość ssaków stale zawiera transferynę lub podobne układy białkowe do transferryny w mleku [9]. Ponadto, zmieniona ekspresja receptorów LTF w neuronach dopaminergicznych zaobserwowana została przy zwiększonym stężeniu jonów żelaza(III) w istocie czarnej mózgu (łac. *substancja nigra*, część mózgu odpowiadająca za koordynację ruchów mimowolnych oraz ruchów szybkich). Stwierdzono także, że aktywowane komórki mikroglejowe mogą produkować LTF. Z kolei, LTF jest związana z patogenezą choroby Alzheimera ze względu na jej obecność w blaszkach amyloidowych w układzie limbicznym mózgu [51]. Ponadto, dla linii komórkowej hepatocytów szczurzych wykazano zwiększone pobieranie LTF przy wysokim stężeniu jonów żelaza(III) w płynie hodowlanym [52]. Wszystko to wskazuje na możliwą ochronną funkcję LTF

przeciwko nadmiernej ilości jonów żelaza(III) w układzie. Ponadto, stwierdzono obecność innych metali takich jak cynk, miedź, magnez, mangan oraz glin w rdzeniach blaszek amyloidowych czy też w innych zmianach patologicznych mózgu [53,54]. Jednak w tym wypadku jedna z sugerowanych właściwości LTF jako białka wiążącego jony metali jest nie tylko ochronną przeciwko ich toksycznemu działaniu, ale także możliwego promotora patogenezy [53]. Warto też zauważyć, że LTF poprzez bardzo skuteczne wychwytywanie jonów żelaza(III) działa jak przeciwutleniacz zapobiegając tworzeniu się aktywnych form tlenu w tak zwanych reakcjach Fentona [55]. Poza tym, LTF także hamuje indukowane lipopolisacharydami wytwarzanie nadtlenku wodoru neutrofilami [9].

2.5.2 Właściwości przeciwdrobnoustrojowe

LTF wykazuje właściwości przeciwdrobnoustrojowe. Białko to występuje w płynach ustrojowych narządów, które mają bezpośredni kontakt ze środowiskiem zewnętrznym, w szczególności dotyczy to układu pokarmowego, oddechowego czy rozrodczego. Podawanie LTF doustnie ma działanie chroniące gospodarza przed drobnoustrojami. Działanie bakteriobójcze LTF zostało szeroko udokumentowane zarówno w przypadku bakterii Gram-dodatnich, jak i Gram-ujemnych [9]. Jednak mechanizm działania przeciwdrobnoustrojowego LTF wciąż jest dyskutowany. Najbardziej znanym mechanizmem działania jest usuwanie jonów żelaza(III) niezbędnych do wzrostu bakterii. Chociaż, *Lactobacilli* są powszechnie uważane za jedyne z nielicznych mikroorganizmów bakteryjnych zdolnych do wzrostu bez obecności jonów żelaza(III) w układach [56]. Stwierdzono także, że LTF wspiera wzrost laktobakterii [9]. W tym samym czasie bakterie kwasu mlekowego znane są ze zdolności wspierania układu odpornościowego człowieka [57], co można uważać za kolejny mechanizm działania LTF. Drugim najbardziej popularnym mechanizmem przeciwdrobnoustrojowego działania LTF jest jej bezpośrednie oddziaływanie z komórkami bakteryjnymi poprzez ujemnie naładowane lipopolisacharydy lub poryny bakterii Gram-ujemnych lub też kwas lipotejchojowy bakterii Gram-dodatnich. Wiązania takie naruszają strukturę i funkcję membran bakteryjnych [9]. Dodatkowo, zdolność do rozrywania błon bakteryjnych może również wynikać ze zdolności LTF do konkurowania o Ca^{2+} z lipopolisacharydowymi miejscami wiązania Ca^{2+} na błonach bakteryjnych [29]. Czynny udział biorą w tym reszty sjalowe N-glikanów LTF. LTF zapewnia również dodatkową ochronę, zapobiegając adhezji bakterii i wirusów do komórek gospodarza [9], gdzie glikozylacja białek może mieć znaczący wpływ na ten proces. Na przykład rodzina *Enterobacteriacae* produkuję fimbrie typu 1, które zdolne są wiązać łańcuchy glikanu wielomannozowego na komórkach eukariotycznych. bLTF charakteryzuje się dużą zawartością struktur wielomannozowych, które niespecyficznie zapobiegają adhezji odpowiednich

bakterii [29]. Ciekawym jest także badanie przeprowadzone przez Barboza M. i wsp., które wykazało, że glikany uwolnione z hLTF wykazują zdolność hamowania adhezji bakterii z rodziny *Salmonella* i *Listeria* (ale nie *Escherichia*) do linii komórkowych Caco-2 [31]. Ochronna funkcja LTF jest także skutkiem jej zdolności regulacji procesów immunologicznych. Związane to jest między innymi z regulacją dojrzewania i migracji komórek układu odpornościowego takimi jak makrofagi, komórki dendrytyczne, komórki NK oraz limfocytów T i B. LTF także reguluje wydzielanie się cytokin i chemokin, które biorą udział w procesie zapalnym [9].

2.5.3 Regulacja procesów biologicznych

LTF posiada także funkcje cząsteczki sygnałowej [58]. Ponadto, jest ona czynnikiem regulującym proliferację oraz migrację wielu komórek ciała. Dzięki temu LTF posiada potencjał w regeneracji licznych struktur anatomicznych, takich jak kości, chrząstki, skóra, błony śluzowe, rogówka, ścięgna, tkanka tłuszczowa, układ naczyniowy. Regenerujące działanie LTF jest skomplikowane i często jest związane z wpływem na ekspresję białek, które biorą udział w różnych procesach fizjologicznych organizmu. Na przykład gojenie się ran rogówki składa się z szeregu zdarzeń fizjologicznych regulowanych przez cytokiny zapalne. Badania *in vitro* oraz *in vivo* wykazują zdolność LTF do regulacji ekspresji tych cytokin, przyspieszając w ten sposób proces gojenia się ran rogówki, mianowicie leczenie z LTF obniżyło poziom IL-1 i stymulowało ekspresję płytkopochodnego czynnika wzrostu i IL-6 [8]. Proces gojenia się ran skórnych też częściowo jest kontrolowany poprzez cytokiny zapalne. Prozapalne cytokiny IL-1, IL-6 oraz TNF-α aktywują fibroblasty i keratynocyty [59]. Z kolei, angiogeneza jest kontrolowana poprzez czynnik wzrostu śródbłonka naczyniowego A (VEGF-A), którego ekspresja jest zwiększona po zastosowaniu LTF [8]. Działanie LTF odbywa się poprzez oddziaływanie z odpowiednimi receptorami komórkowymi. Ponieważ LTF została po raz pierwszy zidentyfikowana jako składnik ochronny mleka i siary, dlatego też pierwszy odkryto receptor LTF w jelicie cienkim. Jest to białko o nazwie intelektyna [60]. Wykazano, że zarówno natywna ludzka LTF, jak i jego fragmenty mogą brać udział w ukierunkowanym transporcie Fe^{3+} do błony śluzowej poprzez wiązanie się z receptorami LTF, co można uznać za specyficzny mechanizm absorpcji żelaza za pośrednictwem nośnika [61,62]. Interesującym jest także fakt, że intelektyna ludzka może wiązać także bLTF oraz jej pochodne peptydy [60]. Chociaż wiązanie się LTF do intelektyny przede wszystkim kojarzone jest z jej zdolnością hamowania adhezji bakterii. Stwierdzono jednak, że niestrawiona cząsteczka LTF jest w stanie dotrzeć do krwi obwodowej z jelita już po 10–20 min po podaniu dożołądkowym. Po pobraniu LTF do krwi jest ona dystrybuowana do różnych tkanek ciała. Wskazuje to na możliwość wykorzystania LTF jako nośnika leków oraz

mikroelementów [63]. Z kolei, LTF podawana dożylnie jest szybko usuwana z krwiobiegu przez hepatocyty, prawdopodobnie przy pomocy receptora LRP-1 [58]. Bardzo ważnym jest fakt, że LTF może przenikać przez barierę mózg-krew, co również jest regulowane przez odpowiednie receptory [64]. Zatem jest to molekuła o dużym potencjale w terapii ukierunkowanej. W **Rozdziale 6.2** wykazano wyniki badań właściwości przeciwdrobnoustrojowych nanokompozytu srebra z bLTF. Stwierdzono, że nanokompozyt wykazuje kilkakrotnie większą zdolność hamowania wzrostu bakterii niż odpowiednie stężenie wolnych Ag^+. Wyniki wskazują na możliwe wykorzystanie tej substancji aktywnej w preparatach farmaceutycznych do leczenia ran przewlekłych. Z kolei, w **Rozdziale 6.3** przedstawiono wyniki cytotoksyczności kompleksu Fe^{3+}-bLTF. Kompleks ten nie wykazywał większej toksyczności niż odpowiednie stężenie Fe^{3+} w formie cytrynianu. Ponadto, badanie uwalniania jonów żelaza z kompleksu w płynach modelowych imitujących warunki w różnych odcinkach układu pokarmowego wykazało, że nawet w kwaśnych warunkach z białkiem pozostaje związanych więcej niż 40% jonów żelaza(III). Wszystko to wskazuje na możliwość wykorzystania kompleksu w preparatach leczniczych oraz suplementach diety do leczenia stanów związanych z niedoborem tego pierwiastka, m. in. niedokrwistości.

3. Problem badawczy

3.1 Oddziaływania metal-białko

Tworzenie się kompleksów metal-białko jest jednym z najważniejszych problemów w biochemii. Z podstaw chemii koordynacyjnej wynika, że właściwości kompleksów metal-białko różnią się w zależności od natury wstępującego w oddziaływania jonu metalu i białka. Białka są polimerami biologicznymi ze złożoną strukturą i licznymi reaktywnymi grupami funkcyjnymi łańcuchów bocznych, które potencjalnie mają zdolność wiązania większości jonów metali, w tym d-elektronowych. W układach biologicznych kationy metali zawsze towarzyszą białkom. Można bezpiecznie założyć, że oprócz metali alkalicznych każdy kation metalu, który trafia do żywego organizmu, spędza znaczną część swojego czasu związany z białkami, zanim zostanie wydalony lub osadzony w tkance szkieletowej [44]. Spośród ogromnej różnorodności naturalnych białek są takie, w których atom metalu stanowi integralną cześć struktury białka po eliminacji, której białko częściowo lub w całości może stracić swoją funkcję biologiczną (aktywność biologiczną). Białka takie określane są mianem metaloprotein. W związku z tym, jony metali są składnikami, które nie tylko współistnieją z innymi cząsteczkami w organizmie, ale są aktywnymi uczestnikami procesów biologicznych [65]. Jony metali, takie jak m.in. kationy cynku (II), wapnia pełnią funkcję: strukturalną, stabilizując prawidłowe ułożenie trójwymiarowe białek poprzez takie struktury jak palce cynkowe, EF ręka (ang. *EF hand*) i in.; kofaktory w enzymach, biorą udział w procesach biosyntezy, detoksykacji oraz wytwarzania energii; jako cząsteczki sygnałowe; w procesach obronnych organizmu; i in. [66–68]. Od dawna naukowcy poszukiwali odpowiedzi na pytania, w jaki sposób zachodzą oddziaływania pomiędzy białkiem a jonami matali, jakie mechanizmy są w to zaangażowane. Ponadto, z rozwojem technologii pojawiły się leki na bazie jonów metali (w tym nanokompozyty) dlatego też ta wiedza jest ważna do przewidywania dróg wchłaniania, transportu, przechowywania, toksyczności i mechanizmu działania na organizm. Interakcja związków z jonami metali z białkami odgrywa również rolę w przemyśle spożywczym i nutraceutycznym [69].

Jony metali oddziałują z białkami, modulując tym samym ich aktywność biologiczną. W przypadku naturalnych metaloprotein prawidłowe działanie jest możliwe tylko po wiązaniu jonów metali na przykład w miejscu aktywnym enzymu. Dla metaloproteiny LTF jej właściwości i funkcje biologiczne zależne są od stopnia wysycenia w jony żelaza [9,29]. Z kolei, dla związków sztucznych (tzn. metalokompleksów oraz nanokompozytów) aktywność biologiczna w dużej mierze zależna jest od użytego do syntezy jonu metalu. Do przykładu silne przeciwdrobnoustrojowe właściwości wykazują nanokompozyty zsyntetyzowane z użyciem jonów cynku oraz owoalbuminy [70] czy też srebra z bLTF[17]. Ważne, aby zaznaczyć, że

niemodyfikowane białka nie wykazywały działania przeciwbakteryjnego przeciwko przebadanym szczepom. Ocena zmian zachodzących w białkach po interakcjach z jonami metali ma niebagatelne znaczenie, ponieważ białka pełnią wiele funkcji w organizmie człowieka i znajdują zastosowanie w wielu gałęziach przemysłu. Kluczowe dla oceny takich zmian są następujące czynniki: (a) grupy funkcyjne oddziałujące z jonem metalu i w konsekwencji siła utworzonych wiązań, (b) tworzenie się nowych miejsc wiążących oraz (c) zmiany w strukturze białka determinujące oddziaływania białka z ligandami, (d) agregacja białek oraz (e) tworzenie się nowych struktur takich jak nanocząstki (NPs) [71].

Poza naturalnie występującymi metaloproteinami, skutkiem interakcji kationów metali z białkami mogą być także metalokompleksy oraz nanokompozyty. Metalokompleksy są sztucznie utworzonymi systemami, do otrzymywania których często są niezbędne specyficzne warunki, w tym dobór odpowiedniego pH, obecność dużych stężeń jonów metalu lub modyfikacja białek [72,73]. Pod czas takich interakcji indukowane przez jony metali zmiany w strukturze białka mogą doprowadzać do powstania nowych (sztucznych) miejsc wiążących. Jednak większość wiązań w metalokompleksach są dużo słabsze niż w metaloproteinach i odbywają się poprzez słabe oddziaływania międzycząsteczkowe takie jak oddziaływania elektrostatyczne, siły Wan-der-Waalsa, wiązania donorowo-akceptorowe lub też wodorowe [71]. Niemniej jednak, pozwala to na uzyskanie związków, w których nie jest zachowana stechiometria tak jak w metaloproteinach. W przypadku, gdy pod czas interakcji metalu z białkiem powstają nowe struktury, takie jak NPs, związki takie nazywane są nanokompozytami [17,70]. Mimo to, grupy funkcyjne, które bezpośrednio oddziałują z NPs najprawdopodobniej będą warunkowane właściwościami metali tworzącymi nanokompozyt [17,74].

Aby właściwie opisać procesy, które mogą zachodzić między oddziałującymi związkami, należy wziąć pod uwagę głęboką chemię wchodzących w reakcję molekuł. Uwzględnienie udziału aminokwasów i peptydów jako budulców białka może uprościć opis oddziaływań tych ostatnich z jonami metali. Następnie ekstrapolacja uzyskanych danych dla peptydów i aminokwasów może być wykorzystana do opisu interakcji bardziej skomplikowanych cząsteczek, takich jak białka. Takie podejście zastosowali T. Sych i wsp. do przewidywania miejsc powstawania klastrów Ag^0_n w białku [74]. N. Tang i L. H. Skibsted przedstawili dyskusję na temat biodostępności Zn^{2+} z serwatki [75]. Z drugiej strony autorzy przedstawili uzyskane dane próbując wyjaśnić rolę poszczególnych aminokwasów w wiązaniu Zn^{2+} z białkiem, a tym samym w homeostazie Zn^{2+}. Ogólnie podejście to jest dobrze znane z pierwszych badań nad tworzeniem się kompleksów aminowych metali [44]. Jednak takie założenie powinno być stosowane ostrożnie, z uwzględnieniem całego spektrum efektów

wewnątrz- i supramolekularnych, które mogą mieć wpływ na interakcje. Na przykład, chociaż jony Zn^{2+} tworzą względnie stabilne kompleksy z glicyną, jednak oddziaływanie to nie jest istotne dla wiązania jonów metali z białkami. W tym przypadku większe znaczenie mają łańcuchy boczne aminokwasów wchodzących w skład białka. W przypadku małych peptydów wykazano, że azot z wiązania peptydowego może uczestniczyć w chelatowaniu jonów metalu [44].

Selektywność oddziaływania jonów metali z bocznymi łańcuchami białek można najlepiej przewidzieć na podstawie teorii miękkich i twardych zasad i kwasów Lewisa (ang. *Hard and Soft Acids and Bases, HSAB*). Teoria ta określa kwasy Lewisa jako substancje chemiczne, które w wiązaniach donorowo-akceptorowych przyjmują parę elektronów od zasad Lewisa. Ponadto, twarde kwasy Lewisa oddziałują z twardymi zasadami, a miękkie z miękkimi. Można także wyodrębnić kwasy i zasady pośrednie. Zgodnie z tą teorią jony srebra, cynku i żelaza(III) należą do trzech różnych grup – odpowiednio do kwasów miękkich, pośrednich oraz twardych. Zatem też Ag^+ z białkami najpewniej oddziałuje poprzez grupy zawierające siarkę lub też pierścień fenolowy. Dla Zn^{2+} najbardziej charakterystycznymi będą wiązania poprzez azot imidazolowy histydyny, indolowy tryptofanu czy też wiązania peptydowego. Z kolei, Fe^{3+} silnie oddziałuję poprzez grupy zawierające atom tlenu, tzn. karboksylowe, hydroksylowe czy też karbonylowe [44,45]. Badania wskazują, że metale te w zależności od warunków mogą oddziaływać także i z innymi grupami funkcyjnymi, jednak tworząc dużo słabsze wiązania. Najszybciej odbywają się interakcje z grupami karboksylowymi kwasów glutaminowego oraz asparaginowego przez oddziaływania elektrostatyczne [17,44,70].

Efektywność tworzenia się kompleksów jest zależna od dostępności odpowiednich grup funkcyjnych i to dlatego, że jony wodorowe będą w dużym stopniu konkurować z jonem metalu o ligandy (grupy funkcyjne). Dostępność grup funkcyjnych można kontrolować poprzez zmianę pH. Dodatkowo, deprotonowanie grup funkcyjnych białka zmienia ogólny ładunek układu biokoloidalnego (jakim są białka), co też w dużym stopniu będzie miało wpływ na efektywność wiązania jonów metali. Wcześniejsze badania wykazały, iż ze względu na dodatni ładunek jonów metali efektywność wiązania się do cząsteczek o tym samym ładunku jest dużo mniejsza [44]. Zatem też ze względu na kationowy charakter molekuły LTF w warunkach fizjologicznych problemem badawczym było określenie warunków, w których można będzie uzyskać stabilne kompleksy. Ważnym zaś była charakteryzacja białka pod względem jego ładunku w mieszaninie reakcyjnej, dlatego też przeprowadzono pomiar ζ-potencjału obu modelowych białek, tzn. bLTF (**Rozdział 6.4**) oraz rekombinowanej hLTF (**Rozdział 6.5**) w zależności od pH roztworu. Pozwoliło to także określić punkt izoelektryczny (pI) obu białek, który wyniósł odpowiednio 7,4

oraz 6,6. Wyniki wskazują, że białka te mają ładunek ujemny, sprzyjający wiązaniu się jonów metali, w warunkach bardziej zasadowych. Jednak przy wyższych pH zachodzi hydroliza akwakompleksów metali z utworzeniem nierozpuszczalnych tlenków [44]. W takim wypadku można używać chelatowania jonów metali związkami niskocząsteczkowymi, co z kolei może zmniejszać efektywność wiązania się jonów metali do białka przez konkurowanie związku chelatującego za dany kation metalu. Co stanowi kolejny problem związany z doborem warunków syntezy bogatych w jony metali kompleksów białkowych. Badania w tym kierunku były przeprowadzone na przykładzie wiązania się jonów cynku do bLTF. Zbadano wpływ pH, zawartość jonów cynku oraz cytrynianu w roztworze na efektywność wiązania (**Rozdział 6.4**). Oznaczono także masę molekularną użytych białek, co jest ważne przy określeniu stechiometrii zachodzących reakcji, która z kolei jest niezbędna do przewidywania zachodzących procesów podczas oddziaływań metal-białko. Dlatego też w tym celu zostały użyte metody rozdzielania w żelu poliakralamidowym oraz spektrometria mas z jonizacją/desorpcją wspomagana matrycą. Ponadto, badanie tę umożliwiły także określenie czystości użytych preparatów względem obecności innych białek (**Rozdziały 6.4, 6.5**).

3.2 Kompleksy srebra z laktoferyną.

W ostatnich latach coraz więcej mówi się o bakteriach lekoopornych. Ważne jest to w leczeniu ran przewlekłych, które dotyka nawet do 2% populacji światowej. Pacjenci z przewlekłymi zakażeniami ran skarżą się na ból i ograniczenie aktywności fizycznej. Ponadto, takie schorzenia wiążą się z ciągłą potrzebą profesjonalnej opieki medycznej, co negatywnie wpływa zarówno na rozkład dnia, jak i finanse osobiste. Stwierdzono, że ponad 70% zakażeń wywołanych jest przez bakterie oporne na jeden lub więcej powszechnie stosowanych antybiotyków. W ostatnim czasie cieszą się zainteresowaniem preparaty na bazie NPs metali, gdyż wykazują one skuteczne działanie przeciwbakteryjne. Ponadto, wykazano, że w połączeniu z innymi związkami bakteriobójczymi można uzyskać środki o ulepszonym działaniu przeciwko bakteriom chorobotwórczym [76].

Najbardziej znanymi są właściwości przeciwdrobnoustrojowe kationów srebra (Ag^+) oraz odpowiednio AgNPs, które są „gorącym tematem" wielu badań naukowych. Zainteresowanie to związane jest przede wszystkim z długą historią skutecznego wykorzystania srebra w medycynie jako środka przeciwbakteryjnego oraz fakt, że do tej pory opisano tylko jedną bakterię, *P. stutceri* (naturalnie występuję w kopalniach srebra), która jest całkowicie odporna na Ag^+[77]. Srebro jest także unikatowym indywiduum pod względem chemicznym. Jest ono najbardziej reaktywnym wśród wszystkich metali „szlachetnych". Metal ten także wykazuje najwyższe przewodnictwo elektryczne i cieplne oraz najniższe temperatury topnienia

i wrzenia, co przekłada się na właściwości AgNPs. Srebro w postaci NPs posiada nawet bardziej unikatowe właściwości, które umożliwiają wykorzystanie ich w wielu dziedzinach techniki i medycyny, np.: w pozyskiwaniu energii słonecznej, w urządzeniach elektronicznych, zaawansowanych technikach analitycznych, m.in. powierzchniowo wzmocniona spektroskopia Ramana (ang. *Surface Enhanced Raman Spectroscopy, SERS*) i laserowa jonizacja/desorpcja próbki wspomagana nanostrukturami (ang. *Nanostrure-Assisted Laser Desorption/Ionization, NALDI*), kataliza i fotokataliza, zastosowania środowiskowe, bioobrazowanie i bioanaliza, jako środek przeciwbakteryjny lub środek w terapii przeciwnowotworowej. Możliwości wykorzystania AgNPs do konkretnych rozwiązań są uwarunkowane właściwościami fizyko-chemicznymi, co między innymi zależne jest od metod ich syntezy. **Rozdział 6.1** niniejszej rozprawy doktorskiej stanowi przegląd literaturowy dotyczący metod syntezy oraz właściwości AgNPs. Praca ta przedstawia także metaanalizę dotyczącą technik instrumentalnych wykorzystywanych do badań właściwości NPs, nanokompozytów oraz innych materiałów i substancji chemicznych. Najbardziej cenne jest wskazanie zalet i wad poszczególnych technik badawczych.

Synteza AgNPs może być przeprowadzona na wiele sposobów z użyciem metod fizycznych, chemicznych czy też biologicznych, gdzie do syntezy AgNPs wykorzystywane są związki i układy pochodzenia naturalnego takie jak ekstrakty, białka, bakterie i in. Najczęściej używanym prekursorem w każdej z rodzajów syntez AgNPs jest azotan srebra, który w obecności nawet śladowych ilości związków organicznych ulega fotoredukcji. Należy nadmienić, iż w wyniku biologicznej syntezy AgNPs często otrzymywane są nanokompozyty, gdzie NPs stanowią tylko małą część uzyskanego materiału. Synteza metodami biologicznymi ma szereg zalet między innymi zmniejszone zużycie i emisja w środowisku szkodliwych związków chemicznych. Ponadto, NPs zsyntetyzowane metodami biologicznymi najczęściej wykazują mniejszą toksyczność wobec komórek eukariotycznych, dzięki czemu mogą być wykorzystywane w rozwiązaniach biomedycznych. Jednak wadą tych metod jest bardzo ograniczona kontrola podstawowych właściwości fizyko-chemicznych NPs podczas syntezy. Stanowi to poważny problem badawczy, ponieważ rozmiar, kształt oraz skład chemiczny NPs określa ich aktywność biologiczną. Zatem w ramach niniejszej rozprawy podjęto próbę określenia wpływu warunków syntezy na właściwości otrzymanych nanokompozytów metal-białko, przede wszystkim rozmiar inkluzji metalicznej (**Rozdział 6.2**). W tym celu do syntezy użyto szereg różnych stężeń srebra oraz zbadano właściwości utworzonych kompleksów. Zaobserwowano zależność, w której przy zwiększeniu stężenia Ag^+ w roztworze zwiększa się zarówno rozmiar jak i zawartość NPs w nanokompozycie. Jednak przy przekroczeniu pewnego

stężenia jonów metali w mieszaninie reakcyjnej mimo znacznego wzrostu zawartości srebra w produkcie zaobserwowano mniejszy rozmiar NPs. Interesującym jest to, że zmiany tę były zbieżne ze zmianami w kształcie krzywej izotermy adsorpcji użytej do opisu procesów mechanizmu adsorpcji Ag^+ na białku. Wskazuje to na możliwość wykorzystania tego podejścia do przewidywania właściwości fizyko-chemicznych nanokompozytów tego typu. Ponadto, podejście to wraz z innymi technikami instrumentalnymi ujawniło złożony charakter adsorpcji Ag^+ oraz heterogenność zachodzących procesów. Obliczono także zmianę wolnej energii Gibbsa (ΔG), która dla najniższych stężeń jonów srebra wynosiła od $-22,76$ do $-24,74$ kJ/mol. Wyniki wskazują na spontaniczny charakter zachodzącej reakcji. Praca pt. „*Synthesis, physicochemical characterization, and antibacterial performance of silver–lactoferrin complexes*" również przedstawia wyniki fizykochemicznej charakteryzacji otrzymanych nanokompozytów. Między innymi pozwoliło to na wskazanie grup funkcyjnych, które biorą udział w tworzeniu się NPs oraz zmian zachodzących w strukturze białka. W tym celu wykorzystano spektroskopię w podczerwieni z transformacją Fouriera (FTIR) oraz Ramana. Są to uzupełniające siebie metody, gdyż grupy funkcyjne, które mają słaby sygnał na widmach Ramana w tym samym czasie mogą wykazywać intensywne pasmo na widmach FTIR. Uzyskane dane dla kompleksów potwierdzają przeprowadzone wcześniej badania modelowania molekularnego dla wiązania się Ag^+ do bLTF [17].

Kolejnym zadaniem związanym z możliwością użycia nowych substancji do wykorzystania w preparatach leczniczych jest zbadanie ich skuteczności oraz cytotoksyczności. Podstawowymi metodami używanymi do tych celów są metody *in vitro* pozwalające określić żywotność komórek w obecności badanego związku chemicznego lub też minimalne stężenie hamujące (MIC). Wyniki przeprowadzonych badań wskazują na to, iż zsyntetyzowany nanokompozyt wykazuje silne działanie przeciwbakteryjne przeciw wybranym bakteriom, które było kilkakrotnie większe niż odpowiednie stężenie wolnych jonów srebra. Jednak wykazuje on podobne działanie toksyczne na komórki L929 fibroblastów mysich. Interesujące jednak jest to, że nanokompozyt hamował wzrost komórek, ale nie doprowadzał do ich apoptozy, co było obserwowane dla układów traktowanych jonami Ag^+. Wskazuje to na inny mechanizm działania toksycznego. Ogólnie dla AgNPs najbardziej znanym mechanizmem działania jest uwalnianie Ag^+, który inaczej nazywany jest mechanizmem „Konia Trojańskiego". Dla nanokompozytów bLTF ze srebrem przeprowadzono badania desorpcji w trzech różnych pH, mianowicie 1,2; 4,5 oraz 6,8. W zależności od pH uwalnianie jonów z nanokompozytu wyniosło od 64 do 81%, co wskazuje na możliwą toksyczność substancji względem uwalnianych Ag^+ (**Rozdział 6.2**). Jednak, przeprowadzona metaanaliza w kierunku określenia możliwych mechanizmów działania

wykazała, że AgNPs ma dużo szerszy spektrum działania toksycznego w porównaniu do wolnych jonów srebra. Wyniki tego badania pozwoliły na wyodrębnienie dwóch dodatkowych mechanizmów polegających na bezpośrednim oddziaływaniu NPs z komórkami żywymi – kwantowo-mechaniczny oraz indukcyjny. Teoretyczne podstawy każdego z mechanizmów bardziej szczegółowo opisano w pracy przeglądowej pt. *„Silver nanoparticles: synthesis, investigation techniques, and properties"*, która stanowi **Rozdział 6.1** przekładanej rozprawy doktorskiej.

3.3 Kompleksy żelaza z laktoferyną.

Niedokrwistość z niedoboru żelaza (ang. *Iron Deficiency Anemia, IDA*) jest problemem o znaczeniu światowym. IDA dotyczy ponad 1,68 miliarda ludzi na całym świecie. Znaczenie żelaza w organizmie jest nie do przecenienia, ponieważ wchodzi ono w skład hemu hemoglobiny i mioglobiny, które biorą udział w transporcie i magazynowaniu tlenu. Ponadto żelazo jest również częścią cytochromów, peroksydaz, syntaz tlenku azotu i innych enzymów, które biorą udział w procesach biosyntezy i produkcji energii, detoksykacji, obronie gospodarza, sygnalizacji komórkowej i in. Żelazo w organizmie człowieka może być wchłaniane w dwóch postaciach: hemowej (z mięsa) i niehemowej. Żelazo niehemowe wchłaniane jest głównie w formie zredukowanej Fe^{2+} poprzez transport niespecyficzny z udziałem transportera dwuwartościowych jonów metali-1 (ang. *Divalent Metal Transporter 1, DMT-1*), natomiast do organizmu dostaje się najczęściej w formie utlenionej Fe^{3+}. Biodostępność Fe^{3+} w dużym stopniu zależy od jego rozpuszczalności, co oznacza, że musi być on związany z białkami lub innymi hydrofilowymi chelatorami [67,78].

Jony Fe^{3+} silnie oddziałują z grupami funkcyjnymi zawierającymi tlen. Charakterystycznym jednak dla żelaza jest także tworzenie się kompleksów wielordzeniowych (wielonuklearnych), w których kilka atomów żelaza łączą się ze sobą w jednym centrum poprzez mostkowe cząsteczki takie jak atom tlenu lub też cząsteczki wody. Struktury takie obserwowane są także w organizmach żywych. Hydroksylaza wyizolowana z *Methylococcus capsulatus* zawiera dwunuklearne centrum w miejscu aktywnym [79]. Znane jest także bardziej interesujące białko, w którym żelazo tworzy nieorganiczne depozyty ferrihydrytu. Białko to nazywano ferrytyna i wykonuję ono w organizmie funkcję magazynowania żelaza. Dla żelaza także wykazana jest możliwość spontanicznej nanomineralizacji z białek bogatych w ten pierwiastek, mianowicie trensferryn [80]. Ponadto, nieorganiczne żelazo jest niestabilne w obecności tlenu i dąży do tworzenia strątów tlenków żelaza(III) już w środowisku słabo kwaśnym pH > 4,0 [81]. Ponadto, żelazo w obecności związków redukujących, którymi są także białka, może ulegać odwracalnej redukcji z utworzeniem reaktywnych form tlenu [82]. Takie procesy mogą

skutkować degradacją białka. Zatem nadrzędnym problemem do rozwiązania było uzyskanie bogatych w żelazo homogennych kompleksów przy jednoczesnym zachowaniu integralności białka. W pracy pt. *„Synthesis and physicochemical characterization of bovine lactoferrin supersaturated complex with iron (III) ions”* opisano wyniki przeprowadzonych badań. Jak i w przypadku z nanokompozytami srebra, do przewidywania właściwości kompleksów bLTF z żelazem przydatnym okazało się zbadanie izotermy adsorpcji. Na podstawie jej kształtu zostały dobrane warunki syntezy homogennego kompleksu. Z kolei, dopasowanie modelu Langmuira umożliwiło dość dokładnie przewidzieć zawartość żelaza w syntetyzowanym kompleksie. Ponadto, podejście to pozwoliło na oszacowanie ΔG reakcji, która w zależności od użytych stężeń Fe^{3+} wynosiła od $-$ 13,9 do $-$ 24,82 kJ/mol. Uzyskane liczby są podobne do tych otrzymanych dla nanokompozytu srebra, gdzie w czasie syntezy tworzą się NPs, co wskazuję na duże powinowactwo Fe^{3+} do bLTF oraz tworzenie się silnych wiązań. Ponadto, ujemne znaczenie ΔG potwierdza spontaniczną naturę zachodzących reakcji. Dodatkowo, badania stabilności kompleksu w modelowych płynach ustrojowych wykazało, że w pH bliskim neutralnemu (pH = 6,8) nie zachodziła desorpcja Fe^{3+}, a nawet w pH = 1,2 desorpcja wynosiła nie więcej niż 60%.

Do określenia możliwych miejsc wiążących Fe^{3+} oprócz spektroskopii w podczerwieni użyto metodę dokowania molekularnego. Pomocnym w tym był serwer przewidywania miejsc wiązania jonów metali i dokowania MIB (ang. *Metal Ion-Binding*) opracowany przez tajwańskich naukowców [83]. Poszukiwanie miejsc wiążących bazowało na porównaniu sekwencji aminokwasów białka badanego z sekwencjami szablonowymi z bazy danych programu. Metoda ta pozwoliła na określenie co najmniej 26 dodatkowych kombinacji reszt aminokwasowych, które mogą tworzyć miejsca wiążące Fe^{3+}. Jednak metoda ta jest ograniczona obecnymi w bazie danych sekwencjami oraz nie uwzględnia innych czynników takich jak cząsteczki wody w sferze koordynacyjnej żelaza. Bardziej dokładny opis uzyskanych wyników znajduje się w **Rozdziale 6.3**. Przedstawiono tam także wstępne badania dotyczące cytotoksyczności uzyskanych kompleksów. Badania *in vitro* na komórkach ludzkiego gruczolaka okrężnicy Caco-2 oraz fibroblastów mysich L929 wykazały, że kompleks bLTF nie posiada większej toksyczności niż odpowiednie stężenie Fe^{3+} podawanego jako sól cytrynianu żelaza.

3.4 Kompleksy cynku z laktoferyną.

Cynk jest drugim po żelazie najbardziej rozpowszechnionym pierwiastkiem śladowym niezbędnym do funkcjonowania wszystkich żywych organizmów. Niedobór cynku może spowodować szereg stanów chorobowych z licznymi objawami takimi jak przewlekła biegunka, łysienie, zaburzenia smaku, niewydolność układu odpornościowego, dysfunkcja mózgu,

upośledzenie gojenia się ran, utrata apetytu, przewlekłe stany zapalne, choroby wątroby oraz zmiany neuropsychologiczne. Cynk odpowiada za szeroki zakres funkcji w organizmie zarówno jak strukturalny czynnik białek oraz bezpośrednio jak cząsteczka sygnałowa. Cynk występuje jako kofaktor w sześciu klasach enzymów: oksydoreduktazy, transferazy, hydrolazy, ligazy oraz liazy. Ponadto jako cząsteczka sygnałowa bierze udział w sygnalizacji zewnątrz i wewnątrzkomórkowej w procesach neuromodulacji, odpowiada za kontrolę produkcji insuliny, inhibicję enzymów, modulację wielu szlaków sygnałowych i in. [66]. W grupie ryzyka niedoboru cynku są dzieci oraz osoby starsze. Niewystarczająca absorpcja cynku z pokarmu wynika z niskiej jego zawartości w żywności związanej z uprawą w glebach ubogich w cynk lub też stratami tego mikroelementu podczas przetwórstwa żywności. Posiłki bogate w kwas fitynowy, ligninę, niektóre włókna pokarmowe zapobiegają wchłanianiu się cynku. Sugeruje się, że ponad 25% światowej populacji jest zagrożone niedoborem cynku, co wskazuje na konieczność dodatkowej suplementacji tego mikroelementu [84]. Dla innych mikroelementów pobieranie cynku jest promowane przez białka oraz peptydy [75]. Wskazuje to na duży potencjał kompleksów cynku zsyntetyzowanych na bazie białek w leczeniu stanów chorobowych związanych z niedoborem tego mikroelementu.

W odróżnieniu od jonów żelaza i srebra, w warunkach fizjologicznych cynk nie ulega reakcjom utleniania-redukcji, co ogranicza jego oddziaływania głównie związane ze zmianami w sferze koordynacyjnej. Zn^{2+} tworzy najbardziej silne wiązania z grupami sulfhydrylowymi (inaczej też grupy tiolowe) białka oraz grupami zawierającymi azot. Jednak, grupy tiolowe w białkach zwykle tworzą mostki dwusiarczkowe co uniemożliwia ich interakcję z większością jonów metali. Z kolei, oddziaływania z grupami aminowymi, indolowymi czy też imidazolowymi utrudnione ze względu na duży stopień ich protonowania w pH neutralnym i kwaśnym, gdzie najniższy pK $\approx$ 6,0 ma grupa imidazolowa histydyny [44,85]. W związku z tym przeprowadzono proces wiązania jonów cynku do bLTF w pH 6,0. Na uwagę zasługuje fakt, iż adsorpcja jonów cynku do białka w tych warunkach nie zaszła. Wskazało to na wpływ innych czynników na oddziaływania tego typu, do których można zaliczyć elektrostatyczne odpychanie dodatnio naładowanych cząsteczek wchodzących w interakcję. Stanowi to poważny problem badawczy, gdyż niesprzyjającym czynnikiem jest także to, że w pH alkalicznym dochodzi do hydrolizy wody w sferze koordynacyjnej cynku, a następnie wytrącaniu się nierozpuszczalnych tlenków. Wymagało to poszukiwanie odpowiednich układów buforowych, które umożliwiłyby skuteczną syntezę bogatych w cynk kompleksów. W tym celu wykorzystano bufory węglanowo-cytrynianowe. W kolejnym kroku, przeprowadzono badania w pH 7,4 (punkt izoelektryczny bLTF) oraz 8,6, co było przydatnym do określenia wpływu ładunku białka na

zdolność wiązania. Praca pt. *„Synthesis and physicochemical characterization of zinc-lactoferrin complexes"* przedstawia uzyskane wyniki. Produkty interakcji z Zn^{2+} zostały zbadane metodami spektroskopowymi. Mimo tego, że wiązania cynku nie zachodziło w pH 6,0 zauważono jednak przesunięcie pasm na widmach FTIR i Ramana. Dalsze badania za pomocą ICP-MS wykazały zmiany w zawartości towarzyszących białku metali, tzn. żelazo, magnez, wapń, sód i potas, co wyjaśnia zachodzące zmiany na widmach. Dla kompleksów Zn-bLTF zsyntetyzowanych w pH 7,4 oraz 8,6 stwierdzona została zmiana w strukturze białka oraz udział głównie grup karboksylowych we wiązaniu cynku. Bardziej dokładny opis uzyskanych wyników znajduje się w **Rozdziale 6.4**.

Dogłębna analiza opisująca mechanizmy wiązania jonów metali z aktywnymi grupami funkcyjnymi białka możliwa była przy wykorzystaniu założeń modelu adsorpcji. Zatem też zbadana została kinetyka i izoterma adsorpcji Zn^{2+} na rekombinowanym hLTF (**Rozdziale 6.5).** Dopasowanie różnych modeli kinetyki wskazało na obecność kilku etapów zachodzących oddziaływań, zaś kształt izotermy adsorpcji oraz użyte do opisu modele potwierdziły heterogenność procesu. Ponadto, obliczono ΔG adsorpcji Zn^{2+} do białka, które w zależności od użytego stężenia wyniosło od −12,68 do −15,85 kJ/mol. Ujemne znaczenie ΔG wskazuję na spontaniczny charakter procesu. Dalsze badania metodami instrumentalnymi potwierdziły podobne zmiany w białku jakie zostały zauważone dla bLTF. Można zatem stwierdzić, że wiązanie jonów metali do badanych białek przechodzi w taki sam sposób. Badania uzupełniono metodami chemii obliczeniowej z uwzględnieniem teorii mechaniki kwantowej, mianowicie modelowanie za pomocą metod MD oraz teorii funkcjonału gęstości (DFT). Pozwoliło to na określenie rzeczywistego mechanizmu wiązania jonów metali do aktywnych grup funkcyjnych, stanowiący fundamentalny problem badawczy w chemii białek. Łączenie eksperymentalnych technik instrumentalnych z technikami chemii obliczeniowej umożliwiło zaproponowanie mechanizmu wiązania się jonów cynku do LTF.

Mechanizm ten obejmuje kilka etapów na co wskazują uzyskane wyniki kinetyki wiązania oraz izotermy adsorpcji. Na początku jony Zn^{2+} oddziałują z najbardziej zewnętrznymi grupami funkcyjnymi, takimi jak grupy karboksylowe kwasów glutaminowego i asparaginowego. W interakcjach takiego typu mogą brać udział także grupy hydroksylowe tyrozyny, seryny czy też treoniny. Reakcja ta zachodzi w sposób spontaniczny i odbywa się bardzo szybko, dlatego też ten etap odpowiada pierwszemu etapowi kinetyki gwałtownej sorpcji. Potwierdzenie postulowanego powyżej mechanizmu znajdujemy w wynikach symulacji metodami dynamiki molekularnej (MD), gdzie przy oddziaływaniu hLTF z jednym jonem cynku nie zaobserwowano żadnych wiązań, a przy oddziaływaniu z 5 jonami cynku już

zaobserwowano wiązania poprzez karboksylową grupę Glu80, Glu523 oraz Asp541. Z kolei, kiedy 10 jonów oddziaływało z jedną molekułą hLTF zauważono także dodatkowe wiązania pomiędzy akwakompleksem cynku a Tyr319 czy też Ser421. Potwierdzeniem były także uzyskane wyniki z izotermy, gdzie przy niskich stężeniach jonów cynku nie zachodziła znacząca sorpcja. Na widmach FTIR oraz Ramana kompleksów zarówno Zn-hLTF jak i Zn-bLTF, zsyntetyzowanych z użyciem niskich stężeń cynku, nie odnotowano dużych zmian pasm drgań. Kolejno, oddziaływania jonów cynku z wystającymi na powierzchni grupami funkcyjnymi indukują zmiany w strukturze białka, co umożliwia tworzenia się kilku wiązań z jedną cząsteczką cynku (chelatowanie jonu), tzn. tworzą się nowe miejsca wiążące jony metalu. Proces ten jest bardziej czasochłonny, jednak powoduje dużą zmianę w sorpcyjnej zdolności hLTF. Szybkość reakcji jest napędzana stężeniem jonów cynku w roztworze, co potwierdzają wyniki kinetyki adsorpcji dla roztworów cynku 300 i 600 mg/l w porównaniu do sorpcji dla roztworu cynku 60 mg/L. Zmiany w strukturze białka także pozwalają na dyfuzję Zn^{2+} do środka cząsteczki. Potwierdzenie tych wyników także odnotowano za pomocą metod obliczeniowych. Kiedy do układu symulującego hLTF dodano od 15 do 45 jonów cynku zaobserwowano możliwość tworzenia się kompleksów chelatowych. Większa różnorodność reszt aminokwasów uczestniczyła w wiązaniach, między innymi, w interakcję wchodziły Glu, Asp, Tyr, Ser Thr, His, Asn, Gln oraz Lys. Możliwy udział funkcyjnych grup tych aminokwasów w wiązaniu także stwierdzono odpowiednio dla uzyskanych wyników z DFT obliczeń. Ponadto, uzyskane widma FTIR i Ramana dla kompleksów Zn-hLTF i Zn-bLTF wskazują na możliwe zmiany w strukturze białka oraz interakcję z akwakompleksami cynku poprzez wyżej wymienione aminokwasy. Zwiększona sorpcja Zn^{2+} powoduje jeszcze większe zmiany w strukturze białka, dochodzi do osłabienia wiązania Fe-LTF. Odpowiednie zmiany zostały zaobserwowane zarówno w symulacjach MD jak i poprzez zastosowanie technik eksperymentalnych. Analiza ICP-MS dla jonów żelaza w kompleksach wykazała znaczne zmniejszenie jego zawartości, która wynosiła do 15% i 30% dla kompleksów Zn-hLTF i Zn-bLTF odpowiednio. Co więcej, rozdzielanie z użyciem elektroforezy kapilarnej łączonej z ICP-MS (CE-ICP-MS) wykazało, iż żelazo w natywnej hLTF jest związane bardzo silnie i dlatego pozostaje związane z białkiem w warunkach badanego procesu. W wypadku kompleksu Zn-hLTF zsyntetyzowanego z użyciem roztworu cynku o stężeniu 300 mg/L zaobserwowano częściową eliminację jonów żelaza z cząsteczki białka w warunkach analizy. Potwierdzają to wyniki otrzymane podczas symulacji MD.

4. Bibliografia:

1.   Massaglia, S.; Borra, D.; Peano, C.; Sottile, F.; Merlino, V. Consumer Preference Heterogeneity Evaluation in Fruit and Vegetable Purchasing Decisions Using the Best–Worst Approach. *Foods* **2019**, *8*, 266, doi:10.3390/foods8070266.

2.   Zakrzewska, B. Sustainable Development and Quality of Life. *AUTOBUSY – Technika, Eksploatacja, Systemy Transportowe* **2019**, *22*, 38–41, doi:10.24136/atest.2019.113.

3.   *What Is the Cost of Producing Milk? Milk Production Costs in Belgium, Denmark, France, Germany, Ireland, Lithuania, Luxembourg, and the Netherlands (EN)*; Büro für Agrarsoziologie und Landwirtschaft (BAL): Gleichen, Germany, **2021**.

4.   Pereira, P.C. Milk Nutritional Composition and Its Role in Human Health. *Nutrition* **2014**, *30*, 619–627, doi:10.1016/j.nut.2013.10.011.

5.   Davoodi, S.H.; Shahbazi, R.; Esmaeili, S.; Sohrabvandi, S.; Mortazavian, A.; Jazayeri, S.; Taslimi, A. Health-Related Aspects of Milk Proteins. *Iran J Pharm Res* **2016**, *15*, 573–591.

6.   Dullius, A.; Goettert, M.I.; de Souza, C.F.V. Whey Protein Hydrolysates as a Source of Bioactive Peptides for Functional Foods – Biotechnological Facilitation of Industrial Scale-Up. *J Funct Foods* **2018**, *42*, 58–74, doi:10.1016/j.jff.2017.12.063.

7.   Tsermoula, P.; Khakimov, B.; Nielsen, J.H.; Engelsen, S.B. WHEY - The Waste-Stream That Became More Valuable than the Food Product. *Trends Food Sci Technol* **2021**, *118*, 230–241, doi:10.1016/j.tifs.2021.08.025.

8.   Antoshin, A.A.; Shpichka, A.I.; Huang, G.; Chen, K.; Lu, P.; Svistunov, A.A.; Lychagin, A. v.; Lipina, M.M.; Sinelnikov, M.Y.; Reshetov, I. v.; et al. Lactoferrin as a Regenerative Agent: The Old-New Panacea? *Pharmacol Res* **2021**, *167*, 105564, doi:10.1016/j.phrs.2021.105564.

9.   Takayama, Y. Lactoferrin Structure Function and Genetics. In *Lactoferrin and its Role in Wound Healing*; Springer Netherlands: Dordrecht, 2012; pp. 43–66.

10.   Zander, Z.; Zander, L.; Mickiewicz, D. Laktoferyna - Multipotencjalne Białko Mleka. *Innowacyjne Mleczarstwo* **2014**, *2*, 18–21.

11.   Turck, D.; Bresson, J.; Burlingame, B.; Dean, T.; Fairweather-Tait, S.; Heinonen, M.; Hirsch-Ernst, K.I.; Mangelsdorf, I.; McArdle, H.J.; Naska, A.; et al. Safety of Whey Basic Protein Isolates as a Novel Food Pursuant to Regulation (EU) 2015/2283. *EFSA Journal* **2018**, *16*, doi:10.2903/j.efsa.2018.5360.

12.   Pryshchepa, O.; Pomastowski, P.; Buszewski, B. Silver Nanoparticles: Synthesis, Investigation Techniques, and Properties. *Adv Colloid Interface Sci* **2020**, *284*, 102246, doi:10.1016/j.cis.2020.102246.

13.   Zlatina, K.; Galuska, S.P. The *N*-Glycans of Lactoferrin: More than Just a Sweet Decoration. *Biochemistry and Cell Biology* **2021**, *99*, 117–127, doi:10.1139/bcb-2020-0106.

14.   Kete, M.; Lokar, B.; Zupancic, J.M.; Strancar, A. US 2021/0388058 A1 Method for Manufacturing Highly Purified Lactoferrin and Lactoperoxidase from Milk, Colostrum and Acid or Sweet Whey 2021.

15.   Krolitzki, E.; Schwaminger, S.P.; Pagel, M.; Ostertag, F.; Hinrichs, J.; Berensmeier, S. Current Practices with Commercial Scale Bovine Lactoferrin Production and Alternative Approaches. *Int Dairy J* **2022**, *126*, 105263, doi:10.1016/j.idairyj.2021.105263.

16.   Franco, I.; Pérez, M.D.; Conesa, C.; Calvo, M.; Sánchez, L. Effect of Technological Treatments on Bovine Lactoferrin: An Overview. *Food Research International* **2018**, *106*, 173–182, doi:10.1016/j.foodres.2017.12.016.

17.   Pomastowski, P.; Sprynskyy, M.; Žuvela, P.; Rafińska, K.; Milanowski, M.; Liu, J.J.; Yi, M.; Buszewski, B. Silver-Lactoferrin Nanocomplexes as a Potent Antimicrobial Agent. *J Am Chem Soc* **2016**, *138*, 7899–7909, doi:10.1021/jacs.6b02699.

18.   Shilpashree, B.G.; Arora, S.; Kapila, S.; Sharma, V. Whey Protein-Iron or Zinc Complexation Decreases pro-Oxidant Activity of Iron and Increases Iron and Zinc Bioavailability. *LWT* **2020**, *126*, 109287, doi:10.1016/j.lwt.2020.109287.

19.   Ma, X.Y.; Liu, S.B.; Lu, L.; Li, S.F.; Xie, J.J.; Zhang, L.Y.; Zhang, J.H.; Luo, X.G. Relative Bioavailability of Iron Proteinate for Broilers Fed a Casein-Dextrose Diet. *Poult Sci* **2014**, *93*, 556–563, doi:10.3382/ps.2013-03296.

20.   Baker, E.N. Structure and Reactivity of Transferrins. *Adv Inorg Chem* **1994**, *41*, 389–469, doi:10.1016/S0898-8838(08)60176-2.

21.   Riskin, A.; Almog, M.; Peri, R.; Halasz, K.; Srugo, I.; Kessel, A. Changes in Immunomodulatory Constituents of Human Milk in Response to Active Infection in the Nursing Infant. *Pediatr Res* **2012**, *71*, 220–225, doi:10.1038/pr.2011.34.

22.   Levay, P.F.; Viljoen, M. Lactoferrin: A General Review. *Haematologica* **1995**, *80*, 252–267.

23.   Fillebeen, C.; Ruchoux, M.-M.; Mitchell, V.; Vincent, S.; Benaïssa, M.; Pierce, A. Lactoferrin Is Synthesized by Activated Microglia in the Human Substantia Nigra and Its Synthesis by the Human Microglial CHME Cell Line Is Upregulated by Tumor Necrosis Factor

α or 1-Methyl-4-Phenylpyridinium Treatment. *Molecular Brain Research* **2001**, *96*, 103–113, doi:10.1016/S0169-328X(01)00216-9.

24.   Marnila, P.; Korhonen, H.J. Lactoferrin for Human Health. In *Dairy-Derived Ingredients*; Elsevier, 2009; pp. 290–307.

25.   https://www.rcsb.org/structure/1BLF.

26.   Rosa, L.; Cutone, A.; Lepanto, M.; Paesano, R.; Valenti, P. Lactoferrin: A Natural Glycoprotein Involved in Iron and Inflammatory Homeostasis. *Int J Mol Sci* **2017**, *18*, 1985, doi:10.3390/ijms18091985.

27.   https://www.rcsb.org/structure/1LFG.

28.   Zlatina, K.; Galuska, S.P. The N -Glycans of Lactoferrin: More than Just a Sweet Decoration. *Biochemistry and Cell Biology* **2021**, *99*, 117–127, doi:10.1139/bcb-2020-0106.

29.   O'Riordan, N.; Kane, M.; Joshi, L.; Hickey, R.M. Structural and Functional Characteristics of Bovine Milk Protein Glycosylation. *Glycobiology* **2014**, *24*, 220–236, doi:10.1093/glycob/cwt162.

30.   Grzesik, K.; Hoja-Łukowicz, D. Rola Glikanów w Rozwoju i Progresji Nowotworu. Zastosowania Kliniczne. *Postepy Biochem* **2021**, doi:10.18388/pb.2021_385.

31.   Barboza, M.; Pinzon, J.; Wickramasinghe, S.; Froehlich, J.W.; Moeller, I.; Smilowitz, J.T.; Ruhaak, L.R.; Huang, J.; Lönnerdal, B.; German, J.B.; et al. Glycosylation of Human Milk Lactoferrin Exhibits Dynamic Changes During Early Lactation Enhancing Its Role in Pathogenic Bacteria-Host Interactions. *Molecular & Cellular Proteomics* **2012**, *11*, M111.015248, doi:10.1074/mcp.M111.015248.

32.   van Veen, H.A.; Geerts, M.E.J.; van Berkel, P.H.C.; Nuijens, J.H. The Role of N-Linked Glycosylation in the Protection of Human and Bovine Lactoferrin against Tryptic Proteolysis. *Eur J Biochem* **2004**, *271*, 678–684, doi:10.1111/j.1432-1033.2003.03965.x.

33.   Yoshida, S.; Wei, Z.; Shinmura, Y.; Fukunaga, N. Separation of Lactoferrin-a and -b from Bovine Colostrum. *J Dairy Sci* **2000**, *83*, 2211–2215, doi:10.3168/jds.S0022-0302(00)75104-6.

34.   Yu, T.; Guo, C.; Wang, J.; Hao, P.; Sui, S.; Chen, X.; Zhang, R.; Wang, P.; Yu, G.; Zhang, L.; et al. Comprehensive Characterization of the Site-Specific N-Glycosylation of Wild-Type and Recombinant Human Lactoferrin Expressed in the Milk of Transgenic Cloned Cattle. *Glycobiology* **2011**, *21*, 206–224, doi:10.1093/glycob/cwq151.

35.   Derisbourg, P.; Wieruszeski, J.M.; Montreuil, J.; Spik, G. Primary Structure of Glycans Isolated from Human Leucocyte Lactotransferrin. Absence of Fucose Residues

Questions the Proposed Mechanism of Hyposideraemia. *Biochemical Journal* **1990**, *269*, 821–825, doi:10.1042/bj2690821.

36.   Fujiyama, K.; Sakai, Y.; Misaki, R.; Yanagihara, I.; Honda, T.; Anzai, H.; Seki, T. *N*-Linked Glycan Structures of Human Lactoferrin Produced by Transgenic Rice. *Biosci Biotechnol Biochem* **2004**, *68*, 2565–2570, doi:10.1271/bbb.68.2565.

37.   Buszewski, B.; Pomastowski, P. Wpływ Heterogeniczności Powierzchni Biokoloidów Na Ich Rozdzielanie Elektroforetyczne. *Wiadomości Chemiczne* **2015**, *69*, 9–10.

38.   Pomastowski, P.; Buszewski, B. Two-Dimensional Gel Electrophoresis in the Light of New Developments. *TrAC Trends in Analytical Chemistry* **2014**, *53*, 167–177, doi:10.1016/j.trac.2013.09.010.

39.   Steijns, J.M.; van Hooijdonk, A.C.M. Occurrence, Structure, Biochemical Properties and Technological Characteristics of Lactoferrin. *British Journal of Nutrition* **2000**, *84*, 11–17, doi:10.1017/S0007114500002191.

40.   Giansanti, F.; Panella, G.; Leboffe, L.; Antonini, G. Lactoferrin from Milk: Nutraceutical and Pharmacological Properties. *Pharmaceuticals* **2016**, *9*, 1–15, doi:10.3390/ph9040061.

41.   Moguilevsky, N.; Retegui, L.A.; Masson, P.L. Comparison of Human Lactoferrins from Milk and Neutrophilic Leucocytes. Relative Molecular Mass, Isoelectric Point, Iron-Binding Properties and Uptake by the Liver. *Biochemical Journal* **1985**, *229*, 353–359, doi:10.1042/bj2290353.

42.   Shimazaki, K.-I.; Kawaguchi, A.; Sato, T.; Ueda, Y.; Tomimura, T.; Shimamura, S. Analysis of Human and Bovine Milk Lactoferrins by Rotofor and Chromatofocusing. *International Journal of Biochemistry* **1993**, *25*, 1653–1658, doi:10.1016/0020-711X(93)90524-I.

43.   Bokkhim, H.; Bansal, N.; GrØndahl, L.; Bhandari, B. Physico-Chemical Properties of Different Forms of Bovine Lactoferrin. *Food Chem* **2013**, *141*, 3007–3013, doi:10.1016/j.foodchem.2013.05.139.

44.   Gurd, F.R.N.; Wilcox, P.E. Complex Formation between Metallic Cations and Proteins, Peptides, and Amino Acids. In *Advances in Protein Chemistry*; 1956; Vol. 11, pp. 311–427.

45.   Bou-Abdallah, F.; Giffune, T.R. The Thermodynamics of Protein Interactions with Essential First Row Transition Metals. *Biochimica et Biophysica Acta (BBA) - General Subjects* **2016**, *1860*, 879–891, doi:10.1016/j.bbagen.2015.11.005.

46.	Kawakami, H.; Dosako, S.; Nakajima, I. Effect of Lactoferrin on Iron Solubility under Neutral Conditions. *Biosci Biotechnol Biochem* **1993**, *57*, doi:10.1271/bbb.57.1376.

47.	Nagasako, Y.; Saito, H.; Tamura, Y.; Shimamura, S.; Tomita, M. Iron-Binding Properties of Bovine Lactoferrin in Iron-Rich Solution. *J Dairy Sci* **1993**, *76*, doi:10.3168/jds.S0022-0302(93)77520-7.

48.	Ainscough, E.W.; Brodie, A.M.; Plowman, J.E. Zinc Transport by Lactoferrin in Human Milk. *Am J Clin Nutr* **1980**, *33*, 1314–1315, doi:10.1093/ajcn/33.6.1314.

49.	Harrington, J.P.; Stuart, J.; Jones, A. Unfolding of Iron and Copper Complexes of Human Lactoferrin and Transferrin. *International Journal of Biochemistry* **1987**, *19*, 1001–1008, doi:10.1016/0020-711X(87)90184-4.

50.	Congiu-Castellano, A.; Boffi, F.; della Longa, S.; Giovannelli, A.; Girasole, M.; Natali, F.; Pompa, M.; Soldatov, A.; Bianconi, A. Aluminum Site Structure in Serum Transferrin and Lactoferrin Revealed by Synchrotron Radiation X-Ray Spectroscopy. *Biometals* **1997**, *10*, 363–367, doi:10.1023/A:1018345021238.

51.	Ndayisaba, A.; Kaindlstorfer, C.; Wenning, G.K. Iron in Neurodegeneration – Cause or Consequence? *Front Neurosci* **2019**, *13*, doi:10.3389/fnins.2019.00180.

52.	McAbee, D.D.; Ling, Y.Y. Iron-Loading of Cultured Adult Rat Hepatocytes Reversibly Enhances Lactoferrin Binding and Endocytosis. *J Cell Physiol* **1997**, *171*, 75–86, doi:10.1002/(SICI)1097-4652(199704)171:1<75::AID-JCP9>3.0.CO;2-E.

53.	Leveugle, B.; Spik, G.; Perl, D.P.; Bouras, C.; Fillit, H.M.; Hof, P.R. The Iron-Binding Protein Lactotransferrin Is Present in Pathologic Lesions in a Variety of Neurodegenerative Disorders: A Comparative Immunohistochemical Analysis. *Brain Res* **1994**, *650*, 20–31, doi:10.1016/0006-8993(94)90202-X.

54.	Maynard, C.J.; Bush, A.I.; Masters, C.L.; Cappai, R.; Li, Q.-X. Metals and Amyloid-β in Alzheimer's Disease. *Int J Exp Pathol* **2005**, *86*, 147–159, doi:10.1111/j.0959-9673.2005.00434.x.

55.	Vogel, H.J. Lactoferrin, a Bird's Eye View. *Biochemistry and Cell Biology* **2012**, *90*, 233–244, doi:10.1139/o2012-016.

56.	Elli, M.; Zink, R.; Rytz, A.; Reniero, R.; Morelli, L. Iron Requirement of Lactobacillus Spp. in Completely Chemically Defined Growth Media. *J Appl Microbiol* **2000**, *88*, 695–703, doi:10.1046/j.1365-2672.2000.01013.x.

57.	O'Hara, A.M.; Keohane, J.; Shanahan, F. Probiotics, Prebiotics, and Inflammatory Bowel Disease. In *Functional Dairy Products*; Elsevier, 2007; Vol. 2, pp. 90–116 ISBN 9781845691530.

58.	Takayama, Y.Lactoferrin as a Signaling Mediator. In *Lactoferrin and its Role in Wound Healing*; Springer Netherlands, 2012; pp. 67–85.

59.	Takayama, Y. Molecular Regulation of Skin Wound Healing. In *Lactoferrin and its Role in Wound Healing*; Springer Netherlands: Dordrecht, 2012; pp. 1–23.

60.	Shin, K.; Wakabayashi, H.; Yamauchi, K.; Yaeshima, T.; Iwatsuki, K. Recombinant Human Intelectin Binds Bovine Lactoferrin and Its Peptides. *Biol Pharm Bull* **2008**, *31*, 1605–1608, doi:10.1248/bpb.31.1605.

61.	Abu Hashim, H.; Foda, O.; Ghayaty, E. Lactoferrin or Ferrous Salts for Iron Deficiency Anemia in Pregnancy: A Meta-Analysis of Randomized Trials. *European Journal of Obstetrics & Gynecology and Reproductive Biology* **2017**, *219*, 45–52, doi:10.1016/j.ejogrb.2017.10.003.

62.	Davidson, L.A.; Lonnerdal, B. Fe-Saturation and Proteolysis of Human Lactoferrin: Effect on Brush-Border Receptor-Mediated Uptake of Fe and Mn. *Am J Physiol Gastrointest Liver Physiol* **1989**, *257*, doi:10.1152/ajpgi.1989.257.6.g930.

63.	Elzoghby, A.O.; Abdelmoneem, M.A.; Hassanin, I.A.; Abd Elwakil, M.M.; Elnaggar, M.A.; Mokhtar, S.; Fang, J.-Y.; Elkhodairy, K.A. Lactoferrin, a Multi-Functional Glycoprotein: Active Therapeutic, Drug Nanocarrier & Targeting Ligand. *Biomaterials* **2020**, *263*, 120355, doi:10.1016/j.biomaterials.2020.120355.

64.	Fillebeen, C.; Descamps, L.; Dehouck, M.-P.; Fenart, L.; Benaïssa, M.; Spik, G.; Cecchelli, R.; Pierce, A. Receptor-Mediated Transcytosis of Lactoferrin through the Blood-Brain Barrier. *Journal of Biological Chemistry* **1999**, *274*, 7011–7017, doi:10.1074/jbc.274.11.7011.

65.	Yannone, S.M.; Hartung, S.; Menon, A.L.; Adams, M.W.; Tainer, J.A. Metals in Biology: Defining Metalloproteomes. *Curr Opin Biotechnol* **2012**, *23*, 89–95, doi:10.1016/j.copbio.2011.11.005.

66.	Kambe, T.; Tsuji, T.; Hashimoto, A.; Itsumura, N. The Physiological, Biochemical, and Molecular Roles of Zinc Transporters in Zinc Homeostasis and Metabolism. *Physiol Rev* **2015**, *95*, 749–784, doi:10.1152/physrev.00035.2014.

67.	Haschka, D.; Hoffmann, A.; Weiss, G. Iron in Immune Cell Function and Host Defense. *Semin Cell Dev Biol* **2021**, *115*, doi:10.1016/j.semcdb.2020.12.005.

68.	Santos, H.O.; Teixeira, F.J.; Schoenfeld, B.J. Dietary vs. Pharmacological Doses of Zinc: A Clinical Review. *Clinical Nutrition* **2020**, *39*, 1345–1353, doi:10.1016/j.clnu.2019.06.024.

69.   Merlino, A. Recent Advances in Protein Metalation: Structural Studies. *Chemical Communications* **2021**, *57*, 1295–1307, doi:10.1039/D0CC08053E.

70.   Buszewski, B.; Žuvela, P.; Król-Górniak, A.; Railean-Plugaru, V.; Rogowska, A.; Wong, M.W.; Yi, M.; Rodzik, A.; Sprynskyy, M.; Pomastowski, P. Interactions of Zinc Aqua Complexes with Ovalbumin at the Forefront of the Zn2+/ZnO-OVO Hybrid Complex Formation Mechanism. *Appl Surf Sci* **2021**, *542*, 148641, doi:10.1016/j.apsusc.2020.148641.

71.   Rodzik, A.; Pomastowski, P.; Sagandykova, G.N.; Buszewski, B. Interactions of Whey Proteins with Metal Ions. *Int J Mol Sci* **2020**, *21*, 1–26, doi:10.3390/ijms21062156.

72.   Dalev, P.G. Utilization of Waste Whey as a Protein Source for Production of Iron Proteinate: An Antianaemic Preparation. *Bioresour Technol* **1994**, *48*, 75–77, doi:10.1016/0960-8524(94)90140-6.

73.   Jabeen, T.; Sharma, S.; Singh, N.; Bhushan, A.; Singh, T.P. Structure of the Zinc-Saturated C-Terminal Lobe of Bovine Lactoferrin at 2.0 Å Resolution. *Acta Crystallogr D Biol Crystallogr* **2005**, *61*, 1107–1115, doi:10.1107/S0907444905016069.

74.   Sych, T.S.; Buglak, A.A.; Reveguk, Z. v; Pomogaev, V.A.; Ramazanov, R.R.; Kononov, A.I. Which Amino Acids Are Capable of Nucleating Fluorescent Silver Clusters in Proteins? *The Journal of Physical Chemistry C* **2018**, *122*, 26275–26280, doi:10.1021/acs.jpcc.8b08979.

75.   Tang, N.; Skibsted, L.H. Zinc Bioavailability from Whey. Enthalpy-Entropy Compensation in Protein Binding. *Food Research International* **2016**, *89*, 749–755, doi:10.1016/j.foodres.2016.10.002.

76.   Allahverdiyev, A.M.; Kon, K.V.; Abamor, E.S.; Bagirova, M.; Rafailovich, M. Coping with Antibiotic Resistance: Combining Nanoparticles with Antibiotics and Other Antimicrobial Agents. *Expert Rev Anti Infect Ther* **2011**, *9*, 1035–1052, doi:10.1586/eri.11.121.

77.   Medici, S.; Peana, M.; Nurchi, V.M.; Zoroddu, M.A. Medical Uses of Silver: History, Myths, and Scientific Evidence. *J Med Chem* **2019**, *62*, 5923–5943, doi:10.1021/acs.jmedchem.8b01439.

78.   Shubham, K.; Anukiruthika, T.; Dutta, S.; Kashyap, A.V.; Moses, J.A.; Anandharamakrishnan, C. Iron Deficiency Anemia: A Comprehensive Review on Iron Absorption, Bioavailability and Emerging Food Fortification Approaches. *Trends Food Sci Technol* **2020**, *99*, 58–75, doi:10.1016/j.tifs.2020.02.021.

79.   Feig, A.L.; Lippard, S.J. Reactions of Non-Heme Iron(II) Centers with Dioxygen in Biology and Chemistry. *Chem Rev* **1994**, *94*, 759–805, doi:10.1021/cr00027a011.

80.   Ghosh, S.; Mukherjee, A.; Sadler, P.J.; Verma, S. Periodic Iron Nanomineralization in Human Serum Transferrin Fibrils. *Angewandte Chemie International Edition* **2008**, *47*, 2217–2221, doi:10.1002/anie.200705723.

81.   Morgan, B.; Lahav, O. The Effect of PH on the Kinetics of Spontaneous Fe(II) Oxidation by O2 in Aqueous Solution – Basic Principles and a Simple Heuristic Description. *Chemosphere* **2007**, *68*, 2080–2084, doi:10.1016/j.chemosphere.2007.02.015.

82.   Adam, F.I.; Bounds, P.L.; Kissner, R.; Koppenol, W.H. Redox Properties and Activity of Iron–Citrate Complexes: Evidence for Redox Cycling. *Chem Res Toxicol* **2015**, *28*, 604–614, doi:10.1021/tx500377b.

83.   Lin, Y.-F.; Cheng, C.-W.; Shih, C.-S.; Hwang, J.-K.; Yu, C.-S.; Lu, C.-H. MIB: Metal Ion-Binding Site Prediction and Docking Server. *J Chem Inf Model* **2016**, *56*, 2287–2291, doi:10.1021/acs.jcim.6b00407.

84.   Maret, W.; Sandstead, H.H. Zinc Requirements and the Risks and Benefits of Zinc Supplementation. *Journal of Trace Elements in Medicine and Biology* **2006**, *20*, 3–18, doi:10.1016/j.jtemb.2006.01.006.

85.   Belitz, H.D.; Grosch, W.; Schieberle, P. *Food Chemistry*; Springer Berlin Heidelberg: Berlin, Heidelberg, 2009; ISBN 978-3-540-69933-0.

5. Cele badawcze:

Nadrzędnym celem badawczym pracy była synteza kompleksów laktoferyny z wybranymi jonami metali d-elektronowymi o znaczeniu biologicznym (srebro, żelazo(III), cynk), zbadanie ich właściwości oraz opis mechanizmów wiązania na podstawie danych uzyskanych przy wykorzystaniu technik molekularnych oraz modelowania molekularnego. Dodatkowym celem pracy badawczej było zbadanie właściwości biologicznych zsyntetyzowanych kompleksów, mianowicie cytotoksyczność oraz działanie przeciwdrobnoustrojowe.

Cel został zrealizowany poprzez:

–Fizykochemiczną charakterystykę białek modelowych: laktoferyny bydlęcej oraz rekombinowanej laktoferyny ludzkiej;

–Przeprowadzenie i modelowanie kinetyki i izotermy adsorpcji jonów metali do białek;

–Badanie właściwości fizykochemicznych otrzymanych kompleksów i nanokompozytów metalo-białkowych za pomocą metod instrumentalnych;

– Przeprowadzenia modelowania molekularnego oraz obliczeń kwantowo-mechanicznych dla kompleksów cynku i żelaza z laktoferyną;

– Badanie właściwości biologicznych na liniach komórkowych oraz wybranych szczepach bakteryjnych.

Do realizacji tych zadań wykorzystano następujące techniki instrumentalne i obliczeniowe:

– Pomiaru elektroforetycznego rozpraszania światła do oznaczania potencjału zeta (ζ-potencjał);

– Spektrometrię mas z laserową jonizacją/desorpcją próbki wspomaganą matrycą z tandemowym analizatorem czasu przelotu;

– Elektroforezę w żelu poliakryloamidowym w układzie jednowymiarowym;

– Spektrometrię mas sprzężona z plazmą wzbudzaną indukcyjnie w tym w trybie *on-line* w połączeniu z elektroforezą kapilarną;

– Spektroskopię w zakresie podczerwieni z transformacją Fouriera oraz rozproszeniowa spektroskopia Ramana;

– Mikroskopia elektronowa transmisyjna i skaningowa w tym w połączeniu z spektroskopią rentgenowską z dyspersją energii;

– Spektroskopia UV-VIS oraz fluorescencyjna;

– Obliczenia i symulację komputerowe z użyciem metod dokowania molekularnego, dynamiki molekularnej oraz teorii funkcjonału gęstości;

– Badanie biologicznej aktywności kompleksu żelaza(III) oraz nanokompozytu srebra *in vitro* przeprowadzano z użyciem spektroskopii UV-VIS oraz fluorescencyjnej przy wykorzystaniu odpowiednich wskaźników żywotności komórek.

Metodyki badań zostały szczegółowo opisane w poszczególnych pracach w **Rozdziałach 6.2-6.5** stanowiących całość niniejszej dysertacji.

6. Publikacje naukowe

6.1 Silver nanoparticles: synthesis, investigation techniques, and properties

O. Pryshchepa, P. Pomastowski, B. Buszewski, *"Silver nanoparticles: synthesis, investigation techniques, and properties"*, Advances in Colloid and Interface Science, 284, 2020: 102246, https://doi.org/10.1016/j.cis.2020.102246

Historical Perspective

Silver nanoparticles: Synthesis, investigation techniques, and properties

Oleksandra Pryshchepa [a,b], Paweł Pomastowski [a], Bogusław Buszewski [a,b,*]

[a] Centre for Modern Interdisciplinary Technologies, Nicolaus Copernicus University in Torun, Wileńska 4, 87-100 Torun, Poland
[b] Department of Environmental Chemistry and Bioanalytics, Faculty of Chemistry, Nicolaus Copernicus University in Torun, Gagarina 7, 87-100 Torun, Poland

ARTICLE INFO

ABSTRACT

The unique silver properties, especially in the form of nanoparticles (NPs), allow to utilize them in numerous applications. For instance, Ag NPs can be utilized for the production of electronic and solar energy harvesting devices, in advanced analytical techniques (NALDI, SERS), catalysis and photocatalysis. Moreover, the Ag NPs can be useful in medicine for bioimaging, biosensing as well as in antibacterial and anticancer therapies. The Ag NPs utilization requires comprehensive knowledge about their features regarding the synthesis approaches as well as exploitation conditions. Unfortunately, a large number of scientific articles provide only restricted information according to the objects under investigation. Additionally, the results could be affected by artifacts introduced with exploited equipment, the utilized technique or sample preparation stages. However, it is rather difficult to get information about problems, which may occur during the studies. Thus, the review provides information about novel trends in the Ag NPs synthesis, among which the physical, chemical, and biological approaches can be found. Basic information about approaches for the control of critical parameters of NPs, i.e. size and shape, was also revealed. It was shown, that the reducing agent, stabilizer, the synthesis environment, including trace ions, have a direct impact on the Ag NPs properties. Further, the capabilities of modern analytical techniques for Ag NPs and nanocomposites investigations were shown, among other microscopic (optical, TEM, SEM, STEM, AFM), spectroscopic (UV-Vis, IR, Raman, NMR, electron spectroscopy, XRD), spectrometric (MALDI-TOF MS, SIMS, ICP-MS), and separation (CE, FFF, gel electrophoresis) techniques were described. The limitations and possible artifacts of the techniques were mentioned. A large number of presented techniques is a distinguishing feature, which makes the review different from others. Finally, the physicochemical and biological properties of Ag NPs were demonstrated. It was shown, that Ag NPs features are dependent on their basic parameters, such as size, shape, chemical composition, etc. At the end of the review, the modern theories of the Ag NPs toxic mechanism were shown in a way that has never been presented before. The review should be helpful for scientists in their own studies, as it can help to prepare experiments more carefully.

© 2020 Published by Elsevier B.V.

Contents

1. Introduction

Over the past few decades, nanotechnology has reached an unprecedented scale. Thus, the increased interest of researchers in the field is not a surprise. Nanotechnology can be described as the field in science and technology involved in the engineering, production, and utilization of nanomaterials [1]. Nanoscale or nanometer objects, as defined by the prefix "nano" meaning 10^{-9}, in general, should fall within the limits of 1–1000 nm. However, according to the European Commission recommendations, to nanomaterials can be accounted any material of natural, incidental or engineered origin, which comprises at least 50% of the particles (in unbound or aggregated form) possessing one or more external dimensions in the range from 1 to 100 nm [2]. However, the objects that exceed the designated limits are often considered by researchers as NPs [3].

The NPs made from coinage metals attract attention due to their unique optical properties coming from the specific behavior under light irradiation, namely the appearance of Localized Surface Plasmon Resonance (LSPR). Among all "noble" metals, silver as a bulk material exhibits the highest electrical and thermal conductivities, the lowest melting and boiling points. Moreover, silver is the most reactive of the "noble" metals, and its cations exert toxic effects against various microorganisms [4]. Silver in form of NPs revealed even more unique properties, which enables them to be utilized in the multiple fields of technique and medicine: solar energy harvesting [5], electronic devices [6], advanced analytical techniques, e.g. SERS (Surface Enhanced Raman Spectroscopy) [7] and NALDI (Nanoassisted Laser Desorption/Ionization) [8,9], catalysis and photocatalysis [10,11], environmental applications [12], bioimaging [13] and bioanalysis [14,15], as antibacterial agent [16–18] or agent in anticancer therapies [19,20].

The utilization of Cu, Au, Pt, or Pd NPs for plasmonic applications is also considered. However, all the mentioned NPs cannot completely replace Ag NPs, since they have the highest quality factor in the plasmonic ability and exhibit the plasmonic band in a wide range of wavelengths (from near ultraviolet to near infrared spectrum), which is provided by numerous known nanostructures [21]. Moreover, in NALDI application the Ag NPs prepared by metal sputtering have shown the highest

ion-desorption efficiency of analyte in comparison to Au, Pd, and Pt NPs [8]. Additionally, the Au and Pt NPs nearly a hundred times more expensive than Ag NPs, while Cu NPs utilization is much more complicated due to high susceptibility to oxidation and very few known nanostructures [21]. Lately, more attention is paid for the utilization of metal oxide NPs in the antibacterial applications, such as ZnO or ZrO_2 [22], which potentially can be a substitute for Ag NPs. However, long-time history of successful silver utilization in medicine as an antibacterial agent as well as the fact that till now it has been reported only one bacteria, *P. stutceri* (its natural habitat is silver mines), which completely resistant to Ag^+ [23], indicate that silver preparations, including in the form of NPs, is hardly can be replaced completely. Thus, Ag NPs still is the "hot topic" of numerous investigations.

One of the most important issues in nanotechnology is the possibility to engineer the NPs with desired properties for corresponding applications. The desired results can be achieved only in case of comprehensive knowledge about the NPs features regarding the synthesis approaches as well as exploitation conditions. A simple search in scientific publication databases reveals the hundreds of thousands of results on keywords like "Ag nanoparticles" or "silver nanoparticles". Unfortunately, a significant amount of the publications comprise highly restricted information regarding the Ag NPs properties, and how they are affected by the synthesis conditions. For instance, in the work by E.-Y. Ahn et al., among thirty utilized plant extracts only seven showed the capability to reduce Ag^+, the comparative characterization of the mentioned extracts or NPs surface functional groups were not performed [24]. Moreover, no correlation between NPs primary features (i.e. size, shape, surface charge, hydrodynamic radii) and biological activity could be derived. The authors attributed the toxicity of the synthesized Ag NPs to the extensively accepted theory of Reactive Oxygen Species (ROS) formation by released Ag^+. However, the Ag NPs show a much wider spectrum of possible toxic routs [25] and the surface chemistry strictly influences the NPs interaction with cells [26,27]. Hence, researchers should consider the possibility of a more comprehensive study of each individual investigated system, rather than to dissipate their resources.

Another subject that has poorly been covered in the literature is the influence of different analytical techniques on the obtained results during the study of Ag NPs. Still, some information can be derived from the scientists' reports, so it can be concluded that depending on the instrumental technique the studied features of Ag NPs can differ significantly [28]. Moreover, the results can be affected by artifacts introduced by the employed equipment, the utilized technique or sample preparation stages [29,30]. Even though the progress in the technologies allows us to eliminate a significant number of artifacts that can be introduced by the apparatus, it is rather impossible to consider or remove all the factors that influence the objects under investigation. Besides, the majority of the techniques have notable limitations and cannot provide exhaustive knowledge about the examined objects. Thus, researchers should carefully prepare their experiments and not avoid to perform additional analysis, as even simple chemical test may result in useful corroborative information.

The influence of Ag NPs on biological systems is also a sensitive issue, which induces numerous discussions in scientific society. Different effects, induced by Ag NPs in the prokaryotic and eukaryotic cells have been described in the literature [25]. Despite, the scientists' numerous attempts to distinguish separately the effects of each agent related to Ag NPs (stabilizer [31], Ag^+ [32], or the NP itself [33]), it is still impossible to perform completely, especially in terms of a time-resolved manner [34]. Moreover, the majority of the investigations are performed in vitro, which cannot reproduce the conditions of real biological systems. It was shown, that plasma proteins adsorption on Ag NPs surface [27,34] and Ag^+ chelation [17] change the NPs interaction with cells as well as their toxicity in general. Thus, the exact mechanism of AgNPs biological activity is still under consideration and is a challenge for future investigations.

Due to high interest in nanotechnology and in particularly in Ag NPs engineering and utilization in last decades a multiple studies have been performed, which in consequence was a reason for publication of several review articles. However, the issue of Ag NPs synthesis, properties, investigation techniques, the action mechanisms and application is so huge so it cannot be fit in the edges of one review. To give an example, M. Oćwieja et al. review is focused on the formation of layered structure of Ag NPs on different substrates [35]. In the article the basic approaches for the Ag NPs synthesis and characterization was shown. However, the main deliverable of the work is the excellent presentation of NPs deposition process on different substrates, including the adsorption kinetic of monolayers formation and its stability. In Rycenga et al. article the formation of Ag NPs structures for plasmonic applications has been revealed [21]. The authors, among others, have paid big attention to the plasmon phenomenon and possible ways to investigate it. P. Dubey with colleagues in their work has reviewed the Ag NPs cytotoxicity [25]. The review presents the information about numerous effects caused by Ag NPs to different cells. Moreover, the issues related to the Ag NPs properties and applications is developed continuously and hundreds of new research articles appears annually.

Thus, the purpose of the present study was to show the trends and achievements of the last years in Ag NPs synthesis and characterization. The latest development in the field of instrumental techniques offers new possibilities in materials science investigations. Hence, the manuscript was prepared with the main focus on the capabilities of modern instrumental techniques in line with NPs and nanocomposites investigations as well as their limitations. Finally, at the end of the review, the attempt to consider the toxic mechanism of Ag NPs on the molecular level was presented in a way that to the best of our knowledge has never been shown before.

2. Synthesis

Since the beginning of the nanotechnology, various routes for Ag NPs synthesis were introduced. The abundance of existing methods can be divided into two basic synthesis approaches, namely *top-down* and

bottom-up. Top-down methods imply the creating of nanoscale structures starting from bulk material by reducing their size through "cutting" to required values. Instead, bottom-up approaches are the variety of synthetic techniques, which utilize the molecular, atomic, or ionic components to produce the more complex nanoscaled assemblies [36]. Further, synthesis techniques can be categorized according to the processes had been used, i.e. physical, chemical, biological methods (Fig. 1). The selection of an appropriate synthesis method is a major issue for engineered NPs production, as it affects their properties. For instance, galactose and mannose-capped Ag NPs possess lower toxicity against hepatocytes and neuronal-like cell lines in comparison to NPs stabilized with citrate [37], so they can be recognized as more biocompatible and therefore are more suitable for exploitation in medical applications. Instead, for NPs utilization in catalytic applications the size, shape, the unique dopants are more important than bioavailability [38]. Hence, the selection of synthesis rout usually is determined by desired NPs utilization features.

2.1. Physical approaches

Physical approaches include the exploitation of the physical agents, such as heat [39], electrical discharge [40], plasma [41], or electromagnetic irradiation [11]. The advantages of physical methods are their speed and minimal chemicals consumption. However, physical synthesis approaches have drawbacks to which the high energy of the process, the wide particle size distribution and low yield can be included [42]. Actually, the *top-down* approach is entirely based on physical synthesis methods. The arc discharge is frequently utilized for bulk silver atomization with subsequent Ag NPs formation, as in general, it considered as a fast and simple technique [43]. What is interesting, M. Miranzadeh with M. Z. Kassaee has shown that in the process the Ag NPs morphology and size can be controlled by utilization of different synthesis media [40]. However, authors have also claimed that synthesis medium influences not only NPs morphology but also their purity, the size distribution, stability against aggregation, and oxidation. Laser ablation is also well-known for NPs synthesis. The primary features (e.g. size, chemical composition) in the method can be influenced by the synthesis environment as well as laser parameters. The laser ablation in the water environment is a well-known technique for the production of ultrapure, monodisperse, and ultrafine Ag NPs [11]. The production of Ag NPs in the open air was also revealed [44]. However, the presence of the oxygen may lead to the undesirable formation of Ag_2O instead of metallic NPs, even with the utilization of Ar jet at the interaction zone. Moreover, the Ag NPs can be produced by thermal bulk silver evaporation/condensation. L. S. Kibis et al. have shown that within the method the final product properties can be changed by synthesis conditions [39]. For instance, the thermal silver evaporation with the simultaneous transfer in the convective gas flow of oxygen led to the formation of oxidized Ag_2O NPs. The same product was obtained with the silver sputtering by radio-frequency discharge in an oxygen atmosphere. By the changes of the oxygen to helium for the first method and to argon in the second case, it was possible to obtain metallic Ag NPs. The features of synthesized NPs by thermal evaporation were also affected by the position of the substrate relative to an evaporation device. Instead, the Ag NPs properties produced by sputtering can be partially controlled by the sputtering time. Another route was introduced by O. Kylian et al., they have produced polymer@Ag NPs deposited on the nylon 6,6 target by plasma during gas-phase synthesis [41]. Finally, for the production of Ag nanosized structures, the lithography can be utilized. The lithography is a technique, which offers precise control over the shape, size, and placement of the synthesized nano-assemblies, which is very desirable in plasmonic applications [36]. However, it should be mentioned that lithography is highly labor-extensive, making the utilization of obtained products very expensive. Some other physical, as well as chemical or biological approaches for Ag NPs synthesis can be seen in the Table 1.
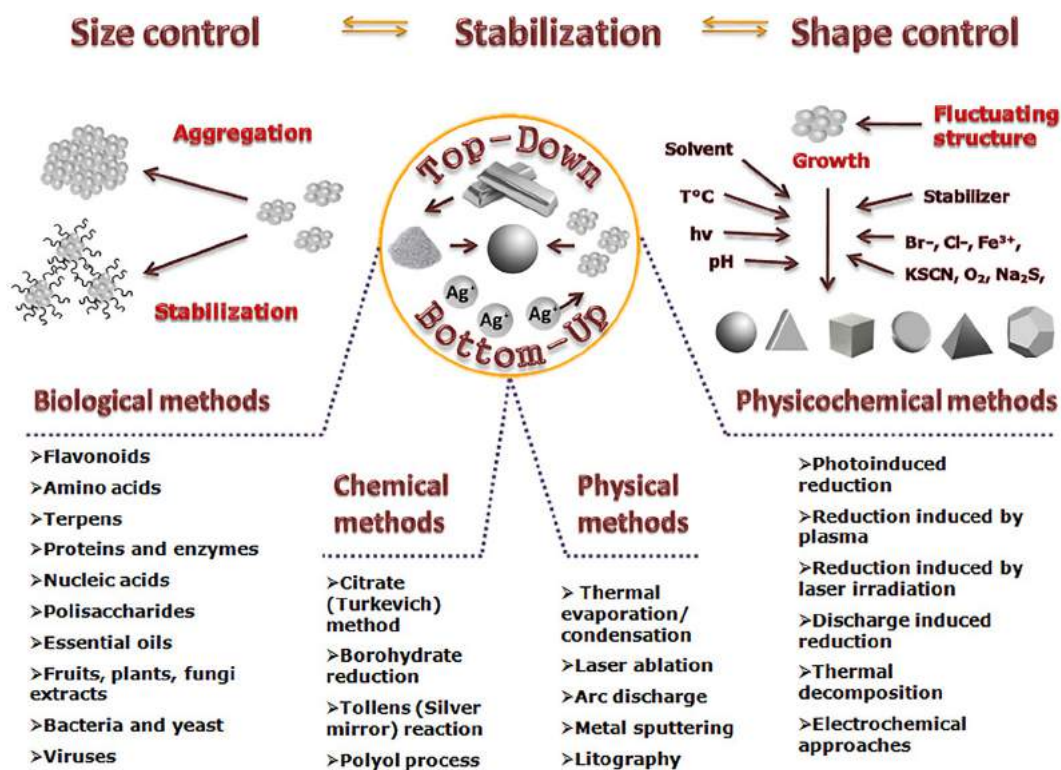
Fig. 1. The principles of Ag NPs synthesis.

2.2. Chemical synthesis

Chemical synthesis implies the NPs production through chemical transformations of the starting materials. The process requires the presence of three main components, namely metal precursor, reducing agent, and stabilizing/capping agents [42]. The fourth important component for NPs synthesis is a solvent, as the majority of the chemically and biologically conducted Ag NPs fabrication performed in the solution. However, in W. H. Eisa et al. the solid-state production of Ag NPs was performed by milling of *Zingiber officianale* powder with silver nitrate salt in desktop vibrating mill machine [45]. The distilled water and ethanol were utilized only at the end of the process for obtained NPs purification from unreacted species. The majority of chemically synthesized Ag NPs are made by four chemical reactions: citrate (Turkevich) method [46,47], borohydride reduction [48–51], Tollens (silver mirror) reaction [10], polyol process [52,53]. Turkevich method involves the utilization of AgNO$_3$ as the metal precursor and trisodium citrate both as a capping and stabilizing agent [46]. Even though the citrate method was one of the very first proposed for Ag NPs synthesis, it is still extensively utilized by researchers. The method is cost-effective and does not require advanced manipulation, so it is often utilized for NPs behavior investigations [47]. The borohydride reduction implies the utilization of NaBH$_4$ as a reducing agent. The borohydride exploitation for NPs synthesis seems to be the most popular among other chemical methods [48–51]. The popularity of NaBH$_4$ for Ag NPs production comes from the fact that it has higher reducing capability than citrate, and therefore it can be utilized for more precise size and shape control in Ag NPs synthesis [54,55]. To give an example, the utilization of NaBH$_4$ for the reduction of Ag$_2$O has provided the possibility to form hollowed Ag NPs [56]. Instead, the utilization of less active reducing agents led either to the formation of a hollowed structure with lower efficiency in case of hydrazine or even did not resulted in hollowed morphologies at all, as it was shown for ascorbic acid. Moreover, the precise utilization of NaBH$_4$ as a reducing agent allows to synthesize NPs with

different shapes and sizes, such as spherical, rod-like, triangle, and even coupled "cookie-like" from the same set of the reagents [54]. However, the uniform colloid was possible to obtain only for spherical NPs, while rod-like and triangle together with spherical NPs occurred in solution as a mixture of different molar ratios. The silver mirror reaction involves the utilization of Tollen's reagent, Ag(NH$_3$)$_2$OH as a precursor, and the aldehyde-group containing reducing agent (which may be sugars) for Ag NPs fabrications. The Tollen's reagent is not as popular in Ag NPs synthesis as AgNO$_3$, but in some cases provides additional possibilities for different valuable synthesis routes. To give an example, P. Yang with colleagues has shown the fascinating approach for tuning Ag@resorcinol-formaldehyde resin core-shell NPs to inverse resorcinol-formaldehyde-core@Ag shell NPs through the formation of Tollen's reagent by the mixture of NH$_3$/O$_2$ gases [10]. Moreover, J. Yoo et al. have produced the Ag NPs via hydrazine reduction of Tollen's reagent obtained from the dissolution of AgCl in ammonium hydroxide solution [57]. Insoluble nature of AgCl makes difficult to utilize it as a precursor in synthesis, but with the transformation to Tollen's reagent, it becomes possible to produce Ag NPs. In turn, the AgCl is one of the products that can be retrieved by recycling of silver-containing scrap. The utilization of polyols for Ag NPs synthesis is related to the possibility to engineer NPs with desired properties. By changes in the reaction conditions, such as temperature, reagent concentration, variations of polyol been used, or the presence of trace ions, the high degree of shape and size control can be achieved [52,53]. What is interesting, in the process polyol serves both as a reducing agent and the solvent. Some other synthesis approaches can be utilized, for instance Y. Tian et al. have prepared the flower-looked Ag NPs by reducing AgNO$_3$ in the presence of ascorbic acid and citrate ions as reducing and capping agents respectively [58]. Besides, the chemical transformation of precursor can be induced by different physical agents, such as heat or electromagnetic irradiation, so this group of methods can be defined as physicochemical approaches. To give an example, H. Le Trong et al. have synthesized Ag NPs by thermal decomposition of silver oxalate [59]. However, long

Table 1
Methods of AgNPs synthesis.

Method	Precursor	Synthesis conditions	Stabilization system	Product	Ref.
Physical	Ag 99.9%	Ar ion beam sputtering, Ag target (Ø 54 mm, 0,1 mm thickness), metal-support distance 80 mm, current 4 mA, t = 4 s, chamber flushed with argon, synthesis P = .04–.05 mbar	Deposited on glass support	Ag NPs 1.7–3.1 nm on glass coverslips	[8]
	Ag 99.9%	Thermal evaporation, Ag target (10 × 10 mm,0.2 mm in thickness) rolled into cylinder, placed in chromel wire helix (previously annealed in O_2 atmosphere at 1000 °C), heated to 700 °C in He (10 Pa) and O_2 (1 kPa) environment	Gold foil (99.9%) support	Ag NPs with 3–9 nm, mean 6 nm Ag_2O NPs 1–5 nm/twinned 8–10 nm (crystallite 2–3 nm)	[39]
	Ag 99.9%	Radio-frequency discharge sputtering, silver electrode Ø 2 mm in O_2 (25 Pa), support was preoxidazed in O_2 (100 Pa) at 300 °C, 30 min	Tantalum (99,9%) foil	Ag_2O/AgO NPs ≈ 4.5 nm	[39]
	Ag 99.9%	Target substrate distance 0.5–1.5 cm, Nd:YVO$_4$ laser, moving speed 100 mm/s, λ = 532 nm, 50 ns pulse, 20 kHz average output 6 W, irradiance of 100 MW/cm^2, open air, in jet of Ar	Deposited on glass support	Ag/Ag_2O NPs from 8 to 40 nm, with mean diameter 14.7 nm	[79]
	Ag 99.9%	Ag target (Ø 20 mm, 4 mm thickness), polished by sandpaper, washed with water and ethanol, immersed in deionized water, treated with pulsed laser ablation, Nd:YAG laser, λ = 1064 nm, 10 ns pulse, 10 Hz frequency, single pulse energy 435, 406 and 365 mJ/pulse	–	Average size Ag NPs depending on pulse energies 3.2 nm, 6.0 nm, 9.1 nm	[11]
	Ag 99.9%	Wires Ø1 mm used as electrodes, submerged in deionized water at 25 °C, arch discharged initial voltage of 135 V, 6,4 A peak current, on-pulse and off-pulse duration - 50 μs	–	Ag NPs with average sizes of 10 nm and 100 nm	[43]
	Ag 99.9%	Ag electrodes (Ø 2 mm, length 40 mm), exposed in different media (glucose/distilled water 10% and 25% w/w, glycerin/distilled water 10% and 25% w/w, phenol/distilled water 5% w/w, Mg(NO$_3$)$_2$•6H$_2$O/distilled water 0.01% w/w and 0,05% w/w, xylene, ethylene glycol, ethyl acetate, and phenol/toluene 5% w/w) with pulses of 5–10 A/cm^2, the cathode-anode gap was ≈ 1 mm, the NPs were separated by centrifugation and dried at 70 °C for 24 h	–	Ag NPs 35 to 100 nm, shape, depending on medium: rice shape, spheres, beads, grapes, platelets, balls, sponge particles, green bean shaped, cloudy leaflets, stacked plates, seeds	[40]
Chemical	AgNO$_3$	Twelve similar mixtures with sodium citrate, PVP and H$_2$O$_2$ were added to AgNO$_3$ solution under stirring. Different amounts of NaBH$_4$ solution were utilized for each mixture, stirred for 3 h, then filtered through 0.2 μm membrane filter	Citrate	Triangle, sphere, rod-like and cookie-like Ag NPs Ø from 3 to 30 nm, different aspect ratios	[54]
	AgNO$_3$ HAuCl$_4$	HAuCl$_4$ solution was added to heated AgNO$_3$ solution, after mixture started to boil sodium citrate was added, keeped boiling for 30 min	Citrate	50 ± 9 nm Au$_{0.5}$Ag$_{0.5}$ NPs with Ag prevalence in the shell	[47]
	AgNO$_3$	AgNO$_3$ was added to 0.4 mM Cetyltrimethylammonium bromide (CTAB) solution under stirring, then NaBH$_4$ solution was added, obtained seeds kept in dark (1 h), then seeds were added to freshly prepared solution of AgNO$_3$, ascorbic acid and 10 mM CTAB	CTAB	Triangular Ag NPs with different edge length (the smallest 46 nm and 14 nm thickness)	[50]
	AgNO$_3$	AgNO$_3$ solution, NaCl and sodium citrate premixed together, quickly added to boiling water, reducing agent - ascorbic acid, heated and stirred for 1 h	Citrate	23 nm Ag NPs seeds	[3]
	[Ag(NH$_3$)$_2$]$^+$	Different amount of AgNPs seeds were added into water at room temperature, then ammonia complex solution and ascorbic acid was added, stirred for 1 h, the AgNPs separated by centrifugation and redispersed in sodium citrate solution	Citrate	40–300 nm Ag NPs, depending on amount of Ag NPs seeds	[3]
	[Ag(NH$_3$)$_2$]$^+$	Mesoporous silica was mixed with [Ag(NH$_3$)$_2$]$^+$, sonicated for 2 h, placed in dark at ambient temperature overnight, then dried at 60 °C in an air-circulated oven	Embedded in silica	Silica-silver nanocomposite	[12]
	AgNO$_3$	AgNO$_3$ with PVP mixed in ethylene glycol, heated at 120 °C for 1 h, cooled solution added to ethanol/water mixture, then TEOS and ammonia were added, stirred for 1 h at room temperature. Further, to induce AgNPs growth on surface the NaBH$_4$ was added to mixture, stirred for 1 h	Silica	65–90 nm Ag@SiO$_2$@Ag$_{seed}$ NPs with surface seeds ≈ 5 nm 70–100 nm Ag@SiO$_2$@Ag NPs with surface Ag NPs ≈ 12 nm	[13]
	AgNO$_3$	The 1:15:15 M ratio of DNA:Ag$^+$:NaBH$_4$ was utilized. Previously the DNA assembly with specific sequences was prepared in phosphate buffer saline in 37 °C for 2 h, then Ag$^+$ ions were added and kept in dark at 4 °C for 1 h, subsequently NaBH$_4$ was added, the reaction maintained for 5 h in dark at 4 °C	DNA	DNA-harbored Ag clusters with ≈ 4 nm size	[15]
	AgNO$_3$	AgNO$_3$ and glutathione (molar ratio 4:3) was added to the flask under nitrogen flow with heated (120 °C) ethylene glycol, kept at 120 °C for 1 min to form colorless solution, then the temperature increased 165 °C with heating rate 20 °C/min. The reaction mixture cooled in ice-water bath in different time points (11, 13, 15, 16, 22, 28 min)	Glutathione	2–10 nm Ag$_2$S NPs, depending on reaction time	[14]
	AgNO$_3$	AgNO$_3$ solution and glutathione was added to ice cold water, pH raised to 12 by NaOH solution the formation of Ag$_2$O-NPs was observed. To the obtained Ag$_2$O nanocrystals separately the 1. NaBH$_4$ solution, 2. ascorbic acid, 3. hydrazine, 4. sodium sulfide or 5. sodium bromide was added at once	Glutathione	1. Hollow Ag NPs, 2. ordinary Ag NPs, 3. hollow in part Ag NPs, 4. hollow Ag$_2$S NPs, 5. hollow AgBr/Ag NPs	[56]

Table 1 (*continued*)

Method	Precursor	Synthesis conditions	Stabilization system	Product	Ref.
	CF_3-CO_2Ag	Ag trifluoroacetat was dissolved in isoamyl ether/oleic acid mixture at 160 °C under N_2 atmosphere, then precipitation was performed with sonication in ehtanol and subsequent centrifugation (3000 rpm)	Oleic acid	Hydrophobic Ag NPs $\approx$ 5.2 nm	[80]
	$AgNO_3$	$NaBH_4$ and citrate mixture heated to 60 °C for 30 min, then $AgNO_3$ was added drop-wise and temperature was raised to 90 °C, then the pH was adjusted to 10.5, the reagent excess was removed by centrifugation (12,000 rpm) and washing with deionized water	Citrate	Ag NPs with size 5–100 nm, depending on Ag^+ amount	[55]
	$AgNO_3$ AgCl	Ethylene glycol (EG) was heated to 140 °C, subsequently the HCl/EG, the $AgNO_3$/EG and PVP/EG solutions were simultaneously introduced, after 8 h the mixture removed from heat, the vial was kept loosely capped for 20 h and then tightened. The tests with addition of different amount of HCl, NaCl and HNO_3 were performed: 1. pure EG (with no HCl), 2. with addition of HNO_3 (no HCl), 3. with NaCl (no HCl), 4. standard procedure, 5. HNO_3 and NaCl (no HCl), 6. HNO_3 and HCl, 7. AgCl and HNO_3	PVP	1. Irregular/polydisperse Ag NPs, 2. truncated octahedra; 3. nanowires, nanocubes and irregular, 4. nanocubes, 5. cuboctahedra and truncated cubes, 6. nanocubes, 7. nanocubes	[52]
	$AgNO_3$	PVP/EG solution was heated to 160 °C, then NaBr/EG solution was added, subsequently dropwise $AgNO_3$ was introduced, kept for 35 min and then transferred to ice-water bath, the product crushed by acetone, separated (2000 rpm) and washed by water	PVP	Ag nanowires, $\approx$ 20 nm diameter	[53]
	$AgNO_3$	The synthesis in microfluidic device, where to the first inlet the mixture solution of $AgNO_3$, trisodium citrate and H_2O_2 and to the second inlet solution of $NaBH_4$ were introduced	Citrate	Triangular Ag NPs	[81]
		To the first inlet the triangular nanoparticles with TEOS and to the second inlet the ammonia in ethanol were introduced	SiO_2 shell	Triangular Ag@SiO_2 NPs	
Physico-chemical	$AgNO_3$	Laser ablation of 99.9% purity silicon target immersed in $AgNO_3$ solution, Nd:YAG laser, $\lambda = 355$ nm, pulses <40 ns frequency 5 Hz, power density per pulse <40 J/cm^2	Silica	Ag@SiO_2 NPs, with 11 $\pm$ 4 nm core and 1–2 nm shell	[82]
	$Ag_2C_2O_4$	Silver oxalate decomposition at 125 °C for 100 h	–	Ag NPs 5–20 nm	[59]
	$AgNO_3$	Dipped platinum anode and stainless-steel capillary tube utilized as cathode immersed in solution of $AgNO_3$ with fructose	Fructose	Polydisperse irregular Ag NPs	[63]
	$AgNO_3$	99.9% titanium anode and cathode Ø 2 mm were immersed in $AgNO_3$ solution, 15 A current and 3 V voltage	Citrate	Ag NPs $\approx$ 18 nm	[62]
Biological	$AgNO_3$	Flavone, chrysin, galangin, 3-hydroxyflavone, kaempferol, quercetin, myricetin, apigenin, luteolin, tricetin mixed with the $AgNO_3$ solution, pH adjusted to different values from 7.2 to 10.1, depending on flavonoid been used, the reaction carried at 23, 40, 70 °C	Flavonoids	Ag NPs 12–39 nm size, which depends on flavonoid been used and synthesis temperature	[7]
	$AgNO_3$	Different amount of beetroot extract were mixed with $AgNO_3$, reaction maintained overnight	Betanin	Ag NPs spherical, triangular and truncated triangular $\approx$ 15 nm	[75]
	$AgNO_3$	Lactoferrin, suspended in 0.09% NaCl, pH = 6, then $AgNO_3$ basic solution was added, the nanocomplex was separated by centrifugation 15,000 rpm, at 4 °C	Lactoferrin	Lactoferrin-conjugated Ag NPs with sizes 8–18 nm	[16]
	$AgNO_3$	Casein suspension in 0.05 M ammonium bicarbonate solution was mixed with $AgNO_3$ solution incubated at room temperature for 24 h, the nanocomplex was separated by centrifugation max speed for 8 min	Casein	Casein-conjugated Ag NPs in size range 4–100 nm	[83]
	$AgNO_3$	Essential oil of orange peel was mixed with $AgNO_3$ solution, stirred at 70 °C for 48 h	Compounds of essential oil	Ag NPs $\approx$ 3 nm	[66]
	$AgNO_3$	Solid state synthesis by milling of *Z. officinale* powder with 0,05–0,5 g of $AgNO_3$ salt, in hardened chromium steel jar with zirconia balls Ø 3 mm, 50 rpm, 30 min, balls:reacting powder was 15:1 w/w	Compounds of *Z. officinale* powder	Ag NPs with average size 11, 16, 20 and 24 nm, depending on $AgNO_3$ amount	[45]
	$AgNO_3$	Aqueous plant extract was mixed with aqueous $AgNO_3$ solution, kept in ambient temperature for 4 h	Compounds of *S. chinensis* L. extract	Coated Ag NPs with size in range 40–80 nm	[20]
	$AgNO_3$	To chitosan (50–190 kDa) dissolved in 0,5% acetic acid at 40 °C, cooled to room temperature, the $AgNO_3$ solution (to corresponding concentration 0.1, 0.2, 0.5, 1.0 and 1.5%) was added, then mixture was kept protecting from light to complete dissolution, films were formed on polystyrene plates and dried at 37 °C for 48 h	Embedded in chitosan	Ag NPs - chitosan films <5 nm, (Ag 0.1–0.5%) and Ag NPs 5–10 nm, (Ag content 1–1.5%)	[17]
	$AgNO_3$	*Bacillus licheniformis* biomass was mixed with $AgNO_3$ solution, then kept on shaker (200 rpm) at 37 °C for 24 h, then the biomass was removed by sonication and centrifugation (4000 $\times$g, 10 min), Ag NPs was purified by dialysis with 12,000 Da cut-off and by ultracentrifugation (200,000 $\times$g at 4 °C for 16 h) from HEPES buffer with sucrose gradient	Compounds of *Bacillus licheniformis* biomass	40–50 nm Ag NPs	[19]

Table 1 (*continued*)

Method	Precursor	Synthesis conditions	Stabilization system	Product	Ref.
	AgNO$_3$	*L. lactis* isolated from milk was incubated for 5 d at 26 °C in Mueller-Hinton broth, culture was centrifuged (9000 rpm), supernatant was combined with AgNO$_3$ solution, kept at 26 °C for 7 d, biocomposite separated by centrifugation (14,000 rpm) for 30 min	Compounds of *L. lactis* supernatant	Biocomposite with Ag NPs $\approx$ 19 nm	[84]
	AgNO$_3$	*O. limnetica* homogenate in phosphate buffer pH 7 mixed with AgNO$_3$ solution, kept at 35 °C under illumination for 48 h	Compounds of *O. limnetica* homogenate	Quasi-spherical Ag NPs with 3–18 nm size	[85]
	AgNO$_3$	Fungal cell filtrate of 1. *Alternaria* species, 2. *F. oxysporum*, 3. *Curvularia species*, 4. *C. indicum*, and 5. *Phoma* grown on potato dextrose broth at 28 °C for 72 h, mixed with AgNO$_3$ solution	Compounds of fungal cell filtrate	Ag NPs of 1. 7–20 nm, 2. 4–13 nm, 3. 5–23 nm, 4. 10–31, 5. 7–20 nm	[86]

heating caused metal sintering, which led to the formation of bigger NPs. Moreover, B. B. Bokhonov with coauthors has shown that thermal decomposition of silver salts of fatty acids led to the formation of self-assembled Ag NPs [60]. The authors have also observed the NPs sintering with an increase in temperature above 260 °C. It was suggested that fatty acids stabilize the Ag NPs assemblies, but the elevation of the temperature led to the desorption of carboxylic acids and subsequent aggregation. Y. Cai with colleagues has performed the deposition of uniform Ag NPs on stainless steel plates by AgNO$_3$ decomposition with laser irradiation [61]. They proposed the NPs formation mechanism, which comprises the AgNO$_3$ decomposition through Ag$_2$O formation with subsequent reduction to Ag under laser heating. However, the authors claim that the laser power should be controlled precisely. It was shown that low laser power was not sufficient to perform high efficient synthesis, while very high laser power led to overheating and to Ag NPs evaporation and sputtering. Additionally, even though, in general, arc discharge usually is utilized for the atomization of the bulk metal in NPs synthesis, it can also be utilized for AgNO$_3$ transformation to Ag NPs [62]. Moreover, the H. M. Yasin with coauthors has revealed the possibility to utilize micro-plasma for Ag$^+$ reduction in the solution to form fructose-coated Ag NPs [63]. The arc discharge as well as micro-plasma are the source of the fast electrons, which take part in the Ag$^+$ reduction. It is obvious that the amount of produced electrons plays a crucial role in the reduction process, thus providing an opportunity to control the synthesis. Moreover, the Ag NPs basic parameters can be controlled with the amount of utilized precursor and capping agent. It was shown, that a lower ratio of stabilizer to precursor led to the formation of bigger NPs with higher polydispersity, which can be explained by the increased contribution of aggregation in the NPs growth [63]. The electrolysis has also been used for Ag$^+$ reduction, where the mechanism of NPs formation is similar to that one with the utilization of micro-plasma [64]. Finally, the synthesis mediated by UV-Vis irradiation allows to change NPs shape [65]. It was suggested that UV-Vis irradiation increases the energy of small Ag nanoseeds, which then caused aggregation with the formation of Ag NPs of different shapes.

2.3. Biological methods

Recently, more attention is paid for the impact of the technologies on the environment. Thus, the so-called "green chemistry" becomes more popular. Regarding Ag NPs, the biological synthesis methods are considered to be eco-friendly, as for their production the harmful chemicals are not involved. Moreover, the biologically synthesized NPs in general exhibit lower toxicity to eukaryotic cells, so they provide a possibility for their exploitation in biomedical applications. The lower toxicity of biologically synthesized NPs is attributed to the fact, that the capping agent is formed with the compounds such as proteins [16], terpenes [66], flavonoids [7], which naturally can be found in an organism. Biological synthesis is based on the same principles as for chemical approaches, only the reducing and capping agents involved in the reactions should be of biological origin.

The "hot topic" in the biological synthesis of Ag NPs is the utilization of plants [45], fruits [20], plant seeds [67], or their extracts [68,69]. Moreover, the Ag NPs production with mushroom extract [70], marine algae [71] and even propolis [72] have been shown. To the active compounds, that can be involved in the Ag$^+$ reduction, and therefore NPs formation, the sugars [67], terpenes [66], amino acids [73], flavonoids [7], and other phenolic compounds [74] can be include. To give an example, R. K. Tomas et al. have produced Ag NPs with chlorogenic acid, which served both as a reducing and capping agent [74]. M. Svecova with coauthors has performed the Ag NPs synthesis with different flavonoids for SERS applications [7]. H. Veisi with colleagues has utilized the orange peel essential oil, composed mostly from limonene, to produce Ag NPs [66]. Moreover, the natural plant-derived pigments such as betanin [75] and curcumin [76] have also shown to be effective in the Ag NPs synthesis. What is interesting, the curcumin-based Ag NPs have revealed the synergistic antibacterial effect against *E. coli* and *B. subtilis*. Finally, in S. Shankar and J.-W. Rhim work the amino acid mediated Ag NPs formation was shown [73]. The authors have also utilized agar for the production of novel functionalized nanomaterials, which supposed to be useful in biodegradable packaging films formation.

The polysaccharide utilization for nanocomposites production in general is very popular in line with their medical applications. The Ag NPs-containing hydrogels and other polymer films are of the big interest for wound healing scaffolds and bandages production. Y. Jiang et al. have investigated the antibacterial and cytotoxic properties of Ag NPs-containing hydrogel based on konjac glucomannan and chitosan [77]. S. Ul-Islam et al. [78] as well as G. Lopez-Carballo et al. [17] have also utilized chitosan for production of new functional materials. Instead, A. K Kodoth et al. have revealed a possibility to utilize pectin for the synthesis of transdermal drug-delivery Ag-containing films [87]. J. H. Lee with coauthors has also exploit pectin and pullulan for antimicrobial films formation [88]. Proteins and nucleic acids are another biopolymers that show beneficial features in Ag NPs production. Recently, in our group, the synthesis of Ag NPs-containing nanocomposites based on whey proteins was performed [16,83]. Moreover, the Ag NPs formation through lysozyme [89], trypsin [90], and cytochrome C [91] was revealed. Finally, the self-assembled Ag NPs formation with G4-DNA has been shown by I. Libitz and A. Kotlyar [92].

Lately, it has become more popular to create Ag NPs via microorganism synthesis. It was shown that bacteria [19,84,93,94], fungi [86], cyanobacteria [85] and even viruses [95] can be utilized for NPs synthesis. The viruses capsid predominantly comprise proteins, so it can be considered as protein-mediated Ag NPs synthesis. Instead, the Ag NPs synthesized by cellular organisms can be performed in several different ways, namely intracellular and by utilization of culture supernatant, bacterial biomass, or cell-free extract [96]. The components of the synthesis mixture act both as a reducing agent and the stabilizer, forming
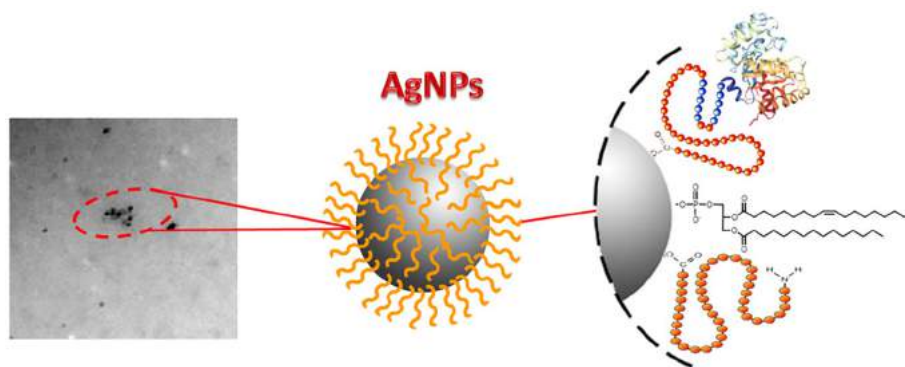
7

Fig. 2. The structure of AgNPs with organic deposits on the surface.

the organic deposits on the surface of the NPs (Fig. 2). Unfortunately, the exact mechanism and substances that are involved in the Ag NPs formation are still unclear. Moreover, S. M. Mehta et al. have revealed the possibility to exploit tryptone, the component of various culture media, for Ag NPs synthesis, which makes the interpretation much more complicated [97]. Additionally, a lot of culture media for microorganisms growth comprise casein hydrolysate, and investigations of our group have shown that casein is able to reduce Ag^+ without any additional conditions [83].

However, it should also be mentioned that with the utilization of the biological synthesis, the control of NPs basic parameters is less precise. Hence, the utilization of biologically synthesized Ag NPs is rather restricted in different devices or in advanced analytical techniques, where the desired optical features of the NPs are obtained by the changes in shape and size. Moreover, the biological systems may include some contaminants that disturb the synthesis. To one of such contaminants the Cl^- can be include, which forms the insoluble AgCl, thus tending to form non-metalic AgCl NPs [71]. Generally, the production of pure metallic NPs is a challenge in biological approaches, which attracts big attention of the scientists. The Cl^- is an integral part of culture media for microorganisms growth. Thus the utilization of microorganisms for Ag NPs synthesis often leads to the formation of undesirable AgCl or composed Ag/AgCl NPs. The main question, which appears during such a synthesis process is which kind of the product has been obtained. In some cases, the scientists make erroneous statements by incorrect interpretation of obtained data. N. Duran et al. have reviewed the articles focused on biogenic Ag and AgCl NPs synthesis and they noticed, that in some cases the researchers claim the production of metallic Ag NPs, while the XRD (X-ray Diffraction) for such products exhibited only the formation of AgCl [98].

2.4. Size and shape control

One of the major issues in the NPs production is a size control, as size determines NPs physical and biological properties. The NPs formation is the complex process, which in general can be divided into several main parts: nucleation, growth through Me^0 incorporation, and the aggregation. The nuclei formation is a thermodynamically dependent process [99]. The surface free energy always being positive, meaning that nuclei appearance is a thermodynamically disadvantageous process. Instead, crystal growth leads to a decrease in system energy. Thus, the growth process mainly depends on the possibility of mass exchange between NPs seeds and the solution as well as from the capability to aggregate. T. K. Nguyen et al. in their excellent review have revealed the theoretical details of the NPs nucleation and growth mechanisms in a solution [99]. It can be derived that Ag NPs size and size distribution are strictly dependent on the time-resolved Ag^0 concentration in the solution, which in turn depends on the amount of metal precursor, that have been used as well as the reaction rate of Ag^+ reduction. The excess of

the metal precursor in general leads to bigger NPs formation [68]. Instead, the high reaction rate at the beginning of the process makes it possible to produce a bigger amount of NPs with a lower size. Thus, it can be derived that the reduction potential and utilized amount of reducing agent, which influences the reaction speed, is one of the major factors. The redox potential of Ag^+ can also be influenced by pH value. Obviously, the reaction can be affected by changes in temperature [3,56,68].

The aggregation plays an essential role in the NPs formation (Fig. 1). The widely accepted theory implies NPs growth through the aggregation of the crystal nuclei [68,99]. Moreover, the liquid-cell TEM have revealed the formation of sub-10-nm Ag nanorods through smaller quasi-spherical particles aggregation, which can be considered as the evidence of previously accepted theories [100]. However, uncontrollable aggregation can lead to the formation of more massive structures, that no longer possess the unique features of NPs. Thus, sufficient stabilization is an indispensable part of NPs synthesis and storage. Still, in A. Suresh et al. work the synthesized uncoated Ag NPs unexpectedly revealed zeta potential −42.5 mV in deionized water, which is considered to be enough for NPs stabilization through electrostatic mechanism [101]. The effect was attributed to the adsorbed nitrate ions on the NPs surface. The H. Kang et al. in their review have shown the variety of approaches involved in the stabilization of plasmonic NPs [102]. Besides the approaches that already have been shown above (i.e. citrate, PVP, flavonoids, proteins, DNA, polysaccharides, etc.) the utilization of inorganic shells induces high interest among the researchers. Silica coatings have shown beneficial properties during metallic NPs utilization [103]. To silica virtue, the high stability to the water environment, various chemicals, and elevated temperatures can be include. Moreover, silica is transparent for electromagnetic irradiation in the wavelength range from 300 to 800 nm, which makes it possible to utilize in the synthesis of different nanocomposites for optical applications. The different silica-containing structures can be easily produced through a highly-controllable Stöber process. More synthesis details and properties of silica-containing structures can be found in B. J. Jankewicz et al. work [104]. It should be noted, that besides the stabilization of the NPs the capping agent also determines the surface charge of the NPs, which in general is a reason for electrosteric stabilization mechanism. To give an example, A. Suresh et al. have synthesized Ag NPs with different capping agents [101]. The Ag NPs stabilized with poly (diallyldimethylammonium) have a positive surface charge of +45 ± 3.1 mV, biologically synthesized NPs have a negative charge of −12 ± 2 mV, finally, the NPs capped with oleate revealed the negative charge of −45.8 ± 4.4 mV. However, the authors have investigated the cytotoxicity of as synthesized NPs, and it was shown that positively charged Ag NPs have revealed the highest cytotoxicity against both macrophage cells and lung epithelial cells. What is interesting, the biogenic Ag NPs, which supposed to be more biocompatible also have revealed higher cytotoxic properties than uncoated and oleate-coated

Ag NPs. The reason for such behavior partially can be explained by the same mechanism as for NPs stabilization, namely electrostatic interactions between charged objects. T. Silva et al., which also have synthesized the positively charged NPs with the utilization of the branched polyethyleneimine as a stabilizer, claim that possible higher toxic behavior is due to the interaction of such NPs with negatively charged cell wall [31]. In the case of biogenic Ag NPs, probably the relatively low surface charge was not able to prevent interaction with cell walls, thus causing a higher toxic effect.

Another approach for size control is the limitation of the NPs formation volume, which implies the utilization of templates. D. J. Lipomi et al. work can illustrate the approach in the simplest way [61]. Authors have produced the Au and Ag nanostructures by creating of protecting epoxy masks on the substrate and subsequent deposition of metallic thin films. The epoxy masks then were etched from the surface, leaving the highly structured plasmonic nanoarrays. Generally, the formation of NPs layers on the substrates is of high interest for multiple applications in technique and science. Therefore this issue is extensively investigated and shown in different articles. To give an example, in K.-M. Ng et al. work the NALDI plates were prepared by argon ion sputtering of Ag plates with subsequent NPs deposition on the glass substrate [8]. In T. Nakamura et al. the Ag NPs were deposited on the hydrogen-terminated silica by vaporization of Ag disk [105]. However, the presented processes is highly labor-extensive, moreover in L.S. Kibis work it was shown that the presence of the oxygen in synthesis zone may provide to formation of undesirable Ag_2O NPs [39]. Thus, the high interest attracts the possibility to form layered structures by deposition of Ag NPs prepared by chemical synthesis. M. Oćwieja with colleagues in their excellent review work have revealed different methods for the AgNPs layers deposition on the substrates together with the kinetics of the process as well as the stability of formed structures [35]. At the end of the work authors have revealed the possible applications of the obtained materials.

However, a more simple way is to use naturally formed templates for NPs size control. For instance, the polymers can be utilized for NPs synthesis, where inter-chain spaces serve as a reaction cavities for NPs formation [106]. Moreover, I. Moglia et al. have synthesized AgNPs in the human ferritin cavity [107]. T. W. Giessen and P. A. Silver have also utilized a bioengineered protein compartment (bacterial encapsulin system) derived from *T. maritima* for uniform and stable AgNPs synthesis [108]. The highly structured frustules of diatoms can also be utilized as a template for NPs synthesis [109]. Moreover, the viruses capside can be considered as nanoreactor for NPs production [110]. Still, the utilization of microfluidic devices in line with their possibility in NPs size and shape control were reported [18]. Moreover, the microemulsion method, where the micelles serve as a microreactors, has also shown to be efficient for size control in AgNPs synthesis [111].

The second important Ag NPs feature that should be controlled during synthesis is their shape, as it affected the NPs optical properties. The possibility to control Ag NPs shape is highly desired in plasmonic applications (surface-enhanced Raman spectroscopy, light energy harvesting, photocatalysis, etc). As it was mentioned above, the NP formation begins from the nuclei or NP seed formation, then it goes through a metastable fluctuating state where the primary structure can be formed. In the end, the particle obtained its final shape, which depends on multiple factors: temperature, the concentration as well as the type of reagents that have been used, the presence of trace ions [48,52]. To give an example, T. Huang with X.-H. N. Xu has performed the Ag NPs synthesis with various shapes by changes in the amounts of $NaBH_4$ added to the reaction mixture [54]. J. Wu et al. have shown that in DNA-mediated Ag NPs synthesis the nucleotide sequence can affect the final morphology [112]. I. Chakraborty with colleagues has also shown that synthesis with different proteins, i.e. lysozyme, apotransferrin, avidin, β-lactoglobulin, BSA (bovine serum albumin), hemoglobin, ovalbumin, and catalase, led to the formation of AgNPs with different shapes [113]. Moreover, the NPs shape can be changed by post-synthesis

transformation under heating or light irradiation [65]. C. -M. Tsai et al. have also shown the AgNPs prisms conversion by KSCN, which was dependent on the reagent concentration [114]. The effect can be explained by NPs partial dissolution with subsequent structure rearrangement, namely the recrystallization process [115].

3. Investigation techniques

The properly planned experiment is a milestone in all investigations. Advances in science and technique have introduced numerous sophisticated devices, which can be utilized for nanomaterials study. The accurately chosen set of techniques can provide comprehensive information about the object under investigation. However, the received results can be affected by drawbacks and artifacts of utilized methods, and in consequence, can lead to false conclusions. Thus, the scientist should consider all possible problems during their investigations. Table 2 presents the scope of the techniques and approaches for AgNPs and their composites study, the more detailed description for them can be found below.

3.1. Optical imaging

Conventional optical microscope due to diffraction barrier is restricted in the ability to distinguish between two points separated by a lateral distance less than half the wavelength of visible light ($\approx$200 nm), which in general makes difficult the direct investigation of nano-objects. However, T. Huang with X.-H. N. Xu in their work showed that the dark-field optical microscope (DFM) can be useful for single-NPs plasmonic microscope investigations [54]. The technique allowed to study Ag NPs LSPR properties in solution depending on their size and shape since NPs under DFM appeared as bright shining and colored spots. However, the dark-field optical microscopy and spectroscopy allow to study only the scattered light, therefore obtained single-NP LSPR represents the scattering of single NP, but not the absorption. Still, dark-field microscopy was useful for single Ag NPs oxidative dissolution monitoring [116]. The changes in the light intensity and color of the NPs over time clearly indicated the electrochemical dissolution process dependence from the applied potential. However, the technique usually requires an intense light source and long exposing time (up to several seconds) in order to collect spectra with satisfactory signal-to-noise ratio, so the fast dynamic observations can be impeded [151].

Fluorescent and confocal microscopy are frequently utilized for investigation of the Ag NPs toxicity and antibacterial properties. To give an example, in T. Liu with colleagues work fluorescence microscope have been utilized for investigation of the surface-attached bacteria and the influence of Ag NPs on bacteria capability to adhere [51]. Additionally, M. Assis et al. have studied the apoptosis and necrosis caused to MB49 and BALB/3 T3 cells by Ag NPs/α-Ag_2WO_4 composite [119]. C. G. Castro-Gonzalez with coauthors has observed the migration and accumulation of Ag NPs in *Stevia rebaudiana B.* leafs by multiphoton fluorescence microscopy, which allowed to identify preferable places of NPs accumulation [120]. The virtue of the fluorescent microscopy is that the cellular components may be labeled through specific molecules, allowing to observe the structures inside a live sample in real-time. However, the conventional fluorescent microscope is limited by low spatial resolution, which is near 200–300 nm in the lateral direction and 500–700 nm in the axial direction [152]. Lately, new possibilities were implemented with such techniques as stimulated emission depletion microscopy and super-resolution fluorescent microscopy performed with single molecule imaging, so the resolution can be enhanced to $\approx$ 30–40 nm in an axial direction [152]. Still, it should be noted that for NPs tracking in different parts of an organism the fluorescent labeling by different ligands is often utilized. However, in C. Kastner et al. work it was shown that the low stability of such complexes may lead to false results, as enhanced fluorescence may be due to free ligand but not the complex [153]. They showed that tyrosine may provide

Table 2
Instrumental techniques for study of Ag-containing NPs and NCs.

Technique	Study purpose	Information	Artifacts/problems	Ref.
Dark-field microscopy	Ag NPs features	Single-NP scattering LSPR for NPs with different shapes were defined	Low sensitivity, which requires intense light source and long exposing time (up to several seconds)	[54]
	Ag NPs dissolution kinetics	Changes in the NPs color and scattering LSPR intensity, which were dependent from applied potential were revealed		[116]
	The influence of surrounding media on LSPR	The red-shifts in Ag NPs LSPR were observed with increasing in refractive index of surrounding media		[117]
	Ag NPs interaction with green algae	The light scattering enhancement from the algae cells treated with Ag NPs was observed in comparison to control sample		[118]
Fluorescent microscopy	Attached bacteria on the surface	The results have shown the lower quantity of attached bacteria on the surfaces doped with Ag NPs	Low spatial resolution, low affinity of labeling molecules to NPs can lead to misinterpreta-tion	[51]
	The Ag NPs/α- Ag$_2$WO$_4$ toxic activity to cells	MB49 and BALB/3 T3 cells stained with acridine orange/ethidium bromide revealed the changes in the color intensity and uniformity, indicating the apoptosis and necrosis		[119]
	NPs migration in leafs	Multiphoton fluorescent microscopy revealed the places of NPs distribution in stem and leafs of *Stevia rebaudiana B.*		[120]
SEM	Ag NPs morphology	SEM images revealed predominantly spherical Ag NPs shape	Non-conductive samples surface charging, sample damage and transformation (i.e. reduction), artifacts from sample preparation (aggregation, size reduction, shape change, sample cracking)	[57,66]
	Surface morphology changes	Images revealed the formation of Ag NPs shell on silica rods and spheres, Ag NPs deposition on polyester and linen fibers		[78,121,122]
	Ag NPs biological activity	SEM revealed damage caused to bacterial cells *B. subtilis, E. coli, S. aureus.* The epidermal fissuring *in C. elegans* was shown		[76,123,124]
	Ultrathin surface morphology	The images of the surface morphology of *R. subcapitata* exposed to Ag NPs were made by more sensitive SE electrons		[118]
	Ag NPs uptake by FIB/SEM	The presence of 3138 $\pm$ 722 Ag NPs within one macrophage was revealed, mostly agglomerated, the distribution inside cell organelles cannot be discriminated		[125]
TEM	Ag NPs features	Ag NPs size and size distribution were defined	Non-conductive samples surface charging, sample damage and transformation (i.e. reduction), aggregation during sample preparation, the technique requires ultra-high vacuum, thin sample < 100 nm	[48,126]
		Ag NPs shape and structure were defined		[54,127]
		The lattice spacing in crystals was measured		[16,90]
	Ag NPs growth	LP-TEM revealed the formation of Ag-nanorod through small spherical NPs aggregation		[100]
Cryo-TEM	Ag NPs assemblies	The formation of chain-like Ag NPs aggregates mediated by 2,2′-bipyridine decorated peptoids was defined		[128]
	Ag$^+$ remediation	The adsorption of Ag$^+$ and distribution all over the bacterial cell surface with subsequent Ag NPs formation was revealed (made by EDX mapping)		[129]
AFM	Ag NPs size	The measured size for 100 NPs $\approx$ 20 $\pm$ 8 nm, while measured by TEM were 22 $\pm$ 6 nm	Electrostatic charging, which can change the movements of cantilever	[130]
	Surface morphology	Spherical Ag NPs formed by glucose were in size 10.3 nm and uniformly distributed on the support surface, while formed with dialdehyde nanofibrillated cellulose were with diameter of 19–37 nm and deposited along the fiber position		[131]
NSOM	Ag NPs	The LSPR for Ag NPs was performed, which revealed the red shift in comparison to UV-Vis due to coupling effect The NPs spherical shape and topography was defined	The interference of emitted by tip light with scattered, coupling effect with conducting tip	[132]
DLS	Ag NPs size	Measured size was 79 $\pm$ 0.5 nm in water, 71 $\pm$ 0.2 nm in cell culture medium	Aggregation, measurements are highly dependent from the surrounding media (the concentration of NPs, ions, proteins and other molecules, pH, viscosity, etc.)	[125]
	Ag NPs aggregation, ζ-potential	ζ-potential of citrate-capped was −27.7 $\pm$ 5 with hydrodynamic radii 27.8 nm (TEM - 10.1 $\pm$ 1.8 nm), prepared with green tea extract −36.2 $\pm$ 5 with hydrodynamic radii 87.7 nm (TEM - 8.3 $\pm$ 3.6 nm). The Ag NPs prepared with green tea extract showed higher aggregation stability in solutions with different content of NaCl, glucose, glutamine, cell culture component and different pH		[49]
UV-Vis	Ag NPs LSPR	Au@Ag nanocuboids longitudial band $\approx$552 nm, and transverse $\approx$461 nm	The sample should be clear with no dust and bubbles	[133]
		Spherical Au$_{0.5}$Ag$_{0.5}$ NPs band $\approx$ 470 nm		[47]
		Hollow Ag NPs LSPR band $\approx$ 480 nm		[56]
		Triangular Ag NPs, out-of-plane quadrupole band 339 nm, out-of-plane dipolar band 414 nm, in-plane dipolar resonance 523–585 nm		[50]
	Ag NPs stability	The freshly synthesized NPs LSPR $\approx$ 400 nm, the NPs exposed to sunlight for 25 days get another bands (470, 600 nm)		[130]

10

Table 2 (*continued*)

Technique	Study purpose	Information	Artifacts/problems	Ref.
Fluorescence	Pb^{2+} quantification	1.45 ± 0.3 nm Ag NPs capped with polymethacrylic acid revealed linear fluorescent enchantment depending on Pb^{2+} concentration in range from 0.0 to 1.0 μM	Inner Filter Effect (IFE I and II), absorbance by impurities and quencher in fluorescent band, the presence of fluorescent impurities	[134]
	Dopamine quantification	Fluorescent AgNPs $\approx$ 10 nm capped with 4-mercapto phenylboronic acid and 40-aminobenzo-18-crown-6 revealed linear quenching depending on dopamine content (0.001–0.1 mM) due to NPs aggregation		[135]
FTIR	Ag NPs formation and functionaliza-tion	1214.5 cm^{-1}, 3072.4 cm^{-1} bands appearance, increase in 1455.7 cm^{-1}, shift 1635.7 cm^{-1} → 1627 cm^{-1} after ampicillin binding	The specific bands hardly can by discriminated due to overlapping and significant shifts depending on molecular structure	[136]
		Presence of 1694 cm^{-1} stretching band of C═O group and 734 cm^{-1} of weak S—S vibration revealed alpha-lipoic acid binding		[137]
		The AgNPs formation and binding to lactoferrin affected the infrared spectra in range 1650–1400 cm^{-1}		[16]
Raman	Ag NPs functionaliza-tion study	The vibration between Ag(0) surface and pyridine nitrogen was revealed by appearance of 241 cm^{-1} on spectra	Fluorescence of sample and impurities as well as adsorption by matrix can burdened the study, heating may damage the sample and can cause blackbody thermal emission	[128]
	SERS study	All SERS spectra of Ag NPs with lyzozyme, BSA, cytochrome-C and hemoglobin has band $\approx$ 240 cm^{-1} attributed to Ag—N and Ag—S, band $\approx$ 1630 cm^{-1}, which replaces the amide I band at 1655 cm^{-1}, the shifts near 1375 cm^{-1} in cytochrome and hemoglobine can be assigned to hem bands		[89]
NMR	Mechanism of Ag NPs formation	The hydride intermediates ($[Ag_7(H)\{Se_2P(O^iPr)_2\}_6]$ and $[Ag_7(H)\{S_2P(OEt)_2\}_6]$) formation was revealed by appearance of doublets 1125. ppm (d, $J_{AgH} = 39.7$ Hz) and 1116.7 ppm (d, $J_{AgH} = 41.1$ Hz) at 298 K as well as octet at 3.50 ppm ($^1J_{H−Ag} = 39.4$ Hz) at 293 K and broad peak 5.65 ppm, ($^1J_{H−Ag} = 39.6$ Hz) at 223 K	Considerably low sensitivity, requires the core digestion of big NPs, $^{107/109}$Ag has low gyromagnetic ratio and big T1 value, which requires special devices and long term analysis	[138]
	Ag NPs effect on cell glutathione content	The glutathione signals in the range 2.51–2.55 ppm have disappeared after Ag NPs treatment, revealing its complete depletion		[139]
	Role of stabilizer and reducing agent in Ag NPs formation	Significant changes in chemical shifts of sodium dodecyl sulfate protons 4.086 ppm → 4.037 ppm, 1.360 ppm → 1.320 ppm, 0.952 ppm → 0.900 ppm after Ag NPs formation in the mixture with trisodium citrate, the decreased intensities of signals from trisodium citrate protons		[140]
XPS	Quantitative binding affinity of taurine	$\approx$2% of Ag as in unbound (elemental) state, Ag—O, Ag—N and Ag—S bounds were found to be ~71%, 11% and 16%, respectively, which revealed the sulphonate group binding to Ag	Sample charging, the sample transformation (i.e. reduction), sample can be examined only on 2 nm depth, requires ultra-high vacuum	[141]
UPS	Photoelectron emission yield	Doped with $\approx$ 4.5 nm Ag NPs hydrogen-terminated Si (111) show the photoelectron yield with p-polarization: $2.8\cdot10^6$, while that without Ag NPs has $1.4\cdot10^4$		[105]
AES	The morphology of Ag growing on Fe_3O_4	The data showed that Ag gas atoms adsorbed on Fe_3O_4 according to hemispherical cap model, which revealed the formation of separated Ag NPs but not the Ag layer	Sample charging, small examination depth, requires ultra-high vacuum, the sample transformation and damage	[142]
	Ag NPs formation	The technique revealed that small (5 nm) particles comprised from Ag have formed on bismuth silicate		[143]
EELS	LSPR modes for Ag NPs embedded in SiO_2	LSPR evolves depending on electron dose from $2.1\cdot10^6 e^{-}\text{Å}^{-2}$ to $18.7\cdot10^6 e^{-}\text{Å}^{-2}$, under lowest dose no LSPR shift was observed, with increasing of electron dose blue-shifts were observed from 2.8 to 3.2 eV (for NP $\approx$ 7 nm)	Sample charging, requires ultra-high vacuum, the sample transformation and damage	[144]
	Elements distribution over the NPs	In the middle of the NPs the electron energy losses corresponding to Ag atoms was observed, on the edges the presence of C, N and Ca was shown		[89]
XRD	in situ annealing behavior of Ag_2S NPs	For NPs heated in air the 2θ signals at $\approx$29°, 31.5°, 38°, 41°, corresponding to monoclinic acanthine α-Ag_2S disappeared, and the 2θ signals 39° and 43° of pure silver appeared. For NPs heated in argon, the XRD pattern changed to more complex, which may be attributed to monoclinic non-stochiometric acanthine α-$Ag_{1.95–1.98}$S	Preferred orientation of non-spherical NPs, low signal intensity for NPs below 10 nm, 2% sensitivity limit for composites	[145]
SAED	Ag NPs crystalline phase examination	Measured d-spacing (nm) were 0.233, 0.203, 0.141, 0.121 which are in good correspondence with Ag(0) hkl (nm) 0.236, 0.204, 0.145, 0.123, and AgO hkl (nm) 0.237 and 0.143	Sample charging and damage, requires ultra-high vacuum	[79]
ICP-MS	Changes in Ag, Fe, N and Mg content in *Stevia rebaudiana B.* treated with Ag NPs	With changes of Ag NPs concentration in culture media from 0 to 200 mg/L the changes in N ($38,067.3 \pm 45.3$ to $55,339.7 \pm 31.1$ μg/g), Mg (882.4 ± 9.5 to 1292.6 ± 11.2 μg/g), Fe (289.3 ± 4.5 to 143.3 ± 0.7 μg/g) and Ag (0.13 ± 0.0 to 188.2 ± 1.6 μg/g) content (calculated on dried weigh) were observed	Atomic (Cd) and polyatomic interferences, samples usually requires mineralization	[120]

Table 2 (*continued*)

Technique	Study purpose	Information	Artifacts/problems	Ref.
SP-ICP-MS	Ag NPs cellular uptake by Neuro-2a cells	Cells treated with 2 μg/mL of Ag NPs with sizes 50 and 75 nm revealed the uptake of 1662 and 605 number/cell respectively, while treated with 10 μg/mL of Ag NPs revealed the uptake 1989 and 1740 number/cell	Aggregation, lower size limit (20 nm), impossible to distinguish different Ag form	[146]
TOF-SIMS	Ag NPs interactions and transformations in municipal wastewater	In positive mode silver-amine ions were observed $AgC_2H_6NO^+$, $AgC_3H_4NO^+$, $AgC_4NO_2H_2^+$ at 167, 177, 203.9 mass and Ag bonded with sulfur $AgSC_2H_3N^+$, $AgSC_3H_6N^+$ at 179.90 and 194.93, mass. In negative mode $AgCOOHCNH_2^-$, $C_3H_2NO_2Ag^-$, $C_5N_3O_2Ag^-$ at 179.91, 192, 241 and $AgC_2H_3SN^-$, $C_3H_2SNAg^-$, $C_3H_7SNO_2Ag^-$ at 179.89, 190.89, and 227.92 mass were observed	Spatial resolution is limited by diameter of primary ion beam, which is often bigger than NPs size	[147]
MALDI-TOF MS	NALDI analysis of benzpyridi-nium	With changes in laser fluence from 15 to 80 mJ/cm^2 the normalized total ion intensities for Ag NPs were from 5 to 35 •10^4 count/mm^2, while for Au NPs from 0 to 21•10^4 count/mm^2	NPs aggregation, analyte fragmentation	[8]
AF4	Ag NPs determination in environmental samples	1. the recoveries of PVP-capped NPs with sizes 30, 60 and 90 nm were shown to be 90.2, 78.6, 69.4 and 55.6% for tap water, river water, effluent and influent of wastewater treatment plant respectively; 2. the better resolution was shown to be in order effluent > river water > influent > tap water (based on UV-Vis detector); 3. the better consistency between measured and original sizes was observed in tap water and effluent (based on DLS detector); 4. ICP-MS detector showed the good separation only in tap water	Membrane fouling by irreversibly bonded NPs, NPs aggregation, non-selective upon size detectors (UV-Vis/MALS)	[148]
CE	Ag NPs separation	1. migration time in single standard analysis for 40 nm capped with branched polyethylenimine, PVP, citrate and polyethylene glycol were 958 ± 21 s, 1048 ± 15 s, 1275 ± 115 s and 958 ± 32 s respectively; 2. four component mixture was not possible to separate; 3. citrate capped was possible separate from PVP and polyethyleneglicol capped in two-component mixture	Aggregation, NPs sticking to capillary walls, low selectivity	[149]
DSC	TiO$_2$-Ag NPs doped gelatin films stability	Glass transition values by DSC were 59.52, 51.77, 52.19, 51.8 and 52.61 °C for films with 0, 1, 2, 3 and 4% of TiO2-Ag respectively	Heating rate is crucial	[150]

unreliable results, since it desorbs from the Ag NPs surface very fast, while fluorescent-marked BSA showed satisfactory Ag NPs-ligand stability.

3.2. Electron microscopy

The very first techniques that should be utilized for NPs characterization are SEM (Scanning Electron Microscope) and TEM (Transmission Electron Microscope) since they give invaluable information about structure and surface morphology of the materials. SEM is an imaging technique which in general deals with backscattered electrons (BSE) [154] and allows to investigate surface morphology of NPs [57,66], further the interactions of NPs with different systems can be studied. The Ag NPs deposition on silica spheres and rods [121], on polyester fibers [122] or on linen [78] and the investigation of the damage caused by Ag NPs to microorganisms [76,123] and nematodes [124] was observed by SEM micrographs. However, some other signals such as secondary electrons (SE) can also be obtained within this technique.

SE show higher sensitivity to surface morphology therefore can provide images with better quality [118]. In SEM incident beam electrons with energy in range 1 keV–30 keV are utilized, which can provide a complementary information, as depending on the electron energy sample can be scanned on the different depth (up to 100 nm for SE and 500 nm for BSE) [118,154,155]. Further extension of the technique can be made by combination with a focused ion beam (FIB), typically Ga$^+$, to make sample cross-sections and imaging by SEM [125]. The non-conducting sample charging is one of the most significant SEM problems that influence the image quality and therefore its interpretation. The negative charged surface can produce undesirable SE and influence on landing energy of the incident electrons, which lead to field enhancement between the surface and the electron detector.

Instead, positive surface charging transforms the sample to an electron trap [156]. An environmental scanning electron microscope (ESEM) is one of the techniques that can deal with the charging effect due to the presence of water vapor in the microscope chamber. What more, wet mode prevents samples from dehydration, which can introduce additional artifacts such as size reduction, shape change, and cracking, so it is extremely useful for biological systems examination [155,157]. For instance, ESEM was utilized to investigate the changes that occurred in earthworms after Ag NPs exposure [158]. Finally, to SEM drawbacks the low signal-to-noise ratio and spatial resolution, in comparison to TEM, can also be included [154].

TEM is one of the most common techniques for NPs structural features study. It provides information about size, shape, arrangement, and NPs structure. TEM exist in several different forms to which CTEM (Conventional TEM), HRTEM (High-resolution TEM), and STEM (Scanning TEM) can be include. The image in CTEM is formed with an appropriate detecting system by transmitted through sample electrons. Adhikari et al. use TEM images to determine size and size distribution of synthesized Ag NPs [126]. However, they noted that in some cases NPs sizes could not be reliably determined due to disproportionate aggregation during sample preparation for analysis. Polte J. with colleagues were also unable to distinguish the Ag NPs sizes due to large aggregation caused by simple drying [48]. Generally, the NPs aggregation is one of the main problems in Electron microscopy (EM) investigations. Donald A. et al. have observed the transformation of AgNPs to a core@shell and hollow Ag@Ag$_2$SNPs, TEM images clearly indicate the changes in structure [127]. Still, TEM-images have 2D-character, so 3D-images made by SEM can provide more details regarding the morphology of the NPs [58,123]. HRTEM technique is based on observation of interference of the electron beam by the sample. This allows to obtain high phase-contrast images, that show details finer than 0,2 nm. In particularly HRTEM provides direct images of the atomic

structure of the samples [159]. By HRTEM it was possible to distinguish the protein coating of different protein-conjugated Ag nanocomposites [89,90] and the lattice spacing between neighboring fringes as it was made for trypsin-Ag conjugates [90]. Still, TEM has its drawbacks to which labor-intensive sample preparation can be include, as the sample should be very thin, so it can allow passing electrons through the sample (not more than 100 nm if possible). In some cases for HRTEM samples should be as thin as 10 nm (generally 50 nm). Additionally, TEM handles with high-voltage electrons (80–300 keV) that may damage the sample [159].

In STEM instruments the principles of the SEM and TEM are combined, where the sample is scanned across by sub-nanometer diameter probe, and the image is formed through transmitted electrons. Microscopy and spectroscopy techniques are shown to be complementary techniques, and the utilization of both can help to avoid inadequate characterization of material [154]. STEM instrument in comparison to CTEM can be employed to spectroscopic analysis, as within the technique some additional valuable signals can be measured, such as SE, BSE, characteristic X-rays, and electron energy loss, so it provides information with much better resolution about sample structure and is also suitable for chemical composition determination [159]. Energy dispersive X-ray spectroscopy (EDX or EDS) is a technique, usually coupled with electron microscopy, where the characteristic X-ray radiation from excited atoms is measured. Within the technique, it is possible to estimate both the compositional information of the whole sample as well as the location of individual elements across the surface. In Pomastowski et al. work by EDX detector the prevalence of Ag ions in synthesized NPs was estimated (Fig. 3), but also the presence of C, O, S and P confirmed the protein participation in NPs stabilization [16].

Blommaerts et al. conducted an EDX mapping of the Au/Ag NPs. The analysis shows the core-shell structure of the particle, with the prevalence of Ag on the surface [47]. EELS (Electron Energy Loss Spectroscopy) combined with STEM was also useful for the chemical composition determination of lysozyme-Ag nanocomplex [89]. Within STEM the Selected Area Electron Diffraction (SAED) can also be conducted. SAED is widely utilized to distinguish crystal structure of AgNPs and it was shown that obtained data is complementary to that one from XRD analysis [74]. Another extension of the technique is Cryo-TEM approach. This technique together with liquid cell sample preparation TEM, which also called liquid-phase TEM (LP-TEM), allow to investigate nanoscale materials formation and nano-objects behavior in solutions. Both techniques are very labor-extensive but partially can fill gaps left by other methods [160]. By LP-TEM in situ particle growth in detail can be observed, as it was made for Ag nanorods [100]. However, the dynamic nature of LP-TEM processes and the presence of liquid decreases the resolution, what more important the incident electron beam can influence on synthesis process [160]. During Cryo-TEM analysis thin (up to 100 nm) frozen films of sample solutions are examined. As all processes in the samples are arrested it became possible to perform X-ray spectroscopic and EELS analysis, what more the 3D structure can be outlined. Ahmad et al. studied silver remediation from aqueous solutions by microorganisms. By Cryo-TEM coupled with EDX mapping the extra- and intracellular Ag NPs formation through silver ion adsorption and conversion was observed [129]. Moreover, Cryo-TEM technique confirmed the presence of chain-like Ag NPs assemblies, mediated by 2,2′-bypiridine decorated peptoids, in solution, as such structures could also be introduced through NPs aggregation induced by dried sample TEM preparation [128]. Still, the object under investigation is highly sensitive to electron beam exposure, which can damage both the sample and vitrified solvent, so the interpretation of the images became more complicated [160].

3.3. Scanning probe microscopy

Scanning probe microscopy (SPM) exploits a very sharp probe tip for local characterization of materials surface and can provide a structural map of the surface in the atomic-resolution scale. Among other SPMs, an atomic force microscope (AFM) is one of the most employed techniques for surface topography determination and is also common for nanostructures investigation. In AFM the moving probe across the surface changes its vertical position depending on roughness and electric properties of the sample, which in most cases is detected by the position-sensitive photodetector. The AFM has been utilized for investigation of Ag NPs deposition on dialdehyde nanofibrillated cellulose. It was possible to determine the Ag NPs sizes distribution, which was in the range between 19.0 and 37.0 nm with an average size 28.14 nm [131]. I. Romer et al. also investigate the Ag NPs by various techniques, the average size of citrate capped AgNPs was measured as 20 ± 8 nm by AFM, while TEM showed the NPs size as 22 ± 6 nm [130]. It should be noted that AFM measurements can be burdened with unwanted artifacts and signals including the motion of the macroscopic body of cantilever due to electrostatic effects between the cantilever body and the sample, which can lead to misinterpretation of obtained results [161].

Near-field scanning optical microscopy (NSOM) is another scanning technique, that can be assumed as an improved version of the conventional optical microscope. In NSOM the properties of evanescent waves are utilized, which implies that scanning probe during the analysis is located not further away than aperture diameter. Thus, it is possible to overcome the resolution limit and obtain information about the optical properties of the sample. Within the technique both the image and the relevant spectra can be obtained [162]. M. Beleites et al. have performed the NSOM topographical investigation of the Ag NPs. They also performed transmission mode measurements, which showed that Ag NP was surrounded with a halo with the increased transmission on the distance up to 200 nm. Such a phenomenon can be explained by interference of the light emitted by scanning tip and scattered light from NP. Finally, it was shown that the LSPR for Ag NPs measured by transmission NSOM exhibit the redshift in comparison to UV-Vis analysis, which may be explained through the coupling effect with the conductive probe [132].

3.4. Dynamic light scattering

Dynamic light scattering (DLS) is a technique with a short time required for measurements and relatively low cost of the apparatus, therefore it frequently exploits for NPs sizing. For instance, DLS is often utilized as the detector during the NPs separation by A4F [148]. However, in general the particles size values derived by DLS are overestimated. In R. Ma work the measured by TEM size for nanostructured Ag NPs was 76.6 ± 20.7 nm, calculated from XRD diameter was 30.4 nm, while hydrodynamic radius measured in 1 mM $NaHCO_3$ was 89.1 ± 1.5. It should be mentioned, that in TEM only the size of the NPs metallic core can be estimated. Instead, in DLS the hydrodynamic radius, which is defined as hypothetical hard sphere that diffuses with the same speed as the particle assayed in DLS [30], of the particles is measured. By XRD the size of crystallite can be calculated, which in case of twinned or poly-crystallite NPs can be several times smaller than whole particle core. In practice, NPs in colloidal dispersion are the combination of the metal core with solvated corona, which has a dynamic character and fluctuates depending on the surrounding environment. Such a phenomenon was shown in Guehrs et al. work where DLS analysis of commercially produced 75 nm size Ag NPs have been performed, the measured values were 79 ± 0.5 nm and 71 ± 0.2 nm for particles dispersed in water and in cell culture media respectively, while TEM measurements revealed NPs sizes as 74 ± 8 nm [125]. Song et al. have also characterized Ag NPs synthesized by silver nitrate reduction with curcumin, and the measured hydrodynamic radius ranged from 30 nm to 90 nm [76]. TEM analysis has revealed that as mentioned Ag NPs were of spherical shape with a relatively uniform diameter of 35 ± 5 nm. Generally, the high concentration of different molecules in the culture media, especially proteins, through surface adsorption can drastically change the hydrodynamic radius of dispersed
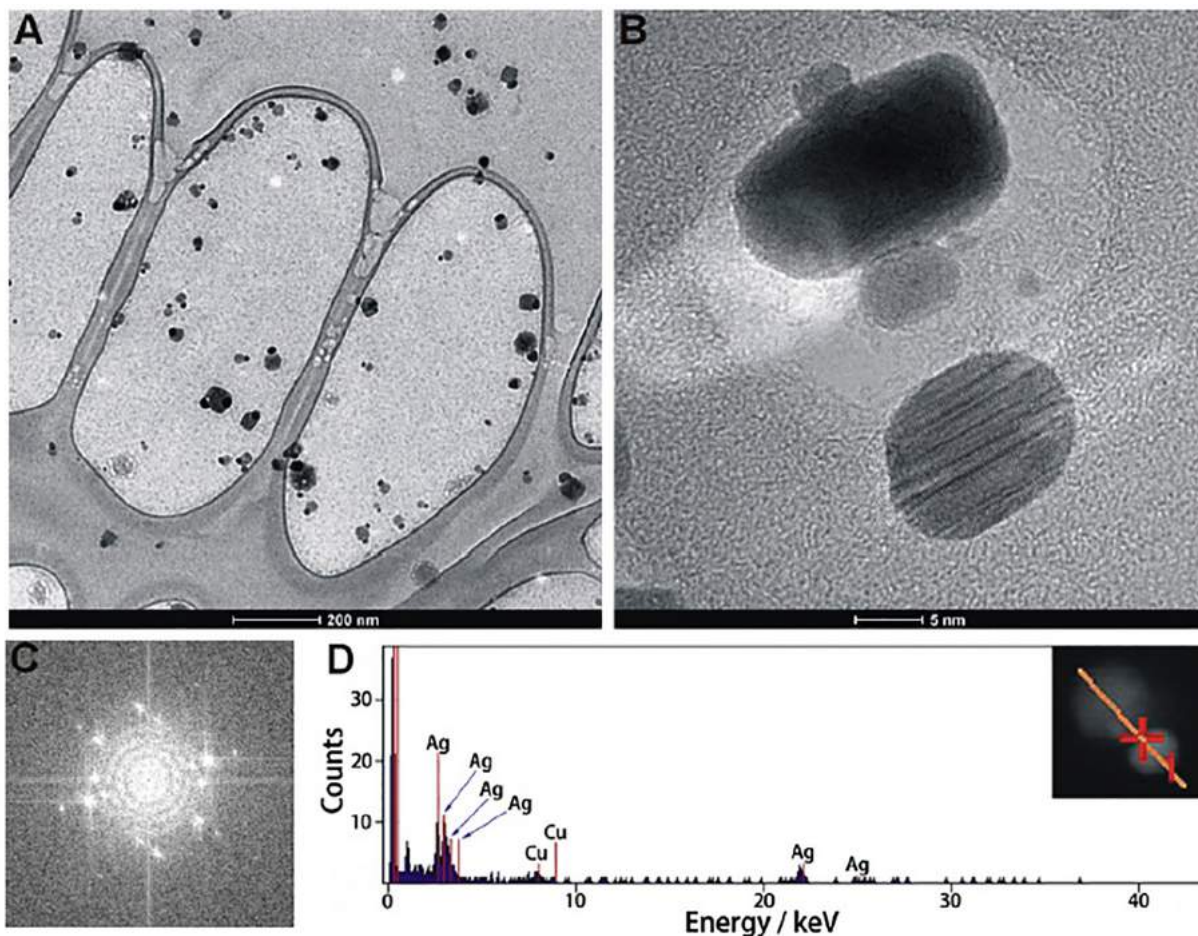
Fig. 3. TEM image of Ag-Lactoferrin nanocomplexes. Bar: (A) 200 nm, (B) 5 nm, (C) Fast Fourier Transformation, and (D) EDX spectra. Reproduced with permission from ref. [16]. Copyright 2016 American Chemical Society.

NPs. Moreover, adsorption is a complex process, which needs time to stabilize, so obtained results can change over time. However, the measurements are also not recommended to perform in deionized water, as it always leads to size overestimation up to 10 nm, which is due to the long-distance interactions between particles in the absence of ions [30]. Additionally, the hydrodynamic radius in DLS is derived from Stokes-Einstein relationship, in which the calculations for spherical shape particles are considered, so for anisotropic particles, it does not correspond to any of their geometrical dimension and can be accounted to the DLS drawbacks. Moreover, in DLS the cumulative analysis for average size estimation is utilized, which is not suitable for polydisperse systems [35]. However, it should also be mentioned that for NPs the anisotropic inelastic Mie scattering is observed that has an angle-dependent character [30]. Moreover, for smaller NPs the absorption cross-section is dominant over scattering cross-section [5,163] thus smaller NPs reveal the lower intensity of scattered light. In some older versions of the DLS instruments the backscattered light was gathered at the angle of 90°, presently detectors are placed at 173°, which allows to avoid the excess of scattered light and unmask scattered light of low intensity, thus contributing in the higher resolution of measurements [30].

The dependence of measured size from solvent characteristics (refractive index, viscosity) was also revealed, which should be considered during the investigations [30]. Belteky et al. have investigated the influence of different electrolytes and pH on Ag NPs hydrodynamic radius and aggregation behavior, which is considered to be the most frequent problem in DLS analysis [49]. Besides environmental conditions, the aggregation may also appear due to NPs high concentration. Moreover, to

the high concentration effects the multiscattering occurrence can be attributed, which results in artificially smaller measured NPs size [30]. Changes in pH and electrolytes concentration in solution also influence charge of NPs surface, which commonly expressed in ζ-potential (or electrokinetic potential) changes. ζ-potential cannot be measured directly, therefore it can be expressed through electrophoretic mobility deduced from Henry's equation [35]:

$$\zeta = \eta\mu_e/\varepsilon f(\kappa d_p) \tag{1}$$

where η – solutions viscosity; μ_e – electrophoretic mobility; ε – dielectric constant of the dispersant, $f(\kappa d_p)$ – Henry's function of dimensionless parameter.

In case when the electric double layer thickness is much smaller than the radius of the particle in particularly for particles much bigger than 100 nm, the Henry's equation with some approximation can be modified to Smoluchowski equation [30,164]:

$$\zeta = \eta\mu_e/\varepsilon_r\varepsilon_0 \tag{2}$$

where η – solutions viscosity; μ_e – electrophoretic mobility; ε_0 – electric permeability in vacuum, ε_r– dielectric constant of the solution.

Instead, for NPs dispersed in low salt concentration, when the electric double layer thickness is much bigger than particle radius and Henry's function of dimensionless parameter is taken as 1 the Hückle equation can be utilized:

$$\zeta = 3\eta\mu_e/2\varepsilon_r\varepsilon_0 \qquad (3)$$

where η – solutions viscosity; μ_e – electrophoretic mobility; ε_0 – electric permeability in vacuum, ε_r– dielectric constant of the solution.

However, the Hückle equation is shown to be not applicable for aqueous solutions [30]. Thus, most often the Smoluchowski model is utilized. However, some scientists claim that Smoluchowski equation should not be utilized for NPs ζ-potential estimation as the measured values by this model in general are smaller than real one, which can be obtained only from Henry's model [35].

The electrokinetic potential is often measured within DLS analysis, as it was made in the above-mentioned work of P. Belteky with coauthors. They have investigated the Ag NPs synthesized with green tea extract in comparison to Ag NPs stabilized with citrate. In consequence, NPs stabilized with green tea extract had about 8,5 mV lower ζ-potential than citrate capped ($-27,8$ mV), which caused better stability in solutions with different content of NaCl, glucose, glutamine, cell culture component and different pH [49]. Generally, the surface charge of the NPs determines their electrokinetic stability in the suspension. In turn, the magnitude and the sign of the surface charge are determined by the adsorbed molecules on the surface of NPs, in particular the capping agent. For instance, the Ag NPs stabilized with poly (diallyldimethylammonium) have positive surface charge, while uncoated Ag NPs which probably contain adsorbed nitrate ions on the surface were negatively charged [101]. According to Derjaguin−Landau−Verway−Overbeek (DLVO) theory, the stability of the NPs suspensions against aggregation is a result of interplay of two opposite forces, i.e. the attractive van der Waals forces and repulsive Coulombic forces of charged particles [102]. It is suggested that absolute ζ-potential values greater than ±25 mV are required for NPs and biocoloids systems stability against rapid aggregation, where the particles would stay in dispersion for a longer period [16]. In work performed in our group, the measured ζ-potential of AgNPs was 0 ± 0.5 mV in pH range 2–4, which in consequence led to the AgNPs aggregation and therefore the measured by DLS sizes varied from 1500 nm to 200 nm [93]. Instead, ζ-potential values in pH range 4.5–10 decrease up to – 25 eV, and the NPs size was estimated as 100 ± 1.5 nm [93]. However, the transfer of NPs from a synthesis solution to the environment of the investigated systems usually leads to the exchange of the surface adsorbed molecules with dissolved one, which in consequence can change the charge and magnitude of the NPs surface and therefore influence their stability and interaction behavior [27,34,147].

3.5. UV-Vis and fluorescence spectroscopy

UV-Vis spectroscopy is a fast, simple and sensitive technique, thus it is widely utilized for Ag NPs initial characterization. UV-Vis spectroscopy can provide both quantitative and qualitative information about investigated material [35]. For example, UV-Vis detectors are typical in separation techniques, such as CE (capillary electrophoresis) or FFF, for Ag NPs quantification and therefore the information about NPs absorption in the UV-Vis range is so valuable [148,165]. However, it should be mentioned that for organic compounds the UV-Vis spectrum is a consequence of the presence of the chromophores, while UV-Vis enormous light absorption extinction of metal NPs is connected to LSPR appearance. LSPR is a complex process and described as excitation and coherent oscillation of electrons under the electromagnetic field of incident light [166]. The main feature of the LSPR in NPs is that the oscillation of the excited electrons is limited by the volume of the NPs [166]. Thus, it plays a dominant role in the excited electrons oscillation frequencies and therefore on the wavelength of the resonant light band. Still, the complexity of LSPR phenomenon implies the influence not only the NPs volume but also their composition [133] and structure [56], shape [50], surrounding media (especially that one that is in the closest vicinity to NPs, in particularly the capping agent/adsorbed

molecules on the NPs surface) [166], and interactions with other NPs (including aggregation) [121,167], which alone with NPs size distributions have an influence on the width of the absorbance band, the shifts of the resonant wavelength as well as the appearance of the additional absorption band [46,166]. For spherical silver NPs the LSPR absorption light band normally is near 400 nm, while for triangular Ag nanoplates the maximum absorption in a range 500 nm - 1000 nm was observed [50,168] and aggregation of the NPs, as well as rod-like shape, leads to the appearance of two peaks: one near 400 nm and additional in the range from 500 nm to 1000 nm [46,169]. The influence of the NPs size distribution on the broadening of LSPR band was shown in M. A. Garcia work [166]. It was calculated that AgNPs with a size of 10 nm and deviation of ±8.5 nm has three time higher full-width-at half maximum of LSPR band than for NPs with the same size but dispersion of ±4.5 nm. T. Huang and X.-H. N. Xu have also shown significant LSPR band broadening in AgNPs of different shapes and size distributions [54]. The majority of the reports note the appearance of the intense absorption band in UV-Vis range as evidence of NPs production and by the changes in the absorbance intensity explain the completeness of the process [93]. To give an example, J Polte et al. have observed the in-situ intensity changes in UV-Vis spectra during $AgClO_4$ reduction by $NaBH_4$. However, during the process they noted that the formation of hydrogen bubbles on the cuvette walls disturbs the kinetic study [48]. Some scientists try to exploit LSPR for synthesizing process development and optimization [68,168]. UV-Vis spectra are also suitable for NPs stability investigation [130]. However, experimental data along with mathematical calculations indicate that seemingly negligible changes (including those related to synthesis) in nanostructures may cause significant changes to the optical features of the Ag NPs [144]. Thus, it should be paid more attention to NPs LSPR investigation, as it may have an influence on results during exploitation in different optical applications such as biosensing and biolabeling, photocathalysis, different photoelectric devices, etc. The knowledge about potential applications associated with plasmonics may be extracted only from a complete understanding of LSPR appearance phenomena, which will contribute in the design of highly specific nanostructures with desired optical properties.

The fluorescence spectra of Ag NPs-containing systems usually are measured in line to determine the possibility for different substances quantification in biological or environmental applications. It was reported that extremely small Ag NPs, which sometimes also called Ag nanoclusters or Ag quantum dots (Ag QDs), exhibit fluorescence emission. Changes in the closest vicinity to Ag QDs surface can either enhance the effect, as it was investigated for Pb^{2+} ion interaction in water [134], or decrease in case of dopamine binding [135]. Additionally, the aggregation of the Ag QDs also lead to the fluorescence disappearance, which was utilized for anti-digoxigenin antibody immunoassay analysis [15]. A.V. Pansare with coauthors exploited Ag QDs synthesized with *N. cadamba* extract to determine the BSA fluorescence quenching [170]. However, it should be strongly considered the mechanism of fluorescence intensity changes during the process, especially for such complex mixtures as in the last example, since some flavonoids, which usually are abundant in the extracts, can exhibit fluorescence properties [171]. In general fluorescence measurements can be affected by Inner Filter Effects (IFE), which include IFE I - the absorbance of exiting energy by impurities and IFE II - the reabsorbance of the emitted light by quencher or other impurities. Finally, the presence of unknown fluorescence substances in the mixture can also interfere the analysis [29].

3.6. Infrared and Raman spectroscopy

At the early stage of infrared investigations, it was noticed that certain functional groups are associated with specific characteristic absorption, and after years of painstaking work of many scientists, it became a technique for the determination of characteristic groups in the sample [172]. The majority of publications that are focused on Ag NPs usually

exploit Fourier Transform Infrared Spectroscopy (FTIR) in MIR (Mid-Infrared extends from 4000 cm^{-1} to 400 cm^{-1}) range as a reliable technique for Ag NPs characterization. FTIR is frequently used for surface functional group investigations [84], surface functionalization control [136,137] or for investigation of the possible groups which take part in Ag NPs formation and/or stabilization by different extracts [45], proteins [16,90], polysaccharides [87], etc. On the flip side, the significant shifts in the characteristic absorption band due to perturbation emerging from neighboring groups or the spatial geometry of the molecule together with the fact that in general more than one functional group absorb in the same region [172], make possible to determinate the individual functional groups only in case when FTIR is coupled with other techniques, which can be NMR (Nuclear magnetic resonance) [173]. To give an example, while it is relatively easy for simple compounds as alpha-lipoic acid to discriminate which groups are involved in Ag NPs binding [137] it becomes more complicated when we try to investigate how metal interacts with proteins or polysaccharide-based nanocomposite [16,87], and almost impossible for extracts or propolis, which are multicomponent mixtures [66,69,72]. NIR-range (Near-Infrared extends from 12,500 cm^{-1} to 4000 cm^{-1}) spectra can serve as an extension of the technique since it can provide valuable information about different hydrogen-containing groups (the majority of the absorption bands in the NIR region are due to CH, NH, and OH) [172]. Furthermore, some Ag NPs exhibit LSPR in NIR absorption region, which also should not be skipped in the Ag NPs investigations [168,169].

In Raman spectroscopy, inelastic scattering of the electromagnetic waves in the infrared range is measured and information about vibrational and rotational modes of the molecules can be gathered. The virtue of the technique is that the groups, which may be weak or inactive under FTIR analysis can exhibit strong bands in Raman spectra, so it provides complementary information. Raman spectra were utilized to investigate the binding of the Ag NPs to 2,2′-piridine decorated peptoids, the presence of the band at 241 cm^{-1} clearly indicate the existence of Ag(0)-(pyridine)N interaction [128]. Pomastowski et al. have also observed the changes that occurred in the Raman spectra of lactoferrin after Ag-ions uptake [16]. Moreover, in the last decades metal nanoparticles are widely studied for SERS. S. Reymond-Laruinaz et al. have observed the enhancement of the signals in Ag- conjugates with lysozyme, BSA, cytochrome-C, and hemoglobin in comparison to intact proteins [89]. However, during spectra interpretation, it should be considered the heating effect of the sample, which may lead to sample decomposition or baseline increasing due to blackbody thermal emission. Additionally, the fluorescence of the sample or the impurities may lead to the appearance of additional bands. Finally, the matrix effect should be considered as it can absorb the scattered waves and decrease the signals [174].

3.7. Nuclear magnetic resonance spectroscopy

NMR is a powerful tool for identification and quantification of molecular species, as it can provide information about the molecular structure of the compounds and the resonance strength is directly proportional to the number of the particular nuclei. The NMR spectra can be recorded for atoms that have a non-zero spin number (have an intrinsic magnetic moment) but the most frequently NMR spectra for ^1H, ^{13}C, ^{15}N, and ^{31}P nuclei are recorded. ^1H NMR is widely utilized for surface functional group determination and quantification [175]. Regarding Ag NPs it was shown that ^1H NMR could be useful for determination how organic compounds are involved in the synthesis process. V. Shah with coauthors suggested the decrease of some signals in ^1H NMR spectra was due to tri-sodium citrate oxidation [140]. What more, ^1H NMR can be utilized for quantitative determination of ligands participation in NPs stabilization [176]. However, quantitative information about adsorbed ligands often requires the NPs core digestion, as they cause significant signal broadening, especially in case of the NPs with larger size [177]. In Pawłowski et al. work the changes in silver caprylate

spectra during Ag NPs synthesis by thermal decomposition can be observed [178]. The authors also noted the broadening of all signals in spectra of silver caprylate in comparison to caprylic acid spectra, which they attributed to presence of small amounts of Ag(0) atoms, exhibiting paramagnetic properties and therefore influence on nuclear spin relaxation. Such effect was utilized by L.E. Marbella and colleagues to investigate magnetic susceptibility of AuCo NPs by Evans' method [179]. C^{13} NMR spectra were also useful in the investigation of Ag-doped Pt NPs formation. The L. C Jones with coauthors noted that PVP-Pt NPs C^{13}-NMR spectrum is very similar to only-PVP spectrum, but after adding of AgNO$_3$ the new shifts at 20 ppm, 46 ppm, and 63 ppm appeared and spectrum became more similar to that one from Ag-PVP. The differences may indicate the differences in Pt and Ag interactions with PVP and also it provided an insight into possible intermediates that play role in directing the Pt$_x$Ag$_y$NP shape [180]. What is interesting, the analysis was performed with the utilization of cross polarization, which is extremely useful for solid-phase NMR, in particular Cross Polarization Magic Angle Spinning NMR (CP-MAS NMR). ^{31}P NMR spectra were also useful for investigation of Ag NPs formation through $[Ag_7(H)\{E_2P(OR)_2\}_6]$ (E = Se, S) conversation. The spectra indicated the creation of $[Ag_8(H)L_6]^+$ as an intermediate prior to the formation of Ag$_7$H clusters. Moreover, the presence of a hydride within the heptanuclear silver was determined by ^1H and ^{109}Ag NMR-analysis [138]. However, the $^{107/109}Ag$ nuclei suffer from low gyromagnetic ratio, which decreases the sensitivity and generally requires specialized measurement devices. Moreover, the T_1 value of Ag nuclei is on the order of hours, so the technique is a highly time-consuming [177]. The conventional NMR in general posses considerably low sensitivity, especially in comparison to other spectroscopic techniques, e.g. fluorescence measurements can be performed for single molecule [181]. Still, the signal-to-noise ratio can be enhanced by magnetic field enhancement. Additionally, Fourier-transform pulsed NMR allows to more than 100-fold increase in sensitivity by utilization of short radiofrequency pulses, which can cover a wide range of excitation frequencies at the same time. Some other approaches for NMR sensitivity enhancement can be found in J. H. Lee et al. work [181]. However, at the end of the last century, the HR-MAS NMR (High-Resolution Magic-Angle Spinning NMR) technique has been introduced and showed high sensitivity and selectivity in the investigation of complex mixtures [182]. Such an approach can be used for the identification and quantification of metabolites from biofluids affected with Ag NPs. For instance, M. J. Piao et al. have measured by HR-MAS NMR the changes in glutathione quantities in human liver cells treated with Ag NPs [139].

3.8. Electron spectroscopy

Photoelectron or photoemission spectroscopy is a technique, where the discrete energy levels (electron orbitals) are studied by measurements of ejected electrons energies from material illuminated with light of a certain length. Depending on the wavelength of utilized light the technique is divided into X-ray Photoelectron Spectroscopy (XPS) and Ultraviolet Photoelectron Spectroscopy (UPS). In XPS the most common Mg Kα and Al Kα X-ray sources with energies 1253.6 eV and 1486.6 eV are utilized, which allows to investigate the core states of the atoms [183]. Taurin interaction with Ag NPs has been studied by XPS as a common technique for chemical composition determination. The technique allowed to estimate not only the percentage composition of Ag, O, N, and S elements on the surface, but also the percentage of Ag–O, Ag–N, and Ag–S bonds [141]. The XPS has also been utilized for chemical composition estimation of Pt NPs doped with Ag. ICP-MS quantification of such composite showed the lower values of Ag in comparison to XPS, which suggested to be due to the limited photoelectron free pass (nearly 2 nm), so the differences may be attributed to Ag surface enrichment [180]. The composition of Ag-content formulations was possible to estimate by Ag 3d level shifts measurements, which also were shown to be sensitive to NPs size. T. Radu with colleagues has measured

the Ag 3d shift dependence from Ag NPs size embedded into bioglasses volume [184]. The authors showed that for bioglasses containing Ag NPs with the average size of 9 ± 0.2 nm the peak position of Ag 3d level on XPS spectra shifted to lower binding energies by 0.3 eV comparing to bioglasses containing Ag NPs with the average size of 7.4 ± 0.2 nm, which was assigned to the influence of Ag NPs dimensions. Still, the final peak position shift which may be observed on the spectrum is due to the competition of two phenomena: initial state effects (partial electron transmission to the clusters) that implies a tendency to shift the peak to lower binding energies and final state effect, which influences the relaxation energy of the system with a tendency to shift the peak to higher binding energies. These two phenomena imply not only the impact of the NPs size and shape but also the nature of the supporting substrate [185]. The extension of the technique – near-ambient pressure XPS, which allows to study NPs in suspension. However, the Ag 3d peak under near-ambient XPS showed the shift in 0,7 eV in comparison to Ag NPs studied in the dried sample on Si-wafer [186]. What more, S. Dahle with colleagues has investigated the interaction of Ag ions with glucose, and by XPS they observed the unexpected reduction of OH groups, which may be attributed to charging effect on insulators during the study [187].

UPS utilizes electromagnetic waves with energies in the range from 3.10 eV to 124 eV, which is suitable for valence and conductive bands investigation [183]. Such information is very valuable since Ag NPs-containing nanocomposites in the last decades are often investigated for photoelectric conversion in different optoelectronic devices [188]. UPS was used for the estimation of photoelectron emission yield for Ag NPs on a hydrogen-terminated Si surface [105]. Still, for all electron spectroscopy techniques, in general, the ultra-high vacuum is essential, which can be included to their drawbacks. The necessity of the ultra-high vacuum is related to the fact, that the electrons have limited free path and additional collisions are unacceptable. Moreover, the molecules presented in the gas phase as well as adsorbed on the surface can lead to the appearance of additional signals. Finally, the high-energy beams can heat the material causing additional changes in their structure [183].

Auger electron spectroscopy (AES) is based on an analysis of electron energies emitted from excited atoms through a series of internal relaxation events, which also called the Auger effect. Auger electrons are very specific regarding elements from which they were ejected, so the technique is common for surface scanning and imaging. J.C. Sharp et al. have studied the growth of Ag NPs on Fe_3O_4 (111), the results indicated that Ag formed 3D islands on the surface with a fixed particle density of 4×10^{12} particle/cm^2 and the average size was ≈ 4 nm [142]. A. E. Abbass et al. have used Auger spectroscopy to investigate Ag NPs embedded in bismuth silicate [143]. They noted that the study was burdened with sample charging effect, which was overcome by providing good sample contact to rough copper holder. Moreover, even though Auger spectroscopy have confirmed the formation of Ag NPs smaller than 5 nm, the information about its distribution through all the sample was not possible to extract, since AES makes possible to scan surface only on the depth of few nm.

Electron energy loss spectroscopy is a technique where the difference in energy of electrons in the incident beam with inelastically scattered electrons are compared. Depending on the level of energy loss the information about bandgap, plasmon modes, valence, and core energy levels can be obtained. EELS in general is integrated in an electron microscope and can be used for imaging as well as for estimation of spatially resolved information [189]. EELS was utilized for chemical composition estimation in Ag NP-lysozyme bioconjugates. The results clearly indicate the presence of Ag, C, N, O, and Ca at different measurment points. The presence of Ca at NPs edges provided additional confirmation of Ag NPs binding to lysozyme, since it was derived from chicken egg white with 90% purity and calcium is a major component of eggs [89]. A. Campos with coauthors has investigated plasmon modes of Ag NPs embedded in silica by STEM-EELS [144]. They noticed

that the electrons incident beam influenced both the NPs and surrounded silica structure, which in consequence influenced LSPR shifts. Initially, the NPs did not exhibit a clear plasmon resonance, as the synthesis conditions have led to Ag_2O formation. The NPs interface clearance from oxygen due to reduction caused the plasmon peak appearance on EELS spectrum and the matrix damage appeared as shifts to higher energies. Moreover, they conclude that small Ag NPs size does influence on LSPR shifts, but these are often masked by environmental influences.

3.9. XRD and SAED investigations

XRD is based on measurements of the angles and intensities of diffracted X-ray beams. Depending on the wavelength of incident X-ray, the wave amplitude can be enhanced due to constructive interference and detected during the analysis. Such enhancement is observed, when Bragg's law is fulfilled, which allows to estimate the relation between the wavelength of the incident electromagnetic radiation to the diffraction angle and the lattice spacing in crystalline sample [190]. The XRD analysis is a common technique by which the crystalline structure of both single Ag NPs [55] as well as incorporated in nanocomposite [87] can be detected. However, the intensity of signals obtained from Ag NPs embedded in organic films usually are at a very low level, so it barely could be noticed [17,87] and signals from Ag NPs deposited on the ZnO were not noticeable at all [191]. Generally, for mixed materials, the detection limit is shown to be approximately 2% [190]. Moreover, within the XRD technique by the Debye—Scherrer equation the NPs size can be estimated as it was made for Ag NPs doped in dialdehyde nanofibrillated cellulose, the calculated crystallite size was in the range from 14,03 to 16,63 nm, while SEM measurements indicated NPs size in the range 20.75 nm - 38.25 nm, which was suggested to the presence of aggregates consisting several crystallites [131]. The NPs size estimation by XRD is based on the fact, that the decrease in particle size leads to peak broadening in XRD patterns. However, for particles with sizes from 1 μm to 50 nm the peak broadening is almost negligible and mainly caused by instrumental effects. In turn, the significant peak broadening for NPs with sizes less than 10 nm lead to extremely low signal intensity and peaks overlap, which in consequence hardly can be distinguished. Such the situation burdened both the NPs size determination as well as crystal characterization [192]. What is interesting, the NPs shape can influence the intensities of the individual signals. The cubic or rod-like particles under the drying process or during precipitation tend to orient with flat faces parallel to the substrate, which called "the preferred orientation" of the sample. The phenomenon can provide additional valuable information but generally is undesirable, especially in quantitative XRD analysis [192].

Selective area electron diffraction (SAED) is another technique for materials crystalline structure investigation. The principle is similar to XRD, only instead of X-rays, the diffraction pattern of the electron beam is obtained. The virtue of the technique is that it can be performed during electron microscopy investigation and that the analysis can be made from a selected area of the sample, which allows obtaining information about the crystalline structure of different parts in composite materials, in particular for individual NPs. To give an example, the SAED analysis was made for Ag NPs derived from thermal decomposition of fatty acids silver salts. Such synthesis allowed to obtain self-assembled Ag NPs with a diameter near 4,5 nm (in the temperature range from 230 to 270 °C) and SAED analysis confirmed the long-range order structure [60]. G. Shen and D. Chen have synthesized the ZnO nanowires decorated with Ag NPs and performed the SAED analysis, in which selective character showed the possibility to investigate area corresponded to ZnO nanowire only. The results indicated that the obtained ZnO nanowires appeared as single crystals with the preferred growth directions alone the [0001] orientation [191]. However, in the XRD analysis by the characteristic angles, the inorganic crystal compounds can be identified, while SAED gives only information

about basic parameters of the materials crystal structure, which often is not enough to distinguish two different compounds. To give an example, B. Boutinguiza et al. have shown that measured by SAED interplanar distances of 0.233 and 0.141 can correspond both to Ag (theoretical 0.236 and 0.145) as well as to Ag_2O (theoretical 0.237 and 0.143) crystal structures, so the discrimination of these Ag forms is complicated.

3.10. Mass spectrometry

The widespread employment of Ag NPs in numerous applications requires very precise techniques for its investigation, as the influence of nanomaterials on different systems is huge, while caused by agents in insignificant amounts. Inductively Coupled Plasma Mass Spectrometry (ICP-MS) has shown to be a powerful tool for accurate trace analysis of Ag content in the samples and possesses excellent detection limit, high resolution power that can reach 10,000. Moreover, the ICP-MS can be utilized for multi-elemental investigations as well as for measuring elemental isotope ratios [193]. Regarding nanosized Ag or its composites the ICP-MS is frequently utilized for silver uptake quantification in different systems. In our group, we have investigated the Ag adsorption by whey proteins lactoferrin [16] and casein [83] during the nanocomposite synthesis. Moreover, C. Tiantian with coauthors has utilized ICP-MS for Ag content estimation in silver-silica nanocomposites [12]. ICP-MS is also suitable for different biological samples investigation. To give an example, C. G. Castro-Gonzales et al. have utilized ICP-MS to study the Ag uptake by *Stevia rebaudiana B.* under exposure of Ag NPs with different concentrations in the culture media [120]. Additionally, J. Tang with colleagues has measured the time-resolved silver distribution in the different parts of rat organism after treatment with Ag NPs and Ag microparticles injections [194]. The Ag NPs biological activity is frequently attributed to the possibility of Ag^+ production. Thus, the ICP-MS is commonly utilized for quantification of Ag^+ release from different silver-containing nanomaterials, as it was made by T. Liu al. [51]. They have investigated the Ag^+ release from Ag NPs enclosed in superhydrophobic polyelectrolyte films, as a possible agent of nanocomposite antibacterial properties. However, as every ICP-MS investigation, the Ag determination is suffered from numerous interferences. The interferences in the quantification of ^{107}Ag are the $^{91}ZrO^+$, $^{90}Zr^{16}OH^+$, and $^{89}Y^{18}O^+$, while to ^{109}Ag interferences the $^{93}Nb^{16}O^+$, $^{92}Zr^{16}OH^+$, and $^{92}Mo^{16}OH^+$ can be included [193].

Lately the single-particle ICP-MS (SP-ICP-MS) is frequently utilized for Ag NPs behavior investigations in different environmental and biological systems. SP-ICP-MS implies the utilization of very diluted NPs suspensions, so it allows to introduce single particle into ICP-MS during the analysis. Moreover, the measurements in SP-ICP-MS mode are performed with very short dwell time, so it allows to estimate both the concentration of the dissolved metal and incorporated in NPs in the sample at the same time [148]. Thus, the technique is frequently utilized for NPs size estimation and quantification. I.-L. Hsiao et al. has investigated the cellular uptake of TiO_2 and Ag NPs for Neuro-2a cells [146]. They utilized conventional ICP-MS, SP-ICP-MS, and laser ablation ICP-MS. The performed analysis showed that the Ag uptake was higher in case with cell treatment by bigger NPs but the higher particle number uptake for smaller NPs. However, the sample preparation for conventional ICP-MS could contribute to a higher quantity of estimated silver uptake, as some of quantified particles may be not due to cell absorption but adsorbed on the culture media plate. On the other hand, the NPs aggregation as well as limited size for detection (20 nm for Ag NPs [148]) can contribute to SP-ICP-MS analysis results. Moreover, A. Keri with colleagues has performed an SP-ICP-MS analysis of Au/Ag bimetallic NPs with different structures and was able to estimate NPs size and their elemental composition [195]. It was shown that in SP-ICP-MS mode the sequential determination of Au and Ag in the particles with calibration by different sized monometallic NPs and subsequent mathematical estimation was the most precise and accurate for both size and molar ratio investigation. The drawbacks of the utilized method are its time- and labor-consuming character. Moreover, as it can be deduced, the chemical composition, as well as the size, were measured not for each particular NP, but for all NPs population. Thus, the obtained data presents the average parameters of all quantified NPs and can be applied with high credibility only for spherical, monodisperse, and uniform in terms of chemical content particles. However, in S. Naasz the size and chemical composition of Au@Ag core-shell NPs were also determined [196]. The authors reported that due to restrictions within the SP-ICP-MS coupled with quadrupole analyzer it is not possible to perform multi-isotope analysis, thus the determination of Au and Ag content in the NPs was performed in two separate runs. Instead, the SP-ICP-MS coupled with the TOF analyzer was able to distinguish all isotopes simultaneously. Moreover, in the work the determination of the chemical composition of more complex multi-component $BiVO_4$ and $(Bi_{0.5}Na_{0.5})TiO_3$ particles was performed. It was shown, that in case of Au@Ag NPs the SP-ICP-MS coupled with TOF instrument could simultaneously detect Au and Ag in 97% of particles events, while the simultaneous determination of Bi and V for $BiVO_4$ as well as Bi and Ti for $(Bi_{0.5}Na_{0.5})TiO_3$ was possible to perform in >90% of all particle events.

Secondary ions mass spectrometry (SIMS) is a technique that implies the surface sputtering of the sample by focused primary ion beam and the analysis of ejected secondary ions. Such technique is suitable for surface 3D chemical mapping with detection sensitivity for even ppb scale. S. Wagener with colleagues has investigated the textiles functionalized by Ag NPs, and it was shown that TOF-SIMS (Time of flight-SIMS) was able to determine not only the chemical composition of Ag species on the fiber surface but also provided the information about its spatial distribution [197]. Additionally, TOF-SIMS allowed to estimate changes that occurred on Ag NPs surface after exposure to wastewater. The analysis indicated that Ag NPs after 72 h in wastewater in TOF-SIMS analysis produce different sulfur-content ions in both negative and positive mode, which may be attributed to the presence of Ag_2S and other silver sulfide species in the sample. Instead, the results from XPS analysis was more precise, and it was possible to distinguish the Ag–S–C organosulfur bonds, which appeared on the Ag NPs surface [147]. Still, SIMS is greatly limited by the diameter of the primary ion beam. The size of NPs, in general, is in order or even smaller than the diameter of primary ion beam, therefore it is rather difficult to investigate the thin structure of nano-objects [198].

Matrix-assisted laser desorption/ionization, that most often coupled with time of flight analyzer mass spectrometry (MALDI-TOF MS), is considered to be a soft ionization mass spectrometry technique as in general within it pseudo-molecular ions are produced. It was shown in S. Dhanya et al. work that small Ag nanocluster with up to 11 atoms could be ionized and analyzed by MALDI-TOF MS directly [199]. E. Oliveira with coauthors have also investigated the Ag nanoclusters, they were able to distinguish nanoclusters with 21 Ag atoms [200]. However, lately, more attention paid to the fact that Ag NPs unique optical properties make possible to use it as a matrix, which contributed to the new approach in MS – NALDI. To give an example, K.-M. Ng et al. has investigated different noble NPs as a possible promoter for benzylpyridinium ionization [8]. The investigation showed that Ag NPs have the biggest ion-desorption efficiency in comparison to Au, Pd, and Pt NPs. However, Ag NPs lead to slight analyte fragmentation and to metal cluster ion appearance (Ag^+ and Ag_2^+). M. Yang with coauthors has shown that signals can be enhanced even more in case of deposition of Ag NPs on zeolite [9]. They suggested that zeolite as a supporter can make the distribution of Ag NPs more homogeneous and prevent the NPs aggregation, which is one of the widest problems in NALDI approaches. Moreover, the active sites on zeolite may influence the electronic state of Ag NPs by reducing the excitation energy threshold. What interesting, in MALDI-TOF-MS analysis the enhanced signals may come from compounds directly bounded to NPs, as it was shown in our work, where we observed the greater signal for α-casein (Fig. 4), which we assumed to be due to it prevalence role in Ag NPs bounding [83]. Finally, it was shown that MALDI-TOF MS is suitable
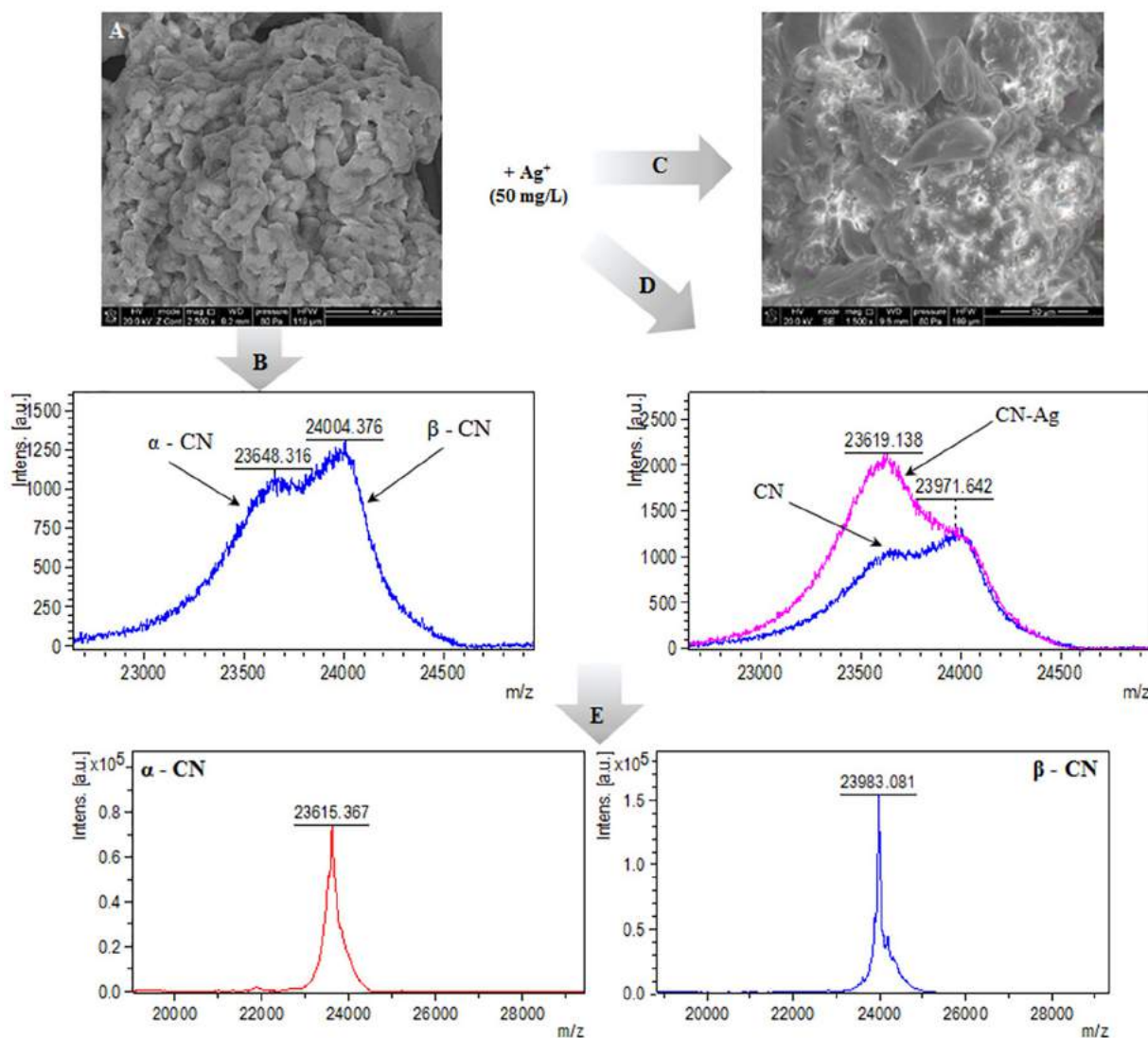
Fig. 4. SEM image of native casein (A); mass spectrum of intact casein (B); SEM image of casein-silver complexes (C); mass spectrum of casein-silver complexes (D) and mass spectrum of intact α- and β-casein standard solutions (E), respectively [83]. Copyright 2019 by the authors. Licensee MDPI, Basel, Switzerland.

for tracking how Ag NPs alone with modification by antibiotics influence the protein profiles of bacteria [201].

3.11. Separation techniques

The physicochemical and biological properties of the NPs are strictly dependent on their size. In the above sections of the article, numerous techniques for size determination were presented, but each of them suffers from limitations, especially in the case of polydisperse samples. Field flow fractionation is frequently mentioned as an effective and low-cost method for NPs sizing. The separation in the technique occurs due to different mobility of particles under the field applied perpendicularly to the parabolic main flow. The applied field may be of several different natures: made by cross-flow and asymmetric cross-flow, centrifugal, gravitational, or thermal field. Asymmetric flow field-flow fractionation (AF4) is one of the most popular variations of the technique and the most typical detectors are UV-Vis, DLS, and MALS (Multi angel light scattering) [148,165]. However, off-line and on-line ICP-MS can also be utilized. In AF4 only one wall of the flow channel makes up of semi-permeable membrane, so it makes possible to perform NPs focusing before fractionation. In consequence, the focusing step prevents peak

broadening and improves resolution [165]. S.T. Kim with colleagues in their work has shown the possibility for AF4 utilization in stability study of Ag NPs-protein conjugates, as they performed the investigation of the aggregation behavior in different conditions of Cytochrome C - conjugated Ag NPs [91]. K. Loeschner et al. reported the successful utilization of the technique for Ag NPs determination in chicken meat [202]. However, they noted that the extracted from meat Ag NPs have shown the earlier elution in comparison to the pristine Ag NPs suspended in water. As the TEM and SP-ICP MS have shown no changes in the NPs size, the difference was attributed to the presence of enzymes. Moreover, in W.-C. Lee et al. work it has been shown that carrier liquid, as well as capping agent, have an influence on the obtained results [148]. The analysis of 30 nm, 60 nm, and 100 nm Ag NPs capped with citrate and PVP has shown that for NPs capped with PVP suspended in deionized water the highest recovery can be obtained. Instead, the fractionation by AF4 could not be efficient for PVP-capped Ag NPs carried in surfactant FL-70 due to interactions between the functional groups of FL-70 and Ag NPs. T. K. Mudalige et al. has also reported the process dependence on the carrier mixture as well as a stabilizing agent of the NPs [203]. They noted that irreversible NPs binding to AF4 membrane at the focusing side leads to membrane fouling, which in consequence

19

decreases the NPs recovery. The problem was possible to overcome by membrane functionalization and NPs stabilization.

NPs in aqueous solutions occur with surface charge originated from functional groups of stabilizing agents or from adsorption on the NPs surface of ions present in the solution. The NPs surface charge makes it possible to use electrophoresis for its separation. Electrophoretic separation is based on differences in electrophoretic mobility of the particles, which in general depends on its charge and size [165]. In CE the separation process is performed in fused silica capillary, which inner surface can be modified on purpose to alter the electroosmotic flow and decrease the analyte adsorption onto capillary walls [204]. H. Qu et al. have performed the optimization for the separation process of both the Ag NPs an Ag^+ by CE [205]. They noted that alkaline conditions are more suitable for such purposes, as it prevents the Ag NPs dissolution and aggregation. Additionally, the necessity of chelating agent usage for Ag^+ capture as well as non-ionic surfactants was emphasized. Moreover, D. Mozhayeva with C. Engelhard has shown that CE can separate Ag NPs with the same size but different coatings [149]. Still, in the case of a five-component mixture, the migration time of 20 nm citrate capped Ag NPs was in the same time window as the migration of 40 nm and 60 nm PVP-capped particles. The investigation has shown that the Ag NPs migration times depend on the mixture, in which they are injected. Thus, the correct discrimination of different species is possible only in case of combination with other techniques, for example, SP-ICP-MS. Finally, B. Michalke and I. Vinkovic-Vrcek in their work have shown, that methods presented in literature not always can be applied for real samples, which was the liver extract [206]. They have tested six different approaches to find satisfactory conditions for Ag NPs and Ag^+ separation. The optimized method proposed by authors implies a strong alkaline condition, usage of tetramethyl-ammonium hydroxide and reverse polarity. The beneficial influence of tetramethyl-ammonium hydroxide was attributed to Ag NPs-sticking prevention.

Gel electrophoresis is another separation technique, which commonly is associated with biopolymers separation and study, i.e. proteins or nucleic acids. The principle is the same as for CE, but the process is performed in the gel. Lately, with progress in nanotechnology gel electrophoresis become popular for NPs and nanocomposites characterization. M. Hanauer with colleagues has shown that metal NPs with different shapes and sizes can be separated by gel electrophoresis [207]. They noted that different capping agent can influence the separation efficiency. Moreover, they performed a mathematical calculation to explain quantitatively the NPs behavior in the process, which also allows to estimate the packing density of polyethylene glycol absorbed on the NPs surface. Gel electrophoresis is also useful for observation of NPs interaction with different biomolecules. I. Moglia et al. have investigated Ag NPs formation in recombinant human L- and H-ferritine [107]. Gel electrophoresis allowed to confirm the formation of Ag NPs in L-ferritine by chemo- and photo-reduction, while chemo-reduction in the H-ferritine did not appear. What is more, the formation of protein dimers and higher monomers induced by Ag^+ was observed. I. Lubitz with A. Kotlyar has performed the preparative gel electrophoresis for G4-DNA-AgNPs (G-rich DNA-quadruplex structure) conjugates, which they subjected for TEM [92]. During the process, the G4-DNA-Ag NPs separation on three different bands was observed. In consequence nanocomposites from each band showed the different NPs content (from one to three pieces). Finally, gel electrophoresis was useful for the observation of changes that take place in cells treated with Ag NPs and their composites. For instance, S. Meenakshisundaram with colleagues has observed the expression levels of various anti-apoptotic, cell cycle regulators and apoptotic genes caused by Ag NPs synthesized with *A. muricata* leaf extract [208].

3.12. Thermal analysis

Thermal behavior is a crucial characteristic of Ag NPs, as their utilization in electronics and catalysis implies the elevated thermal conditions.

Moreover, the NPs are often incorporated in different materials in line to give antibacterial properties, so it may alter the thermal stability of such composites. Thus, thermal analysis is frequently utilized for Ag NPs and Ag-nanocomposites characterization, which can be performed in several different ways. S. I Sadovnikov et al. have carried out high-temperature in situ XRD analysis of nanosized Ag_2S, which is a promising substitute for germanium and silicon-containing semiconductors [145]. The results indicated that in the oxidizing medium the NPs were in form of α-Ag_2S up to 448 K and in the form of β-Ag_2S in the temperature range from 453 to 623 K. After the temperature has reached 673 K the formation of metal Ag has begun and in the temperature range from 723 to 773 K signals only from metal Ag were observed. The thermal annealing of as mentioned NPs has also been performed under conditions without oxygen and moisture at 393, 423, 453, 493, and 930 K. The analysis showed the appearance of monoclinic non-stochiometric acanthine α-$Ag_{1.95-1.98}S$ and the NPs size growth at a temperature above 453 K.

Another technique for thermal investigation is thermogravimetric analysis (TGA), where the mass loss of the sample over the temperature dependence is investigated. S. M K. Thiagamani with coauthors has utilized TGA for cellulose-based hybrid nanocomposites investigation [209]. It was shown, that nanocomposite comprised from cellulose matrix, banana peel powder as a filler and incorporated Ag NPs was more resistant to thermal decomposition in comparison to pure cellulose. This might be due to the higher thermal stability of the banana peel powder filler. S. Boughriba with colleagues has investigated the changes in thermal stability in *Rhinobatos cemiculus* gelatin films modified by TiO_2-doped Ag NPs [150]. The first three stages for all films were attributed to water (60–100 °C) and glycerol (250 °C) evaporation as well as small weight gelatin fraction decomposition. Gelatin films modified with 2, 3, and 4% of TiO_2-Ag NPs showed enhanced stability, so the degradation peak at 500 °C was not present in comparison to material with less amount of filler. Moreover, the differential scanning calorimetry (DSC) was performed for as-prepared samples. DSC is a thermoanalytical method, which allows to study phase changes. The technique is based on measurements of the temperature changes depending on the portion of applied heat. At transition point the heat is spent on the changes in the structure, the additional heat portion does not lead to temperature growth till all samples turn into other phase states [210]. *Rhinobatos cemiculus* gelatin glass transition temperature (Tg) was estimated as 150 °C, while gelatin film Tg value was about 59,5 °C. The TiO_2-AgNPs incorporation decreases the Tg value up to 52,6 °C for 4%-composite. The changes were attributed to a disordered state caused by NPs among the gelatin molecule's net-like structure.

4. Physicochemical properties

The first most important property of the Ag-content NPs is their chemical composition. Metallic Ag NPs are the central object of the majority of publications. However, other forms of nanosized Ag should also not be avoided, as they exhibit beneficial features, so they can be utilized in different applications. Ag_2S NPs have shown to be a promising biocompatible contrast agent for dual-energy mammography and computer tomography [14]. Ag_2O NPs are reported to be a good filler for pastes for the production of printed electrical devices [6]. Additionally, the Ag_2O NPs the same as Ag NPs showed the antibacterial properties against various Gram-positive and Gram-negative bacteria [211]. Moreover, the metallic Ag NPs can undergo changes through sulfidation, chlorination, oxidation, and aggregation, which drastically change their properties: decreasing in bioavailability and bioactivity, poor solubility, etc. S. Karimi et al. have shown that utilization of the marine algae extract of *Chaetomorpha sp* for Ag NPs synthesis led to Ag@AgCl NPs formation [71]. Additionally, M. Azodi with coauthors has shown the metallic AgNPs transformation in the complex mixtures, which the wastewater is, through surface oxidation to Ag_2O and subsequent S-content NPs formation [147]. D. Chen et al. have also reported the

Ag$_2$S surface formation in presence of S$_2$O$_3^{2-}$ ions [212]. They emphasized the crucial role of phenolic groups of the tannic acid, which served as Ag NPs stabilizing agent, in the S$_2$O$_3^{2-}$ reduction. All these indicate that the presence of different ions in the synthesis mixture or in the investigated systems should be considered, as the formation of different Ag-containing impurities may influence on the obtained results.

To the Ag-containing NPs variations can be include several different groups: pure Ag NPs, alloys, core-shell, and doped metallic NPs (AgAu [47,195], AgPd and AgPt [180], etc.), nanocomposites (Ag/TiO$_2$ [213], Ag@AgCl [71], SiO$_2$@Ag [122], etc). To the Ag NPs chemical features the capping agent and/or surface modifier can also be include, as it determines NPs physical, chemical, and biological behavior. The capping agent is directly responsible for the sign and magnitude of the NPs surface charge, which in turn influences hydrodynamic radii and aggregation stability [49]. Moreover, the metallic NPs LSPR plasmon maximum is strictly dependent on the stabilizer, as it changes the dielectric constant of the surrounding media near the NPs surface. Finally, C. D. Walkey et al. have investigated the influence of the surface modifiers on the NPs interaction with serum proteins [26]. It was shown that the capping agent has influenced the protein corona composition, which formed on the NPs surface. Thus, the stabilizer may influence the NPs mechanism interaction with cells and therefore can influence cell regulation routes [27].

Size is another important feature, which together with chemical composition determines the majority of NPs properties. The size-dependent characteristics of NPs are attributed to the so-called "quantum size effect". The properties of bulk material are determined by the average of all the quantum forces affecting all the atoms from which the material is made. By decreasing the size of the objects it can be reached the point, where the averaging no longer works. The distinctive behavior of the atoms or molecules in small clusters in comparison to that one from bulk material is called quantum size effect. Besides, the surface energy excess also contributes to specific properties of the nanoscale objects, as the specific surface is increased drastically with decreases in the particles size [214]. However, the size of the NPs can be determined by several methods and each of the methods will provide controversial data. It was shown, that size measured by DLS, in general, is overestimated. R. Ma with coauthors in their study has shown that the DLS measured NPs size can be even 20 times bigger, than that one obtained by TEM [28]. The hydrodynamic diameter for Ag NPs coated with gum arabic was measured as 99.1 ± 1.1 nm by DLS and 5.5 ± 1.7 nm by TEM. The effect is attributed to hydrated corona on the NPs surface, which behave rather as a hard shell than the liquid causing the light scattering [30]. Moreover, the NPs aggregation also could result in higher measured values of NPs size. Even though DLS estimated size is not the exact radii of the NP, it may contribute to the results obtained for desirable NPs characteristics. DLS is a spectroscopic technique operating in the visible part of the electromagnetic radiation. Thus, it may indicate the alters in the UV-Vis spectra, conventionally utilized for LSPR measurements. B.-J. Liu et al. have shown in their work, that depending on the NPs size and shape the scattered and absorbed light contribution in the overall extinction spectrum may differ significantly [163]. They also noted, that in fact the direct discrimination of the scattered and absorbed part of the light is cannot be performed with existing measurement tools, therefore only mathematical calculations may slightly shed light on the issue. In the abovementioned work of R. Ma et al. the XRD diameter evaluation was also performed [28]. The crystallite diameter for uncoated Ag NPs and coated with PVP, in general, have shown the calculated sizes twice lower than TEM investigations. The obtained data may be due to the presence of twinned particles, which cannot be distinguished by TEM.

Shape influence on the metallic NPs properties may be assigned to several factors. Firstly, the shape factor alters the specific surface area, and therefore the thermodynamic characteristics of the NPs. In the simplest approximation for two NPs of the same volume, the spherical NP will have 2.5 times lower surface in comparison to the rod-like NP

with a 16:1 aspect ratio [215]. The second effect may be explained by the limitations for electron movement inside the metallic NP surrounded by an insulator. The electron behavior in the metallic particles was explained by M. A. Garcia, where the rod-like shape influence on LSPR was illustrated [166]. The electromagnetic field of the incident light causes the electron movement to the NPs surface. Such electron accumulation on one side of the NP causes the negative charge, whereas other electron-deficient part stays positively charged. The created dipole forces electrons to return to the equilibrium position, causing the electron oscillation with a certain frequency, named the plasmonic frequency or resonant frequency. Larger electron displacement creates larger dipole and in consequence larger restoring force altering the resonant frequency. The electron movement along the rod axis in rod-like NPs creates greater charge accumulation on the surface, which in consequence shifts the resonant frequency to a higher wavelength. However, the shape-depended NPs properties caused by more complex phenomena. Besides the light adsorption, the NPs shape also alters the light scattering [5]. Moreover, the anisotropic NPs structure changes the energy distribution on the surface. In general, the atoms on apexes and edges possess more energy than atoms on faces, which for example causes the faster Ag NPs dissolution on the apexes [216]. Additionally, the adsorption, desorption processes as well as adsorbed molecules distribution changes on the NPs with different shapes [217]. The higher surface-to-volume ratio implies the higher adsorption, which in consequence changes the surface charge and therefore the behavior in the solution, making possible for example to separate NPs with different shapes by gel electrophoresis [207]. Moreover, R. Vankayala et al. have revealed that singlet oxygen formation by Au and Ag NPs greatly depended on the NPs shape [218]. The authors noted, that oxygen exists in molecular form only on the Ag(111) plane, and decompose on the atomic form on both Ag(100) and Ag(110). Finally, the NPs shape influences their interaction with cells [219]. S. Dasgupta et al. by calculations of the curvature energies of lipid bilayer membranes combined with a contact adhesion energy for the particle—membrane interaction have revealed the complexity of the endocytosis process for non-spherical/non-ellipsoid NPs [220]. The calculations showed that cellular uptake depends not only on global parameters like aspect ratio but also on local geometrical parameters, like extrema of the local mean curvature.

The combination of three abovementioned NPs characteristics determines other physicochemical and biological NPs properties. To the features that differ the Ag behavior in the form of NPs from that one in the bulk material, the optical, thermal, and catalytic properties can be included. The optical properties of Ag NPs are the most emphasized and discussed in the literature. As it was mentioned in the other sections of the review the LSPR is the major effect of the unique behavior of the metallic NP and commonly is related to the light absorption of specific wavelengths. The absorbed light depends on the size and shape of the NPs, and in consequence, determines the NPs color (Fig. 5). T. Huang with X.-H. N. Xu has synthesized Ag NPs with different colors [54]. The color of synthesized colloids was dependent from the shape of the NPs and was light yellow for spherical NPs with a diameter of 2.6 ± 0.8 nm ($\lambda_{max} = 393$ nm) and orange-red for the mixture of predominantly spherical NPs (91.2%) with a diameter of 9.5 ± 3.2 nm and rod-shaped NPs (7.9%) with size 13.5 ± 4.2 nm $\times$ 10.5 ± 3.9 nm ($\lambda_{max} = 461$ nm). The colloids with the purple, purple violet, violet and blue colors ($\lambda_{max} = 536$ nm, 552 nm, 572 nm, and 606 nm respectively) were the mixtures of a nearly equal amount of spherical NPs with sizes 16.7–20.3 nm and rod-shaped NPs with aspect ratios 23–27 nm $\times$ 15–19 nm (37–54% of each), and with small amount of triangle NPs (8.8–15.2%). However, the LSPR is also significantly modified by surrounding media, in particular, the refractive index has a big influence on the changes in resonant wavelength and therefore in the NPs color. J. J. Mock et al. have observed the NPs color changes subjected to dark-field microscope investigation [117]. In their work, the spherical 40–90 nm-sized Ag NPs immobilized on SiO$_2$ wafer appears in the blue color in the local dielectric interface of air, while in oil with refractive index 1,44 the color is shifted to green/yellow.
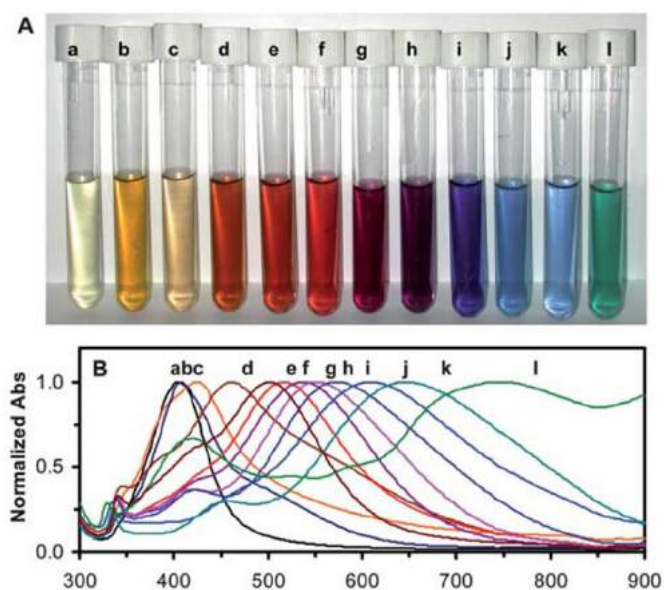
Fig. 5. Study of absorption and scattering plasmonic optical properties of colloidal Ag NPs using UV-Vis absorption spectroscopy: (A) photos of colloids with AgNPs of different shapes, (B) normalized absorbance of UV-Vis absorption spectra of AgNPs colloids shown on (A). Reproduced with permission from ref. [54]. Copyright 2010 Royal Society of Chemistry.

A. P. Kulkarni et al. have also investigated the influence of the refractive index on the LSPR band, they performed the Ag NPs transition from a water environment to polar organic solvents [221]. The transfer of Ag nanoprisms to methanol, 2-propanol, dimethylformamide, and dimethylsulfoxide have shown that the in-plane LSPR band slightly broadened and redshifted, the relevant shifts were higher in case of higher refractive indexes. Instead, the change of water media to acetone causes significant in-plane band broadening.

To LSPR induced effects the formation of so-called "hot electrons" (electrons with high kinetic energy) can be included [222]. The hot electrons formation can be utilized in solar energy harvesting. Moreover, hot electrons can directly interact with molecules adsorbed on the metal surface. Thus, Ag NPs exhibit enhanced catalytic properties in photochemical reactions. To give an example, P. Jiang et al. have observed the dehalogenation of 4-iodothiophenol, 4-bromothiophenol, and 4-chlorothiophenol by in-situ SERS detection [223]. It was shown, that dehalogenation reaction rate performed on 80 nm Ag NPs was much higher than that one for 40 nm or 80 nm Au NPs. Finally, as it was mentioned earlier, the optical properties of NPs also include fluorescence, which was reported for extremely small NPs with diameters below 10 nm. For example, L. Burratti et al. [134] have investigated the fluorescence features of NPs with 1.45 ± 0.26 nm size. C. Li et al. [15] also reported the fluorescence behavior of 3.9 ± 0.7 nm-sized NPs. However, Oliveira with colleagues [200] suggested that the fluorescence exhibit only extremely small Ag-clusters containing several silver atoms (up to 4). The fluorescence of larger nanoparticles is a consequence of as mentioned nanoclusters adsorption on the surface of the particles. Oliveira et al. in their work concluded that the investigation of such small objects is impossible due to low stability under the electron beam of HRTEM. Bigger Ag NPs also can exhibit photoluminescence properties, but the excitation mechanism greatly differs. To force the big NPs to emit light the two-photon excitation can be utilized. F. Han with coauthors has investigated the influence of the Ag NPs size on the two-photon excitation photoluminescence intensity [224]. Moreover, they have utilized the plasmon coupling, which was reported to be responsible for the enhancement of the phenomenon. The 14-fold enhancement of two-photon excitation photoluminescence was observed for coupled with poly(diallyldimethylammonium chloride) 50 nm Ag NPs, which is

the maximum enhancement among all studied Ag NPs. The obtained results may be due to increased extinction at the excitation wavelength, which was caused by the formation of a strong longitudinal band, resonant with the excitation band.

The discrete character of the NPs makes them a semiconductor even though silver as a bulk material has the highest electrical conductivity among all metals. The NPs behavior as a semiconductor emerges from the fact that the size of the NPs is in the same order as the exciton Borh radius, which is a distance between electron and hole of exciton. The electron-hole pair, called the exciton, is originated from the excited state of the semiconductor when the electron leaves the hole on the valence band by transferring to the conductive band [1]. The UV-Vis spectroscopy usually is exploited for optical band gap determination. The band gap study, in general, shows the properties of the whole Ag NPs-containing system rather than Ag NPs alone, as the metallic NPs are often utilized in order to improve the optoelectronic properties of the materials. W. L. Wang et al. has investigated the TiO_2 nanotubes decorated with AgNPs [225]. It was shown that the band gap of TiO_2 nanotubes were 3.18 eV and by changes in Ag content from 12.5% to 17.8% it was possible to adjust the cut-off for band gap from 420 nm (2.95 eV) to 430 nm (2.88 eV). Instead, S. I. Mogal with coauthors has noticed that the band gap for pure TiO_2 particles was 3.08 eV [213], which is between the measured values for anatase (3.2 eV) and rutile (3.0 eV) [226]. The modification with 0.75% Ag shows two ban gaps 2.99 eV and 2.35 eV. The further increase of Ag content caused the shifts in band gap absorption edges and the disappearance of the visible absorption band. These indicated the absence of a doping effect for composites with higher Ag-content. The XPS analysis of as-prepared nanocoposites shows that on the surface of low silver-content NPs predominant silver species were in the form of oxides and increase of the silver content led to Ag^0 nanoclusters formation. However, it was shown by N. T. Tsendzulghul et al. that AgO, depending on deposition condition, had the band gap in the range between 2.3 eV (539 nm) and 3.1 eV (388 nm) [227]. Moreover, as it was shown earlier the XPS analysis of insulators can cause the surface group reduction due to charging effect, which could contribute to results shown by S. I. Mogal et al. Still, K. H. Mahmoud et al. have also noticed the non-linear influence of Ag NPs on band gap of the gelatin [228]. The authors have calculated the optical band gap changes from 4.60 eV for pure gelatin to 3.85 eV for gelatin doped with 0.6% of Ag NPs and 4.2 eV for gelatin doped with 1.0% Ag.

The thermodynamic properties of the material can be divided into two constituents: bulk quantity and surface quantity [229]. The significant size reduction leads to considerable magnification of surface component influence on the material properties. The result of the relatively highly-energetic state of the Ag NPs is a lower melting temperature in comparison to the bulk material. C.-W. Chiu et al. have investigated the melting point of Ag NPs synthesized in the interlayer space of synthetic fluorinated mica clay [230]. The DSC analysis indicated that 8.1 nm Ag NPs has melting point ≈ 118 °C, while 11.7 nm particles ≈135 °C. R.-X. Dong et al. have also studied the thermal stability of 26 nm Ag NPs synthesized on bentonite clay, the reported melting point was 110 °C [223]. However, the investigation was performed in a different way, namely the Ag NPs after synthesis were subjected for 2 h drying at 110 °C, and then observed under FE-SEM. The coalescence of as-prepared NPs has been revealed. Such behavior can be explained by Hanszen's theory of the pre-melting process, which implies the appearance of a quasi-liquid film on the NPs surface before melting, which can occur even at temperatures lower than the melting point and cause the NPs coalescence [231]. Under the pre-melting process, the NPs core can stay solid, while DSC analysis shows the ending point of the phase transformation process for whole NPs volume.

5. Biological activity

Biological activity can be defined as direct action (positive or negative) on a living organism, i.e. bacterial, plant, or animal cells [232].

The Ag NPs biological activity frequently is associated with their antibacterial properties. Indeed, Ag NPs and their composites were reported as effective agents for a variety of Gram-positive and Gram-negative bacteria's growth inhibiting. The trypsin-conjugated Ag composite was able to inhibit the growth of *E. coli* and *S. aureus* [90]. Besides, B. Das et al. have demonstrated the effectiveness of Ag NPs synthesized with *Ocimum gratissimum* leaf extract in case of a multidrug-resistant form of the abovementioned microorganisms [123]. A. Rogowska et al. have reported the antimicrobial activity of Ag NPs synthesized with *Actinomietes* strain CGG11n against Gram-negative *K. pneumoniae*, *E. coli* and *P. aeruginosa* as well as Gram-positive *S. aureus* and *S. epidermidis* [136]. Finally, K. Rafińska with colleagues has shown the susceptibility of *B. subtilis* to as-mentioned CGG11n-synthesized Ag NPs [201]. Still, Ag$^+$ ions were more effective, as they completely inhibited the *B. subtilis* growth in the concentration of 12.5 μg/mL, while the Ag NPs in the concentration of 100 μg/mL inhibited the growth only by about 13% in comparison to the control.

In addition to antibacterial properties, Ag NPs and their nanocomposites were reported as antifungal, antiamoebic, antiviral, antiangiogenic agents. S. S. Dakshayani et al. have shown both the antibacterial activity against *E. coli* and *S. aureus* as well as antifungal against *A. niger* of Ag NPs synthesized with *Selaginella* plant extract [69]. The Ag NPs conjugated with Guanebenz have been shown to be toxic for *Acanthamoeba castellanii* and *Naegleria fowleri* [233]. S. Gaikwad et al. have synthesized the Ag NPs by different fungi (*Alternaria species*, *Fusarium oxysporum*, *Curvularia species*, *Chaetomium indicum*, *Phoma specie*) and the as-synthesized NPs were subjected to antiviral capability investigations [86]. The Ag NPs produced with *Alternaria species* and *Phoma species* revealed to be toxic at a concentration of 10 mg/mL, but the viral inhibition with lower Ag NPs concentrations was on a relatively low level (between 0% to 40%). Instead, the inhibitory activity against herpes simplex virus type 1 (HSV-1) and human parainfluenza virus type 3 (HPIV-3) of Ag NPs synthesized with *F. oxysporum* and *C. indicum* showed the highest scores. The reduction in virus infectivity can be reached up to 80% for Ag NPs produced by *F. oxysporum* against HSV- 1, and 90% for Ag NPs produced by *C. indicum* against HPIV-3. Ag NPs produced by *Curvularia species* shows the resembling activity as *F. oxysporum* and *C. indicum* for HSV-1 virus, however no effect with HPIV-3. Moreover, L. Lu with colleagues have revealed that compounds with Ag in various oxidation states, such as AgNO$_3$, [Ag^{II}(*meso*-tetraphenylporphyrin)], and [Ag^{III} (*meso*-triphenylcorrole)], had no significant anti-viral activity against hepatitis B virus (HBV) [234].

Ag NPs also exhibit toxic effects against a variety of cancer and normal cell cultures. Additionally, the Ag NPs anticancer activity can be attributed to their antiangiogenic properties. S. Gurunathan with colleagues has investigated the antiangiogenic properties of Ag NPs synthesized with *Bacillus licheniformis* [19]. The antiangiogenic properties for as-prepared NPs were attributed to decreased viability of endothelial cells (up to 50% in the concentration of 500 nM), their reduced migration and altered formation of tubular structures. The Ag NPs synthesized with *Bacillus* spp. were shown to affect the viability of breast cancer cells MCF-7 [94]. The cell toxicity was dose-depended and at the concentration of 30 μg/mL the cell viability was calculated as 80%, while at the concentration of 50 μg/mL cell viability was substantially decreased as 15%. Even though the growth inhibition was not very significant, the Ag NPs treated cells also exhibit decreased adhesion capacity, changes in cell shape and size. K. Jadhav et al. have also performed the in vitro investigation of anticancer activity for phytosynthesized 40–80 nm-sized Ag NPs against a number of cancer cell cultures, among others liver HepG2, lungs L-132, pancreas MIA-Pa-Ca-2, breast MDA-MB-231, oral KB cells, prostate PC-3, and cervical HeLa cancer cell lines [20]. The IC$_{50}$ value (half-maximal inhibitory concentration) was estimated as 6.31, 4.002, 5.228, 8.452, 14.37, 7.46, and 6.55 μg/mL for each abovementioned cancer cell cultures respectively. Moreover, the cytocompatibility assay with normal human fibroblast L929 cell lines indicated that the as-synthesized NPs have no significant toxicity in

therapeutic concentration (the viability was ≥95% in the presence of 78.62, 39.31, 19.65, 9.82, 4.91, and 2.45 μg/mL of NPs). Finally, the Ag NPs in the concentration of 78.67 ± 3.60 μg/mL displayed <3% hemolysis, which lies within the biocompatible range in accordance to ISO/TR 7406 [20]. However, Ag NPs can exhibit toxic properties against normal cell cultures. A. K. Suresh with coauthors has investigated the cytotoxic effect of Ag NPs against mouse macrophage and lung epithelial cell lines [101]. Four different types of Ag NPs were utilized, namely poly (diallyldimethylammonium)-Ag, biogenic-Ag, uncoated-Ag, and oleate-Ag with sizes in the range 4–9 nm. The IC$_{50}$ concentrations for RAW-264.7 cells were found to be 0.1, 0.125, 1.1, and 4.9 μg/mL for each of the abovementioned Ag NPs respectively and 0.45, 0.7, 1.6, and 6.3 μg/mL for C10 lung cells. The authors emphasized that the surface coatings alone had no toxic effect, but the direct correlation between the Ag NPs surface charge and toxic effect can be observed. Moreover, the authors revealed that as-mentioned oleate-coated Ag NPs nanoparticles were found to be nontoxic or noninhibitory to prokaryotic Gram-negative *E. coli, S. oneidensis*, and Gram-positive *B. subtilis*.

Ag NPs can cause various physiological effects on the cell level and therefore on an organism in general. The Ag NPs can activate mitochondria-mediated stress. For instance, J. S. Teodoro et al. have revealed that Ag NPs impaired the oxidative phosphorylation capacity and depressed transmembrane potential in isolated rat liver mitochondria [235]. Moreover, the authors have shown that mitochondria pre-incubated with Ag NPs exhibit increased susceptibility to calcium-induced permeability transition. P.V. AshaRani with colleagues has also investigated the cellular Ca^{2+} homeostasis and changes in mitochondria permeability of Ag NPs-treated human lung fibroblast [236]. However, the perturbation in Ca^{2+} cellular homeostasis influences not only the mitochondria normal functioning, but also injures the cytoskeleton. The cytoskeleton injury blocks the chromosome segregation and cytokinesis. Similarly, in the M. Piao et al. work the Ag NPs treatment influenced the mitochondrial transmembrane potential and caused the cytochrome C release [139]. The authors have shown, that transmembrane potential loss is a result of the down-regulation of Bcl-2 and up-regulation of Bax. A. Sachdev et al. have also shown that carbon dots-Ag@ZnO nanocomposite down-regulated the Bcl-2 gene, which could lead to the expression of pro-apoptotic genes [237]. R Zhang et al. have revealed that Ag NPs can induce the endoplasmic reticulum mediated stress by affecting the PERK/eIF2α signaling pathway, IRE1 phosphorylation, and ATF6 cleavage [238]. The Ag NPs were also shown to alter the ion interplay in the biological fluids, among other the formation and accumulation of Ag$_2$Se and Ag$_2$S insoluble salts [239]. Moreover, the high Ag$^+$ affinity to S and Se can affect the selenoprotein synthesis [240] or S-containing peptides, proteins and enzymes activity, such as glutathione or dehydratases [241,242]. Besides, glutathione is considered to be a major cell antioxidant that removes ROS from an organism and maintains cellular oxidation-reduction homeostasis. However, the Ag NPs mediated oxidative stress is connected not only with glutathione elimination. The cells subjected to NPs exposure had the decreased activity of antioxidant enzymes [243] and the changes in expression of genes connected to oxidative stress regulation [244]. N. Mei with colleagues has shown that 5 nm Ag NPs induced the expression of 59 from 84 genes related to oxidative stress in mouse lymphoma cells [245]. Moreover, they have revealed the mutagenic activity of Ag NPs. The authors presented the results of LOH (loss of heterozygosity) analysis in dose ranged of 3–6 μg/mL, the mutant formation in cells treated with 5 μg/mL Ag NPs was sevenfold higher than in control. Ag NPs can also influence cell proliferation and differentiation. The Ag NPs can enter cells in several different ways: autophagy (through membrane channels), clathrin-mediated or caveolar endocytosis, phagocytosis, pinocytosis. In P. Dubey et al. work the routes of NPs in-cell intercalation and distribution are presented in a more detailed way [25]. Additionally, a more exhaustive description of effects, that Ag NPs can cause to living cells is presented.

23

5.1. Mechanism of Ag NPs biological toxicity

The toxic mechanism of metallic NPs is the main issue of a large number of scientific publications. Even though the numerous effects can be observed in bacterial and eukaryotic cells treated with Ag NPs the exact molecular mechanism of their action still has no clear elucidation. Fig. 6. graphically presents the scope of the chapter. There is plenty of publications, which attributed the biological activity of the Ag NPs to their possibility to release Ag^+ by oxidation. Such a mechanism, where Ag NPs are considered only as an Ag^+ carrier, some researchers called "Trojan horse" mechanism. The Ag^+ was reported to have an affinity to phosphate, carboxyl, amino, and thiol groups. The O. Gordon et al. have investigated the impact on bactericidal properties of Ag^+ ions in the presence of DNA, phosphate, cysteine, and glutamine amino acids [241]. The authors concluded, that only the Ag^+ interaction with thiol groups is the reason for their bactericidal properties, as only the presence of thiol-containing amino acid abolished the antibacterial activity. Further, to confirm the theory, the Ag^+ influence on succinate dehydrogenase deactivation was shown, which was possible to avoid by adding cysteine-containing tripeptide glutathione. Moreover, in C. N. Banti et al. the lipoxygenase inhibition by Ag^+ complexes with anti-inflammatory agents (2-hydroxybenzoic acid, salicylic acid, and aspirin) has been shown [246]. However, the as-mentioned Ag^+ containing complexes were also able to interact with DNA. The hypochromism observed in the UV spectra for Ag-containing complexes with calf thymus DNA was attributed to the intercalated or electrostatic binding mode. Additionally, the Ag^+ complexes with anti-inflammatory agents caused the DNA fragmentation in leiomyosarcoma cancer cells.

The Ag^+ is also considered to be responsible for ROS formation. H. J. Park et al. has shown that Ag^+ induced the expression of superoxide-sensor protein production, which can indicate the superoxide radical formation [247]. The authors noticed that earlier studies had shown the controversial results, but the process is depended on Ag^+ concentration and dramatically decreases at a concentration higher than 0.5 mg/L, which could be the reason for negative results. Furthermore, the hydroxyl radical formation in *S. epidermidis* treated with Ag^+ was observed, which could be due to the silver interactions with enzyme iron-sulfur clusters [241]. The addition of the Fenton reaction-specific quencher, thiourea, which does not consist thiol groups, led to decreased hydroxyl radical occurrence. Even though, the ICP-MS measurements in *S. epidermidis* lysates indicated that silver itself is not able to liberate coordinated Fe ions, their role in ROS formation cannot be dismissed completely. F. F. Xu et al. have also investigated the influence of Ag^+ on $[4Fe-4S]^+$ clusters of dehydratases, in particular fumarase [242]. They noticed, that malate (fumarase substrate/product) can partially prevent the damage, as the malate by the active site occupation make it more difficult for Ag^+ reach it.

The Ag^+ has also reported to electrostatically interact with membrane phospholipids and proteins, which can cause the depolarization and destabilization of cellular membrane and leakage of H^+ [248]. The Ag^+ release from the Ag NPs is a generally accepted fact, as it was confirmed by multiple investigations [32,77,249,250]. The Ag^+ release through the oxidative dissolution of the Ag NPs is the main issue in the assessment of their toxicity and fate in biological systems and the environment. M. Azodi et al. has investigated the dissolution behavior of Ag NPs in municipal wastewater [147]. The process was dependent on the amount of dissolved oxygen and the initial concentration of the Ag NPs. For deionized water suturated with oxygen the highest dissolution rate was revealed, while the presence of the inorganic reduced sulfur in the form of HS^- in the wastewater may contribute to a lower dissolution by forming insoluble sulfides. Moreover, the utilization of higher concentration of Ag NPs (1000 ppb over 10 ppb) led to a smaller extent particles size reduction, but to a higher Ag^+ content in the solution. S. Kittler et al. have performed the dialysis study of citrate and PVP-stabilized Ag NPs, which confirmed the low-rate NPs dissolution even in the absence of specific oxidizing agents [249]. The authors suggested
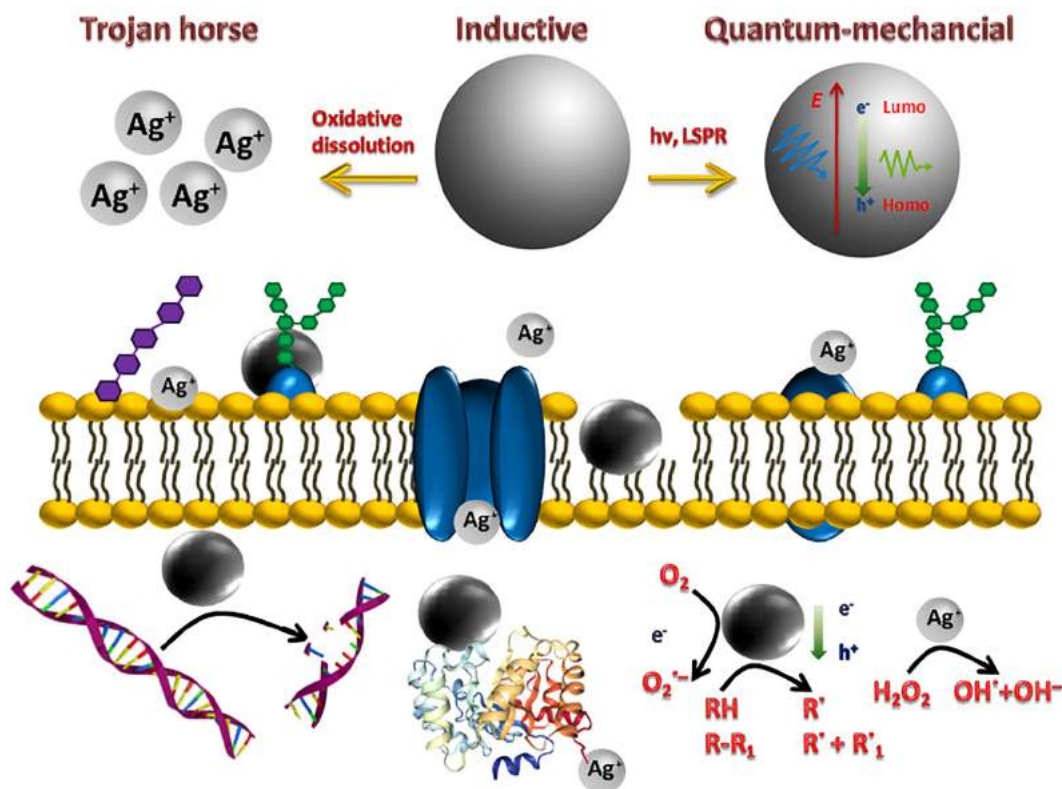

Fig. 6. The mechanisms of silver nanoparticles toxic action.

24

the process occurrence due to dissolved oxygen in the solution, but noticed that observed dissolution kinetic can be explained neither by the possible oxygen diffusion nor by residual solved oxygen, which may indicate the more complex process. In R. Ma et al. work the size-dependent dissolution of Ag NPs has shown [28]. It was revealed that the solubility of Ag NPs was increased in the case of smaller particles. However, the dependence was not linear in accordance with the surface area of the NPs, meaning that the ratio of released Ag^+ to the surface area was not constant for NPs of different sizes. Thus, it can be concluded that surface area alone could not explain the differences in dissolution rate, but the surface tension may provide reasonable information about Ag NPs solubility in the aqueous solubility. Additionally, the investigations also showed that the coating type and synthesis method has no significant impact on the Ag NPs dissolution kinetic. Finally, in C. Graf et al. the shape-dependent character of Ag NPs dissolution has been revealed [216]. The authors observed fast dissolution of the nanoprisms' tips, followed by a slowdown of the process when NPs become spherical, which was attributed to a higher energy on apexes and edges. In general, the oxidative dissolution is a dynamic process, which depends on environmental conditions. In B. Tang work it was shown that under light irradiation the Ag NPs can be partially dissolved, which in consequence led to changes in NPs shape from nanoprism to nanodisc [251]. The authors have revealed that after removing the light irradiation, the dissolved Ag^+ adsorbed again on the NPs surface, so the final size of the Ag nanodisc was larger than that one which can be inscribed in the initial nanoporism. Moreover, it was possible to turn nanodisc to nanoprisms again, with addition of extra citrate. However, the newly obtained nanoprisms were of larger size than the initial one.

Still, the Ag^+ release only cannot explain the higher biological activity of Ag NPs. A. Ivask et al. have shown that the Ag NPs toxicity increased with decreasing in size, and the correlation was observed for all investigated organisms: *E. coli*, *P. fluorescence*, *S. cerevisiae*, *P. subcapita*, *D. magna* and murine fibroblast line BALB/3 T3 [250]. What is interesting, the highest size-depended difference in toxicity was observed for *D. magna*, while the smallest for mammalian fibroblast. The size-depended toxicity was attributed to the Ag^+ release capability, which correlated for all tested NPs size, except the smallest one (10 nm). The authors suggested that 10 nm Ag NPs have additional not-dissolution driven toxicity. The C. Beer et al. work has also shown that suspension of Ag NPs with 16–20 nm size revealed higher toxicity against A549 human lung carcinoma cell, than its corresponding supernatant with Ag^+ fraction between 1 and 2.6% [32]. Still, the Ag NPs suspension with higher Ag^+ fraction (5.5–6.0%) did not differ in toxicity from their supernatant.

The Ag NPs itself can disorder the different cell organelles function due to adhesion to their surface. The NPs then can induce changes in structure or activate cellular destructive mechanisms, which leads to organelles' inappropriate functioning, therefore it can be called "Inductive" toxicity mechanism. Ag NPs adhesion can occur in several different ways, i.e. through electrostatic attraction or weak interaction forces, where the capping agent has a dominant role. X. Sun with colleagues has shown that Ag NPs can induce the VE-cadherin (endothelium specific cell-adherent protein) internalization in human umbilical vein endothelial cells, while the Ag^+ had no effect [33]. The direct evidence for Ag NPs adhesion on the cell surface was proved by BSE-SEM imaging and EDX spectra. Moreover, the experiment with direct and indirect (trough ultrathin 1–2 nm membranes) Ag NPs treatment was carried out. The results indicated, that in both cases the total cell VE-cadherin amount in lysates was not affected, but the direct exposure to Ag NPs influenced on a higher amount of internalized VE-cadherin. Additionally, M. E. Villanueva et al. have investigated the Ag NPs interaction with model biomembranes [80]. The oleic acid was used as a stabilizer with the aim to provide hydrophobic properties to Ag NPs. The changes in surface pressure-area isotherms of the membrane lipids indicated the Ag NPs incorporation into the films as a non-ideal mixture.

The changes in surface compression modulus value C_s^{-1} for Ag NPs/lipids mixtures as a function of the surface pressure provided the information about monolayer in-plane packaging elasticity. The decreased C_s^{-1} values for lipid monolayer in the presence of Ag NPs at low and high pressure were observed, which indicated the higher compressibility and therefore the more fluidic and expanded character. Thus, the Ag NPs induce greater disorder at the molecular level of lipid layers. Moreover, the Brewster Angle Microscopy was able to distinguish the coexistence of different phases in stratum corneum mimic membrane, which indicated the phase segregation induced by Ag NPs and can be as evidence of their destructive role on cell membranes.

The charge influence on the Ag NPs toxicity has been shown in T. Silva et al. work [31]. The toxicity of positively charged branched polyethyleneimine-coated, moderate negatively charged PVP-coated and negatively charged citrate-coated Ag NPs were inspected. The positively charged Ag NPs exhibited higher toxicity both to prokaryotic (*E. coli*) and eukaryotic (*D. magna*) cells, which is attributed, similar to Ag^+, to the possibility for more easy interaction with negatively charged cell membranes. However, A. Lesniak et al. have compared the polystyrene-NPs adhesion to human adenocarcinoma alveolar basal epithelial A549 cells, and they noted that protein corona formed on NPs surface influenced on their adhesive properties [34]. The cells exposure to NPs in complete cell culture medium supplemented with 10% fetal bovine serum indicated lover adhesion rate than that one cultured in serum-free medium. Additionally, S. Juling et al. have revealed that the metabolic response to the Ag NPs treatment in Caco-2 human intestinal epithelial cells is dependent on the protein corona formed on the NPs surface [27]. G. Lopez-Carballo et al. have also noticed the higher antibacterial capacity against *E. coli* and *S. aureus* of chitosan films, containing silver nanoparticles, in diluted MHB comparing to normal culture media [17]. The effect was attributed to the chelating capability of proteins, that decreased the availability of ions to exert antimicrobial activity. Hence, even though the primary stabilizer has an influence on the NPs toxicity, it can be changed significantly depending on the surrounding environment. The A. Lesniak et al. has also emphasized that in general the adhesion process as well as NPs uptake is difficult to disentangle as they occur simultaneously, so the time-resolving toxic mechanism investigation is the task for future investigations [34].

The third Ag NPs toxicity mechanism can be attributed to the consequence of plasmon modes and quantum states of the metallic NPs - the unique light propagation, enhanced reactivity of hot electrons, or the relaxation mechanisms of excited NPs. Thus, it can be denominated as a "Quantum-mechanical" mechanism. As a consequence of such a mechanism, the photodynamic therapy with metallic NPs can be performed. In classical photodynamic therapy, the molecule of the photosensitizer can receive the long-term excited triplet state by a non-radiative transition from the singlet state, which the molecule reached after photon absorption. The photosensitizer triplet state can be decay by energy transfer to surrounding molecules producing radicals, radical ions, or excited singlet oxygen ($^1O_2$) [252]. The LSPR-induced hot electron dynamics and thermalization is also described in the literature. The hot electrons in noble NPs can decay through two different actions, namely electron-electron and electron-phonon interactions [253]. The successful transfer of Ag NPs energy, provided by LSPR, through electron-electron interactions requires the direct substrate molecules deposition on NPs surface. R. Vankayala et al. have revealed that Ag NPs were able to promote the formation of $^1O_2$, but only in the lightened conditions, confirming the LSPR-depended nature of the process. Moreover, the sensitization process has shown to be strongly dependent from NPs morphology [218]. To give an example, O. Erdogan et al. have investigated the photo-induced enhanced toxicity of the Ag NPs synthesized via *Cynara scolymus* leaf extract [243]. The as-synthesized NPs alone had no influence on adenocarcinoma MCF7 cell viability in concentration 10 μg/mL, but in combination with photodynamic therapy, it inhibited the cell growth, viability, and migration by 50%. The ROS formation under the irradiation was confirmed by the decrease in the

superoxide dismutase, catalase and glutathione peroxidase activity. In contrast, the electron-phonon interactions lead to thermal diffusion (heat transfer) outside the NPs, which is the basis for photothermal therapy. K. Manivannan et al. have shown that core-shell Ag@SiO$_2$@Ag$_{seed}$ NPs can reach 43 °C under visible light irradiation, so it is enough to get the tumor cell cytotoxicity and tumor vascular tissue destruction, which occurs at 41.1 °C and 43 °C respectively [13]. However, for the Ag@SiO$_2$@Ag NPs, the visible light was able to induce heat only up to 40.5 °C. Moreover, the Ag@SiO$_2$@Ag$_{seed}$ NPs exhibited fluorescence properties, so it can be utilized as a bioimaging probe. The utilization of metallic NPs in the photodynamic and photothermal therapies has multiple virtues in comparison to conventional photosensitizers. The NPs are more stable under irradiation, metallic NPs have significantly higher extinction coefficient due to LSPR, which additionally can be tuned by changes in NPs form and size, so their adsorption band will be in a biological transparency window (650 to 1300 nm) [218,252]. An additional virtue of NPs is that they can be utilized as a carrier for different substances, which can enhance the photodynamic and photothermal action [254]. In the case of Ag NPs the increased Ag$^+$ production under irradiation is also considered. G. Fuertes with colleagues has shown that Ag NPs coated with silica received the antimicrobial properties against *E. coli* only in case of irradiation with light of LSPR band [255]. The irradiation with light of 387 nm wavelength caused the changes in NPs structure and characteristic "staining" of bacterial cells, so the NPs toxic properties were assigned to photo-induced Ag$^+$ release.

6. Conclusions and perspectives

Ag NPs have shown to be the objects with unique properties that allow to exploit them in multiple applications such as electronic devices and solar energy harvesting, advanced analytical techniques, medical diagnostics and treatment, catalysis and environmental applications. Ag NPs show different physical properties comparing to bulk silver, among other decreased melting point and enormous extinction in UV-Vis range due to LSPR. Additionally, they exhibit catalytic and photocatalytic properties, which were presented in the article. Moreover, the Ag NPs biological activity attracts high researchers' interest, among other antibacterial, antifungal, antiviral, antiameobic, antiangiogenic properties as well as cytotoxicity against cancer and normal cell lines, so this issue was also revealed in the article.

Herein we reviewed different aspects of the Ag NPs synthesis and their influence on the NPs features. It was shown that the basic NPs properties (size, shape, etc.) can be controlled by synthesis system selection, e.g. using different precursors, stabilizers, pH, and temperature changing as well as using different advanced synthesis devices. Moreover, the synthesis can be influenced by multiple physical agents such as electromagnetic irradiation or sonication. Further, the multiple techniques were shown, that can be utilized for the Ag NPs and their composites investigation. The basic principles and capability of the techniques were revealed. The drawbacks and artifacts of the technique, that may appear during measurements were shown. According to the provided information, it should be strongly considered the flaws in the experiments to avoid results misinterpretation and therefore the appearance of erroneous statements.

In the final part of the review, the Ag NPs physicochemical and biological properties were shown. It was revealed that Ag NPs size has a significant impact on their features, which is related to the so-called "quantum size effect". However, the NPs shape also influences their properties, as it leads to changes in surface-to-volume ratio, and therefore the NPs surface energy. Moreover, the presence of faces, edges, and apexes leads to NPs surface differentiation according to energy level or electrons distribution. Additionally, the influence of chemical composition, including the capping agent, was revealed. Finally, the several ways of Ag NPs toxicity mechanism were presented, which in general may have a collaborative effect. The Ag NPs toxicity mechanism is highly discussed in the literature, however, its exact elucidation is still unknown, and is the issue of future investigations.

Even though the study of Ag NPs has begun several decades ago there is still a lot of unclear aspects in their properties. The continuous development of more sophisticated techniques brings new knowledge about objects under investigation. The new facts about Ag NPs properties allow to utilize them in a more precise way and provide a possibility for a more wide range of their applications. In turn, new applications encourage to develop new routes for Ag NPs synthesis, which will satisfy the conditions of their utilization. Lately, the NPs utilization in the NALDI technique gained a lot of interest among researches. Still, the issue of Ag NPs utilization in solar energy harvesting, bioimaging, SERS, and different medical preparation is not exhausted and needs new considerations.

Declaration of Competing Interest

The authors declare that they have no known competing financial interests or personal relationships that could have appeared to influence the work reported in this paper.

Acknowledgements

References

[1] Rogers B, Adams J, Pennathur S. Nanotechnology: understanding small systems. . 3rd ed.Boca Raton: CRC Press; 2014.

[2] European Commission. Definition – nanomaterials – environment – European commission. European Commission; 2015. https://ec.europa.eu/environment/chemicals/nanotech/faq/definition_en.htm (accessed March 8, 2020).

[3] Xing L, Xiahou Y, Zhang P, Du W, Xia H. Size control synthesis of monodisperse, quasi-spherical silver nanoparticles to realize surface-enhanced Raman scattering uniformity and reproducibility. ACS Appl Mater Interfaces 2019;11:17637–46. https://doi.org/10.1021/acsami.9b02052.

[4] Massey AG, Thompson NR, Johndon BFG. The chemistry of copper, silver and gold. Elsevier, Oxford; 1973. https://doi.org/10.1016/C2013-0-02676-X.

[5] Yang S, Liu P, Zhang Y, Guo Q-N, Chen Y. Effects of silver nanoparticles size and shape on light scattering. Optik (Stuttg) 2016;127:5722–8. https://doi.org/10.1016/j.ijleo.2016.03.071.

[6] Chun S, Grudinin D, Lee D, Kim S-H, Yi G-R, Hwang I. Roll-to-roll printing of silver oxide pastes and low temperature conversion to silver patterns. Chem Mater 2009;21:343–50. https://doi.org/10.1021/cm802475m.

[7] Švecová M, Ulbrich P, Dendisová M, Matějka P. SERS study of riboflavin on green-synthesized silver nanoparticles prepared by reduction using different flavonoids: what is the role of flavonoid used? Spectrochim Acta Part A Mol Biomol Spectrosc 2018;195:236–45. https://doi.org/10.1016/j.saa.2018.01.083.

[8] Ng K-M, Chau S-L, Tang H-W, Wei X-G, Lau K-C, Ye F, et al. Ion-desorption efficiency and internal-energy transfer in surface-assisted laser desorption/ionization: more implication(s) for the thermal-driven and phase-transition-driven desorption process. J Phys Chem C 2015;119:23708–20. https://doi.org/10.1021/acs.jpcc.5b05957.

[9] Yang M, Hashimoto K, Fujino T. Silver nanoparticles loaded on ammonium exchanged zeolite as matrix for MALDI-TOF-MS analysis of short-chain n-alkanes. Chem Phys Lett 2018;706:525–32. https://doi.org/10.1016/j.cplett.2018.07.002.

[10] Yang P, Xu Y, Chen L, Wang X, Mao B, Xie Z, et al. Encapsulated silver nanoparticles can be directly converted to silver nanoshell in the gas phase. Nano Lett 2015;15:8397–401. https://doi.org/10.1021/acs.nanolett.5b04328.

[11] Kang W-J, Cheng C-Q, Li Z, Feng Y, Shen G-R, Du X-W. Ultrafine Ag nanoparticles as active catalyst for electrocatalytic hydrogen production. ChemCatChem 2019;11:5976–81. https://doi.org/10.1002/cctc.201901364.

[12] Cao T, Li Z, Xiong Y, Yang Y, Xu S, Bisson T, et al. Silica-silver nanocomposites as regenerable sorbents for Hg0 removal from flue gases. Environ Sci Technol 2017;51:11909–17. https://doi.org/10.1021/acs.est.7b01701.

[13] Manivannan K, Cheng C-C, Anbazhagan R, Tsai H-C, Chen J-K. Fabrication of silver seeds and nanoparticle on core-shell Ag@SiO2 nanohybrids for combined

photothermal therapy and bioimaging. J Colloid Interface Sci 2019;537:604–14. https://doi.org/10.1016/j.jcis.2018.11.051.

[14] Hsu JC, Cruz ED, Lau KC, Bouché M, Kim J, Maidment ADA, et al. Renally excretable and size-tunable silver sulfide nanoparticles for dual-energy mammography or computed tomography. Chem Mater 2019;31:7845–54. https://doi.org/10.1021/acs.chemmater.9b01750.

[15] Li C, Yang W, Yuan R, Xu W. Antibody-responsive signal-off fluorescence of DNA-harbored silver nanoclusters for direct, rapid and sensitive immunoassay. Sens Actuators B 2019;301:127148. https://doi.org/10.1016/j.snb.2019.127148.

[16] Pomastowski P, Sprynskyy M, Žuvela P, Rafińska K, Milanowski M, Liu JJ, et al. Silver-lactoferrin nanocomplexes as a potent antimicrobial agent. J Am Chem Soc 2016;138:7899–909. https://doi.org/10.1021/jacs.6b02699.

[17] López-Carballo G, Higueras L, Gavara R, Hernández-Muñoz P. Silver ions release from antibacterial chitosan films containing in situ generated silver nanoparticles. J Agric Food Chem 2013;61:260–7. https://doi.org/10.1021/jf304006y.

[18] Yang C-H, Wang L-S, Chen S-Y, Huang M-C, Li Y-H, Lin Y-C, et al. Microfluidic assisted synthesis of silver nanoparticle–chitosan composite microparticles for antibacterial applications. Int J Pharm 2016;510:493–500. https://doi.org/10.1016/j.ijpharm.2016.01.010.

[19] Gurunathan S, Lee K, Kalishwaralal K, Sheikpranbabu S, Vaidyanathan R, Eom SH. Antiangiogenic properties of silver nanoparticles. Biomaterials 2009;30:6341–50. https://doi.org/10.1016/j.biomaterials.2009.08.008.

[20] Jadhav K, Deore S, Dhamecha D, Rajeshwari HR, Jagwani S, Jalalpure S, et al. Phytosynthesis of silver nanoparticles: characterization, biocompatibility studies, and anticancer activity. ACS Biomater Sci Eng 2018;4:892–9. https://doi.org/10.1021/acsbiomaterials.7b00707.

[21] Rycenga M, Cobley CM, Zeng J, Li W, Moran CH, Zhang Q, et al. Controlling the synthesis and assembly of silver nanostructures for plasmonic applications. Chem Rev 2011;111:3669–712. https://doi.org/10.1021/cr100275d.

[22] Sultana S, Rafiuddin MZ, Khan M. Shahadat, development of ZnO and ZrO2 nanoparticles: their photocatalytic and bactericidal activity. J Environ Chem Eng 2015;3:886–91. https://doi.org/10.1016/j.jece.2015.02.024.

[23] Medici S, Peana M, Nurchi VM, Zoroddu MA. Medical uses of silver: history, myths, and scientific evidence. J Med Chem 2019;62:5923–43. https://doi.org/10.1021/acs.jmedchem.8b01439.

[24] Ahn E-Y, Jin H, Park Y. Assessing the antioxidant, cytotoxic, apoptotic and wound healing properties of silver nanoparticles green-synthesized by plant extracts. Mater Sci Eng C 2019;101:204–16. https://doi.org/10.1016/j.msec.2019.03.095.

[25] Dubey P, Matai I, Kumar SU, Sachdev A, Bhushan B, Gopinath P. Perturbation of cellular mechanistic system by silver nanoparticle toxicity: cytotoxic, genotoxic and epigenetic potentials. Adv Colloid Interface Sci 2015;221:4–21. https://doi.org/10.1016/j.cis.2015.02.007.

[26] Walkey CD, Olsen JB, Song F, Liu R, Guo H, Olsen DWH, et al. Protein corona fingerprinting predicts the cellular interaction of gold and silver nanoparticles. ACS Nano 2014;8:2439–55. https://doi.org/10.1021/nn406018q.

[27] Juling S, Niedzwiecka A, Böhmert L, Lichtenstein D, Selve S, Braeuning A, et al. Protein corona analysis of silver nanoparticles links to their cellular effects. J Proteome Res 2017;16:4020–34. https://doi.org/10.1021/acs.jproteome.7b00412.

[28] Ma R, Levard C, Marinakos SM, Cheng Y, Liu J, Michel FM, et al. Size-controlled dissolution of organic-coated silver nanoparticles. Environ Sci Technol 2012;46:752–9. https://doi.org/10.1021/es201686j.

[29] Lewandowska-Andralojc A, Marciniak B. Five major sins in fluorescence spectroscopy of light-harvesting hybrid materials. ACS Energy Lett 2019;4:1898–901. https://doi.org/10.1021/acsenergylett.9b01146.

[30] Bhattacharjee S. DLS and zeta potential – what they are and what they are not? J Control Release 2016;235:337–51. https://doi.org/10.1016/j.jconrel.2016.06.017.

[31] Silva T, Pokhrel LR, Dubey B, Tolaymat TM, Maier KJ, Liu X. Particle size, surface charge and concentration dependent ecotoxicity of three organo-coated silver nanoparticles: comparison between general linear model-predicted and observed toxicity. Sci Total Environ 2014;468–469:968–76. https://doi.org/10.1016/j.scitotenv.2013.09.006.

[32] Beer C, Foldbjerg R, Hayashi Y, Sutherland DS, Autrup H. Toxicity of silver nanoparticles—nanoparticle or silver ion? Toxicol Lett 2012;208:286–92. https://doi.org/10.1016/j.toxlet.2011.11.002.

[33] Sun X, Shi J, Zou X, Wang C, Yang Y, Zhang H. Silver nanoparticles interact with the cell membrane and increase endothelial permeability by promoting VE-cadherin internalization. J Hazard Mater 2016;317:570–8. https://doi.org/10.1016/j.jhazmat.2016.06.023.

[34] Lesniak A, Salvati A, Santos-Martinez MJ, Radomski MW, Dawson KA, Åberg C. Nanoparticle adhesion to the cell membrane and its effect on nanoparticle uptake efficiency. J Am Chem Soc 2013;135:1438–44. https://doi.org/10.1021/ja309812z.

[35] Oćwieja M, Adamczyk Z, Morga M, Kubiak K. Silver particle monolayers — formation, stability, applications. Adv Colloid Interface Sci 2015;222:530–63. https://doi.org/10.1016/j.cis.2014.07.001.

[36] Biswas A, Bayer IS, Biris AS, Wang T, Dervishi E, Faupel F. Advances in top–down and bottom–up surface nanofabrication: techniques, applications & future prospects. Adv Colloid Interface Sci 2012;170:2–27. https://doi.org/10.1016/j.cis.2011.11.001.

[37] Kennedy DC, Orts-Gil G, Lai C-H, Müller L, Haase A, Luch A, et al. Carbohydrate functionalization of silver nanoparticles modulates cytotoxicity and cellular uptake. J Nanobiotechnol 2014;12:59. https://doi.org/10.1186/s12951-014-0059-z.

[38] Schauermann S, Nilius N, Shaikhutdinov S, Freund H-J. Nanoparticles for heterogeneous catalysis: new mechanistic insights. Acc Chem Res 2013;46:1673–81. https://doi.org/10.1021/ar300225s.

[39] Kibis LS, Stadnichenko AI, Pajetnov EM, Koscheev SV, Zaykovskii VI, Boronin AI. The investigation of oxidized silver nanoparticles prepared by thermal evaporation and radio-frequency sputtering of metallic silver under oxygen. Appl Surf Sci 2010;257:404–13. https://doi.org/10.1016/j.apsusc.2010.07.002.

[40] Miranzadeh M, Kassaee MZ. Solvent effects on arc discharge fabrication of durable silver nanopowder and its application as a recyclable catalyst for elimination of toxic p-nitrophenol. Chem Eng J 2014;257:105–11. https://doi.org/10.1016/j.cej.2014.06.088.

[41] Kylián O, Kuzminova A, Štefaníková R, Hanuš J, Solař P, Kúš P, et al. Silver/plasma polymer strawberry-like nanoparticles produced by gas-phase synthesis. Mater Lett 2019;253:238–41. https://doi.org/10.1016/j.matlet.2019.06.069.

[42] Zhang X-F, Liu Z-G, Shen W, Gurunathan S. Silver nanoparticles: synthesis, characterization, properties, applications, and therapeutic approaches. Int J Mol Sci 2016;17:1534. https://doi.org/10.3390/ijms17091534.

[43] Tien D-C, Tseng K-H, Liao C-Y, Huang J-C, Tsung T-T. Discovery of ionic silver in silver nanoparticle suspension fabricated by arc discharge method. J Alloys Compd 2008;463:408–11. https://doi.org/10.1016/j.jallcom.2007.09.048.

[44] Khan I, Bahuguna A, Krishnan M, Shukla S, Lee H, Min SH, et al. The effect of biogenic manufactured silver nanoparticles on human endothelial cells and zebrafish model. Sci Total Environ 2019;679:365–77. https://doi.org/10.1016/j.scitotenv.2019.05.045.

[45] Eisa WH, Zayed MF, Anis B, Abbas LM, Ali SSM, Mostafa AM. Clean production of powdery silver nanoparticles using *Zingiber officinale*: the structural and catalytic properties. J Clean Prod 2019;241:118398. https://doi.org/10.1016/j.jclepro.2019.118398.

[46] Desai R, Mankad V, Gupta SK, Jha PK. Size distribution of silver nanoparticles: UV-visible spectroscopic assessment. Nanosci Nanotechnol Lett 2012;4:30–4. https://doi.org/10.1166/nnl.2012.1278.

[47] Blommaerts N, Vanrompay H, Nuti S, Lenaerts S, Bals S, Verbruggen SW. Unraveling structural information of Turkevich synthesized plasmonic gold–silver bimetallic nanoparticles. Small 2019;15:1902791. https://doi.org/10.1002/smll.201902791.

[48] Polte J, Tuaev X, Wuithschick M, Fischer A, Thuenemann AF, Rademann K, et al. Formation mechanism of colloidal silver nanoparticles: analogies and differences to the growth of gold nanoparticles. ACS Nano 2012;6:5791–802. https://doi.org/10.1021/nn301724z.

[49] Bélteky P, Rónavári A, Igaz N, Szerencsés B, Tóth IY, Pfeiffer I, et al. Silver nanoparticles: aggregation behavior in biorelevant conditions and its impact on biological activity. Int J Nanomedicine 2019;14:667–87. https://doi.org/10.2147/IJN.S185965.

[50] Hegde H, Santhosh C, Sinha RK. Seed mediated synthesis of highly stable CTAB capped triangular silver nanoplates for LSPR sensing. Mater Res Express 2019;6:105075. https://doi.org/10.1088/2053-1591/ab3d8c.

[51] Liu T, Yin B, He T, Guo N, Dong L, Yin Y. Complementary effects of nanosilver and superhydrophobic coatings on the prevention of marine bacterial adhesion. ACS Appl Mater Interfaces 2012;4:4683–90. https://doi.org/10.1021/am301049v.

[52] Chen Z, Balankura T, Fichthorn KA, Rioux RM. Revisiting the polyol synthesis of Silver nanostructures: role of chloride in nanocube formation. ACS Nano 2019;13:1849–60. https://doi.org/10.1021/acsnano.8b08019.

[53] da Silva RR, Yang M, Choi S-I, Chi M, Luo M, Zhang C, et al. Facile synthesis of sub-20 nm silver nanowires through a bromide-mediated polyol method. ACS Nano 2016;10:7892–900. https://doi.org/10.1021/acsnano.6b03806.

[54] Huang T, Xu X-HN. Synthesis and characterization of tunable rainbow colored colloidal silver nanoparticles using single-nanoparticle plasmonic microscopy and spectroscopy. J Mater Chem 2010;20:9867–76. https://doi.org/10.1039/c0jm01990a.

[55] Agnihotri S, Mukherji S, Mukherji S. Size-controlled silver nanoparticles synthesized over the range 5–100 nm using the same protocol and their antibacterial efficacy. RSC Adv 2014;3:3974–83. https://doi.org/10.1039/C3RA44507K.

[56] Ben Moshe A, Markovich G. Synthesis of single crystal hollow silver nanoparticles in a fast reaction-diffusion process. Chem Mater 2011;23:1239–45. https://doi.org/10.1021/cm102991z.

[57] Yoo J, So H, Yang M, Lee K. Applied surface science effect of chloride ion on synthesis of silver nanoparticle using retrieved silver chloride as a precursor from the electronic scrap. Appl Surf Sci 2019;475:781–4. https://doi.org/10.1016/j.apsusc.2019.01.032.

[58] Tian Y, Liu H, Chen Y, Zhou C, Jiang Y, Gu C, et al. Seedless one-spot synthesis of 3D and 2D Ag nanoflowers for multiple phase SERS-based molecule detection. Sens Actuators B 2019;301:127142. https://doi.org/10.1016/j.snb.2019.127142.

[59] Le Trong H, Kiryukhina K, Gougeon M, Baco-Carles V, Courtade F, Dareys S, et al. Paramagnetic behaviour of silver nanoparticles generated by decomposition of silver oxalate. Solid State Sci 2017;69:44–9. https://doi.org/10.1016/j.solidstatesciences.2017.05.009.

[60] Bokhonov BB, Sharafutdinov MR, Whitcomb DR, Burleva LP. In situ self-assembly of silver nanoparticles. J Phys Chem C 2014;118:11980–9. https://doi.org/10.1021/jp501508a.

[61] Cai Y, Luo X, Maclean M, Qin Y, Duxbury M, Ding F. A single-step fabrication approach for development of antimicrobial surfaces. J Mater Process Technol 2019;271:249–60. https://doi.org/10.1016/j.jmatprotec.2019.04.012.

[62] Ashkarran AA. A novel method for synthesis of colloidal silver nanoparticles by arc discharge in liquid. Curr Appl Phys 2010;10:1442–7. https://doi.org/10.1016/j.cap.2010.05.010.

[63] Yasin HM, Ahmed W, Ali A, Bhatti AS, Rehman NU. Micro-plasma assisted synthesis of multifunctional D-fructose coated silver nanoparticles. Mater Res Express 2019;6:1050a2. https://doi.org/10.1088/2053-1591/ab3fed.

[64] Si MZ, Kang YP, Liu RM. Surface-enhanced Raman scattering (SERS) spectra of three kinds of azo-dye molecules on silver nanoparticles prepared by electrolysis. Appl Surf Sci 2012;258:5533–7. https://doi.org/10.1016/j.apsusc.2011.12.118.

[65] Stamplecoskie KG, Scaiano JC. Light emitting diode irradiation can control the morphology and optical properties of silver nanoparticles. J Am Chem Soc 2010;132: 1825–7. https://doi.org/10.1021/ja910010b.

[66] Veisi H, Dadres N, Mohammadi P, Hemmati S. Green synthesis of silver nanoparticles based on oil-water interface method with essential oil of orange peel and its application as nanocatalyst for A3 coupling. Mater Sci Eng C 2019;105:110031. https://doi.org/10.1016/j.msec.2019.110031.

[67] Hernández-Morales L, Espinoza-Gómez H, Flores-López LZ, Sotelo-Barrera EL, Núñez-Rivera A, Cadena-Nava RD, et al. Study of the green synthesis of silver nanoparticles using a natural extract of dark or white *Salvia hispanica* L. seeds and their antibacterial application. Appl Surf Sci 2019;489:952–61. https://doi.org/10.1016/j.apsusc.2019.06.031.

[68] Sangar S, Sharma S, Vats VK, Mehta SK, Singh K. Biosynthesis of silver nanocrystals, their kinetic profile from nucleation to growth and optical sensing of mercuric ions. J Clean Prod 2019;228:294–302. https://doi.org/10.1016/j.jclepro.2019.04.238.

[69] Dakshayani SS, Marulasiddeshwara MB, Sharath SK, Golla R, Raghavendra Kumar P, Devaraja S, et al. Antimicrobial, anticoagulant and antiplatelet activities of green synthesized silver nanoparticles using Selaginella (Sanjeevini) plant extract. Int J Biol Macromol 2019;131:787–97. https://doi.org/10.1016/j.ijbiomac.2019.01.222.

[70] Anthony KJP, Murugan M, Jeyaraj M, Rathinam NK, Sangiliyandi G. Synthesis of silver nanoparticles using pine mushroom extract: a potential antimicrobial agent against *E. coli* and *B. subtilis*. J Ind Eng Chem 2014;20:2325–31. https://doi.org/10.1016/j.jiec.2013.10.008.

[71] Karimi S, Samimi T. Green and simple synthesis route of Ag@AgCl nanomaterial using green marine crude extract and its application for sensitive and selective determination of mercury. Spectrochim Acta Part A Mol Biomol Spectrosc 2019;222: 117216. https://doi.org/10.1016/j.saa.2019.117216.

[72] Barbosa VT, Souza JKC, Alvino V, Meneghetti MR, Florez-Rodriguez PP, Moreira RE, et al. Biogenic synthesis of silver nanoparticles using Brazilian propolis. Biotechnol Prog 2019;35:1–9. https://doi.org/10.1002/btpr.2888.

[73] Shankar S, Rhim JW. Amino acid mediated synthesis of silver nanoparticles and preparation of antimicrobial agar/silver nanoparticles composite films. Carbohydr Polym 2015;130:353–63. https://doi.org/10.1016/j.carbpol.2015.05.018.

[74] Thomas RK, Sukumaran S, Sudarsanakumar C. An insight into the comparative binding affinities of chlorogenic acid functionalized gold and silver nanoparticles with ctDNA along with its cytotoxicity analysis. J Mol Liq 2019;287:110911. https://doi.org/10.1016/j.molliq.2019.110911.

[75] Kosa SA, Zaheer Z. Betanin assisted synthesis of betanin@silver nanoparticles and their enhanced adsorption and biological activities. Food Chem 2019;298:125014. https://doi.org/10.1016/j.foodchem.2019.125014.

[76] Song Z, Wu Y, Wang H, Han H. Synergistic antibacterial effects of curcumin modified silver nanoparticles through ROS-mediated pathways. Mater Sci Eng C 2019; 99:255–63. https://doi.org/10.1016/j.msec.2018.12.053.

[77] Jiang Y, Huang J, Wu X, Ren Y, Li Z, Ren J. Controlled release of silver ions from AgNPs using a hydrogel based on konjac glucomannan and chitosan for infected wounds. Int J Biol Macromol 2020;149:148–57. https://doi.org/10.1016/j.ijbiomac.2020.01.221.

[78] Shahid-ul-Islam BS, Butola D, Verma. Facile synthesis of chitosan-silver nanoparticles onto linen for antibacterial activity and free-radical scavenging textiles. Int J Biol Macromol 2019;133:1134–41. https://doi.org/10.1016/j.ijbiomac.2019.04.186.

[79] Boutinguiza M, Comesaña R, Lusquiños F, Riveiro A, del Val J, Pou J. Production of silver nanoparticles by laser ablation in open air. Appl Surf Sci 2015;336:108–11. https://doi.org/10.1016/j.apsusc.2014.09.193.

[80] Villanueva ME, Lanterna AE, Vico RV. Hydrophobic silver nanoparticles interacting with phospholipids and stratum corneum mimic membranes in Langmuir monolayers. J Colloid Interface Sci 2019;543:247–55. https://doi.org/10.1016/j.jcis.2019.02.069.

[81] Hao N, Nie Y, Xu Z, Zhang JXJ. Ultrafast microfluidic synthesis of hierarchical triangular silver core-silica shell nanoplatelet toward enhanced cellular internalization. J Colloid Interface Sci 2019;542:370–8. https://doi.org/10.1016/j.jcis.2019.02.021.

[82] Jiménez E, Abderrafi K, Abargues R, Valdés JL, Martínez-Pastor JP. Laser-ablation-induced synthesis of SiO 2 -capped Noble metal nanoparticles in a single step. Langmuir 2010;26:7458–63. https://doi.org/10.1021/la904179x.

[83] Pryshchepa O, Sagandykova GN, Pomastowski P, Railean-Plugaru V, Król A, Rogowska A, et al. A new approach for spontaneous silver ions immobilization onto casein. Int J Mol Sci 2019;20:3864. https://doi.org/10.3390/ijms20163864.

[84] Railean-Plugaru V, Pomastowski P, Meller K, Złoch M, Rafinska K, Buszewski B. Lactococcus lactis as a safe and inexpensive source of bioactive silver composites. Appl Microbiol Biotechnol 2017;101:7141–53. https://doi.org/10.1007/s00253-017-8443-x.

[85] Hamouda RA, Hussein MH, Abo-elmagd RA, Bawazir SS. Synthesis and biological characterization of silver nanoparticles derived from the cyanobacterium *Oscillatoria limnetica*. Sci Rep 2019;9:1–17. https://doi.org/10.1038/s41598-019-49444-y.

[86] Swapnil G, Avinash I, Aniket G, Mahendra R, Annarita F, Novella I, et al. Antiviral activity of mycosynthesized silver nanoparticles against herpes simplex virus and human parainfluenza virus type 3. Int J Nanomedicine 2013;8:4303–14. https://doi.org/10.2147/IJN.S50070.

[87] Kodoth AK, Ghate VM, Lewis SA, Prakash B, Badalamoole V. Pectin-based silver nanocomposite film for transdermal delivery of Donepezil. Int J Biol Macromol 2019;134:269–79. https://doi.org/10.1016/j.ijbiomac.2019.04.191.

[88] Hun J, Jeong D, Kanmani P. Study on physical and mechanical properties of the biopolymer/silver based active nanocomposite films with antimicrobial activity. Carbohydr Polym 2019;224:115159. https://doi.org/10.1016/j.carbpol.2019.115159.

[89] Reymond-Laruinaz S, Saviot L, Potin V, del Carmen Marco de Lucas M. Protein–nanoparticle interaction in bioconjugated silver nanoparticles: a transmission electron microscopy and surface enhanced Raman spectroscopy study. Appl Surf Sci 2016;389:17–24. https://doi.org/10.1016/j.apsusc.2016.07.082.

[90] Qin D, Yang G, Wang Y, Zhou Y, Zhang L. Green synthesis of biocompatible trypsin-conjugated Ag nanocomposite with antibacterial activity. Appl Surf Sci 2019;469: 528–36. https://doi.org/10.1016/j.apsusc.2018.11.057.

[91] Kim ST, Lee YJ, Hwang YS, Lee S. Study on aggregation behavior of Cytochrome C-conjugated silver nanoparticles using asymmetrical flow field-flow fractionation. Talanta 2015;132:939–44. https://doi.org/10.1016/j.talanta.2014.05.060.

[92] Lubitz I, Kotlyar A. Self-assembled G4-DNA-silver nanoparticle structures. Bioconjug Chem 2011;22:482–7. https://doi.org/10.1021/bc1004872.

[93] Railean-Plugaru V, Pomastowski P, Wypij M, Szultka-Mlynska M, Rafinska K, Golinska P, et al. Study of silver nanoparticles synthesized by acidophilic strain of actinobacteria isolated from the of *Picea sitchensis* forest soil. J Appl Microbiol 2016;120:1250–63. https://doi.org/10.1111/jam.13093.

[94] Almalki MA, Khalifa AYZ. Silver nanoparticles synthesis from Bacillus sp KFU36 and its anticancer effect in breast cancer MCF-7 cells via induction of apoptotic mechanism. J Photochem Photobiol B Biol 2020;204:111786. https://doi.org/10.1016/j.jphotobiol.2020.111786.

[95] Bromley KM, Patil AJ, Perriman AW, Stubbs G, Mann S. Preparation of high quality nanowires by tobacco mosaic virus templating of gold nanoparticles. J Mater Chem 2008;18:4796–801. https://doi.org/10.1039/b809585j.

[96] Singh R, Shedbalkar UU, Wadhwani SA, Chopade BA. Bacteriagenic silver nanoparticles: synthesis, mechanism, and applications. Appl Microbiol Biotechnol 2015;99: 4579–93. https://doi.org/10.1007/s00253-015-6622-1.

[97] Mehta SM, Sequeira MP, Muthurajana H, D'Souza JS. Rapid synthesis of gold and silver nanoparticles using tryptone as a reducing and capping agent. Appl Nanosci 2018;8:759–69. https://doi.org/10.1007/s13204-018-0684-1.

[98] Durán N, Nakazato G, Seabra AB. Antimicrobial activity of biogenic silver nanoparticles, and silver chloride nanoparticles: an overview and comments. Appl Microbiol Biotechnol 2016;100:6555–70. https://doi.org/10.1007/s00253-016-7657-7.

[99] Thanh NTK, Maclean N, Mahiddine S. Mechanisms of nucleation and growth of nanoparticles in solution. Chem Rev 2014;114:7610–30. https://doi.org/10.1021/cr400544s.

[100] Dong M, Wang W, Wei W, Hu X, Qin M, Zhang Q, et al. Understanding the ensemble of growth behaviors of sub-10-nm silver nanorods using in situ liquid cell transmission electron microscopy. J Phys Chem C 2019;123:21257–64. https://doi.org/10.1021/acs.jpcc.9b05267.

[101] Suresh AK, Pelletier DA, Wang W, Morrell-Falvey JL, Gu B, Doktycz MJ. Cytotoxicity induced by engineered silver nanocrystallites is dependent on surface coatings and cell types. Langmuir 2012;28:2727–35. https://doi.org/10.1021/la2042058.

[102] Kang H, Buchman JT, Rodriguez RS, Ring HL, He J, Bantz KC, et al. Stabilization of silver and gold nanoparticles: preservation and improvement of plasmonic functionalities. Chem Rev 2019;119:664–99. https://doi.org/10.1021/acs.chemrev.8b00341.

[103] Zhang Q, Lee I, Joo JB, Zaera F, Yin Y. Core-shell nanostructured catalysts. Acc Chem Res 2013;46:1816–24. https://doi.org/10.1021/ar300230s.

[104] Jankiewicz BJ, Jamiola D, Choma J, Jaroniec M. Silica-metal core-shell nanostructures. Adv Colloid Interface Sci 2012;170:28–47. https://doi.org/10.1016/j.cis.2011.11.002.

[105] Nakamura T, Hirata N, Nagaoka S, Nakajima A. Two-photon photoemission spectroscopy for silver nanoparticles on a hydrogen-terminated Si(111) surface: metal nanoparticle-enhanced photoemission. Chem Phys Lett 2010;489:69–74. https://doi.org/10.1016/j.cplett.2010.02.010.

[106] Chook SW, Yau SX, Chia CH, Chin SX, Zakaria S. Carboxylated-nanocellulose as a template for the synthesis of silver nanoprism. Appl Surf Sci 2017;422:32–8. https://doi.org/10.1016/j.apsusc.2017.05.242.

[107] Moglia I, Santiago M, Soler M, Olivera-Nappa A. Silver nanoparticle synthesis in human ferritin by photochemical reduction. J Inorg Biochem 2020;206:111016. https://doi.org/10.1016/j.jinorgbio.2020.111016.

[108] Giessen TW, Silver PA. Converting a natural protein compartment into a nanofactory for the size-constrained synthesis of antimicrobial silver nanoparticles. ACS Synth Biol 2016;5:1497–504. https://doi.org/10.1021/acssynbio.6b00117.

[109] Toster J, Swaminathan Iyer K, Burtovyy R, Burgess SSO, Luzinov IA, Raston CL. Regiospecific assembly of gold nanoparticles around the pores of diatoms: toward three-dimensional nanoarrays. J Am Chem Soc 2009;131:8356–7. https://doi.org/10.1021/ja901806y.

[110] De La Escosura A, Nolte RJM, Cornelissen JJLM. Viruses and protein cages as nanocontainers and nanoreactors. J Mater Chem 2009;19:2274–8. https://doi.org/10.1039/b815274h.

[111] Bulavchenko AI, Arymbaeva AT, Demidova MG, Popovetskiy PS, Plyusnin PE, Bulavchenko OA. Synthesis and concentration of organosols of silver nanoparticles stabilized by AOT: emulsion versus microemulsion. Langmuir 2018;34:2815–22. https://doi.org/10.1021/acs.langmuir.7b04071.

[112] Wu J, Tan LH, Hwang K, Xing H, Wu P, Li W, et al. DNA sequence-dependent morphological evolution of silver nanoparticles and their optical and hybridization properties. J Am Chem Soc 2014;136:15195–202. https://doi.org/10.1021/ja506150s.

[113] Chakraborty I, Feliu N, Roy S, Dawson K, Parak WJ. Protein-mediated shape control of silver nanoparticles. Bioconjug Chem 2018;29:1261–5. https://doi.org/10.1021/acs.bioconjchem.8b00034.

[114] Tsai CM, Hsu MS, Chen JC, Huang CL. Mechanistic study of shape evolution of silver nanoprisms in the presence of KSCN. J Phys Chem C 2012;116:461–7. https://doi.org/10.1021/jp209840n.

[115] Tang B, Xu S, An J, Zhao B, Xu W. Photoinduced shape conversion and reconstruction of silver nanoprisms. J Phys Chem C 2009;113:7025–30. https://doi.org/10.1021/jp810711a.

[116] Wonner K, Evers MV, Tschulik K. The electrochemical dissolution of single silver nanoparticles enlightened by hyperspectral dark-field microscopy. Electrochim Acta 2019;301:458–64. https://doi.org/10.1016/j.electacta.2019.01.129.

[117] Mock JJ, Smith DR, Schultz S. Local refractive index dependence of plasmon resonance spectra from individual nanoparticles. Nano Lett 2003;3:485–91. https://doi.org/10.1021/nl0340475.

[118] Sekine R, Moore KL, Matzke M, Vallotton P, Jiang H, Hughes GM, et al. Complementary imaging of silver nanoparticle interactions with green algae: dark-field microscopy, electron microscopy, and nanoscale secondary ion mass spectrometry. ACS Nano 2017;11:10894–902. https://doi.org/10.1021/acsnano.7b04556.

[119] Assis M, Robeldo T, Foggi CC, Kubo AM, Mínguez-Vega G, Condoncillo E, et al. Ag nanoparticles/α-Ag2WO4 composite formed by electron beam and femtosecond irradiation as potent antifungal and antitumor agents. Sci Rep 2019;9:9927. https://doi.org/10.1038/s41598-019-46159-y.

[120] Castro-González CG, Sánchez-Segura L, Gómez-Merino FC, Bello-Bello JJ. Exposure of stevia (*Stevia rebaudiana* B.) to silver nanoparticles in vitro: transport and accumulation. Sci Rep 2019;9:10372. https://doi.org/10.1038/s41598-019-46828-y.

[121] Choma J, Jamioła D, Ludwinowicz J, Jaroniec M. Deposition of silver nanoparticles on silica spheres and rods. Colloids Surf A Physicochem Eng Asp 2012;411:74–9. https://doi.org/10.1016/j.colsurfa.2012.07.004.

[122] Liu KG, Abbasi AR, Azadbakht A, Hu ML, Morsali A. Deposition of silver nanoparticles on polyester fiber under ultrasound irradiations. Ultrason Sonochem 2017;34:13–8. https://doi.org/10.1016/j.ultsonch.2016.04.006.

[123] Das B, Dash SK, Mandal D, Ghosh T, Chattopadhyay S, Tripathy S, et al. Green synthesized silver nanoparticles destroy multidrug resistant bacteria via reactive oxygen species mediated membrane damage. Arab J Chem 2017;10:862–76. https://doi.org/10.1016/j.arabjc.2015.08.008.

[124] Kim SW, Nam SH, An YJ. Interaction of silver nanoparticles with biological surfaces of *Caenorhabditis elegans*. Ecotoxicol Environ Saf 2012;77:64–70. https://doi.org/10.1016/j.ecoenv.2011.10.023.

[125] Guehrs E, Schneider M, Günther CM, Hessing P, Heitz K, Wittke D, et al. Quantification of silver nanoparticle uptake and distribution within individual human macrophages by FIB/SEM slice and view. J Nanobiotechnol 2017;15:1–11. https://doi.org/10.1186/s12951-017-0255-8.

[126] Adhikari L, Larm NE, Baker GA. Argentous deep eutectic solvent approach for scaling up the production of colloidal silver nanocrystals. ACS Sustain Chem Eng 2019;7:11036–43. https://doi.org/10.1021/acssuschemeng.9b01777.

[127] Robinson DA, White HS. Electrochemical synthesis of individual Core@Shell and hollow Ag/Ag2S nanoparticles. Nano Lett 2019;19:5612–9. https://doi.org/10.1021/acs.nanolett.9b02144.

[128] Tigger-Zaborov H, Maayan G. Aggregation of Ag(0) nanoparticles to unexpected stable chain-like assemblies mediated by 2,2′-bipyridine decorated peptoids. J Colloid Interface Sci 2019;533:598–603. https://doi.org/10.1016/j.jcis.2018.08.094.

[129] Ahmad F, Ashraf N, Bin Zhou R, Chen JJ, Liu YL, Zeng X, et al. Optimization for silver remediation from aqueous solution by novel bacterial isolates using response surface methodology: recovery and characterization of biogenic AgNPs. J Hazard Mater 2019;380:120906. https://doi.org/10.1016/j.jhazmat.2019.120906.

[130] Römer I, Wang ZW, Merrifield RC, Palmer RE, Lead J. High resolution STEM-EELS study of silver nanoparticles exposed to light and humic substances. Environ Sci Technol 2016;50:2183–90. https://doi.org/10.1021/acs.est.5b04088.

[131] Li J, Kang L, Wang B, Chen K, Tian X, Ge Z, et al. Controlled release and long-term antibacterial activity of dialdehyde nanofibrillated cellulose/silver nanoparticle composites. ACS Sustain Chem Eng 2019;7:1146–58. https://doi.org/10.1021/acssuschemeng.8b04799.

[132] Beleites M, Matyssek C, Blaschek HH, Seifert G. Near-field optical microscopy of femtosecond-laser-reshaped silver nanoparticles in dielectric matrix. Nanoscale Res Lett 2012;7:2–5. https://doi.org/10.1186/1556-276X-7-315.

[133] Sethi A, Rafiee M, Chandra S, Ahmed H, McCormack S. Unified methodology for fabrication and quantification of gold nanorods, gold core silver shell nanocuboids, and their polymer nanocomposites. Langmuir 2019;35:13011–9. https://doi.org/10.1021/acs.langmuir.9b01481.

[134] Burratti L, Ciotta E, Bolli E, Kaciulis S, Casalboni M, De Matteis F, et al. Fluorescence enhancement induced by the interaction of silver nanoclusters with lead ions in water. Colloids Surf A Physicochem Eng Asp 2019;579:123634. https://doi.org/10.1016/j.colsurfa.2019.123634.

[135] Sivakumar P, Priyatharshni S, Kumar K. Fluorescent silver nanoparticles for sensitive and selective detection of dopamine. Mater Chem Phys 2020;240:122167. https://doi.org/10.1016/j.matchemphys.2019.122167.

[136] Rogowska A, Rafińska K, Pomastowski P, Walczak J, Railean-Plugaru V, Buszewska-Forajta M, et al. Silver nanoparticles functionalized with ampicillin. Electrophoresis 2017;38:2757–64. https://doi.org/10.1002/elps.201700093.

[137] Teeparuksapun K, Prasongchan N, Thawonsuwan A. Alpha-lipoic acid functionalized Silver nanoparticles for colorimetric detection of copper ion. Anal Sci 2019;35:371–7. https://doi.org/10.2116/analsci.18P442.

[138] Liu CW, Lin Y-R, Fang C-S, Latouche C, Kahlal S, Saillard J-Y. [Ag 7 (H){E 2 P(OR) 2 } 6] (E = Se, S): precursors for the fabrication of silver nanoparticles. Inorg Chem 2013;52:2070–7. https://doi.org/10.1021/ic302482p.

[139] Piao MJ, Kang KA, Lee IK, Kim HS, Kim S, Choi JY, et al. Silver nanoparticles induce oxidative cell damage in human liver cells through inhibition of reduced glutathione and induction of mitochondria-involved apoptosis. Toxicol Lett 2011;201:92–100. https://doi.org/10.1016/j.toxlet.2010.12.010.

[140] Shah V, Bharatiya B, Mishra MK, Ray D, Shah DO. Molecular insights into sodium dodecyl sulphate mediated control of size for silver nanoparticles. J Mol Liq 2019;273:222–30. https://doi.org/10.1016/j.molliq.2018.10.042.

[141] Maiti N, Thomas S, Debnath A, Kapoor S. Raman and XPS study on the interaction of taurine with silver nanoparticles. RSC Adv 2016;6:56406–11. https://doi.org/10.1039/c6ra09569k.

[142] Sharp JC, Yao YX, Campbell CT. Silver nanoparticles on Fe 3 O 4 (111): energetics by Ag adsorption calorimetry and structure by surface spectroscopies. J Phys Chem C 2013;117:24932–6. https://doi.org/10.1021/jp408956x.

[143] Abbass AE, Swart HC, Coetsee E, Kroon RE. Enhanced terbium emission due to plasmonic silver nanoparticles in bismuth silicate. J Am Ceram Soc 2016;99:876–80. https://doi.org/10.1111/jace.14011.

[144] Campos A, Troc N, Cottancin E, Pellarin M, Weissker HC, Lermé J, et al. Plasmonic quantum size effects in silver nanoparticles are dominated by interfaces and local environments. Nat Phys 2019;15:275–80. https://doi.org/10.1038/s41567-018-0345-z.

[145] Sadovnikov SI, Vovkotrub EG. Thermal stability of nanoparticle size and phase composition of nanostructured Ag2S silver sulfide. J Alloys Compd 2018;766:140–8. https://doi.org/10.1016/j.jallcom.2018.06.351.

[146] Hsiao IL, Bierkandt FS, Reichardt P, Luch A, Huang YJ, Jakubowski N, et al. Quantification and visualization of cellular uptake of TiO2 and Ag nanoparticles: comparison of different ICP-MS techniques. J Nanobiotechnol 2016;14:1–13. https://doi.org/10.1186/s12951-016-0203-z.

[147] Azodi M, Sultan Y, Ghoshal S. Dissolution behavior of silver nanoparticles and formation of secondary silver nanoparticles in municipal wastewater by single-particle ICP-MS. Environ Sci Technol 2016;50:13318–27. https://doi.org/10.1021/acs.est.6b03957.

[148] Lee WC, Lee BT, Lee S, Hwang YS, Jo E, Eom IC, et al. Optimisation, evaluation and application of asymmetrical flow field-flow fractionation with single particle inductively coupled plasma mass spectrometry (SP-ICP-MS) to characterise silver nanoparticles in environmental media. Microchem J 2016;129:219–30. https://doi.org/10.1016/j.microc.2016.06.030.

[149] Mozhayeva D, Engelhard C. Separation of Silver nanoparticles with different coatings by capillary electrophoresis coupled to ICP-MS in single particle mode. Anal Chem 2017;89:9767–74. https://doi.org/10.1021/acs.analchem.7b01626.

[150] Boughriba S, Souissi N, Jridi M, Li S, Nasri M. Thermal, mechanical and microstructural characterization and antioxidant potential of *Rhinobatos cemiculus* gelatin films supplemented by titanium dioxide doped silver nanoparticles. Food Hydrocoll 2020;103:105695. https://doi.org/10.1016/j.foodhyd.2020.105695.

[151] Liu M, Chao J, Deng S, Wang K, Li K, Fan C. Dark-field microscopy in imaging of plasmon resonant nanoparticles. Colloids Surf B Biointerfaces 2014;124:111–7. https://doi.org/10.1016/j.colsurfb.2014.06.001.

[152] Huang B, Bates M, Zhuang X. Super-resolution fluorescence microscopy. Annu Rev Biochem 2009;78:993–1016. https://doi.org/10.1146/annurev.biochem.77.061906.092014.

[153] Kästner C, Böhmert L, Braeuning A, Lampen A, Thünemann AF. Fate of fluorescence labels – their adsorption and desorption kinetics to silver nanoparticles. Langmuir 2018;34:7153–60. https://doi.org/10.1021/acs.langmuir.8b01305.

[154] O'Connor DJ, Sexton BA, Smart RSC. Surface analysis methods in materials science. Berlin, Heidelberg: Springer Berlin Heidelberg; 2003. https://doi.org/10.1007/978-3-662-05227-3.

[155] Yu X, Arey B, Chatterjee S, Chun J. Improving in situ liquid SEM imaging of particles. Surf Interface Anal 2019;51:1325–31. https://doi.org/10.1002/sia.6700.

[156] Kim KH, Akase Z, Suzuki T, Shindo D. Charging effects on SEM/SIM contrast of metal/insulator system in various metallic coating conditions. Mater Trans 2010;51:1080–3. https://doi.org/10.2320/matertrans.M2010034.

[157] Stabentheiner E, Zankel A, Pölt P. Environmental scanning electron microscopy (ESEM)—a versatile tool in studying plants. Protoplasma 2010;246:89–99. https://doi.org/10.1007/s00709-010-0155-3.

[158] Antisari LV, Laudicina VA, Gatti A, Carbone S, Badalucco L, Vianello G. Soil microbial biomass carbon and fatty acid composition of earthworm Lumbricus rubellus after exposure to engineered nanoparticles. Biol Fertil Soils 2015;51:261–9. https://doi.org/10.1007/s00374-014-0972-1.

[159] Williams DB, Carter CB. Transmission electron microscopy: a textbook for materials science. New York: Springer; 2009.

[160] De Yoreo JJ, Sommerdijk NAJM. Investigating materials formation with liquid-phase and cryogenic TEM. Nat Rev Mater 2016;1:16035. https://doi.org/10.1038/natrevmats.2016.35.

[161] Collins L, Liu Y, Ovchinnikova OS, Proksch R. Quantitative electromechanical atomic force microscopy. ACS Nano 2019;13:8055–66. https://doi.org/10.1021/acsnano.9b02883.

[162] Vobornik D, Vobornik S. Scanning near-field optical microscopy. Bosn J Basic Med Sci 2008;8:63–71. https://doi.org/10.17305/bjbms.2008.3000.

[163] Liu BJ, Lin KQ, Hu S, Wang X, Lei ZC, Lin HX, et al. Extraction of absorption and scattering contribution of metallic nanoparticles toward rational synthesis and application. Anal Chem 2015;87:1058–65. https://doi.org/10.1021/ac503612b.

[164] Dziubakiewicz E, Buszewski B. Principles of electromigration techniques. In: Buszewski B, Dziubakieicz E, Szumski M, editors. Electromigr. tech. Heidelberg: Springer-Verlag; 2013. p. 5–26. https://doi.org/10.1007/978-3-642-35043-6_2.

[165] Mudalige TK, Qu H, Van Haute D, Ansar SM, Linder SW. Capillary electrophoresis and asymmetric flow field-flow fractionation for size-based separation of engineered metallic nanoparticles: a critical comparative review. TrAC Trends Anal Chem 2018;106:202–12. https://doi.org/10.1016/j.trac.2018.07.008.

[166] Garcia MA. Surface plasmons in metallic nanoparticles: fundamentals and applications. J Phys D Appl Phys 2011;44:283001. https://doi.org/10.1088/0022-3727/44/28/283001.

29

[167] Hooshmand N, El-Sayed MA. Collective multipole oscillations direct the plasmonic coupling at the nanojunction interfaces. Proc Natl Acad Sci 2019;116:19299–304. https://doi.org/10.1073/pnas.1909416116.

[168] Wijaya YN, Kim J, Choi WM, Park SH, Kim MH. A systematic study of triangular silver nanoplates: one-pot green synthesis, chemical stability, and sensing application. Nanoscale 2017;9:11705–12. https://doi.org/10.1039/c7nr03077k.

[169] Luo M, Huang H, Choi S-I, Zhang C, da Silva RR, Peng H-C, et al. Facile synthesis of Ag nanorods with no plasmon resonance peak in the visible region by using Pd decahedra of 16 nm in size as seeds. ACS Nano 2015;9:10523–32. https://doi.org/10.1021/acsnano.5b05053.

[170] Pansare AV, Shedge AA, Chhatre SY, Das D, Murkute P, Pansare SV, et al. AgQDs employing black box synthetic strategy: photocatalytic and biological behavior. JOL 2019;212:133–40. https://doi.org/10.1016/j.jlumin.2019.04.014.

[171] Monago-Maraña O, Durán-Merás I, Galeano-Díaz T, Muñoz De La Peña A. Fluorescence properties of flavonoid compounds. Quantification in paprika samples using spectrofluorimetry coupled to second order chemometric tools. Food Chem 2016; 196:1058–65. https://doi.org/10.1016/j.foodchem.2015.10.041.

[172] Socrates GG. Infrared and Raman characteristic group frequencies: tables and charts. . 3rd ed.Chichester, West Sussex: John Wiley & Sons, Ltd; 2004.

[173] Syed B, Nagendra Prasad MN, Satish S. Synthesis and characterization of silver nanobactericides produced by Aneurinibacillus migulanus 141, a novel endophyte inhabiting *Mimosa pudica* L. Arab J Chem 2019;12:3743–52. https://doi.org/10.1016/j.arabjc.2016.01.005.

[174] Bowie BT, Chase DB, Lewis IR, Griffiths PR. Anomalies and artifacts in Raman spectroscopy. In: Griffiths PR, editor. Handb. vib. spectrosc. Chichester, UK: John Wiley & Sons, Ltd; 2006. https://doi.org/10.1002/0470027320.s3103.

[175] Hanrahan MP, Fought EL, Windus TL, Wheeler LM, Anderson NC, Neale NR, et al. Characterization of silicon nanocrystal surfaces by multidimensional solid-state NMR spectroscopy. Chem Mater 2017;29:10339–51. https://doi.org/10.1021/acs.chemmater.7b03306.

[176] Retout M, Brunetti E, Valkenier H, Bruylants G. Limits of thiol chemistry revealed by quantitative analysis of mixed layers of thiolated-PEG ligands grafted onto gold nanoparticles. J Colloid Interface Sci 2019;557:807–15. https://doi.org/10.1016/j.jcis.2019.09.047.

[177] Marbella LE, Millstone JE. NMR techniques for noble metal nanoparticles. Chem Mater 2015;27:2721–39. https://doi.org/10.1021/cm504809c.

[178] Pawłowski R, Kiełbasiński K, Sobik P, Pawłowski B, Wita H, Konefał R, et al. Obtaining of silver nanopowders by the thermal decomposition of fatty silver salts with various chain length. Mater Res Express 2019;6:065046. https://doi.org/10.1088/2053-1591/ab086b.

[179] Marbella LE, Andolina CM, Smith AM, Hartmann MJ, Dewar AC, Johnston KA, et al. Gold-cobalt nanoparticle alloys exhibiting tunable compositions, near-infrared emission, and high T 2 relaxivity. Adv Funct Mater 2014;24:6532–9. https://doi.org/10.1002/adfm.201400988.

[180] Jones LC, Buras Z, Gordon MJ. Partial hydrogenation of C 2H 2 on Ag-doped pt nanoparticles. J Phys Chem C 2012;116:12982–8. https://doi.org/10.1021/jp304632v.

[181] Lee JH, Okuno Y, Cavagnero S. Sensitivity enhancement in solution NMR: emerging ideas and new frontiers. J Magn Reson 2014;241:18–31. https://doi.org/10.1016/j.jmr.2014.01.005.

[182] Zhi Hu J. Magic angle spinning NMR metabolomics. Metabolomics 2016;6. https://doi.org/10.4172/2153-0769.1000e147.

[183] Ma G, Allen HC. Handbook of spectroscopy. Wiley-VCH Verlag GmbH: Weinheim; 2003. https://doi.org/10.1002/3527602305.

[184] Radu T, Benea D, Ciceo-Lucacel R, Barbu-Tudoran L, Simon S. X-ray photoelectron spectroscopic characterization of Ag nanoparticles embedded bioglasses. J Phys Chem C 2012;116:17975–9. https://doi.org/10.1021/jp306035n.

[185] Han Y, Xu Q, Wang W, Zhu J. Atomic-scale insight into the metal–support interaction: a case for Ag nanoparticles on ordered ZrO 2 (111) thin films. J Phys Chem C 2015;119:4235–41. https://doi.org/10.1021/jp5129035.

[186] Kjærvik M, Hermanns A, Dietrich P, Thissen A, Bahr S, Ritter B, et al. Detection of suspended nanoparticles with near-ambient pressure X-ray photoelectron spectroscopy. J Phys Condens Matter 2017;29:474002. https://doi.org/10.1088/1361-648X/aa8b9d.

[187] Dahle S, Meuthen J, Viöl W, Maus-Friedrichs W. Adsorption of silver on glucose studied with MIES, UPS, XPS and AFM. Appl Surf Sci 2013;284:514–22. https://doi.org/10.1016/j.apsusc.2013.07.126.

[188] Scudiero L, Wei H, Eilers H. Photoemission spectroscopy and atomic force microscopy investigation of vapor-phase codeposited silver/poly(3-hexylthiophene) composites. ACS Appl Mater Interfaces 2009;1:2721–8. https://doi.org/10.1021/am900582w.

[189] Pal R, Sikder AK, Saito K, Funston AM, Bellare JR. Electron energy loss spectroscopy for polymers: a review. Polym Chem 2017;8:6927–37. https://doi.org/10.1039/C7PY01459C.

[190] Bunaciu AA, Udriștioiu E Gabriela, Aboul-Enein HY. X-Ray diffraction: instrumentation and applications. Crit Rev Anal Chem 2015;45:289–99. https://doi.org/10.1080/10408347.2014.949616.

[191] Shen G, Chen D. Transparent silver-nanoparticles/nanorods-decorated zinc oxide nanowires. J Phys Chem C 2010;114:21088–93. https://doi.org/10.1021/jp107213q.

[192] Holder CF, Schaak RE. Tutorial on powder X-ray diffraction for characterizing nanoscale materials. ACS Nano 2019;13:7359–65. https://doi.org/10.1021/acsnano.9b05157.

[193] Guo W, Hu S, Zhang J, Zhang H. Elimination of oxide interferences and determination of ultra-trace silver in soils by ICP-MS with ion–molecule reactions. Sci Total Environ 2011;409:2981–6. https://doi.org/10.1016/j.scitotenv.2011.04.011.

[194] Tang J, Xiong L, Wang S, Wang J, Liu L, Li J, et al. Distribution, translocation and accumulation of silver nanoparticles in rats. J Nanosci Nanotechnol 2009;9:4924–32. https://doi.org/10.1166/jnn.2009.1269.

[195] Kéri A, Kálomista I, Ungor D, Bélteki Á, Csapó E, Dékány I, et al. Determination of the structure and composition of Au-Ag bimetallic spherical nanoparticles using single particle ICP-MS measurements performed with normal and high temporal resolution. Talanta 2018;179:193–9. https://doi.org/10.1016/j.talanta.2017.10.056.

[196] Naasz S, Weigel S, Borovinskaya O, Serva A, Cascio C, Undas AK, et al. Multi-element analysis of single nanoparticles by ICP-MS using quadrupole and time-of-flight technologies. J Anal At Spectrom 2018;33:835–45. https://doi.org/10.1039/C7JA00399D.

[197] Wagener S, Dommershausen N, Jungnickel H, Laux P, Mitrano D, Nowack B, et al. Textile functionalization and its effects on the release of silver nanoparticles into artificial sweat. Environ Sci Technol 2016;50:5927–34. https://doi.org/10.1021/acs.est.5b06137.

[198] Priebe A, Barnes J-P, Edwards TEJ, Pethö L, Balogh I, Michler J. 3D imaging of nanoparticles in an inorganic matrix using TOF-SIMS validated with STEM and EDX. Anal Chem 2019;91:11834–9. https://doi.org/10.1021/acs.analchem.9b02545.

[199] Dhanya S, Saumya V, Rao TP. Synthesis of silver nanoclusters, characterization and application to trace level sensing of nitrate in aqueous media. Electrochim Acta 2013;102:299–305. https://doi.org/10.1016/j.electacta.2013.04.017.

[200] Oliveira E, Santos HM, Garcia-Pardo J, Diniz M, Lorenzo J, Rodríguez-González B, et al. Synthesis of functionalized fluorescent silver nanoparticles and their toxicological effect in aquatic environments (Goldfish) and HEPG2 cells. Front Chem 2013;1:1–11. https://doi.org/10.3389/fchem.2013.00029.

[201] Rafińska K, Pomastowski P, Buszewski B. Study of *Bacillus subtilis* response to different forms of silver. Sci Total Environ 2019;661:120–9. https://doi.org/10.1016/j.scitotenv.2018.12.139.

[202] Loeschner K, Navratilova J, Grombe R, Linsinger TPJ, Købler C, Mølhave K, et al. In-house validation of a method for determination of silver nanoparticles in chicken meat based on asymmetric flow field-flow fractionation and inductively coupled plasma mass spectrometric detection. Food Chem 2015;181:78–84. https://doi.org/10.1016/j.foodchem.2015.02.033.

[203] Mudalige TK, Qu H, Sánchez-Pomales G, Sisco PN, Linder SW. Simple functionalization strategies for enhancing nanoparticle separation and recovery with asymmetric flow field flow fractionation. Anal Chem 2015;87:1764–72. https://doi.org/10.1021/ac503683n.

[204] Štěpánová S, Kašička V. Recent applications of capillary electromigration methods to separation and analysis of proteins. Anal Chim Acta 2016;933:23–42. https://doi.org/10.1016/j.aca.2016.06.006.

[205] Qu H, Mudalige TK, Linder SW. Capillary electrophoresis coupled with inductively coupled mass spectrometry as an alternative to cloud point extraction based methods for rapid quantification of silver ions and surface coated silver nanoparticles. J Chromatogr A 2016;1429:348–53. https://doi.org/10.1016/j.chroma.2015.12.033.

[206] Michalke B, Vinković-Vrček I. Speciation of nano and ionic form of silver with capillary electrophoresis-inductively coupled plasma mass spectrometry. J Chromatogr A 2018;1572:162–71. https://doi.org/10.1016/j.chroma.2018.08.031.

[207] Hanauer M, Pierrat S, Zins I, Lotz A, Sönnichsen C. Separation of nanoparticles by gel electrophoresis according to size and shape. Nano Lett 2007;7:2881–5. https://doi.org/10.1021/nl071615y.

[208] Meenakshisundaram S, Krishnamoorthy V, Jagadeesan Y, Vilwanathan R, Balaiah A. *Annona muricata* assisted biogenic synthesis of silver nanoparticles regulates cell cycle arrest in NSCLC cell lines. Bioorg Chem 2020;95:103451. https://doi.org/10.1016/j.bioorg.2019.103451.

[209] Thiagamani SMK, Rajini N, Siengchin S, Varada Rajulu A, Hariram N, Ayrilmis N. Influence of silver nanoparticles on the mechanical, thermal and antimicrobial properties of cellulose-based hybrid nanocomposites. Compos Part B Eng 2019;165:516–25. https://doi.org/10.1016/j.compositesb.2019.02.006.

[210] Zheng Q, Zhang Y, Montazerian M, Gulbiten O, Mauro JC, Zanotto ED, et al. Understanding glass through differential scanning calorimetry. Chem Rev 2019;119:7848–939. https://doi.org/10.1021/acs.chemrev.8b00510.

[211] Haq S, Rehman W, Waseem M, Meynen V, Awan SU, Saeed S, et al. Fabrication of pure and moxifloxacin functionalized silver oxide nanoparticles for photocatalytic and antimicrobial activity. J Photochem Photobiol B Biol 2018;186:116–24. https://doi.org/10.1016/j.jphotobiol.2018.07.011.

[212] Dong C, Wang Z, Zhang Y, Ma X, Iqbal MZ, Miao L, et al. High-performance colorimetric detection of thiosulfate by using silver nanoparticles for smartphone-based analysis. ACS Sensors 2017;2:1152–9. https://doi.org/10.1021/acssensors.7b00257.

[213] Mogal SI, Gandhi VG, Mishra M, Tripathi S, Shripathi T, Joshi PA, et al. Single-step synthesis of silver-doped titanium dioxide: influence of silver on structural, textural, and photocatalytic properties. Ind Eng Chem Res 2014;53:5749–58. https://doi.org/10.1021/ie404230q.

[214] Chapter 4. The future is flat—two-dimensional nanomaterials. Nanotechnology. Cambridge, England: Royal Society of Chemistry; 2016. p. 85–114. https://doi.org/10.1039/9781782628873-00085.

[215] Harris LK, Theriot JA. Surface area to volume ratio: a natural variable for bacterial morphogenesis. Trends Microbiol 2018;26:815–32. https://doi.org/10.1016/j.tim.2018.04.008.

[216] Graf C, Nordmeyer D, Sengstock C, Ahlberg S, Diendorf J, Raabe J, et al. Shape-dependent dissolution and cellular uptake of silver nanoparticles. Langmuir 2018;34:1506–19. https://doi.org/10.1021/acs.langmuir.7b03126.

[217] Aherne D, Ledwith DM, Gara M, Kelly JM. Optical properties and growth aspects of silver nanoprisms produced by a highly reproducible and rapid synthesis at room temperature. Adv Funct Mater 2008;18:2005–16. https://doi.org/10.1002/adfm.200800233.

30

[218] Vankayala R, Kuo C-L, Sagadevan A, Chen P-H, Chiang C-S, Hwang KC. Morphology dependent photosensitization and formation of singlet oxygen (1Δg) by gold and silver nanoparticles and its application in cancer treatment. J Mater Chem B 2013;1:4379. https://doi.org/10.1039/c3tb20806k.

[219] Nejati S, Mohseni Vadeghani E, Khorshidi S, Karkhaneh A. Role of particle shape on efficient and organ-based drug delivery. Eur Polym J 2020;122:109353. https://doi.org/10.1016/j.eurpolymj.2019.109353.

[220] Dasgupta S, Auth T, Gompper G. Shape and orientation matter for the cellular uptake of nonspherical particles. Nano Lett 2014;14:687–93. https://doi.org/10.1021/nl403949h.

[221] Kulkarni AP, Munechika K, Noone KM, Smith JM, Ginger DS. Phase transfer of large anisotropic plasmon resonant silver nanoparticles from aqueous to organic solution. Langmuir 2009;25:7932–9. https://doi.org/10.1021/la900600z.

[222] Hartland GV, Besteiro LV, Johns P, Govorov AO. What's so hot about electrons in metal nanoparticles? ACS Energy Lett 2017;2:1641–53. https://doi.org/10.1021/acsenergylett.7b00333.

[223] Jiang P, Dong Y, Yang L, Zhao Y, Xie W. Hot electron-induced carbon–halogen bond cleavage monitored by in situ surface-enhanced Raman spectroscopy. J Phys Chem C 2019;123:16741–6. https://doi.org/10.1021/acs.jpcc.9b03238.

[224] Han F, Guan Z, Tan TS, Xu Q-H. Size-dependent two-photon excitation photoluminescence enhancement in coupled noble-metal nanoparticles. ACS Appl Mater Interfaces 2012;4:4746–51. https://doi.org/10.1021/am301121k.

[225] Wang W-L, Yang C-S. Silver nanoparticles embedded titania nanotube with tunable blue light band gap. Mater Chem Phys 2016;175:146–50. https://doi.org/10.1016/j.matchemphys.2016.03.005.

[226] Guo L, Yin H, Xu M, Zheng Z, Fang X, Chong R, et al. In situ generated plasmonic silver nanoparticle-sensitized amorphous titanium dioxide for ultrasensitive photoelectrochemical sensing of formaldehyde. ACS Sensors 2019;4:2724–9. https://doi.org/10.1021/acssensors.9b01204.

[227] Tsendzughul NT, Ogwu AA. Physicochemical aspects of the mechanisms of rapid antimicrobial contact-killing by sputtered silver oxide thin films under visible light. ACS Omega 2019;4:16847–59. https://doi.org/10.1021/acsomega.9b01856.

[228] Mahmoud KH, Abbo M. Synthesis, characterization and optical properties of gelatin doped with silver nanoparticles. Spectrochim Acta Part A Mol Biomol Spectrosc 2013;116:610–5. https://doi.org/10.1016/j.saa.2013.07.106.

[229] Luo W, Hu W, Xiao S. Size effect on the thermodynamic properties of silver nanoparticles. J Phys Chem C 2008;112:2359–69. https://doi.org/10.1021/jp0770155.

[230] Chiu C, Hong P, Lin J. Clay-mediated synthesis of silver nanoparticles exhibiting low-temperature melting. Langmuir 2011;27:11690–6. https://doi.org/10.1021/la202661n.

[231] Alarifi HA, Atiş M, Özdoğan C, Hu A, Yavuz M, Zhou Y. Determination of complete melting and surface premelting points of silver nanoparticles by molecular dynamics simulation. J Phys Chem C 2013;117:12289–98. https://doi.org/10.1021/jp311541c.

[232] Sagandykova GN, Pomastowski PP, Kaliszan R, Buszewski B. Modern analytical methods for consideration of natural biological activity. TrAC Trends Anal Chem 2018;109:198–213. https://doi.org/10.1016/j.trac.2018.10.012.

[233] Anwar A, Mungroo MR, Anwar A, Sullivan WJ, Khan NA, Siddiqui R. Repositioning of Guanabenz in conjunction with gold and silver nanoparticles against pathogenic amoebae *Acanthamoeba castellanii* and *Naegleria fowleri*. ACS Infect Dis 2019;5: 2039–46. https://doi.org/10.1021/acsinfecdis.9b00263.

[234] Lu L, Sun RW-Y, Chen R, Hui C-K, Ho C-M, Luk JM, et al. Silver nanoparticles inhibit hepatitis B virus replication. Antivir Ther 2008;13:253–62.

[235] Teodoro JS, Simões AM, Duarte FV, Rolo AP, Murdoch RC, Hussain SM, et al. Assessment of the toxicity of silver nanoparticles in vitro: a mitochondrial perspective. Toxicol In Vitro 2011;25:664–70. https://doi.org/10.1016/j.tiv.2011.01.004.

[236] AshaRani P, Hande MP, Valiyaveettil S. Anti-proliferative activity of silver nanoparticles. BMC Cell Biol 2009;10:65. https://doi.org/10.1186/1471-2121-10-65.

[237] Sachdev A, Matai I, Gopinath P. Dual-functional carbon dots–silver@zinc oxide nanocomposite: in vitro evaluation of cellular uptake and induction of apoptosis. J Mater Chem B 2015;3:1217–29. https://doi.org/10.1039/C4TB02043J.

[238] Zhang R, Piao MJ, Kim KC, Kim AD, Choi J-Y, Choi J, et al. Endoplasmic reticulum stress signaling is involved in silver nanoparticles-induced apoptosis. Int J Biochem Cell Biol 2012;44:224–32. https://doi.org/10.1016/j.biocel.2011.10.019.

[239] Liu J, Wang Z, Liu FD, Kane AB, Hurt RH. Chemical transformations of nanosilver in biological environments. ACS Nano 2012;6:9887–99. https://doi.org/10.1021/nn303449n.

[240] Srivastava M, Singh S, Self WT. Exposure to silver nanoparticles inhibits selenoprotein synthesis and the activity of thioredoxin reductase. Environ Health Perspect 2012;120:56–61. https://doi.org/10.1289/ehp.1103928.

[241] Gordon O, Vig Slenters T, Brunetto PS, Villaruz AE, Sturdevant DE, Otto M, et al. Silver coordination polymers for prevention of implant infection: thiol interaction, impact on respiratory chain enzymes, and hydroxyl radical induction. Antimicrob Agents Chemother 2010;54:4208–18. https://doi.org/10.1128/AAC.01830-09.

[242] Xu FF, Imlay JA. Silver(I), mercury(II), cadmium(II), and zinc(II) target exposed enzymic iron-sulfur clusters when they toxify *Escherichia coli*. Appl Environ Microbiol 2012;78:3614–21. https://doi.org/10.1128/AEM.07368-11.

[243] Erdogan O, Abbak M, Demirbolat GM, Birtekocak F, Aksel M, Pasa S, et al. Green synthesis of silver nanoparticles via *Cynara scolymus* leaf extracts: the characterization, anticancer potential with photodynamic therapy in MCF7 cells. PLoS One 2019;14:e0216496. https://doi.org/10.1371/journal.pone.0216496.

[244] Kaveh R, Li Y-S, Ranjbar S, Tehrani R, Brueck CL, Van Aken B. Changes in *Arabidopsis thaliana* gene expression in response to silver nanoparticles and silver ions. Environ Sci Technol 2013;47:10637–44. https://doi.org/10.1021/es402209w.

[245] Mei N, Zhang Y, Chen Y, Guo X, Ding W, Ali SF, et al. Silver nanoparticle-induced mutations and oxidative stress in mouse lymphoma cells. Environ Mol Mutagen 2012;53:409–19. https://doi.org/10.1002/em.21698.

[246] Banti CN, Giannoulis AD, Kourkoumelis N, Owczarzak AM, Poyraz M, Kubicki M, et al. Mixed ligand–silver(i) complexes with anti-inflammatory agents which can bind to lipoxygenase and calf-thymus DNA, modulating their function and inducing apoptosis. Metallomics 2012;4:545. https://doi.org/10.1039/c2mt20039b.

[247] Park H-J, Kim JY, Kim J, Lee J-H, Hahn J-S, Gu MB, et al. Silver-ion-mediated reactive oxygen species generation affecting bactericidal activity. Water Res 2009;43: 1027–32. https://doi.org/10.1016/j.watres.2008.12.002.

[248] Dibrov P, Dzioba J, Gosink KK, Häse CC. Chemiosmotic mechanism of antimicrobial activity of Ag+ in vibrio cholerae. Antimicrob Agents Chemother 2002;46: 2668–70. https://doi.org/10.1128/AAC.46.8.2668-2670.2002.

[249] Kittler S, Greulich C, Diendorf J, Köller M, Epple M. Toxicity of silver nanoparticles increases during storage because of slow dissolution under release of silver ions. Chem Mater 2010;22:4548–54. https://doi.org/10.1021/cm100023p.

[250] Ivask A, Kurvet I, Kasemets K, Blinova I, Aruoja V, Suppi S, et al. Size-dependent toxicity of silver nanoparticles to bacteria, yeast, algae, crustaceans and mammalian cells in vitro. PLoS One 2014;9:e102108. https://doi.org/10.1371/journal.pone.0102108.

[251] Tang B, Xu S, Hou X, Li J, Sun L, Xu W, et al. Shape evolution of silver nanoplates through heating and photoinduction. ACS Appl Mater Interfaces 2013;5:646–53. https://doi.org/10.1021/am302072u.

[252] Lucky SS, Soo KC, Zhang Y. Nanoparticles in photodynamic therapy. Chem Rev 2015;115:1990–2042. https://doi.org/10.1021/cr5004198.

[253] Saavedra JRM, Asenjo-Garcia A, García de Abajo FJ. Hot-electron dynamics and thermalization in small metallic nanoparticles. ACS Photon 2016;3:1637–46. https://doi.org/10.1021/acsphotonics.6b00217.

[254] Du B, Tung C-H. Enzyme-assisted photodynamic therapy based on nanomaterials. ACS Biomater Sci Eng 2020;6:2506–17. https://doi.org/10.1021/acsbiomaterials.9b00968.

[255] Fuertes G, Sánchez-Muñoz OL, Pedrueza E, Abderrafi K, Salgado J, Jiménez E. Switchable bactericidal effects from novel silica-coated silver nanoparticles mediated by light irradiation. Langmuir 2011;27:2826–33. https://doi.org/10.1021/la1045282.

6.2 Synthesis, physicochemical characterization and antibacterial performance of silver-lactoferrin complexes

O. Pryshchepa, P. Pomastowski, K. Rafińska, A. Gołębiowski, A. Rogowska, M Monedeiro-Milanowski, G. Sagandykova, B. Michalke, P. Schmitt-Kopplin, M. Gloc, R. Dobrucka, K. Kurzydłowski, B. Buszewski, *"Synthesis, physicochemical characterization and antibacterial performance of silver-lactoferrin complexes"*, International Journal of Molecular Sciences, 23 (13), 2022: 7112, https://doi.org/10.3390/ijms23137112

Article

Synthesis, Physicochemical Characterization, and Antibacterial Performance of Silver—Lactoferrin Complexes

Oleksandra Pryshchepa [1,2,*], Paweł Pomastowski [1], Katarzyna Rafińska [2], Adrian Gołębiowski [1,2],
Agnieszka Rogowska [1,2], Maciej Monedeiro-Milanowski [1], Gulyaim Sagandykova [1], Bernhard Michalke [3],
Philippe Schmitt-Kopplin [3,4], Michał Gloc [5], Renata Dobrucka [5,6], Krzysztof Kurzydłowski [7] and
Bogusław Buszewski [1,2]

1   Centre for Modern Interdisciplinary Technologies, Nicolaus Copernicus University in Torun,
    87-100 Torun, Poland; p.pomastowski@umk.pl (P.P.); adrian.golebiowski@doktorant.umk.pl (A.G.);
    aga4356@wp.pl (A.R.); milanowski.maciej@gmail.com (M.M.-M.); sagandykova.gulyaim1@gmail.com (G.S.);
    b.busz@umk.pl (B.B.)
2   Department of Environmental Chemistry and Bioanalytics, Faculty of Chemistry, Nicolaus Copernicus
    University in Torun, 87-100 Torun, Poland; katraf@umk.pl
3   Research Unit Analytical BioGeoChemistry, Helmholtz Zentrum Muenchen, 85764 Neuherberg, Germany;
    bernhard.michalke@helmholtz-muenchen.de (B.M.); schmitt-kopplin@helmholtz-muenchen.de (P.S.-K.)
4   Chair of Analytical Food Chemistry, Technische Universität München, 85354 Freising, Germany
5   Faculty of Materials Science and Engineering, Warsaw University of Technology, 02-507 Warsaw, Poland;
    michal.gloc.wim@pw.edu.pl (M.G.); renata.dobrucka@pw.edu.pl (R.D.)
6   Department of Industrial Products and Packaging Quality, Institute of Quality Science, Poznań University of
    Economics and Business, 61-875 Poznań, Poland
7   Faculty of Mechanical Engineering, Białystok University of Technology, 15-351 Białystok, Poland;
    k.kurzydlowski@pb.edu.pl
*   Correspondence: pryshchepa.alexie@gmail.com

Publisher's Note: MDPI stays neutral
with regard to jurisdictional claims in
published maps and institutional affil-
iations.

Abstract: Antibiotic-resistant bacteria pose one of the major threats to human health worldwide. The issue is fundamental in the case of chronic wound treatment. One of the latest trends to overcome the problem is the search for new antibacterial agents based on silver. Thus, the aim of this research was to synthesize the silver-lactoferrin complex as a new generation of substances for the treatment of infected wounds. Moreover, one of the tasks was to investigate the formation mechanisms of the respective complexes and the influence of different synthesis conditions on the features of final product. The batch-sorption study was performed by applying the Langmuir and Freundlich isotherm models for the process description. Characterization of the complexes was carried out by spectroscopy, spectrometry, and separation techniques, as well as with electron microscopy. Additionally, the biological properties of the complex were evaluated, i.e., the antibacterial activity against selected bacteria and the impact on L929 cell-line viability. The results indicate the formation of a heterogeneous silver–lactoferrin complex that comprises silver nanoparticles. The complex has higher antibacterial strength than both native bovine lactoferrin and Ag^+, while being comparable to silver toxicity.

Keywords: sorption isotherm study; metalloproteins; silver nanoparticles; silver–lactoferrin nanocomplex; antibacterial properties; cytotoxicity

1. Introduction

Pathogenic bacteria annually cause a significant number of human infections and deaths [1], where chronic wounds infections affect 1–2% of the population. They belong to the type of diseases that significantly decrease life quality. Patients with chronic wound infections complain about pain and limitation in physical activity. Moreover, such medical conditions are connected with the constant need for professional medical care, which negatively affects both the daily schedule and personal finances [2]. Wound-infection

treatment includes the utilization of antibiotics, and the chronic character of the process leads to appearance of multidrug-resistant microorganism strains. Over 70% of infections are caused by bacterial strains resistant to one or more commonly used antibiotics. Thus, the development of metal-based preparations with antimicrobial properties, especially in the form of nanoparticles (NPs), have been of high interest recently among researchers [3].

Metal NPs such as silver [4] or zinc oxide [5] mostly reveal higher antimicrobial activity than respective ions. In the case of silver-nanoparticle (AgNPs) utilization, the advantages also account for the fact that to date no pathogenic bacteria that have total resistance against silver have been identified. However, metal NPs exhibit a wide spectrum of toxic effects on organisms, which restricts their utilization [4]. Still, in the case of palliative wound healing, any strategies that may reduce patients' suffering are acceptable [6]. Moreover, NPs can be utilized as drug carriers. The combined effect of NPs with other antibacterial agents has shown to have a synergistic effect against pathogenic bacteria [7]. For instance, Rogowska et al. revealed that AgNPs functionalized with ampicillin had lower minimum inhibitory concentration (MIC) in comparison to both free NPs and ampicilline [8]. The approach enables the reduction of the required amount of utilized NPs to achieve positive results. Thus, the toxic effects caused by treatment also can be reduced. The reduced toxicity was also reported for biologically synthesized NPs, e.g., produced with utilization of probiotic bacteria, proteins, plant extracts, etc. [4].

The interactions of Ag^+ with proteins have been investigated previously [9–12]. The Ag^+ according to the Lewis theory belongs to soft acids and can interact with the soft basis, which includes, among others, sulfur-containing groups. This knowledge can be utilized for the prediction of metal binding to the protein-binding sites. The interactions of soft-acid metals with soft bases usually have covalent character [12]. It was shown that Ag^+ can rapidly split disulfide bridges and form bonds with proteins through cysteines. The same was also observed only for Hg^+ [9]. However, it is noteworthy to mention that in Pomastowski et al.'s work, the molecular modeling of the Ag^+ interaction with bovine lactoferrin (bLTF) was performed [10]. The study revealed the significant impact of glutamic and aspartic acids in the Ag^+ binding by protein. Still, earlier studies showed that Ag^+ forms stronger bonds with N-containing functional groups rather than with O-containing ones [9]. Moreover, the distinctive feature of silver compounds is that they usually are photosensitive, i.e., they undergo reduction with the formation of metallic silver. The most popular Ag^+ salt silver nitrate is not photosensitive, but the presence of organic traces promotes photoreduction [13]. Thus, interaction of Ag^+ with proteins usually leads to the formation of metallic AgNPs [4,10,11].

In turn, bLTF is a non-heme iron-binding metalloprotein from the transferrin family. It is assumed that the main function of all transferrins is Fe^{3+}-ion transport and regulation. However, lactoferrin (LTF) is also known for its role in host immune response during infections and inflammation [14]. Moreover, LTF also possesses antimicrobial [15], antiviral [16], antifungal [17], immunoregulatory and anti-inflammatory properties [18]. LTF has shown to be involved in cell proliferation and migration, among others, and topical administration of bLTF enables enhancement of the wound-closure process [19]. Several mechanisms of antibacterial properties have been reported for LTF. The ability to sequester Fe^{3+} with high efficacy affects growth of some Gram-positive and Gram-negative bacteria [19]. However, the activity is dependent on the iron saturation level and is abrogated in the case of holo-LTF. Moreover, it was revealed that bLTF can compete with lipopolysaccharide Ca^{2+}-binding sites on bacterial membranes, which are involved in the outer cell-membrane stabilization. The sialic acid of bLTF glycans plays a role in Ca^{2+} chelating, thus indicating the importance of the protein glycosylation. Additionally, the presence of high-mannose structures on bLTF may nonspecifically prevent pathogen interaction with eukaryotic cells [20]. The antibacterial properties of LTF are also attributed to its highly cationic character. The beginning of the N-lobe contains a sequence with high content of arginines and lysines, which forms a so-called "cationic loop". The cleavage of the LTF by pepsin can release the respective peptide called lactoferricin. The binding of either LTF or lactoferricin to the bacteria membrane disturbs its

function [19]. In connection with the presented information, the use of bLTF for the production of antibacterial protein-based metallocomposites seems attractive.

Silver nitrate is the most popular precursor utilized in the synthesis of nanocomposites with antibacterial properties. However, silver ions (Ag^+) of this precursor exist only in acidic conditions, while the increased pH above 6 causes the formation of insoluble silver oxide (Ag_2O) [21]. In turn, it was shown that the interaction of metals with proteins occurs more effectively at higher pH [9,22]. The respective nanocomposites are also more stable in basic pH. In the previous work of our group [10], the investigation on the formation of Ag-LTF nanocomposite was performed with the utilization of the so-called "Tollens' reagent", i.e., silver in the form of a complex with ammonia $[Ag(NH_3)_2]^+$. The utilization of silver complexation with ammonia enables the solubilization of silver in basic conditions, but significantly complicates the chemistry of the process. Therefore, it is interesting to investigate how bLTF will interact with Ag^+ in acidic conditions. Moreover, the impact of different Ag^+ concentrations on the features of the respective Ag-bLTF complexes should be studied.

Thus, the aim of the study was to synthesize Ag-bLTF complexes and evaluate their biological activity, in particular antibacterial performance. Moreover, one of the tasks was to investigate the formation mechanisms of the respective complexes and the influence of different synthesis conditions on the features of final product. The work presents the results of the batch-sorption study performed by applying the Langmuir and Freundlich isotherm models for the process description. Meanwhile, characterization of the complexes was carried out by spectroscopy (ATR-FTIR, Raman, Fluorescence), spectrometry (MALDI-TOF-MS, ICP-MS), and separation (SDS-PAGE, CE-ICP-MS) techniques, as well as with electron microscopy (STEM-EDX, HTREM-SAED). The results enabled us to describe the process of Ag^+ immobilization onto protein and to predict the possible mechanism of metal–protein interactions. The possible negative effects of the Ag-bLTF on living organisms were also evaluated by metal desorption analysis and cytotoxicity against the L929 cell line.

2. Results and Discussion

2.1. Batch-Sorption Study

The isotherm study enabled us to evaluate the maximum sorption capacity and other sorption parameters of bLTF in utilized conditions. The isotherm of Ag^+ sorption onto bLTF and bar chart of a sorption efficiency for the entire range of utilized metal concentrations are shown in Figure 1A,B, respectively. The isotherm has a classical shape distinctive for multilayer adsorption, and according to IUPAC classification can be assigned to isotherm type II [23].

In turn, Figure 1C presents the modified BET (Brunauer–Emmet–Teller) isotherm proposed by M. Sprynskyy et al. [24]. Previously, the use of such an approach was successfully applied for the description of multilayer metal sorption onto proteins [11,25]. In general, in both presented works the real character of the sorption was not possible to specify only by the shape of the classical isotherm. Instead, the modified BET isotherm enabled the clear outlining of the concentration ranges required for the formation of each subsequent layer. In the present study, the approach did not provide much additional information. Still, it was possible to distinguish two adsorption layers, where the first one was observed for the initial Ag^+ concentrations up to 900 mg/L. Meanwhile, the beginning of the second adsorption layer started with utilization of initial Ag^+ concentration of 1200 mg/L. The kinetic studies performed by P. Pomastowski et al. also confirmed the complex character of the process. Their investigation indicated that three stages of the sorption process can be distinguished. The first initial rapid-sorption step is related to the surface sorption, which is followed by gradual sorption with rate-limiting intraparticle diffusion. Finally, the process ends up with the equilibrium stage. Interestingly, in the P. Pomastowski et al. studies silver solution with concentration of 50 mg/L was utilized, and respective adsorption reached 73.6% and 8.1 mg/g [10]. Meanwhile, in the present study for the initial concentration of 45 and 60 mg/L, the adsorption efficiency was ≈98% in both cases and respective adsorp-

tion accounted for 8.78 and 11.62 mg/g, respectively. It can be concluded that silver in the form of amino complex is less available for the interaction with protein. Instead, acidic conditions have a low impact on the sorption efficiency of Ag^+ by bLTF.
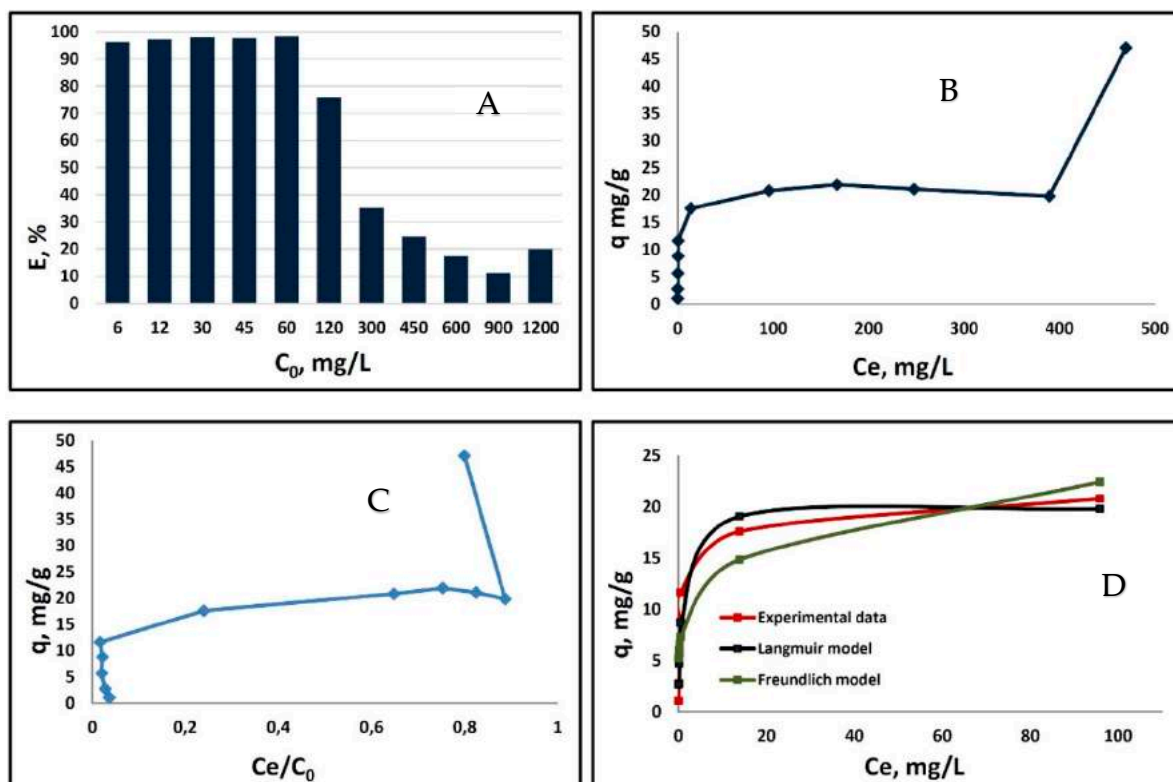

Figure 1. Batch isotherm study for Ag^+ sorption onto bLTF: (**A**) isotherm of Ag^+ adsorption onto bLTF for entire concentration range; (**B**) bar chart of a sorption efficiency of metal onto bLTF depending on the initial concentration of Ag^+; (**C**) modified BET isotherm, which presents adsorption as a function of a ratio C_e/C_0; (**D**) the fit of first sorption step to Langmuir and Freundlich models.

Further, the Langmuir and Freundlich isotherm models were applied. The respective models are simple, and thus are often used for the description of the sorption processes. Previously, the approach was successfully utilized to derive sorption parameters for Ag^+ and Zn^{2+} binding to caseins, Ova-albumin, and β-lactoalbumin [11,25,26]. However, it is noteworthy to mention that the Langmuir and Freundlich models can only be applied to isotherm type I [23]. Thus, we utilized it to our investigation, but only for the first step of the obtained isotherm (Figure 1D). The higher value of the correlation coefficient R^2 was obtained for the Langmuir model (significance level $p > 0.05$), indicating its better fit to experimentally derived data. The Langmuir model assumptions are the monolayer character of the adsorption and homogeneous surface in terms of binding-site energies [23]. Conversely, the Freundlich model assumes the heterogeneous nonideal character of the adsorption process and is not restricted to monolayer formation [27]. For the respective model, the correlation coefficient R^2 was only 0.905, but the significance level $p < 0.02$.

Interestingly, the Ag^+ adsorption onto bLTF was calculated as 47.06 ± 0.25 mg/g for the initial metal solution with concentration of ≈ 1200 mg/L, while the ICP-MS analysis of the respective complex (AgLTF1200) revealed that only 2.48 ± 0.46 mg/g (differing slightly from batch to batch) of silver remain after the washing steps. Additionally, even though the Ag^+ binding process was performed in acidic conditions, it did not cause significant loss of iron. The Fe^{3+} content in the complex was 1.31 ± 0.13 mg/g, which is almost the same as in native bLTF (1.45 ± 0.06 mg/g, protein-to-metal ratio $\approx 1:2$ [22]). The results show the surface character of Ag^+ binding and high correlation of the estimated

silver content in the complex with derived q_m from the Langmuir model. Moreover, this fact confirms the fairness of the utilization of the above-mentioned model in describing metal–protein interactions. Considering the protein molecular weight ($\approx$82 kDa by MALDI-TOF MS) the Ag:bLTF ratio in the complex was determined which is 1.78:1. Table 1 summarizes the calculated values for the utilized models (derived by CurveExpert Basic 2.2.3 software). In the previous study on the Zn^{2+} binding to proteins, namely Ova-albumin and β-lactoglobulin, the formation of ZnONPs in first case and the formation of homogeneous metal-protein complex was observed [25,26]. For the Zn^{2+}/ZnO-Ova nanocomposite, the same as in present study, the relatively high Langmuir constant and low q_m were calculated, e.g., 1.95 L/mg and 10.97 mg/g. In comparison, for the homogeneous Zn-β-lactoglobulin complex, the respective parameters were 0.01 L/mg and 104.40 mg/g. Thus, in the case of Ag-bLTF interactions, the formation of AgNPs can be predicted. Still, for the silver interactions with caseins, the sorption parameters were more similar to Zn-β-lactoglobulin (e.g., 0.02 L/mg and 77.44 mg/g). This fact may be connected to caseins' complex structure, which appears in the solution in the form of highly organized micelles [11].

Table 1. Calculated values derived from Freundlich and Langmuir isotherm models.

Freundlich Isotherm				Langmuir Isotherm			
K_F [mg/g]	1/n	S	R^2	K_L [L/mg]	q_m [mg/g]	S	R^2
8.465	0.213	3.45	0.905	19.94	1.55	1.93	0.971

The changes of the free Gibbs energies ΔG were calculated based on the value of the distribution coefficient (K_D). In general, the data indicate that Ag^+ binding to bLTF has spontaneous character. Moreover, some interesting correlations can be observed. For instance, in cases where solutions of low Ag^+ concentration (6–60 mg/L) were utilized, the calculated ΔG were almost similar and were in the range between -22.76 and -24.741 kJ/mol. The lowest value was when the Ag^+ concentration of 6 mg/L was used, which may be connected to the formation of AgNPs, since the formation of a new surface is a thermodynamically unfavorable process [4]. Instead, for Ag^+ concentrations of 15–60 mg/L, the differences in calculated ΔG are in the range of standard deviation, which is complementary to the better fit of the Langmuir model to the experimentally obtained adsorption isotherm. For higher Ag^+ concentrations (120–900 mg/L), the calculated ΔG values gradually decrease from -17.58 to -9.67 kJ/mol, which may indicate that some of the Ag^+ bonds to bLTF through weak electrostatic interactions. Instead, the breaking of the energy barrier and formation of a new adsorption layer resulted in a slight increase in ΔG to -11.34 kJ/mol, which was observed for Ag^+ solution with a concentration of 1200 mg/L.

2.2. Physicochemical Characterization of Synthesized Complexes

2.2.1. Electron Microscopy

Silver ions tend to reduce in the presence of organic compounds with the formation of metallic nanoparticles. Thus, electron microscopy was utilized for the AgLTF complexes' examination. Representative images of samples AgLTF30, AgLTF45, AgLTF120, AgLTF450, AgLTF600, and AgLTF1200 are shown in Figure 2.
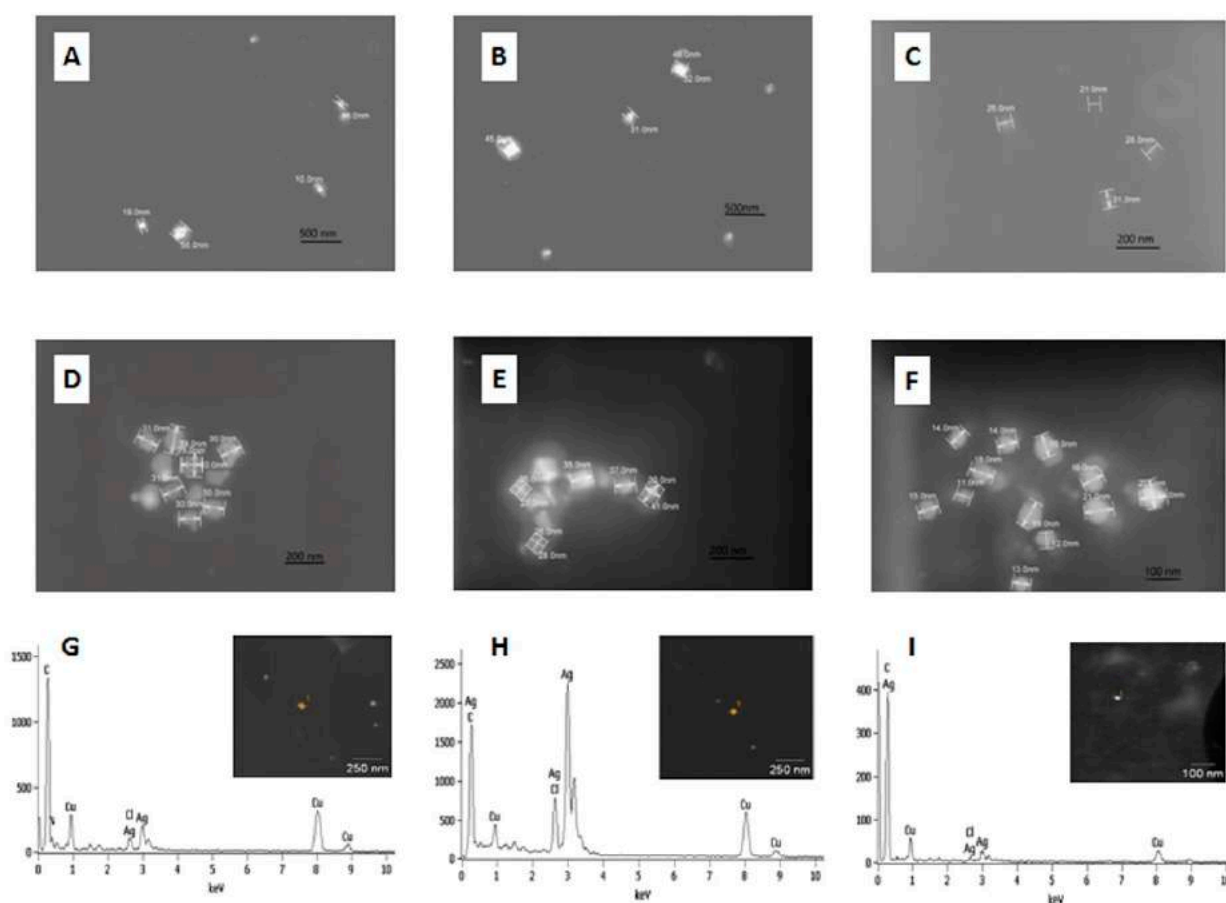
Figure 2. STEM images of AgLTF complexes with marked particle sizes: (**A**) AgLTF30; (**B**) AgLTF45; (**C**) AgLTF120; (**D**) AgLTF450; (**E**) AgLTF900; (**F**) and STEM-EDX spectra of samples: (**G**) AgLTF30, (**H**) AgLTF45, (**I**) AgLTF1200.

The images reveal the presence of mostly spherical silver nanoparticles in all studied samples of AgLTF. The size of the AgNPs fell within the range of 10–56 nm. It was noticed that samples obtained with lower Ag^+ concentrations in the reaction mixture were characterized by the presence of less agglomerated, smaller, mostly spherical structures. Interestingly, for AgLTF1200 the presence of smaller nanoparticles with sizes <20 nm was observed. Moreover, the biggest NPs were noticed for the complexes AgLTF45-AgLTF900.

The formation of NPs happens through a process comprised of several stages: nucleation, growth by Me^0 incorporation, and aggregation [4]. Each of the stages is dependent on the time-resolved Me^0 concentration and the amount of capping agent, which in consequence influences the size and size distribution of the formed NPs. Thus, by controlling the amount of free Ag^+, the bLTF (acting both as the reducing and capping agent), and metal/protein ratio, the nanocomposite with the desired features can be obtained. Our studies show that with the increase in the silver in the reaction mixture at the stable bLTF concentration, the size of nanoparticles becomes bigger, up to an Ag^+ concentration of 45 mg/L. This should indicate that a smaller amount of AgNP nuclei was formed but a higher rate of NP growth occurred. For reaction mixtures where Ag^+ concentration was in the range between 45 and 900 mg/L, the NPs size was almost the same, but their amount was higher when higher metal concentrations were used. When the concentration of Ag^+ reached 1200 mg/L, a higher amount of nuclei formed, but the Ag^0 concentration may have been too low for NP growth. Thus, a large amount of AgNPs with smaller sizes were formed. As can be seen, the resulted features of the formed nanocomposites correlate with the isotherm-sorption studies. Further, EDX analysis was performed, which confirmed that the particles of interest contain a high concentration of silver. Similarly, as in previous

works [1], the presence of copper was due to the use of a copper mesh for analysis and proteins for stabilization of the Ag nanoparticles. However, the EDX analysis also revealed the presence of chlorides in the sample. In the case of biogenic AgNPs, contamination with the chloride ion is one of the most common contaminations. AgCl is also photosensitive and its irradiation with daylight should also lead to the formation of metallic NPs in the end [28]. However, such NPs have the synthesis mechanism of other characters in comparison to the direct formation of AgNPs by reduction with functional groups of the protein.

The samples were also subjected to TEM-SAED analysis. Figure 3 shows TEM-images of the AgLTF450 and corresponding SAED pattern. From Figure 3A, it can be seen that the complex is comprised of a high amount of protein, which disturbs the SAED analysis. Thus, even though SAED reveals the crystalline structure of the formed AgNPs, it was not possible to determine the interplanar distances.
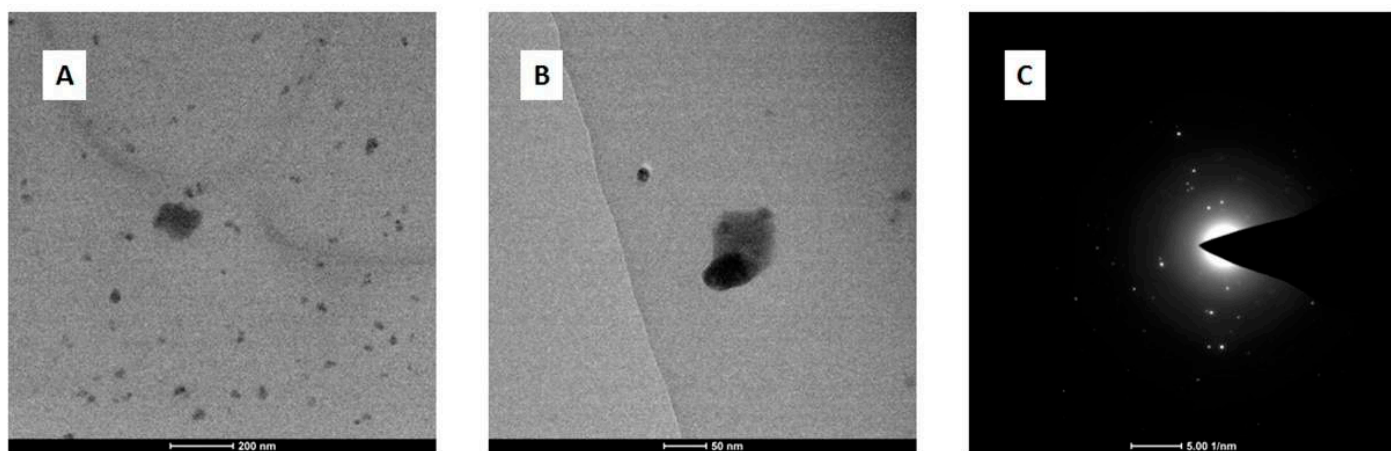
Figure 3. TEM images of AgbLTF450 at different magnifications (**A,B**) and (**C**) SAED pattern recorded for AgbLTF450.

2.2.2. Fourier Transform Infrared Spectroscopy (FTIR)

FTIR is a technique that allows the tracking of changes in absorbance of certain functional groups upon protein interactions [12]. Figure 4 presents the absorption spectra recorded for native bLTF and the complexes synthesized with utilization of Ag^+ solutions with concentration of 45, 450, and 1200 mg/L. The spectrum of native bLTF reveals the pattern of absorption bands distinctive for proteins. The region 2800–3700 cm^{-1} presents the vibrations of hydrogen-containing groups. The wide band with a maximum at 3280 cm^{-1} corresponds to vibrations of O-H and N-H that take part in hydrogen bonds. The band at 3078 cm^{-1} comes from C-H in aromatic rings, while bands with maxima in the range from 2800–3000 cm^{-1} can be assigned to doublets of C-H asymmetric and symmetric vibrations of methyl and methylene groups [29]. The redshift and changes in the intensities of corresponding signals after bLTF interaction with Ag^+ can be observed, which indicates the occurrence of structural modifications in the protein. Both the Ag^+ and AgNPs' incorporation to protein should induce such changes. For instance, the band at 2969 cm^{-1} of bLTF shifted to 2957, 2962, and 2964 cm^{-1} of AgLTF45, AgLTF450, and AgLTF1200 cm^{-1}, respectively. The additional bands for respective groups also can be detected: $\delta_{as}(CH_3)$ at 1472 cm^{-1} and $\delta(CH_2)$ at 1451 cm^{-1} [29,30]. Alhazmi et al. in their work based on the study performed on bovine serum albumin (BSA) also came to the conclusion that incorporation of any of the metal leads to the changes in protein structures [12].
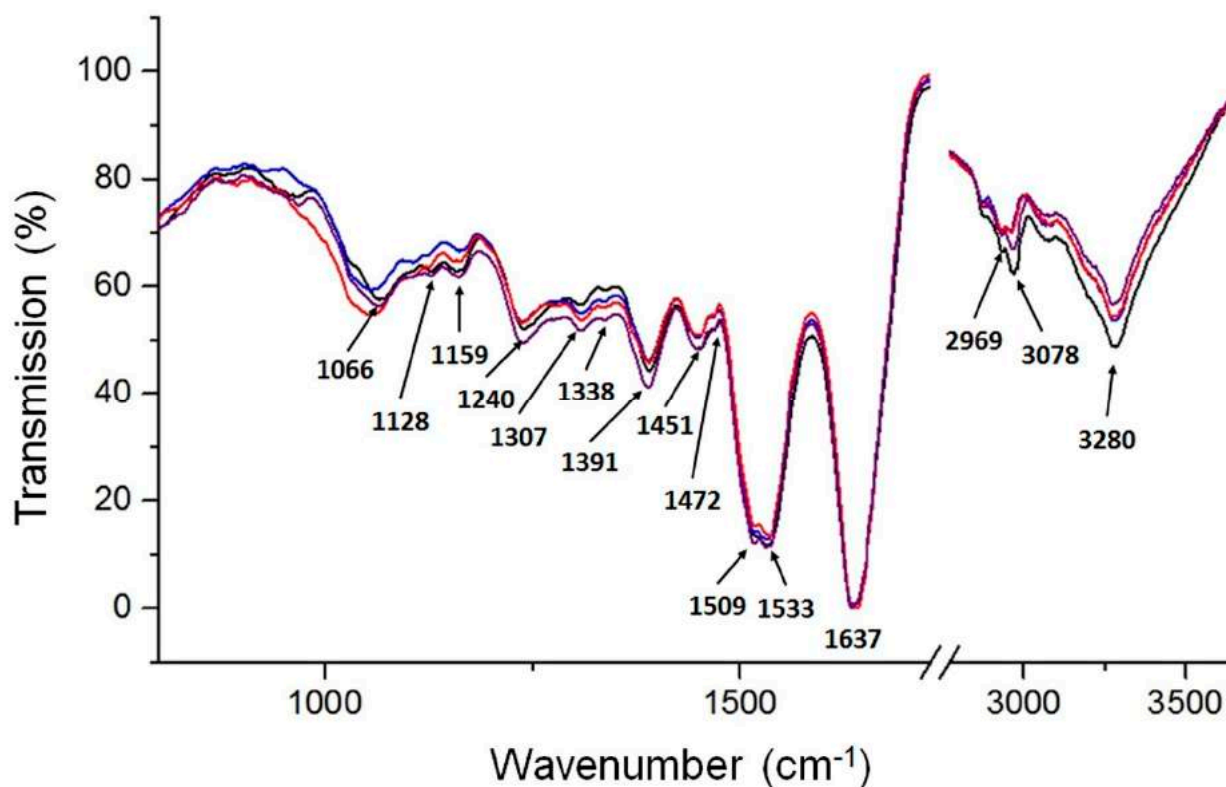
Figure 4. ATR-FTIR spectrum of native bLTF (black) and its complexes synthesized with silver solutions of 45 mg/L (blue), 450 mg/L (red), and 1200 mg/L (purple).

The common protein bands of amide I and amide II for all samples were observed at 1637 cm^{-1} and 1533 cm^{-1}. It is noteworthy to mention that the position of amide I indicates the structural features of the protein, and in case of bLTF shows the high content of the β-sheet in protein [30–32]. However, more accurate information about protein's secondary structure can be deduced from amide III modes [30,32]. The spectrum for native bLTF reveals bands of amide III at 1338 cm^{-1}, 1307 cm^{-1} which come from α-helix structures. Instead, more strong absorption at 1240 cm^{-1} of the β-sheet was observed. The corresponding bands did not shift after Ag$^+$ binding to bLTF, but the slight broadening of the band at 1240 cm^{-1} was detected. Moreover, the band at 1276 cm^{-1} (random coils) for AgLTF450 became visible. Such band shifts, in combination with the alterations in band intensities, also revealed the changes in the protein structure [12,30]. Additionally, after Ag$^+$ binding, the second maxima at 1509 cm^{-1} appeared in all studied complexes. The corresponding band may come from vibrations of tyrosine and tryptophane residues [30]. Moreover, the relative band intensities of $\nu_s(COO^-)$ of glutamic and aspartic acids (intense signal at 1391 cm^{-1}) were also changed after bLTF interaction with Ag$^+$. Interestingly, no shifts of respective bands were observed, while literature data indicate that they can shift significantly (+60/−90 cm^{-1}) [29] upon metal chelation. Still, in Pomastowski et al. [10], the molecular dynamics and quantum mechanics calculations of Ag$^+$ interaction with bLTF were performed, which indicate that aspartic and glutamic acids of bLTF were the dominant residues for Ag$^+$ binding. Furthermore, the $\nu(C-O)$ vibrations of serine, threonine, glutamic, and aspartic acids in bLTF are presented by bands at 1159, 1128, and 1066 cm^{-1} [30]. In case of AgLTF45, the significant shifts and signal split were observed. The bands at 1163, 1124, 1107, 1100, and 1055 cm^{-1} were detected. On the spectrum of AgLTF450, the corresponding region was also distorted. The bands at 1155, 1148, 1125, 1105, and 1053 cm^{-1} were observed. In the case of AgLTF1200, the band with the maximum at 1065 cm^{-1} broadened significantly upon Ag$^+$ binding. The respective band may overlay other signals in the studied absorption region. It should be noted that the band at 1105/1107 cm^{-1} can come

from ν(CN) vibrations of histidine, indicating the influence of Ag^+ on the respective amino acid [30]. Summing up, it can be assumed that all of the abovementioned amino acids should somehow be involved in the binding process. The bands presented in the region between 1000–900 cm^{-1} may come from ν(CO) or ν(CC) of serine. However, bLTF is a glycoprotein, the glycan content of which ranges from 6.7 to 11.2% of the total molecular weight [20]. Thus, the bands below 1000 cm^{-1} can also be assigned to ν(C-O), ν_{st}(C-O), ν_{st}(C-C) of glycans [33], while below 900 cm^{-1} may correspond to νCO+δCCH+ν_{asy} of the pyranose ring and νCC+δCCH+δCHβ-pyranose of glycans. Therefore, the changes that occur in the corresponding region may be due to either interaction with side chains of respective amino acids or with components of protein glycans. It is worth mentioning that the main disadvantage of spectroscopy in the infrared range is that bands corresponding to several functional groups can appear in the same region. Hence, it makes it difficult to distinguish which functional group has the most significant impact on metal bonding by protein.

2.2.3. Raman Spectroscopy

Some functional groups that are weak or inactive within FTIR can exhibit strong bands in Raman; thus, appropriate analysis was performed to complement the study. On the Raman spectrum (Figure 5) of native bLTF, the band at 3325 cm^{-1}, the same as in FTIR, comes from O-H and N-H groups involved in hydrogen bonds [31], but has lower intensity. Similarly, C-H vibrational bands are at 2931 and 2873 cm^{-1}. Instead, the band at 3055 cm^{-1} can be assigned to N-H str. vibrations. The analysis of the amide I and amide III bands' positions in Raman can also provide a significant amount of information regarding the secondary structure of the protein. The amide I band was detected at 1664 cm^{-1}, while the amide III region presented bands at 1280 cm^{-1} and 1329 cm^{-1} [34]. Likewise, in FTIR the position of the respective bands indicates the presence of all of the structures with prevalence of β-sheets [34,35]. The literature data reveal that the amide II band should rather have low-intensity Raman spectra [31,32]. However, the spectrum of native bLTF comprises the medium-intensity band at 1503 cm^{-1}, which may be assigned to amide II vibrations. The relative band can also come from aromatic rings of indole or imidazole from tryptophan and histidine. Moreover, the imidazole of histidine may give the-low intensity band at 1391 cm^{-1}, while indole ring modes of tryptophan are observed at 1550 cm^{-1}. Other tryptophan bands can be detected at 874 and 755 cm^{-1} [34,35]. The band characteristic for aromatic amino acids, i.e., tryptophan, tyrosine, and phenylalanine, were also presented by a band at 1604 cm^{-1}. Additionally, the tyrosine bands also appeared at 1206, 1171, and 835 cm^{-1}. Instead, phenylalanine bands were detected at 1035, 1003, and 962 cm^{-1}. The bands of C-H and C-N deformation stretching were observed at 1450 cm^{-1} and 1096 cm^{-1}, respectively [35]. The region at 500–600 cm^{-1} is characteristic for stretching vibrations of different conformers of S-S bonds [34]. Finally, the bands that appear near $\approx$410 cm^{-1} come from Fe-O or Fe-NO complexes in iron-binding proteins [36].

After Ag^+ binding to bLTF, the significant shifts and signal enhancement of bands in the fingerprint region can be observed on the spectra of AgLTF45 and AgLTF450 complexes. Instead, the Raman spectrum for the AgLTF1200 complex was not possible to obtain, as it undergoes burning under laser irradiation even with the lowest energy. The observed effect may be connected to the formation of Ag nanoparticles (AgNPs). A specific feature of the metallic NPs is the appearance of LSPR (localized surface-plasmon resonance) [4]. Surface plasmon of AgNPs can enhance the signals in Raman, which is the basis of a powerful technique, namely SERS (surface-enhanced Raman spectroscopy). The signal enhancement can be expected from the functional groups that are directly bonded to the NPs' surface. Thus, according to obtained results, it may be deduced that a small number of incorporated NPs caused the increase in signal intensity of appropriate functional groups in AgLTF45 and AgLTF450 complexes. However, the LSPR is also the reason of the NPs' catalytic activity, which should be a reason for the protein degradation in the AgLTF1200 complex within Raman.
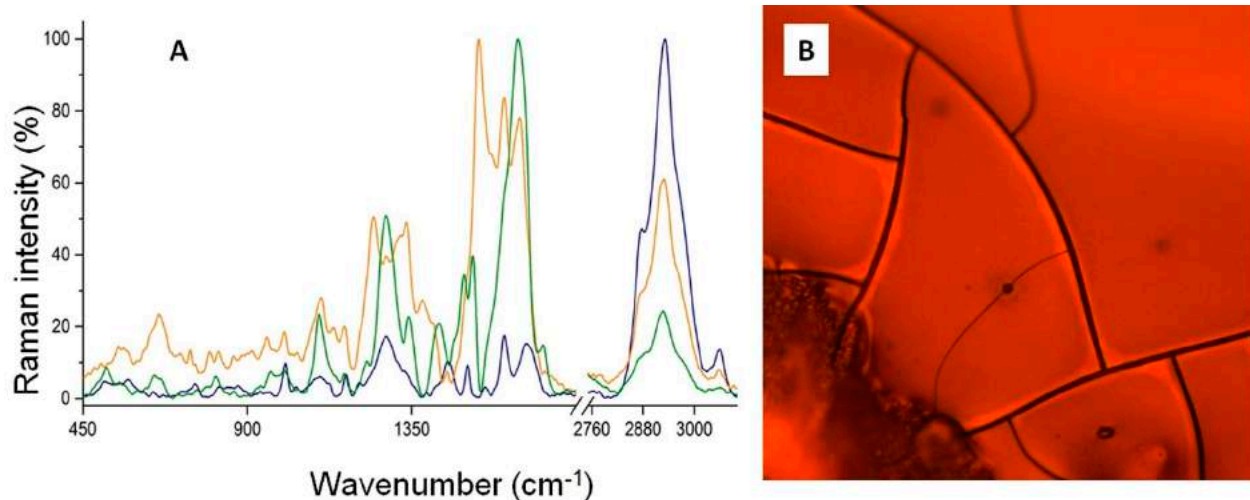
Figure 5. (**A**) Raman spectra of native bLTF (blue), AgLTF45 (green), and AgLTF450 (orange), (**B**) The picture of AgLTF1200 complex under microscope objective, where blue arrows show the places of protein degradation.

On the Raman spectrum of AgLTF45, the amide I band shifted significantly from 1664 to 1644 cm^{-1}. Conversely, the most distinctive band for ring modes of all aromatic residues shifted only to 1602 cm^{-1}, but increased significantly. Furthermore, the band with the maximum at 1532 cm^{-1} rose. The band is characterized with a wide base that occupies a range between $\approx$1480 and 1600 cm^{-1}, and thus hides other bands visible on the spectrum of native bLTF. The corresponding band can be assigned for the indole ring modes that mainly come from C$_2$=C$_3$ stretching vibrations, and is affected by the torsion angle of about C3-Cβ and Cβ-Cα [37]. The obtained data, the same as in FTIR, may indicate Ag$^+$ interaction with heteroatoms of peptide bonds. It is noteworthy to mention that Ag$^+$ can coordinate both O and N, but forms stronger bonds with the latter [9]. Thus, Ag$^+$ should preferably interact with nitrogen-containing groups. The spectrum recorded for AgLTF450 in the respective absorption range revealed even more drastic changes. The band at 1639 cm^{-1}, which was assigned to the amide I vibrations, underwent an enormous increase, so it hid the band at $\approx$1600 cm^{-1}. Moreover, on the spectrum the bands at 1513 and 1493 cm^{-1} can be distinguished, which may come from C=C of aromatic rings of tryptophan and histidine, respectively. The pioneer studies of Sidgwick in the field have revealed that a higher number of substituents in amines decreases the stability of its complexes with the metals. However, he also pointed out that pyridines and imidazole act rather as primary amines than as tertiary ones [9]. Thus, Ag$^+$ should favor the interaction with histidines and tryptophans, which may be a reason for the mentioned changes on Ag-bLTF spectra. The band of C-H deformation vibrations at 1448 cm^{-1} of native bLTF is the same for AgLTF45, but on the spectrum of AgLTF450, a much more intense band at 1426 cm^{-1} can be observed. Instead, the band at $\approx$1100 cm^{-1} has not changed its position. On the spectrum of AgLTF45, bands at 1409 and 1381 cm^{-1} have appeared. The respective band may come from the cationic form of the imidazole ring (histidine) [37], confirming its possible interaction with Ag$^+$. On the spectrum of AgLTF450, the respective bands may be overlaid by the band at 1426 cm^{-1}, and thus cannot be distinguished. The amide III band of native bLTF at 1329cm^{-1} shifted to 1336 cm^{-1} and 1342 cm^{-1} for AgLTF45 and AgLTF450, respectively. Instead, only the intensification of the band at 1280 cm^{-1} was observed. Additional bands assigned to amide III rose to 1246 and 1228 cm^{-1} for AgLTF45 and AgLTF450, respectively. The peak at 1171 cm^{-1} of native bLTF coming from tyrosine shifted to $\approx$1166 cm^{-1} after Ag$^+$ binding. It appeared that the intensity of the phenylalanine bands at 1035, 1003, and 962 cm^{-1} decreased. However, in comparison to the band of C-H stretching at 2931 cm^{-1}, no changes were observed. Interestingly, on the spectrum of AgLTF45, the intensity of the S-S bands at 561 and 520 cm^{-1} decreased, with a respective increase in the C-S band stretching at 658 cm^{-1},

which may indicate the destruction of disulfide bridges. However, on the spectrum of AgLTF450, the band intensities for both the S-S as well as C-S vibrations increased, indicating that only part of the disulfide bonds may have been ruptured. According to the literature data, Hg^+ and Ag^+ are the only metals that can readily split disulfide bridges. Moreover, only Hg^+ has a higher affinity to sulfhydryl groups than Ag^+ [9]. Thus, the obtained results are consistent with previously discovered knowledge.

2.2.4. Fluorescence Study

Fluorescence spectroscopy can be utilized to outline the nature of the protein interactions. Native bLTF revealed an emission maximum of tryptophan at λ_{em} = 335 nm, and intensity was nearly 7100 a. u. in case when excitation wavelength of λ_{ex} = 280 was utilized. After Ag^+ immobilization onto bLTF, the respective emission maximum has not changed, but the fluorescence intensity decreased twofold to ≈3800 a. u. (Figure 6).
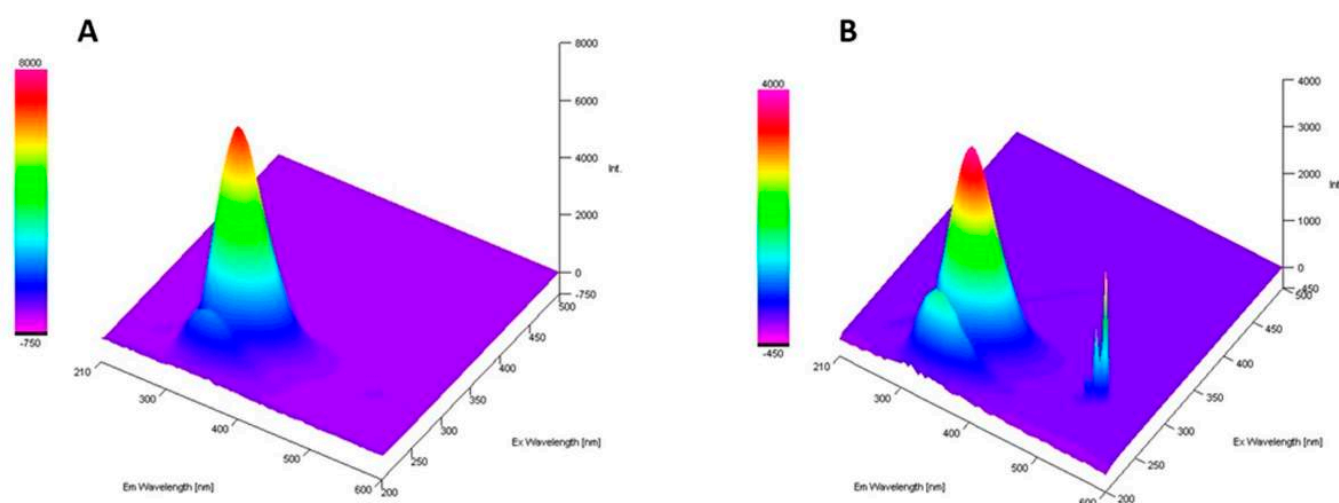
Figure 6. The 3D-spectra fluorescence of (**A**) native bLTF and (**B**) AgLTF1200 complex.

Unlike bands of other aromatic residues, the band of the tryptophan emission maximum is highly sensitive to the local environment, which enables it to be utilized for the tracking of changes in protein structure [38]. It was shown that tryptophan embedded deep into a hydrophobic pocket in native folded Azurin has $\lambda_{em} \approx 308$ nm, while fully denatured proteins have $\lambda_{em} \approx 350$ nm [39]. Thus, obtained data showed that no protein unfolding occurred and that the fluorescence quenching has a static character. The charge transfer from ligand to metal should be a reason for such drastic changes, which indicates the Ag^+ interaction with bLTF through tryptophan residues [40]. However, the additional signal also appeared at $\lambda_{ex}/\lambda_{em}$ = 270/540 with an intensity of ≈3050 a. u. The respective band should arise due to the formation of AgNPs. N. Paseban et al. investigated AgNPs synthesized with regia green-husk aqueous extract [41]. They showed that as-synthesized NPs depending on excitation wavelength had fluorescence in the range from 487 to 580 nm. The proportional increase in fluorescence from AgNPs to the decrease in tryptophan fluorescence may indicate the transfer of energy adsorbed by tryptophan to newly formed NPs. Still, it noteworthy to mention that tyrosine also adsorbs in the same region [38]. Thus, both of the mentioned residues may be involved in the protein interactions with silver.

2.2.5. Matrix-Assisted Laser Desorption/Ionization Time-of-Flight Mass Spectrometry

The MALDI-TOF-MS spectrum of native bLTF is shown on Figure 7A. The signal at ≈82.3 kDa represents the protein monomer $[M+H]^+$. The signals from the protein dimer $[2M+H]^{2+}$ at ≈164.8 kDa and multiple-charged monomer ($[M+2H]^{2+}$ 41.2 and $[M+3H]^{3+}$ 27.4 kDa) or trimer ($[3M+2H]^{2+}$ 123.8 kDa) also can be distinguished on the spectrum.

Other signals (from A to D) were assigned to protein impurities, which mainly come from the protein fragmentation during storage or production [22].
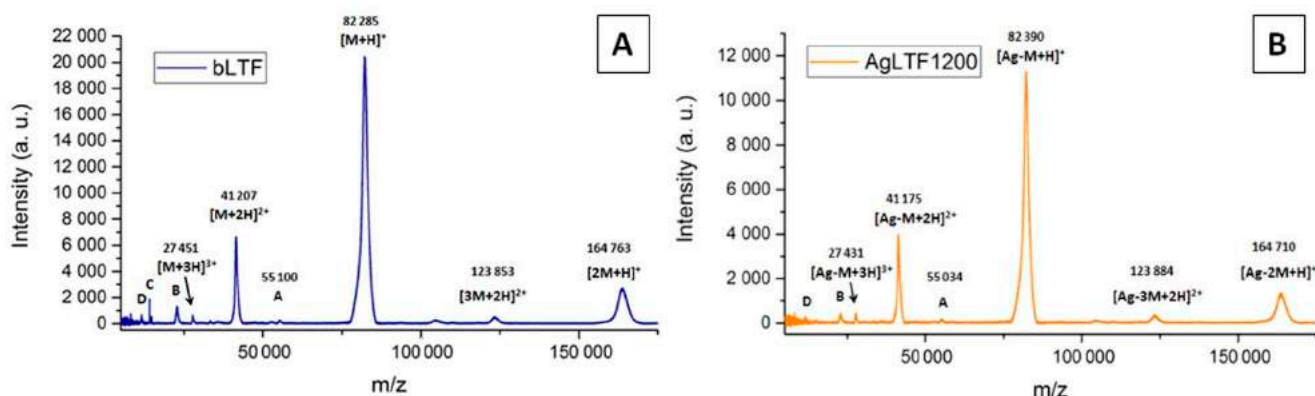

Figure 7. MALDI-TOF MS spectra of (**A**) native bLTF and (**B**) Fe-bLTF complex.

After silver immobilization onto bLTF, the decrease in all signals' intensity can be observed. The signal-intensity decrease is connected to their suppression by unbonded or loosely bonded Ag^+. Some signals of impurities even become almost undistinguishable. To other effects, the signal shifts to higher *m/z* values can be noticed indicating the formation of silver adducts with protein. Moreover, some signals have shifted to lower *m/z* values, which may be connected to protein oxidation.

2.2.6. SDS-PAGE Analysis

The SDS-PAGE analysis (Figure 8) showed that in both nonreduced and reduced modes, the electrophoretic velocity of AgLTF1200 was slightly higher in comparison to native bLTF. Similar was detected for iron-saturated bLTF in comparison to apo-form. L. Voswinkel et al. investigated the holo-, apo-, and native (partially saturated) forms of bLTF with PAGE-IEF, and they were able to differentiate all of them by comparison of protein-band position [42]. The effect may be connected to the formation of a more compact structure of the protein after Ag^+ binding. It also explains the differences in protein-band position on the SDS-PAGE performed in reduced and nonreduced modes [43]. However, it is noteworthy to mention that protein reduction with DTT causes the breaking of disulfide bonds and loss of the globular structure. In consequence, no differences in electrophoretic velocity should be observed. Thus, the detected changes may be connected with the influence of the formed AgNPs on the electromigration behavior of synthesized nanocomposite. Interestingly, the study of Zn^{2+} binding to bLTF has revealed the opposite effect, namely that the protein bands appeared slightly higher after metal adsorption [22]. The highest protein-band position was observed for the Zn-LTF complex with the highest Zn^{2+} content. This can be explained by the much lower strength of zinc interaction with bLTF in comparison to silver or iron. Hence, the Zn^{2+} released during the analysis affected the separation process.
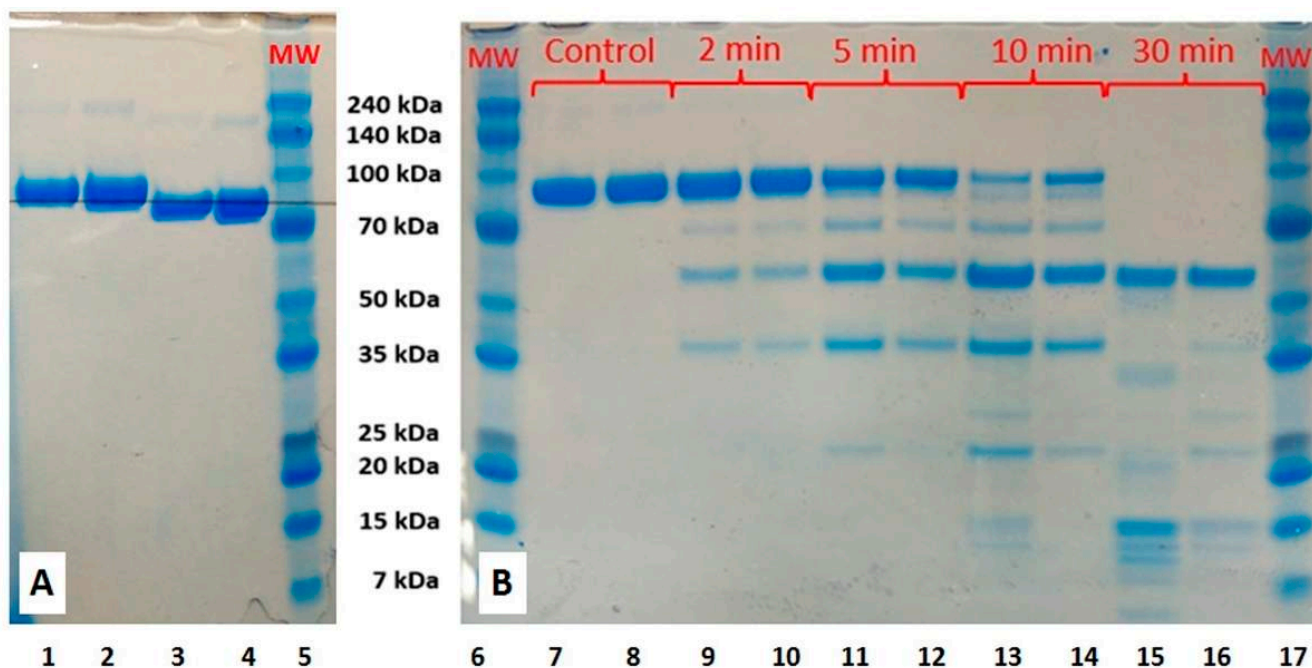
Figure 8. SDS-PAGE of (**A**) bLTF and AgbLTF1200 in reduced (1,2) and nonreduced mode (3,4), and (**B**) the peptic digestion kinetics, where bLTF is presented on 1,3,7,9,11,13,15, AgLTF1200 complex on 1,3,8,10,12,14,16, and markers on 5, 6, 17.

2.2.7. Analysis by Capillary Electrophoresis Coupled with ICP-MS

The capillary electrophoresis (CE) coupled online with ICP-MS was employed to more precisely describe the nature of silver-ion binding by bLTF. Previous research indicated that this approach enables analysis of metal–protein complexes [44]. Figure 9 summarizes the obtained electropherograms for bLTF before and after modification with different initial silver-ion concentrations.
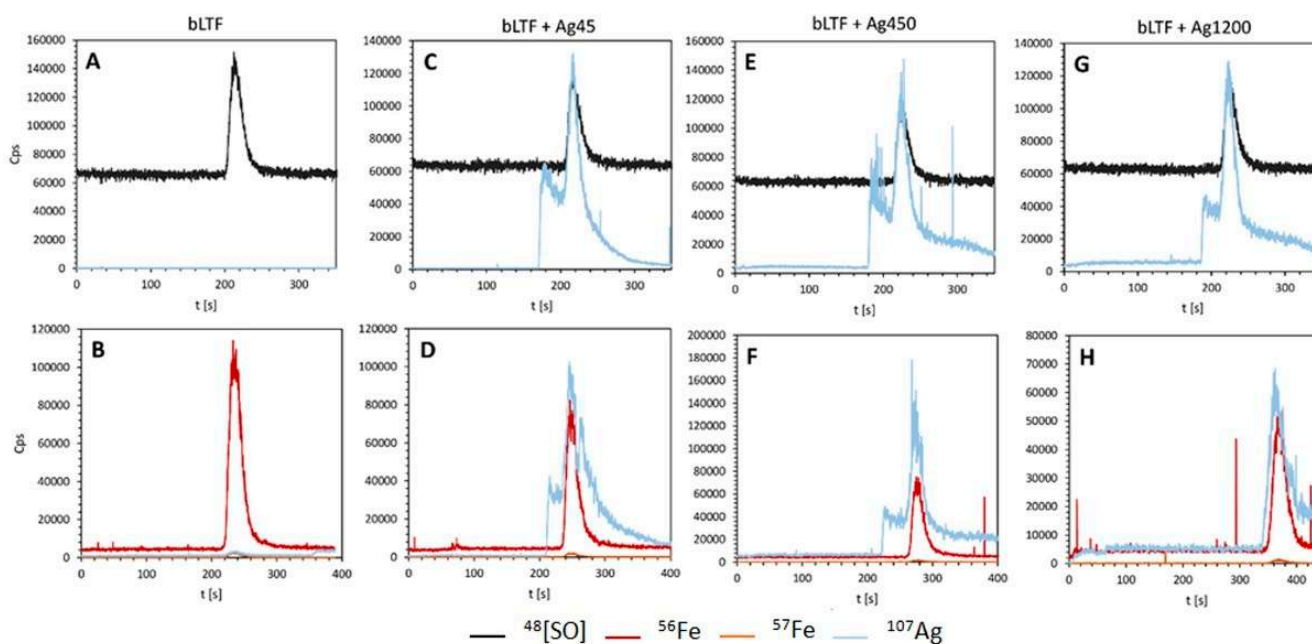

Figure 9. Electropherograms obtained using CE-ICP MS system for native bLTF (**A,B**) and AgLTF45 (**C,D**), AgLTF450 (**E,F**), and AgLTF1200 (**G,H**), after applying as a DRC gas oxygen (**A,C,E,G**) or ammonia (**B,D,F,H**).

It was shown that native bLTF does not contain silver. On the other hand, the presence of silver signals on electropherograms for Ag-bLTF complexes confirmed the effective performance of the immobilization process. Moreover, two signals from silver were noted. The first one probably corresponds to unbound or weakly bound silver ions. The second one, occurring at the same retention time as a signal from sulfur oxide (protein) and iron bound with bLTF, can be attributed to silver ions strongly bound with protein. Again, the results are complementary to the isotherm study. The silver in the form of AgNPs is probably strongly bonded to the protein and should correspond to alculated from the Langmuir isotherm. In turn, the loosely bonded silver represents the excess adsorption. The respective silver probably bonded with bLTF through weak electrostatic interactions. However, the free Ag^+ can also appear as a result of applied current. K. Wonner et al. investigated the oxidative dissolution of single AgNPs during the linear-sweep voltammetry [45]. The dissolution of the AgNPs has already appeared under the current below 1.5 V. Finally, it is noteworthy to mention that the presence of the unchanged signal from iron suggests that the silver ions' sorption did not affect ability of the protein to bind to iron. Moreover, as it was shown previously, even the highest Ag^+ concentration did not cause significant Fe^{3+} elimination from bLTF (the reaction was performed in acidic conditions pH = 5). Instead, when bLTF was incubated with Zn^{2+}, the loss in Fe^{3+}—depending on the utilized conditions—could reach 45% [22].

2.2.8. Ag^+ Desorption Study

Silver desorption was performed in three different buffers that imitate conditions in different parts of the digestive tract. The choice of the utilized buffers was performed taking into account the "Dissolution test for solid dosage form" standardized by European pharmacopoeia (EP). However, normally in order to provide appropriate conditions, the 0.1 M hydrochloric solution and phosphate buffers are utilized. Unfortunately, chloride and phosphate ions form insoluble salts with silver. Thus, we selected the MOPS buffer for pH 6.8 based on L. Babel et al.'s work [46], acetate buffer pH 4.5 recommended by EP as alternative to phosphate, and HNO_3 solution pH 1.2. After 2 hours of the desorption process, the released silver was quantified by ICP-MS. The desorption was calculated as 80.5, 64.3, and 72.2% at pH 1.2, 4.5, and 6.8, respectively, with actual silver concentrations in the filtrate of 1.89, 1.51, and 1.70 ppm. One of the mechanisms of silver NPs and nanocomposites' cytotoxicity is attributed to the possibility of Ag^+ release. It is extensively discussed in literature and acquired the name "Trojan horse" mechanism [4]. Thus, numerous studies have been performed to evaluate the influence of different conditions on the Ag^+ release. Among the factors that have the impact on the process are the presence of oxygen, light irradiation, temperature, and pH. For instance, Kosa et al.'s work shows that at basic pH 10.0 the dissolution was almost absent (0.8×10^{-4} s^{-1}), while at neutral and acidic pH of 7.0 and 4.0 it was fast and differed only on a few tenths of a unit (2.5 and 1.8 s^{-1}, respectively) [47]. The presence of the different ligands in the solution should also have an impact on the dissolution rate, which explains the higher desorption at pH 6.8 in comparison to pH 4.5. Taking into account the assumption of the mentioned theory, the high Ag^+ desorption rate from the obtained complex could raise anxiety about safety of the synthesized complexes. However, according to the work presented in Hadrup et al., the orally administrated silver in 90–98% undergoes fecal excretion depending on the species. [48]. Still, it was shown that negative toxic effects can be observed for cells exposed to Ag^+ concentration of even 0.5 ppm [49].

2.3. The Study of Complex Biological Activity

2.3.1. Assessment of the Impact of Ag^+ Binding to bLTF on Its Susceptibility to Peptic Degradation

To complement the Ag^+ desorption study, an assessment of the AgbLTF1200 complex's susceptibility to pepsin digestion was performed. The peptides, compared to proteins, are more effectively absorbed in the gastrointestinal tract [50]. Thus, the efficiency of

nanocomposite digestion should provide additional information about its safety. Figure 8B shows the SDS-PAGE analysis that represents the kinetic study of bLTF peptic digestion. After 5 and 10 min of digestion, for native bLTF compared to AgLTF1200 the appearance of a higher amount of peptides in a mass range between 35 and 70 kDa can be observed. Instead, the band corresponding to intact protein decreased slightly faster in the case of native bLTF. The results may be connected with the Ag^+ release from the nanocomposite. Previous studies showed that Ag^+ released from nanocomposites, with its subsequent binding to proteins, in particular enzymes, disturbs their function [4]. Thus, it can be attributed to one of the possible mechanisms of silver nanocomposites' cytotoxic and antibacterial properties. However, our study showed that changes in the peptic digestion process are much more complex than it may seem on first sight. In case, when protein was subjected for digestion during 10 and 30 min, the decrease in bigger peptides occurred much faster in the case of AgbLTF1200. This fact may indicate that Ag^+ binding to bLTF induces changes in the protein structure, which makes the cleavage of places more accessible for enzymes [51]. In general, the Ag^+ binding to protein almost did not influence the pepsin activity, while changes in structure even sped up the digestion process.

2.3.2. Determination of Minimum Inhibitory Concentration

Diabetic foot infection (DFI) is the most common compilation of diabetes, which is strictly connected with the formation of chronic wounds. Lately, DFI has become an issue of a global range and has magnified significantly as the population of diabetes has increased. Thus, we decided to evaluate the antibacterial properties of the synthesized complex against the three most common bacterial strains isolated from DFI wounds [52]: two Gram-positive *S. aureus* and *E. faecalis,* and one Gram-negative *P. aeruginosa.* Moreover, it was shown that topical application of lactic-acid bacteria (LAB) can improve wound healing, which encouraged us to examine the toxic effect of AgbLTF1200 onto two of them, namely *L. lactis* and *L. paracasei* isolated from fermented vegetables.

All of the as-mentioned bacteria were identified with utilization of the MALDI-TOF-MS technique based on the Raw spectra. The identification was performed according to the standard protocol supplied by the equipment and software producer (Bruker Daltonics, Bremen, Germany), i.e., by the analysis of bacterial-protein extracts obtained with the use of 70% formic acid. The bacteria were identified with a high confidence level, Score Value $\geq$1.999, i.e., *S. aureus* 2.380; *E. faecalis* 2.420; *P. aeruginosa* 2.160; *L. lactis* 2.280; *L. paracasei* 2.220. Figure 10 shows the phyloproteomic relationships of the identified bacteria. The most closely related strains identified by MALDI Biotyper Compass platform are also included.

Despite multiple reports about antibacterial properties of lactoferrins [15,17,19,20], in our investigations the studied bacteria did not show susceptibility to bLTF with concentration up to 5 mg/mL. In previous studies of our group, bLTF also did not show antibacterial activity against *S. aureus* and *E. faecalis* from ATCC collection, but slight inhibition of *P. aeruginosa* ATCC 27853 was revealed [10]. Still, only 75.7% inhibition of *P. aeruginosa* ATCC 27853 growth was observed when bLTF in concentration of 50 μg/mL was utilized. The lower antibacterial activity of bLTF observed in the present study may be connected with its iron saturation, namely the holo-bLTF that was utilized. Instead, the saturation level was not examined in 2016. In turn, for all pathogenic bacteria, an MIC value of Ag^+ was established at 80 μg/mL, while for LAB it was 40 μg/mL. The combination of silver with bLTF significantly increased the antibacterial activity of the AgbLTF1200 in comparison to both bLTF and Ag^+. The MIC value of AgbLTF1200 for *S. aureus* and *E. faecalis* was determined as 1.25 mg/L and 0.625 mg/L for the rest of the tested bacteria, which was 5.0 and 2.5 μg/L of Ag^+, respectively. The lower MIC values could be due to the formation of AgNPs during the reaction of Ag^+ with bLTF. It was shown that AgNPs revealed higher toxicity against both eucaryotic and procaryotic cells [4]. Moreover, bLTF can promote Ag^+'s entrance inside the bacterial cells, thus showing the synergistic effect of antibacterial action. In P. Pomastowski et al.'s work, the antibacterial properties of the synthesized Ag-bLTF complex were much higher. The growth of some bacteria was completely inhibited

with the Ag-bLTF concentration of 0.05 mg/mL. This could be connected to the preparation procedure, which did not include the washing steps; thus, a higher amount of silver should remain in the complex [10]. Interestingly, the combination of bLTF with other d-metals can lead to the formation of complexes that promote the growth of the LAB [53]. It was reported previously that bLTF itself can promote LAB growth [19]. However, K. Śpiewak et al. showed in their work that only high bLTF concentration in both apo- and holo-form (e.g., 40 mg/mL) slightly influenced the growth of *L. plantarum*. Instead, Mn_2-bLTF even in concentration of 0.6 mg/mL promoted their growth.
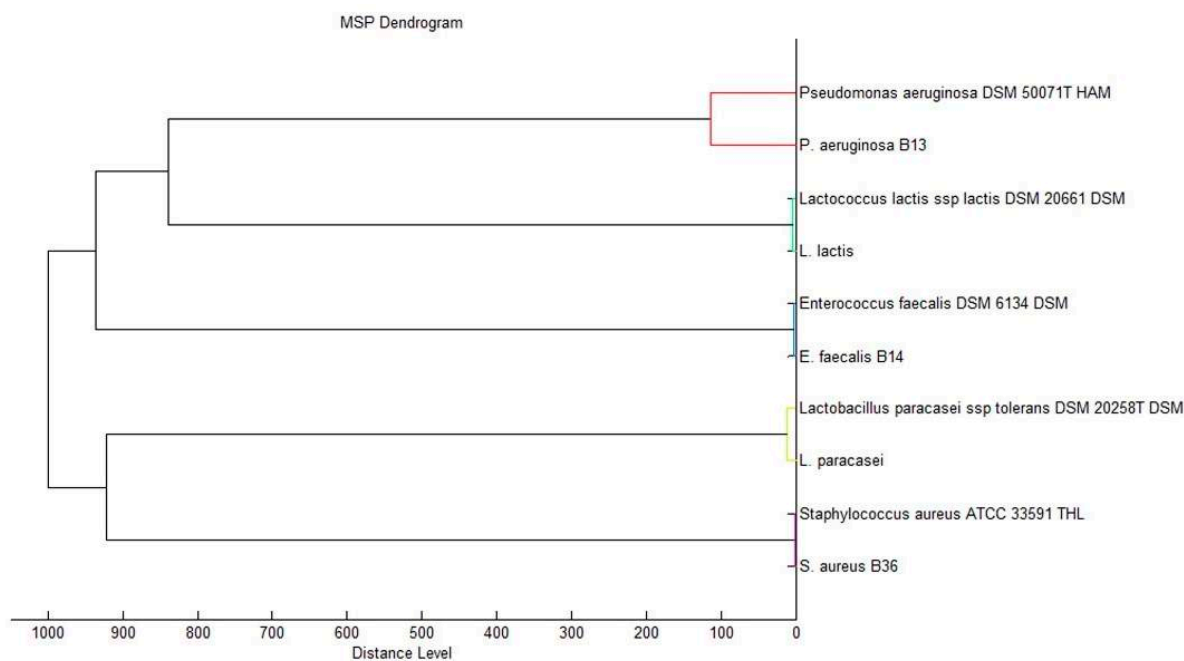
Figure 10. Phyloproteomic tree of the isolated bacterial strains, identified by MALDI Biotyper Compass platform.

2.3.3. Cytotoxicity Study

Cytotoxicity of AgbLTF1200 was determined by the MTT method on the L929 mouse fibroblast cell line. This cell line is usually used for testing the biocompatibility of new materials according to ISO 10993-5 and ISO 10993-12 norm. In our experiment, both AgbLTF1200 and Ag^+ were utilized. The concentration of the complex was in the range from 0.08 mg to 10 mg/mL, which corresponds to the Ag^+ concentration from 0.32 to 40 µg/mL, respectively. The results are presented in Figure 11.

When a complex with a concentration above 0.16 mg/mL (Ag^+ 0.64 µg/mL) was utilized, the cell viability significantly decreased to below 20% (Figure 11A). The same was observed for the Ag^+ solution of respective concentration. At a complex concentration of 0.08 mg/mL, cell viability for AgbLTF1200 was about 40%, whereas for the corresponding Ag^+, concentration was two times higher. This may suggest that bLTF and silver act synergistically and that lactoferrin may promote Ag^+ entry into cells. The results are complementary to the results of antimicrobial activity, where AgLTF1200 had much lower MIC in comparison to Ag^+ silver. Pure bLTF did not display cytotoxicity in the range from 0.08 to 5 mg/mL. Only the highest tested concentration, i.e., 10 mg/mL, caused a decrease in cell viability to about 40%. In the sample treated with AgbLTF1200 (10 mg/mL), there were significantly fewer cells compared to the control, but most of them still adhered to the substrate (Figure 11B). Only single ones changed the shape to the rounded. In samples treated with Ag^+, all cells showed a balloon-like cell shape and expanding cytosol, indicating the activation of the apoptosis process. Evidently, the AgLTF1200 complex has

a different mechanism of action, which may change the processes that take part in cell division, but does not activate the apoptosis.
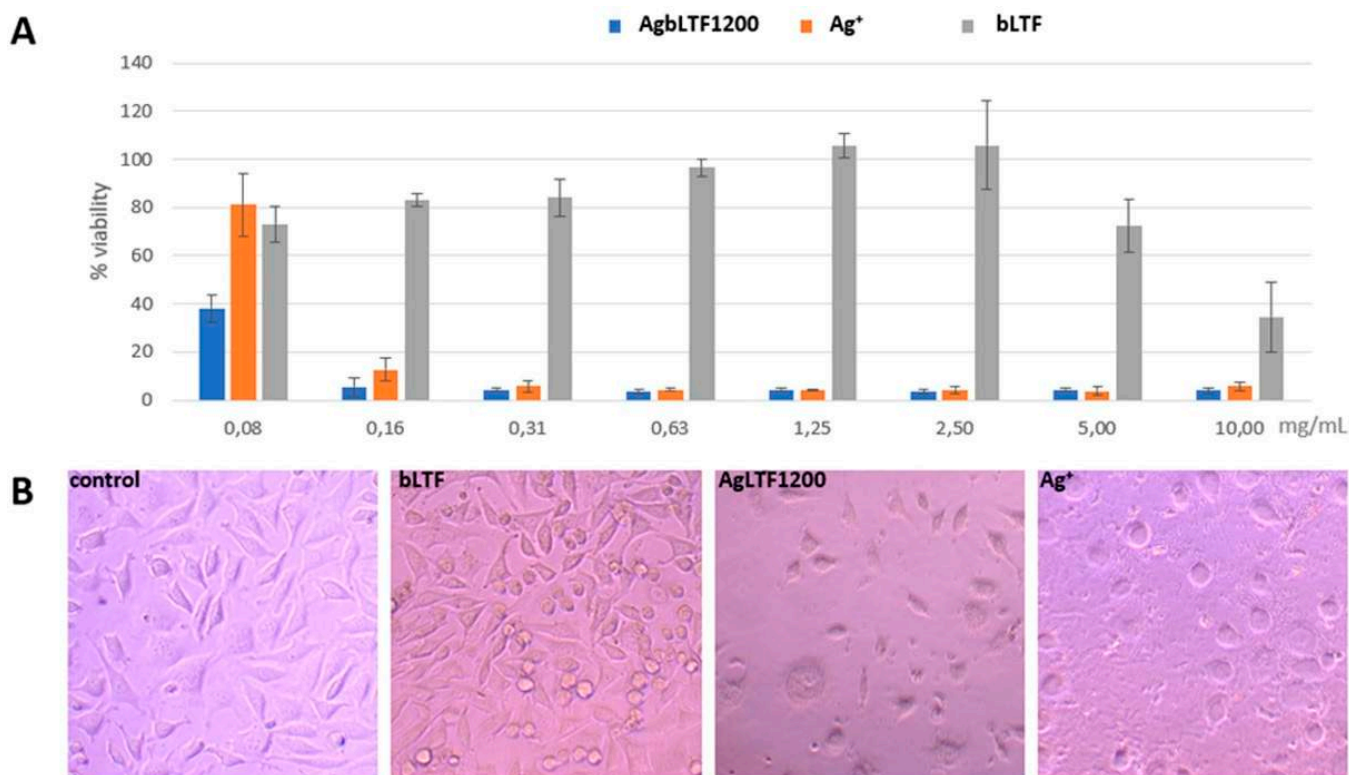

Figure 11. (**A**) Represents cell viability measured by MTT assay. Histograms show the percentage, with respect to control cells (100%), of viable cells after exposure to AgLTF1200, Ag$^+$ and bLTF. Data show the mean $\pm$ SE (n = 5); (**B**) Morphology of L929 control cells and after exposure to bLTF, AgLTF1200, and Ag$^+$.

3. Materials and Methods

3.1. Chemicals and Materials

Sigma-Aldrich (Steinheim, Germany) supplied the following chemicals and materials: lactoferrin from bovine milk (bLTF), ammonium iron (III) citrate, sodium chloride, sodium hydroxide, MS-grade nitric acid, hydrochloric acid, Amicon® Ultra Centrifugal membrane filters, ICP multi-element standard solution IV and scandium standard solution for ICP, trypsin, fetal bovine serum (FBS), Dulbecco's Modified Eagle's Medium (DMEM), phosphate-buffered saline (PBS), EDTA, penicillin-streptomycin solution, L929 normal mouse fibroblast cells and Caco-2 cells, MTT assay kit, and LDH release assay kit. Invitrogen Bolt™ 4–12% Bis-Tris Plus polyacrylamide gel 12 wells, Simply Blue™ Safe Stain (Coomassie G$_{250}$ stain), 20X MES SDS Running Buffer, load sample buffer, sample reducing agent, and borosilicate microscope slides were obtained from ThermoFisher Scientific (Waltham, MA, USA). Perfect™ Color Protein Ladder was from EUR$_X$ Sp. z o.o. (Gdansk, Poland). Set of automatic pipettes and laboratory plastics were obtained from Eppendorf (Hamburg, Germany). Moreover, deionized water was obtained with Milli-Q RG system from Millipore (Millipore Intertech, Bedford, MA, USA).

3.2. Batch-Sorption Analysis

3.2.1. Preparation of Solutions for the Batch-Sorption Study and Complex Synthesis

All Ag$^+$ solutions were prepared in deionized water with no additional modifications. The exact Ag$^+$ concentration in the solutions was quantified by ICP-MS analysis. Here and in all other analyses, metal quantification was performed on Shimadzu ICP-MS 2030 (Kyoto,

Japan) with scandium (^{45}Sc) as an internal standard. The quantification was performed taking into account the ^{107}Ag isotope. The 1% HNO$_3$ was utilized for the dilution. Instead, the bLTF suspension was prepared in deionized water with concentration of 5 mg/mL (by weight) and adjusted to pH 5.0. The pH adjustment was performed with 1% HNO$_3$ or 0.1 NaOH. For the study, bLTF standard purchased from Sigma-Aldrich (Steinheim, Germany) was utilized. Before the study, the physicochemical characterization of the bLTF was performed; among others, the iron content was determined. According to obtained data, the utilized bLTF was in holo-form. The results are presented in the article by O. Pryshchepa et al. (2022) [22]. The bLTF from the same batch was utilized in both studies.

3.2.2. Isotherm Study of Ag$^+$ Adsorption

Study was performed with utilization of Ag$^+$ solutions with concentration of 6, 15, 30, 45, 60, 120, 300, 450, 600, 900, and 1200 mg/L. bLTF suspension was mixed with Ag$^+$ solution (1:1 ratio) in black polypropylene microcentrifuge tubes. The samples were incubated for 24 h at room temperature ($\approx$23 °C). Subsequently, the mixtures were filtrated through Amicon® Ultra Centrifugal Filters cut-off 3 kDa at room temperature. The parameters for centrifugation were as follows: room temperature, 20,000× g, 5 min. The filtrate was subjected to quantification of Ag$^+$, which remained in the solution by ICP-MS. Instead, the retentate containing the synthesized AgLTF complexes was washed twice with deionized water, collected to Eppendorf tubes, and lyophilized for subsequent analyses. The respective complexes were encoded as AgLTF6-AgLTF1200 depending on the amount of silver that was utilized for the synthesis.

The Ag$^+$ adsorption onto protein was calculated accordingly:

$$q_e = \frac{(C_0 - C_e) \times V}{m} \tag{1}$$

where q_e is the Ag$^+$ adsorption on protein, m is the mass of the bLTF in the reaction mixture (g), C_0 and C_e are the initial and equilibrium concentration of Ag$^+$ in the reaction mixture (mg/L), and V is the volume of the reaction mixture (L).

The sorption efficiency (E) was calculated and expressed in % according to:

$$E = \frac{100 \cdot (C_0 - C_e)}{C_0} \tag{2}$$

The changes in the Gibbs free energy were calculated as follows [10,24]:

$$\Delta G = -RT\ lnK_D \tag{3}$$

where ΔG is the free energy change in kJ/mol (the adsorption energy), R is the gas constant (8.314 J/mol·K), T is the reaction absolute temperature in Kelvin (295 K), and K_D is the distribution coefficient.

The K$_D$ coefficient expresses the affinity of metal to the protein and can be calculated according to the equation:

$$K_D = q_e/C_e \tag{4}$$

where q_e is the amount of Ag$^+$ adsorbed onto bLTF (mg/g) and C_e is the equilibrium concentration of Ag$^+$ in solution (mg/L).

The modeling of the adsorption data was performed with utilization of Freundlich and Langmuir isotherms and isotherm as function of C_e/C_0 [11].

3.3. Physicochemical Characterization of Synthesized Complexes

3.3.1. Electron Microscopy Studies

The investigations were conducted with scanning electron microscope (SEM) capable of imaging in scanning transmission electron microscopy (STEM) mode, model Hitachi S5500 equipped with EDX system. Observations were performed under accelerating

voltage of 30.0 kV in transmission and surface mode. Samples were prepared by dispersion in deionized water. Droplets of the solution were deposited onto carbon-coated copper TEM grids (Lacey Carbon Support Film 400 mesh; Electron Microscopy Sciences) and dried on air at room temperature. STEM and SEM observations were performed using secondary electron (SE) detector and STEM detector. X-ray mode in DF (dark field) phase contrast and BF (bright field) contrast were used. Moreover, as-prepared samples of AgLTF45, AgLTF450, and AgLTF1200 were subjected to TEM-SAED. The analysis was performed on FEI Tecnai F20 X-Twin (Hillsboro, OR, USA).

3.3.2. Fourier Transform Infrared Spectroscopy (FTIR)

FTIR analysis of the synthesized complexes and native bLTF was carried out in the MIR range (4000–400 cm^{-1}) with utilization of attenuated total reflection (ATR) mode on Alpha FTIR spectrometer (Bruker, Billerica, MA, USA). Normalized FTIR spectra were plotted using the Origin software (v. 2015, OriginLab Corporation, Northampton, MA, USA) followed by normalization operation.

3.3.3. RAMAN Spectroscopy

The RAMAN spectra were recorded on SENTERRA II Dispersive Raman Microscope (Bruker, Billerica, MA, USA) in the MIR range and excitation wavelength at λ = 532 nm. Raman spectra were processed (normalization/baseline correction) and plotted using the Origin software (v. 2015, OriginLab Corporation, Northampton, MA, USA).

3.3.4. Fluorescence-Spectroscopy Analysis

The solutions of bLTF and AgLTF1200 complex with concentration of 0.25 mg/mL were prepared in deionized water. The 3-D fluorescence spectra were obtained with utilization of Jasco FP-8300 spectrofluorometer (JASCO, Easton, MD, USA) in the excitation range λ = 200–735 nm and emission range λ = 210–750 nm.

3.3.5. Matrix-Assisted Laser Desorption/Ionization—Time-of-Flight Mass Spectrometry (MALDI-TOF-MS)

Sinapinic acid (SA) was utilized as a matrix for MALDI analysis. Intact protein and AgLTF1200 complex were suspended in 0.1% trifluoroacetic acid to concentration of ≈1 mg/mL. The saturated solution of SA was prepared in the TA30 solvent (30:70 [*v/v*] acetonitrile: 0.1% trifluoroacetic acid). A total of 1 μL of the samples were applied on GroundSteeltarget plate by dried-droplet technique and overlaid with 1 μL of the matrix solution. Protein-calibration standard II was used for mass calibration. All the MS spectra were obtained using the MALDI-TOF/TOF mass spectrometer UltrafleXtreme (Bruker Daltonics, Bremen, Germany) equipped with modified neodymium-doped yttrium aluminum garnet (Nd:YAG) laser operating at the wavelength of 355 nm and frequency of 2 kHz. The system was controlled using the Bruker Daltonics software (flexControl and flexAnalysis). MS spectra were obtained in the linear positive mode in an *m/z* range of 5000−200,000, applying an acceleration voltage of 25 kV. Spectra were acquired by summing up three individual spectra obtained with 500 laser shots each and were plotted using the Origin software (v. 2015, OriginLab Corporation, Northampton, MA, USA) from raw data without any modifications.

3.3.6. Ag$^+$ Desorption Study

Silver desorption tests for AgLTF1200 were performed in three buffers, namely in HNO$_3$ solution pH 1.2, acetic buffer pH 4.5 [54] and 0.1 M MOPS buffer pH 6.8, which imitates acid-base conditions in different parts of the digestive tract. The AgLTF1200 suspension with concentration of 10 mg/mL was prepared in deionized water. Next, 50 μL of the suspension (≈0.5 mg of the complex) was transferred to the Eppendorf tubes and mixed with 200 μL of buffers. The mixtures were incubated for 2 h at 37 °C. Subsequently,

mixtures were filtrated with Amicon® Ultra Centrifugal Filters cut-off 3 kDa. Finally, the Ag^+ content in the filtrate was determined.

At the same time, the silver and iron content in the complex was determined. For the complex mineralization, 50 µL of suspension ($\approx$0.5 mg of AgLTF1200) was transferred to Eppendorf tubes and mixed with 0.2 mL of MS-Grade nitric acid. Next, tubes were closed tightly and heated at 80 °C for 3 h. Then, the obtained samples were diluted with deionized water and subjected to ICP-MS analysis.

3.3.7. SDS-PAGE Analysis

The samples with concentrations of $\approx$0.5 mg/mL were prepared in deionized water. Next, the protein solutions were analyzed with utilization of 4–12% Bis-Tris Plus polyacrylamide gel (Thermo Scientific, Waltham, MA, USA) in reduced and nonreduced mode, and 1X MES Running Buffer (0.05M MES, 0.05 M Tris, 1 mM EDTA and 0.1% SDS, pH—7.3) was applied according to the standard procedure recommended by manufacturer. Gel staining was performed with Coomassie Blue R-350 ready-to-use stain.

3.3.8. Analysis by Capillary Electrophoresis Coupled with ICP-MS

For the capillary electrophoresis separation, the lyophilized powder of protein and complex were suspended separately in borate buffer (30.183 g of Na-Borat in 0.5 L of water; pH = 7.8) to final concentration of 1 mg/mL. The separation was performed in noncoated fused silica capillary (90 cm × 75 µm ID) with usage of PrinCe 760 capillary electrophoresis (CE) system (Prince Technologies B.V.). Each analysis was preceded by rinsing the capillary sequentially for 1 min with: 0.1 M NaOH, Milli-Q water and borate running buffer. The applied pressure during the sample injection was 250 mbar for 20 s. The CE separation was performed using +20 kV voltage and 250 mbar pressure.

The CE-capillary was connected to the NexIon 300D ICP-mass spectrometer (Perkin Elmer) using an inhouse interface [55]. This setup enabled element-selective electropherograms to be directly monitored on-line by ICP-MS using dynamic reaction cell (DRC) mode at isotopes ^{48}[SO], ^{56}Fe, ^{57}Fe, and ^{107}Ag. For each sample, analysis was performed using two types of DRC gas. For detection of iron isotopes, the DRC gas was ammonia (0.6 mL/min, RPq = 0.45) and for detection of sulfur as ^{48}[SO] oxygen was used. Both DRC gases allowed detection of silver isotopes. The RF power was 1250 W and plasma gas was set at 16 L Ar/min. Nebulizer gas flow rate was established at 0.98 Ar/min.

3.4. The Study of Complex Biological Activity

The assessment of biological activity was performed for AgLTF complex synthesized with utilization of Ag^+ solution of 1200 mg/L (AgbLTF1200).

3.4.1. Evaluation of the Impact of Ag^+ Binding to bLTF on Its Susceptibility to Peptic Degradation

The analysis was performed in simulated gastric fluid free of pepsin according to adjusted protocol from R. Wang et al. [50] The media was prepared as follows: 2.0 g of sodium chloride was mixed with 80 mL of 1 M hydrochloric acid and diluted to 1000 mL. The pepsin stock solution with the concentration of 2000 U/mL was prepared in deionized water considering the enzyme activity declared by supplier in certificate of analysis. Subsequent enzyme dilutions were performed with simulated gastric fluid to obtain the solution with concentration of 5 U/mL. The native bLTF and Ag-bLTF complex was suspended in deionized water to concentration of 5 mg/mL. Next, the mixture with enzyme-to-substrate ratio of 0.1 U:100 µg was prepared in reaction media, where the protein's final concentration was 1 mg/mL. The mixture was incubated at 37 °C for 2, 5, 10, and 30 min. The reaction was terminated by addition of 0.7 M Na_2CO_3 at 35% of the reaction volume, namely 35 µL of solution being added to 100 µL of reaction mixture. The control samples were treated in the same manner with the incubation time of 30 min, but with the addition of appropriate

amount of buffer instead of pepsin solution. Next, all prepared samples were diluted twice and subjected to SDS-PAGE analysis in reduced mode.

3.4.2. Determination of Minimum Inhibitory Concentration (MIC)

MIC was determined by broth microdilution method with the use of 96-well plates and Mueller–Hinton broth (MHB) as a culture medium. The antibacterial agent solutions were prepared in MHB by serial dilution method. The Ag^+ solutions with concentration of 1.25, 2.5, 5.0, 10.0, 20.0, 40.0, 80.0, and 160 µg/mL were tested. For bLTF and AgLTF1200, the solutions with concentration of $\approx$ 0.31, 0.62, 1.25, 2.5, 5.0, and 10.0 mg/mL were prepared. The MIC determination was on the microorganisms from deposit of Centre for Modern Interdisciplinary Technologies Nicolaus Copernicus University in Torun, performed for three pathogenic bacterial strains isolated from diabetic foot wounds *S. aureginosa*, *S. aureus*, and *E. fecalis* (permission of Ethic Committee of NCU in Toruń KB 68/20019) and two probiotic bacteria isolated from fermented vegetables *L. lactis* and *L. paracasei*. A 24 h bacterial culture was diluted to the concentration of 0.5 McFarland, which was further diluted 100-fold. The prepared bacterial suspension was mixed with antibacterial agent solutions at a ratio of 1:1. The negative control and positive control were also performed. The incubation was carried out at 37 °C for 24 h with mixing. The detection was performed based on the fluorescence measurements with utilization of microplate reader (Multiskan, ThermoFisher) and in vitro Toxicology Assay Kit, resazurin-based (Sigma-Aldrich) according to protocol provided by kit supplier.

3.4.3. Cytotoxicity Study

L929 cell line of mouse fibroblasts from European Collection of Authenticated Cell Cultures operated by Public Health England (Sigma) were cultured in DMEM supplemented with 10% (*v/v*) fetal bovine serum, 2 mM glutamine, and 100 U/mL penicillin, and 100 µg/mL streptomycin (Sigma). These cell lines were cultured in 75 cm^2 flasks at 37 °C and 5% CO^2. The cells were harvested by trypsinization using 0.25% trypsin/EDTA every 3–4 days.

For MTT assays, cells were cultured on 96-well plates at density 2×10^5 cells/mL and incubated for 24 h. Then, the medium was replaced with a new one containing Ag^+ of the appropriate concentration and incubated for 24 h. Then, 10% (*v/v*) of Thiazolyl Blue Tetrazolium Bromide (MTT) solution (5 mg/mL in PBS) was added and incubated for 4 hours at 37 °C. Next, the medium from wells was removed and the formazan crystals were dissolved in DMSO for 10 min by mixing. Absorbance was measured using a microplate reader (Multiskan, ThermoFisher) at 570 nm and 650 nm as background absorbance.

4. Conclusions

In conclusion, we have investigated the sorption process of Ag^+ onto bLTF based on the batch isotherm study. The results indicate that the approach can be utilized for the prediction of the metal–protein complexes' features. Based on isotherm results, selected AgbLTF complexes were subjected to multi-instrumental analysis. The electron microscopy revealed the formation of nanoparticles. However, the capillary electrophoresis results also indicate that part of the Ag^+ should remain in ionic form and bond with protein through weak interaction forces. The spectroscopic techniques enabled us to predict places of silver binding to protein, e.g., amino acids such as tryptophan or methionine, but also nitrogen of peptide bonds and other heteroatoms. Finally, the biological activity of AgbLTF1200 was estimated. The results revealed that the combination of bLTF with silver has a synergistic effect. Thus, the obtained complex has higher toxicity against both the procaryotic and eucaryotic cells. Moreover, the changes in morphology of L929 mouse fibroblast indicates that the mechanism of its biological activity differs from the toxic mechanisms of Ag^+ itself, which requires additional studies. Still, the obtained complex has a promising application as an antibacterial agent in the treatment of chronic wounds; among others, the wounds accompanying the diabetic foot infections. However, it requires extended studies with

utilization of animal models, e.g., murine or porcine skin models, to evaluate the possible benefits and risks of the obtained product.

References

1. Singh, S.R.; Krishnamurthy, N.B.; Mathew, B.B. A Review on Recent Diseases Caused by Microbes. *J. Appl. Environ. Microbiol.* **2014**, *2*, 106–115.
2. Kapp, S.; Miller, C.; Santamaria, N. The Quality of Life of People Who Have Chronic Wounds and Who Self-Treat. *J. Clin. Nurs.* **2018**, *27*, 182–192. [CrossRef] [PubMed]
3. Dizaj, S.M.; Lotfipour, F.; Barzegar-Jalali, M.; Zarrintan, M.H.; Adibkia, K. Antimicrobial Activity of the Metals and Metal Oxide Nanoparticles. *Mater. Sci. Eng. C* **2014**, *44*, 278–284. [CrossRef] [PubMed]
4. Pryshchepa, O.; Pomastowski, P.; Buszewski, B. Silver Nanoparticles: Synthesis, Investigation Techniques, and Properties. *Adv. Colloid Interface Sci.* **2020**, *284*, 102246. [CrossRef]
5. Krol, A.; Pomastowski, P.; Rafinska, K.; Railean-Plugaru, V.; Buszewski, B. Zinc Oxide Nanoparticles: Synthesis, Antiseptic Activity and Toxicity Mechanism. *Adv. Colloid Interface Sci.* **2017**, *249*, 37–52. [CrossRef]
6. Beers, E.H. Palliative Wound Care. *Surg. Clin. N. Am.* **2019**, *99*, 899–919. [CrossRef]
7. Allahverdiyev, A.M.; Kon, K.V.; Abamor, E.S.; Bagirova, M.; Rafailovich, M. Coping with Antibiotic Resistance: Combining Nanoparticles with Antibiotics and Other Antimicrobial Agents. *Expert Rev. Anti-Infect. Ther.* **2011**, *9*, 1035–1052. [CrossRef]
8. Buszewski, B.; Rogowska, A.; Railean-Plugaru, V.; Złoch, M.; Walczak-Skierska, J.; Pomastowski, P. The Influence of Different Forms of Silver on Selected Pathogenic Bacteria. *Materials* **2020**, *13*, 2403. [CrossRef]
9. Gurd, F.R.N.; Wilcox, P.E. Complex Formation between Metallic Cations and Proteins, Peptides, and Amino Acids. In *Advances in Protein Chemistry*; Academic Press: New York, NY, USA, 1956; Volume 11, pp. 311–427.
10. Pomastowski, P.; Sprynskyy, M.; Žuvela, P.; Rafińska, K.; Milanowski, M.; Liu, J.J.; Yi, M.; Buszewski, B. Silver-Lactoferrin Nanocomplexes as a Potent Antimicrobial Agent. *J. Am. Chem. Soc.* **2016**, *138*, 7899–7909. [CrossRef]

11. Pryshchepa, O.; Sagandykova, G.N.; Pomastowski, P.; Railean-Plugaru, V.; Król, A.; Rogowska, A.; Rodzik, A.; Sprynskyy, M.; Buszewski, B. A New Approach for Spontaneous Silver Ions Immobilization onto Casein. *Int. J. Mol. Sci.* **2019**, *20*, 3864. [CrossRef]

12. Alhazmi, H. FT-IR Spectroscopy for the Identification of Binding Sites and Measurements of the Binding Interactions of Important Metal Ions with Bovine Serum Albumin. *Sci. Pharm.* **2019**, *87*, 5. [CrossRef]

13. Massey, A.G.; Thompson, N.R.; Johndon, B.F.G. *The Chemistry of Copper, Silver and Gold*; Elsevier: Oxford, UK, 1973; ISBN 9780080188607.

14. Lambert, L.A. Molecular Evolution of the Transferrin Family and Associated Receptors. *Biochim. Biophys. Acta (BBA)-Gen. Subj.* **2012**, *1820*, 244–255. [CrossRef] [PubMed]

15. Yoshida, S.; Wei, Z.; Shinmura, Y.; Fukunaga, N. Separation of Lactoferrin-a and -b from Bovine Colostrum. *J. Dairy Sci.* **2000**, *83*, 2211–2215. [CrossRef]

16. Waarts, B.-L.; Aneke, O.J.C.; Smit, J.M.; Kimata, K.; Bittman, R.; Meijer, D.K.F.; Wilschut, J. Antiviral Activity of Human Lactoferrin: Inhibition of Alphavirus Interaction with Heparan Sulfate. *Virology* **2005**, *333*, 284–292. [CrossRef]

17. Andersson, Y.; Lindquist, S.; Lagerqvist, C.; Hernell, O. Lactoferrin Is Responsible for the Fungistatic Effect of Human Milk. *Early Hum. Dev.* **2000**, *59*, 95–105. [CrossRef]

18. Grigorieva, D.V.; Gorudko, I.V.; Shamova, E.V.; Terekhova, M.S.; Maliushkova, E.V.; Semak, I.V.; Cherenkevich, S.N.; Sokolov, A.V.; Timoshenko, A.V. Effects of Recombinant Human Lactoferrin on Calcium Signaling and Functional Responses of Human Neutrophils. *Arch. Biochem. Biophys.* **2019**, *675*, 108122. [CrossRef]

19. Takayama, Y. *Lactoferrin and Its Role in Wound Healing*; Springer: Dordrecht, The Netherlands, 2012; ISBN 978-94-007-2466-2.

20. O'Riordan, N.; Kane, M.; Joshi, L.; Hickey, R.M. Structural and Functional Characteristics of Bovine Milk Protein Glycosylation. *Glycobiology* **2014**, *24*, 220–236. [CrossRef]

21. Zamora-Garcia, I.R.; Alatorre-Ordaz, A.; Ibanez, J.G.; Garcia-Jimenez, M.G.; Nosaka, Y.; Kobayashi, T.; Sugita, S. Thermodynamic and Electrochemical Study on the Mechanism of Formation of $Ag(OH)^{4-}$ in Alkaline Media. *Electrochim. Acta* **2013**, *111*, 268–274. [CrossRef]

22. Pryshchepa, O.; Sagandykova, G.; Rudnicka, J.; Pomastowski, P.; Sprynskyy, M.; Buszewski, B. Synthesis and Physicochemical Characterization of Zinc-Lactoferrin Complexes. *J. Dairy Sci.* **2022**, *105*, 1940–1958. [CrossRef]

23. Kumar, K.V.; Gadipelli, S.; Wood, B.; Ramisetty, K.A.; Stewart, A.A.; Howard, C.A.; Brett, D.J.L.; Rodriguez-Reinoso, F. Characterization of the Adsorption Site Energies and Heterogeneous Surfaces of Porous Materials. *J. Mater. Chem. A* **2019**, *7*, 10104–10137. [CrossRef]

24. Sprynskyy, M.; Kowalkowski, T.; Tutu, H.; Cukrowska, E.M.; Buszewski, B. Adsorption Performance of Talc for Uranium Removal from Aqueous Solution. *Chem. Eng. J.* **2011**, *171*, 1185–1193. [CrossRef]

25. Buszewski, B.; Žuvela, P.; Król-Górniak, A.; Railean-Plugaru, V.; Rogowska, A.; Wong, M.W.; Yi, M.; Rodzik, A.; Sprynskyy, M.; Pomastowski, P. Interactions of Zinc Aqua Complexes with Ovalbumin at the Forefront of the Zn^{2+}/ZnO-OVO Hybrid Complex Formation Mechanism. *Appl. Surf. Sci.* **2021**, *542*, 148641. [CrossRef]

26. Buszewski, B.; Rodzik, A.; Railean-Plugaru, V.; Sprynskyy, M.; Pomastowski, P. A Study of Zinc Ions Immobilization by β-Lactoglobulin. *Colloids Surf. A Physicochem. Eng. Asp.* **2020**, *591*, 124443. [CrossRef]

27. Al-Ghouti, M.A.; Da'ana, D.A. Guidelines for the Use and Interpretation of Adsorption Isotherm Models: A Review. *J. Hazard. Mater.* **2020**, *393*, 122383. [CrossRef]

28. Durán, N.; Nakazato, G.; Seabra, A.B. Antimicrobial Activity of Biogenic Silver Nanoparticles, and Silver Chloride Nanoparticles: An Overview and Comments. *Appl. Microbiol. Biotechnol.* **2016**, *100*, 6555–6570. [CrossRef]

29. Nandiyanto, A.B.D.; Oktiani, R.; Ragadhita, R. How to Read and Interpret FTIR Spectroscope of Organic Material. *Indones. J. Sci. Technol.* **2019**, *4*, 97. [CrossRef]

30. Barth, A. Infrared Spectroscopy of Proteins. *Biochim. Biophys. Acta (BBA)-Bioenerg.* **2007**, *1767*, 1073–1101. [CrossRef]

31. Socrates, G.G. *Infrared and Raman Characteristic Group Frequencies: Tables and Charts*, 3rd ed.; John Wiley & Sons, Ltd.: Chichester, UK, 2004; ISBN 978-0-470-09307-8.

32. Jacob, C.R.; Luber, S.; Reiher, M. Analysis of Secondary Structure Effects on the IR and Raman Spectra of Polypeptides in Terms of Localized Vibrations. *J. Phys. Chem. B* **2009**, *113*, 6558–6573. [CrossRef]

33. Kozłowicz, K.; Różyło, R.; Gładyszewska, B.; Matwijczuk, A.; Gładyszewski, G.; Chocyk, D.; Samborska, K.; Piekut, J.; Smolewska, M. Identification of Sugars and Phenolic Compounds in Honey Powders with the Use of GC–MS, FTIR Spectroscopy, and X-Ray Diffraction. *Sci. Rep.* **2020**, *10*, 16269. [CrossRef]

34. Wen, Z. Raman Spectroscopy of Protein Pharmaceuticals. *J. Pharm. Sci.* **2007**, *96*, 2861–2878. [CrossRef]

35. Rygula, A.; Majzner, K.; Marzec, K.M.; Kaczor, A.; Pilarczyk, M.; Baranska, M. Raman Spectroscopy of Proteins: A Review. *J. Raman Spectrosc.* **2013**, *44*, 1061–1076. [CrossRef]

36. Ashton, L.; Brewster, V.L.; Correa, E.; Goodacre, R. Detection of Glycosylation and Iron-Binding Protein Modifications Using Raman Spectroscopy. *Analyst* **2017**, *142*, 808–814. [CrossRef] [PubMed]

37. Takeuchi, H. Raman Structural Markers of Tryptophan and Histidine Side Chains in Proteins. *Biopolymers* **2003**, *72*, 305–317. [CrossRef] [PubMed]

38. Yang, H.; Xiao, X.; Zhao, X.; Wu, Y. Intrinsic Fluorescence Spectra of Tryptophan, Tyrosine and Phenyloalanine. In *Proceedings of the Chinese Society for Optical Engineering Conferences, Beijing, China, 22–26 July 2016*; Lv, Y., Le, J., Chen, H., Wang, J., Shao, J., Eds.; SPIE: Bellingham, WC, USA, 2017; p. 102554M.

39. Ghisaidoobe, A.B.T.; Chung, S.J. Intrinsic Tryptophan Fluorescence in the Detection and Analysis of Proteins: A Focus on Förster Resonance Energy Transfer Techniques. *Int. J. Mol. Sci.* **2014**, *15*, 22518–22538. [CrossRef]

40. Lakowicz, J.R. *Principles of Fluorescence Spectroscopy*; Springer: Boston, MA, USA, 2006; pp. 1–954. [CrossRef]

41. Paseban, N.; Ghadam, P.; Pourhosseini, P.S. The Fluorescence Behavior and Stability of AgNPs Synthesized by Juglans Regia Green Husk Aqueous Extract. *Int. J. Nanosci. Nanotechnol.* **2019**, *15*, 117–126.

42. Voswinkel, L.; Vogel, T.; Kulozik, U. Impact of the Iron Saturation of Bovine Lactoferrin on Adsorption to a Strong Cation Exchanger Membrane. *Int. Dairy J.* **2016**, *56*, 134–140. [CrossRef]

43. Marangon, M.; van Sluyter, S.C.; Waters, E.J.; Menz, R.I. Structure of Haze Forming Proteins in White Wines: Vitis Vinifera Thaumatin-Like Proteins. *PLoS ONE* **2014**, *9*, e113757. [CrossRef]

44. Prange, A.; Pröfrock, D. Application of CE–ICP–MS and CE–ESI–MS in Metalloproteomics: Challenges, Developments, and Limitations. *Anal. Bioanal. Chem.* **2005**, *383*, 372–389. [CrossRef]

45. Wonner, K.; Evers, M.V.; Tschulik, K. The Electrochemical Dissolution of Single Silver Nanoparticles Enlightened by Hyperspectral Dark-Field Microscopy. *Electrochim. Acta* **2019**, *301*, 458–464. [CrossRef]

46. Babel, L.; Bonnet-Gómez, S.; Fromm, K. Appropriate Buffers for Studying the Bioinorganic Chemistry of Silver(I). *Chemistry* **2020**, *2*, 193–202. [CrossRef]

47. Kosa, S.A.; Zaheer, Z. Biogenic Fabrication of Silver Nanoparticles, Oxidative Dissolution and Antimicrobial Activities. *J. Saudi Chem. Soc.* **2022**, *26*, 101414. [CrossRef]

48. Hadrup, N.; Lam, H.R. Oral Toxicity of Silver Ions, Silver Nanoparticles and Colloidal Silver—A Review. *Regul. Toxicol. Pharmacol.* **2014**, *68*, 1–7. [CrossRef] [PubMed]

49. Greulich, C.; Braun, D.; Peetsch, A.; Diendorf, J.; Siebers, B.; Epple, M.; Köller, M. The Toxic Effect of Silver Ions and Silver Nanoparticles towards Bacteria and Human Cells Occurs in the Same Concentration Range. *RSC Adv.* **2012**, *2*, 6981. [CrossRef]

50. Wang, R.; Edrington, T.C.; Storrs, S.B.; Crowley, K.S.; Ward, J.M.; Lee, T.C.; Liu, Z.L.; Li, B.; Glenn, K.C. Analyzing Pepsin Degradation Assay Conditions Used for Allergenicity Assessments to Ensure That Pepsin Susceptible and Pepsin Resistant Dietary Proteins Are Distinguishable. *PLoS ONE* **2017**, *12*, e0171926. [CrossRef]

51. van Veen, H.A.; Geerts, M.E.J.; van Berkel, P.H.C.; Nuijens, J.H. The Role of N-Linked Glycosylation in the Protection of Human and Bovine Lactoferrin against Tryptic Proteolysis. *Eur. J. Biochem.* **2004**, *271*, 678–684. [CrossRef]

52. Złoch, M.; Maślak, E.; Kupczyk, W.; Jackowski, M.; Pomastowski, P.; Buszewski, B. Culturomics Approach to Identify Diabetic Foot Infection Bacteria. *Int. J. Mol. Sci.* **2021**, *22*, 9574. [CrossRef]

53. Śpiewak, K.; Majka, G.; Pilarczyk-Żurek, M.; Nowak, P.M.; Woźniakiewicz, M.; Pietrzyk, P.; Korzeniak, T.; Stochel-Gaudyn, A.; Fyderek, K.; Strus, M.; et al. Mn^{3+}-Saturated Bovine Lactoferrin as a New Complex with Potential Prebiotic Activities for Dysbiosis Treatment and Prevention—On the Synthesis, Chemical Characterization and Origin of Biological Activity. *J. Funct. Foods* **2017**, *38*, 264–272. [CrossRef]

54. *European Pharmacopoeia 7.0 Volume 1*; European Directorate for the Quality of Medicines & HealthCare, Council of Europe Publishing: Strasbourg, France, 2011; ISBN 978-9287167002.

55. Michalke, B.; Willkommen, D.; Venkataramani, V. Setup of Capillary Electrophoresis-Inductively Coupled Plasma Mass Spectrometry (CE-ICP-MS) for Quantification of Iron Redox Species (Fe(II), Fe(III)). *J. Vis. Exp.* **2020**, *159*, e61055. [CrossRef]

6.3 Synthesis and physicochemical characterization of bovine lactoferrin supersaturated complex with iron (III) ions

O. Pryshchepa, K. Rafińska, A. Gołębiowski, M. Sugajski, G. Sagandykova, P. Madajski, B. Buszewski, P. Pomastowski, *"Synthesis and physicochemical characterization of bovine lactoferrin supersaturated complex with iron (III) ions"*, Scientific Reports, 12 (1), 2022: 12695, https://doi.org/10.1038/s41598-022-15814-2

scientific reports

OPEN

Synthesis and physicochemical characterization of bovine lactoferrin supersaturated complex with iron (III) ions

Oleksandra Pryshchepa[1,2 ✉], Katarzyna Rafińska[2], Adrian Gołębiowski[1,2], Mateusz Sugajski[1,2], Gulyaim Sagandykova[1], Piotr Madajski[3], Bogusław Buszewski[1,2] & Paweł Pomastowski[1]

The aim of the study was to investigate the process of Fe^{3+} binding to bLTF. Moreover, the physicochemical characterization of the respective supersaturated complex was studied. The knowledge should be important for the description of processes that may take place in dairy products fortified with iron. Additionally, the synthesized complex can be utilized as a dietary supplement for the treatment of iron deficiency anemia (IDA). Finally, it was shown that formation of supersaturated iron-protein structures which include LTF often accompanies development of neurodegenerative diseases such as Alzheimer or Parkinson. Thus, the study can reveal some aspects of its pathogenesis process. The methodology of the investigation comprised the utilization of batch sorption study and applying Freundlich and Langmuir models. The complex also was characterized by numerous techniques: spectrometric (ICP-MS), spectroscopic (UV–Vis, ATR-FTIR), electron microscopy (TEM–EDX), SDS-PAGE. Based on obtained results the potential mechanisms of iron interaction with protein were described. Moreover, the molecular docking was applied to visualize possible metal binding sites. The respective complex contains $\approx$ 33.0 mg/g of iron which is nearly 50 Fe^{3+} per one protein molecule. The cytotoxicity of the obtained complex was evaluated by MTT reduction and LDH release assays on Caco-2 and nL929 cell lines.

Lately, big attention is paid to the production of so-called "functional food". The term has been derived from knowledge about the link between nutrition and health. The concept implies the production of food with beneficial effects on health by enrichment with the biologically active components, e.g. vitamins, microelements, probiotic bacteria, etc.[1,2]. Consumption of dairy products by humans is known from ancient times. Thus, substances derived from milk are considered safe and healthy. Milk proteins, and in particular lactoferrin (LTF), are the compounds that show the widest spectrum of biological activity in the organism[1,3,4]. Thus, the production of new biologically active substances based on milk proteins attracts much attention as a part of "functional food" development[1,2].

Iron deficiency anemia (IDA) is an issue of worldwide importance. More than 1.68 billion people are affected by IDA globally[5]. The importance of iron in the organism cannot be overestimated, as it makes up heme of hemoglobin and myoglobin which take part in oxygen transport and storage. Moreover, iron also is part of the cytochromes, peroxidases, nitric oxide synthases, and other enzymes that are involved in the processes of biosynthesis and energy production, detoxification, host defense, cellular signaling, etc.[6]. Iron in the human body can be absorbed in two forms, namely heme- (from meat) and non-heme. The non-heme iron is mainly absorbed in reduced Fe^{2+} form through non-specific transport with involvement of divalent metal ion transporter-1, while usually enters to the body in oxidized form Fe^{3+}[5]. However, Fe^{3+} bioavailability is highly dependent on its solubility meaning that it needs to be bound to proteins or other hydrophilic chelators[6].

[1]Centre for Modern Interdisciplinary Technologies, Nicolaus Copernicus University in Torun, Wileńska 4, 87-100 Torun, Poland. [2]Department of Environmental Chemistry and Bioanalytics, Faculty of Chemistry, Nicolaus Copernicus University in Torun, Gagarina 7, 87-100 Torun, Poland. [3]Department of Chemistry of Materials Adsorption and Catalysis, Faculty of Chemistry, Nicolaus Copernicus University in Torun, Gagarina 7, 87-100 Torun, Poland. ✉email: pryshchepa.alexie@gmail.com

For IDA treatment oral preparations of Fe^{2+} (e.g., fumarate, or sulfate) are often utilized, which can lead to gastrointestinal side effects. Instead, the utilization of bovine LTF (bLTF) has shown to have the same effect in improving hematological parameters accompanying IDA (serum ferritin and iron levels) as ferrous sulfate salt, but with lower gastrointestinal side effects[7]. The bLTF impact can be connected to its structure, which is highly homologous to the human LTF[3] and hence bLTF, as well as its peptides, can interact with specific intestine lacto-ferrin receptors (human intelectin)[8]. In turn, it was shown that both native human LTF and its fragments can take part in directed transport of the Fe^{3+} to the brush-border membrane by binding to lactoferrin receptors, which can be considered as a specific carrier-mediated iron uptake mechanism[7,9]. Moreover, the effect of LTF can be also connected to the modulation of action of iron regulatory proteins, which promotes iron efflux from cells to the blood. Additionally, high affinity of iron to bLTF may enhance the Fe^{3+} solubility in the gastrointestinal tract[7].

Literature data also reveals that microelements, in particular iron, in form of complexes with proteins, i.e., so-called proteinates, has higher bioavailability than inorganic salts[10–12]. There are several studies and patents presenting the synthesis of respective complexes based on the milk and whey proteins. For instance, Dalev (1993) in its work presents the technology for the preparation of iron-protein complexes based on the whey[13]. The procedure, among others, implies heat denaturation of all proteins to obtain precipitate. However, such procedure leads to the loss of the biological activity of the proteins. Another example is the synthesis of succinylated caseinate iron complex[14,15]. The succinylation is a process that aimed to enrich the protein with carboxylic groups and thus to improve the functional properties of proteins, among others, better emulsifying, foaming, gelation but also to increase the iron-binding ability[16]. Thus, the possibility to obtain iron-rich complexes based on unmodified proteins is of great interest and bLTF seems to be the most suitable for such preparations.

bLTF is the protein belonging to the transferrin family, which are the non-heme iron-binding proteins. Transferrins typically consist of a single polypeptide chain comprised of 670–700 amino acids, which form two globular lobes (N- and C-lobes) with one iron-binding site each[3,4,17].The meaning „iron saturated" is usually utilized for the description of bLTF that has both binding sites filled with iron and called holo-lactoferrin. However, it was shown that bLTF can bind much more iron than can be predicted by its structure which should result information of supersaturated complex. The existence of such complexes can be a reason of beneficial effect on the non-heme iron bioavalability from food and dietary supplements which is poorly lightened in the literature[18,19]. However, it is also noteworthy to mention, that LTF has been indicated to take part in Alzheimer's disease due to its presence in senile plaque, while the formation of amyloids is often connected to iron overload. One of the important aspects is that senile plaque can include iron-oxide magnetic nanoparticles in its core[20], which shows the negative aspects of the formation of supersaturated Fe-protein complexes. Thus, there is the need for the comprehensive study of the formation mechanisms of the Fe-bLTF complex as well as its physicochemical and biological properties. Such studies may provide knowledge about the fate of iron in products fortified with microelements. Moreover, the corresponding complex can be utilized as dietary supplements and thus can be a solution in the treatment of IDA. Still, the studies can also provide additional information about mechanisms of iron toxicity, among others on the development of neurodegenerative diseases.

Hence, the work aimed to synthesize the supersaturated complex of bLTF with Fe^{3+}. Additionally, the mechanisms which are involved in the formation of the respective complexes were investigated. The respective knowledge can be useful for the prediction of bLTF behavior in iron-rich solutions, among others in nutrient formulas. The synthesized complex was also subjected to physicochemical characterization. Moreover, the stability and cytotoxicity of the synthesized complex were evaluated.

Results and discussion

The batch sorption study of Fe^{3+} interaction with bLTF.
The isotherm study was performed to investigate the maximum sorption capacity of bLTF and to predict possible processes which may take place during the interaction. Figure 1A. presents the results of the batch isotherm study for the entire range of utilized Fe^{3+} concentrations. As can be seen from the experimental data the process has heterogeneous character—the formation of "several adsorption layers" can be predicted. Moreover, the obtained isotherm belongs to IV/VI type according to IUPAC classification, meaning that during the interaction the layer-by-layer adsorption occurs[21]. Langmuir and Freundlich isotherm models are often utilized for the description of the sorption processes. Both of the mentioned models are simple and were shown to be useful for the description of the processes of protein interaction with such metals as Ag^+ and Zn^{2+}[22,23]. However, the models can be applied only to isotherm type I, which corresponds to the first step of the IV/VI type isotherm[21].

Previous studies[22,23] have shown that utilization of the modified BET isotherm proposed by Sprynskyy et al.[24] was useful for the description of the multilayer adsorption process and enabled to distinguish concentration ranges for the formation of each subsequent layer. In the present study, such an approach has shown that in the entire concentration range the formation of three adsorption layers on the surface of the bLTF can be predicted (Fig. 1C). The first layer is formed when the Fe^{3+} solutions of initial concentration up to 300 mg/L was utilized, which can be seen more evidently from the bar chart of bLTF sorption efficiency (Fig. 1D). The formation of the second layer was observed for the Fe^{3+} concentrations between 600 and 1400 mg/L. Third layer formation begins at a Fe^{3+} concentration of 1600 mg/L. It is noteworthy to mention, that classical isotherm models were developed for the description of surface sorption where the adsorbate in second adsorption layer is characterized by lower energy of adsorption. In case of protein interactions, the formation of multiple "adsorption layers" should indicate the interaction of different nature, i. e. the formation of nanoparticles, metal chelation, or electrostatic interactions. Interestingly, before the study, the physicochemical characterization of the protein was performed. The results are presented in our previous work[25]. It turned out that purchased from Sigma-Aldrich bLTF has both metal-binding sites filled with iron (the Fe^{3+} content in the unmodified protein accounts 1.45 ± 0.06 mg/g). Thus, it can be argued that iron-binding occurs outside the previously described metal-binding sites.
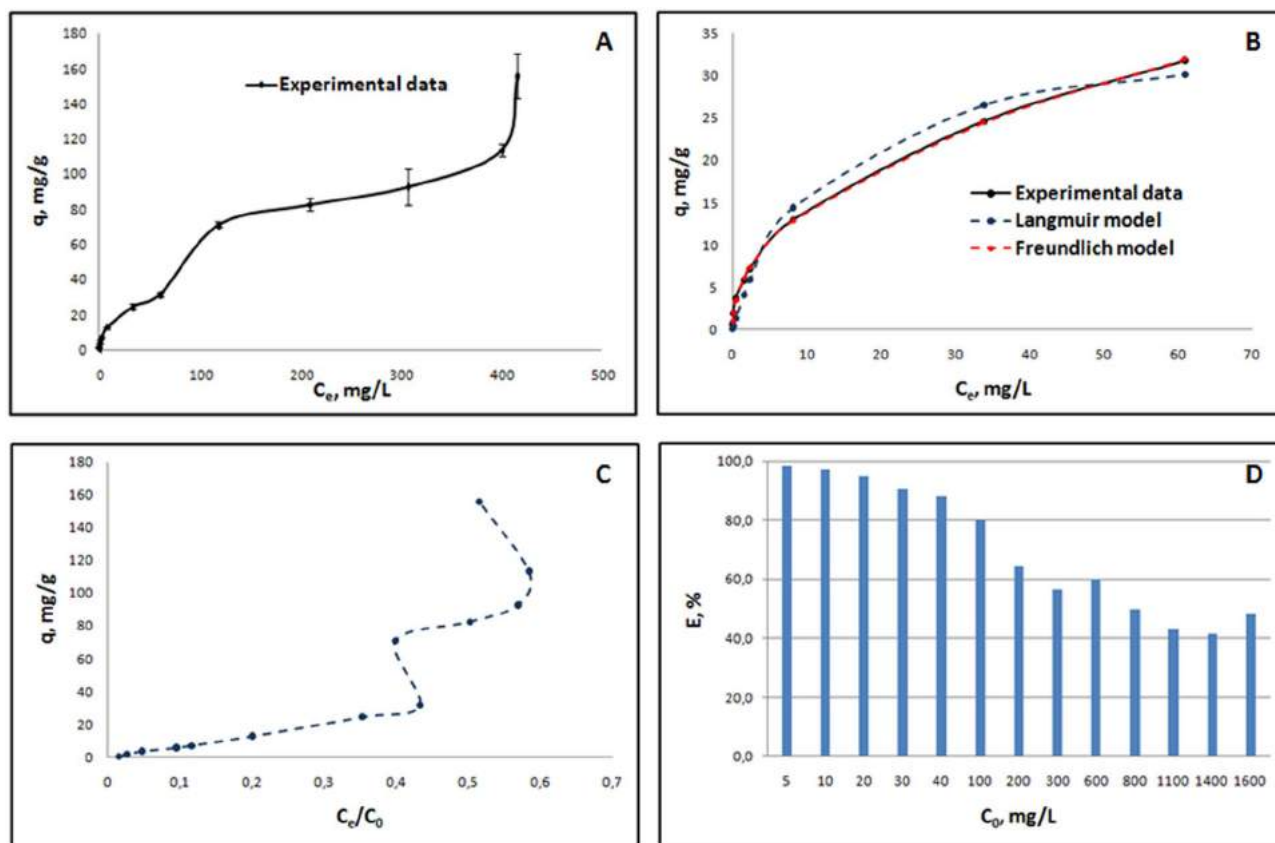
Figure 1. Batch isotherm study of Fe^{3+} sorption onto bLTF: (**A**) isotherm of Fe^{3+} adsorption onto bLTF for entire concentration range, (**B**) the fit of first sorption step to Langmuir and Freundlich models, (**C**) modified BET isotherm, which presents adsorption as a function of a ratio C_e/C_0, (**D**) bar chart of a sorption efficiency of bLTF depending on the initial concentration of Fe^{3+}.

Freundlich isotherm				Langmuir isotherm			
K_F [mg/g]	1/n	S	R^2	K_L [L/mg]	q_m[mg/g]	S	R^2
4.956	0.454	$2.7 \cdot 10^{-6}$	0.9994	0.080	36.29	18.1	0.9770

Table 1. The calculated values derived from Freundlich and Langmuir isotherm models.

Further, the Freundlich and Langmuir models were applied to the outlined first adsorption step. Figure 1B presents the fit of the first adsorption step of the obtained isotherm, while Table 1 summarizes the calculated value for the utilized models. For the calculations, the minimal Residual Sum Squared (RSS) method and Solver (the Excel add-in) were applied. Langmuir model assumes the adsorption on the homogeneous adsorbent, i.e. the same binding energies of all binding sites. Additionally, the model implies the monolayer adsorption character[21]. It is also noteworthy to mention that both Langmuir and Freundlich constants express the binding affinity of the adsorbate to the adsorbent. Thus, in case of metal-protein interactions, first adsorption layer may indicate the Fe^{3+} chelation or nanoparticles formation. Instead, iron in second and all subsequent layers should bond less strongly, e. g. through electrostatic interactions. Thus, taking into account the estimated molecular weight of the bLTF utilized in the study ($\approx$ 83 kDa by MALDI-TOF MS[25]) and q_m derived from isotherm it can be predicted $\approx$ 54 additional binding sites on the surface of the protein. However, the values of the statistical metrics, i.e. square of the correlation coefficient R^2 and standard error S, have shown the more accurate description of the first sorption stage by Freundlich isotherm. Freundlich model belongs to the oldest and most commonly used isotherm expressions. The model assumes the heterogeneous non-ideal character of the adsorption process. Moreover, the model is not restricted to monolayer formation[26]. Finally, comparing the obtained data of maximum adsorption and Langmuir constant for Fe^{3+} binding to bLTF (36.29 mg/g and 0.08 L/mg) with the data of Zn^{2+} binding to Ova-albumin (10.97 mg/g and 1.95 L/mg[23]) and β-lactoglobulin (104.40 mg/g and 0.01 L/mg[27]) it may be assumed the formation of a homogeneous Fe-bLTF complex, but not the formation of nanoparticles. In the case of Ova-albumin, the relatively high Langmuir constant can be explained by the formation of Zn/ZnO nanoparticles.

Additionally, the changes of Gibbs free energy ΔG of iron binding to protein were calculated. The determined ΔG for the first adsorption stage gradually decreased depending on the concentration of the utilized Fe^{3+} and

was in the range from − 24.82 to − 15.40 kJ/mol (the shown values represent Gibbs free energy observed for the lowest and highest Fe^{3+} concentrations). The results indicate the spontaneous nature of the sorption process and the heterogeneous character of the protein surface in terms of binding energies. ΔG values for the second stage were in the range from − 15.74 to − 13.90 kJ/mol and for the last concentration point (the beginning of the third adsorption stage) equals − 14.59 kJ/mol. The calculated values indicate that the majority of iron should bond loosely to the protein and do not induce the formation of new metal-binding sites. The binding energies of metals in structurally defined metal-binding sites such as active sites of an enzymes or zinc fingers usually are much higher. For instance, F. Bou-Abdallah and T. Giffune have performed the measurements of binding energies for Fe^{2+} and Zn^{2+} to apo-human transferrin by isothermal titration calorimetry (ITC)[28]. The determined ΔG depending on utilized conditions was in the range from nearly − 171 to − 195 kJ/mol which is comparable to the energies of some covalent bonds. The affinity of Fe^{3+} to transferrins has shown to be even higher[4] than Fe^{2+} or Zn^{2+}, thus the binding energyfor the respective specie should also be higher.Moreover, it is worth noting that the calculated in our studies values represent the average binding energies for several ions. Thus, for the differentiation of each particular iron ion, there is a need to perform additional studies in the future.

Still, it should be noted that Fe^{3+} in complexes more often have octahedral geometry and can form multinuclear coordination compounds. Iron in the proteins also can appear in the multinuclear form. For instance, the hydroxylase protein of *Methylococcuscapsulatus* has a dinuclear iron center at the active site[29]. The connections between iron atoms are made with oxygen-containing ligands, e.g. hydroxide, glutamic acid, acetate. The very extreme case of the Fe-rich protein complexes can be illustrated by unique Fe-storage protein—ferritin. The form of the iron in the ferritin depends on the number of bounded Fe^{3+}[30]. When a small amount of Fe^{3+} is bound to ferritin they are coordinated to oxygen-containing groups. With the increased amount of bounded iron, the inorganic Fe-containing core with the crystal structure of ferrihydrite forms inside the ferritin cavity. Interestingly, Ghosh et al. have observed the formation of iron nanomineralization within fibrillation of holo human serum transferrin[31]. The iron mineral cores were shown to have a similar form which is ordinarily accumulated within ferritin[32]. Thus, such structures may also form in Fe-bLTF complexes as all transferrins have highly homologous structures and reveal similar properties. The authors also suggested that such the spontaneous processes involving transferrins may occur in the tissues and can lead to neurodegenerative disorders, but additional studies should be provided. However, the goal of our study was to obtain a homogeneous Fe-rich protein complex, which can be utilized as food additives. Thus, the synthesis of the Fe-bLTF complex for further investigations was performed with the utilization of Fe^{3+} solution with a concentration of 600 mg/L. The excess of the iron was utilized to obtain complex with fully filled monolayer and with maximum yield.

Molecular docking. 3D structure of bLTF downloaded from rcsb website contains particles that interfere MIB analysis. Thus, using Molegro Molecular Viewer 7 all particles of water and cofactors were removed. The MIB algorithm compares the query of protein structure with metal-binding template in the database and shows the results of fit by the score where the highest score indicates the higher probability of the binding[33]. The molecular docking analysis within MIB showed as many as 32 potential binding sites for Fe^{3+} interaction with bLTF (Table S. 1.). The most common amino acid residue taking part in the Fe^{3+} was cysteine (14). Despite the indication of cysteine as the amino acid that most frequently interacts with the Fe^{3+}, the result for this binding does not reach the highest scores. Instead, the best results were obtained for aspartic acid (7.844), histidine (7.844) and tyrosine (7.844). The Table S. 2. shows the remaining amino acids with the calculated Score value and the number of occurrences. The obtained results are consistent with literature data which indicate that residues containing carboxyl and hydroxyl groups form the strongest bonds with Fe^{3+}[34]. Moreover, from 32 predicted binding sites 6 combinations correspond to the previously described iron-binding sites in N- and C- lobes[4,17] of bLTF which confirms the usefulness of the utilized algorithm. Still, it was shown that at least 26 additional combinations of amino acid residues can form Fe^{3+}-binding sites in bLTF. The graphical presentation some of them can be find on Fig. S. 4. The obtained results indicate that MIB is a fast and simple tool for the prediction of metal-binding sites. However, it has lots of limitations as the prediction is made only within the templates included in the database which may be not enough for the determination of all possible binding sites. Moreover, water molecules are indispensable part of such kind of interactions[23,25] and should not be omitted in molecular docking analysis as it can change dramatically the final result. Thus, more sophisticated calculations should be performed in the future.

Characterization of Fe-bLTF complex. The synthesized complex was subjected to ICP-MS analysis for iron content quantification. The adsorption capacity of bLTF was determined as 71.37 ± 1.53 mg/g when Fe^{3+} solution with a concentration of 600 mg/L was utilized. However, the complex synthesis procedure, among others, comprises a double washing step, which was used to remove iron excess.Thus, the resulting complex contained only 32.97 ± 4.41 mg/g of iron which equals to ≈ 50 iron ions per one protein molecule. Previous studies have revealed that at unfavorable conditions, when the metal-protein complex formation did not occur the as performed washing procedure was enough to eliminate non-bonded and loosely-bonded metal from protein[25]. Interestingly, the maximum adsorption capacity calculated from the Langmuir model equals 36.29 mg/g. The results may indicate, that the first adsorption layer was fully filled with iron in the obtained complex. Moreover, the Fe^{3+} form relatively strong bonds with the protein in this layer, as it remains in the complex even after washing steps.

TEM images of the synthesized complexes have revealed the formation of a homogeneous metal-protein complex, predicted from isotherm study (Fig. 2). In addition, the utilization of EDX within electron microscopy enabled the detection of an increase in Fe content in the protein. The Fe atoms were not possible to detect in
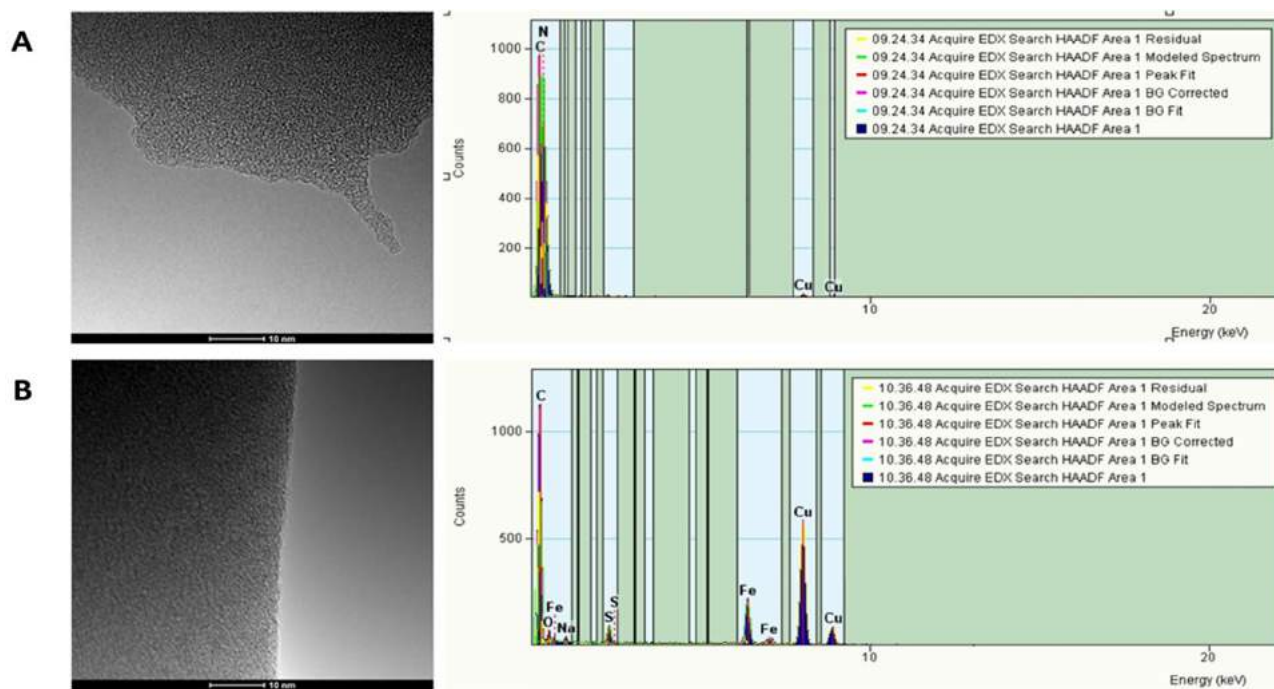
Figure 2. The TEM images and EDX spectra of (**A**) native bLTF and (**B**) Fe-bLTF complex.

the native protein, while in the EDX spectrum of the Fe-bLTF complex the appearance of peaks corresponding to Fe was observed.

The SDS-PAGE analysis of obtained complex was performed (Fig. 3). The previous study performed by PAGE-IEF for different forms of bLTF has revealed changes in electrophoretic mobility of iron-saturated protein in comparison to its apo-form[35]. The present study has shown that changes in electrophoretic mobility of Fe-bLTF were observed in the case when non-reducing SDS-PAGE was utilized. The proteins' velocity increased slightly which may indicate the formation of a more compact structure after Fe^{3+} binding[36]. Instead, the addition of a reducing agent causes the breaking of disulfide bonds and loss of the globular structure of the protein and thus should influence the metal binding ability. Consequently, no difference in bands position for bLTF and Fe-bLTF was observed in reduced SDS-PAGE, but the higher position of the bands in comparison to the non-reduced mode.

Interestingly, after the interaction of the protein with iron, the increase in the intensity of the bands between 140 and 240 kDa in both non-reduced and reduced mode was observed. Moreover, in reduced mode the bands between 50 and 70 kDa have appeared indicating partial degradation of bLTF. The results indicate the impact of Fe^{3+} on the formation of protein oligomers. Protein aggregation and fibrillation are the topics of numerous investigations. Protein fibrillation and oligomerization are considered as the leading cause of neurodegenerative disorders such as Alzheimer's and Parkinson's diseases. The process is suggested to be connected with the environmental factors, where the imbalance of metal ion homeostasis is one of the significant factors[37]. Forced transferrin fibrillation can be performed with the utilization of dithiothreitol[38]. The method was developed for the production of nanoparticles from transferrins. Such nanoparticles are of high interest as they can be utilized as drug carriers. Dithiothreitol is the reducing agent, which breaks the S–S bonds in the protein with the formation of thiol (or sulfhydryl) groups. Then, the formation of protein oligomers can occur via chaotic uncontrolled interactions between monomers, where the rebuilding of disulfide bridges may play the main role in the aggregation process. However, the present study indicates that an increase in the dimer content rather has non-disulfide bonding nature as in other cases the intensification of dimer band would have differed for reduced and non-reduced SDS-PAGE modes.

The occurred changes can be explained by the utilized conditions, i.e. the reaction mixture comprised not only bLTF and Fe^{3+} but also a small amount of citrate ions (the iron ammonium citrate salt was utilized as a source of Fe^{3+}). Citrate is well known mild reducing and stabilizing agent, which is often utilized in metallic nanoparticles synthesis[39]. It was shown that iron in the presence of citrate ions can undergo reversible reduction from Fe^{3+} to Fe^{2+}[40]. During reversible metal reduction, the formation of superoxide occurs[41], which belongs to the so-called "reactive oxygen species" (ROS). The ability of iron to promote superoxide formation is considered as one of the mechanisms of its toxicity. ROS cause the oxidation of biomolecules with the appearance of more active functional groups (e.g. peroxide or formyl) and thus can lead to the formation of protein oligomers. Moreover, the Fe^{3+} can form cross-links between protein monomers[37]. The oxidation process also can lead to protein degradation, which should be the reason for the protein degradation seen on the reducing SDS-PAGE. Thus, obtained results may indicate one of the possible mechanisms of iron's impact on the development of neurodegenerative disorders. For instance, S. Ghosh et al. have investigated the spontaneous process of human serum transferrin fibrillation[31]. The authors claim that the aggregation process can occur even after relatively small changes in the protein structure (e.g., change in the relative orientation of two lobes). From the study, it
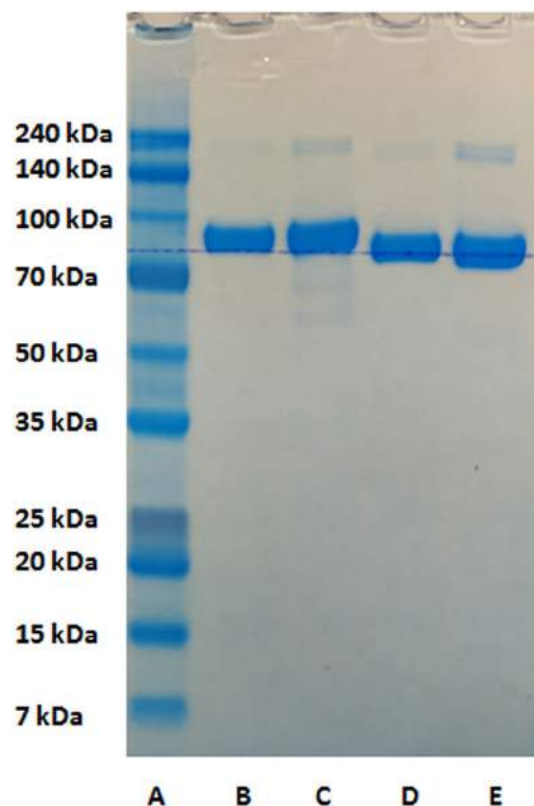
Figure 3. SDS-PAGE of the Fe-bLTF complex, where (**A**)—protein markers, (**B**) and (**C**)—native bLTF and Fe-bLTF complex prepared in reduced mode, (**D**) and (**E**)—native bLTF and Fe-bLTF complex prepared in non-reduced mode. The full-size electropherogram is presented in Fig. S. 4 of supplementary materials.

can be deduced that protein fibrillation is more extensively occur from aged protein solutions. Further results of this group were presented in Booyjzsen et al. work[32] where the fibrillation process for recombinant human serum transferrin was presented. The study revealed that the formation of fibrils more often occurs in protein with higher content of dimers. While, it should be noted that iron in iron overload diseases can present as non-transferrin complexes consisting of iron, citrate, and BSA. Such complexes may lead to the formation of bLTF oligomers with subsequent fibrillation.

The FTIR analysis was performed to distinguish the functional groups which may take part in the metal binding to protein (Fig. 4). In the characteristic region for stretching vibrations of hydrogen-containing groups (2800–3700 cm^{-1}) the wide absorption band with a maximum at 3280 cm^{-1} was assigned to vibrations of O–H and N–H involved in the hydrogen bonds. Symmetric and asymmetric str. vibrations CH$_3$- and CH$_2$-groups on spectra of native bLTF are represented by doublets at 3078/2980 cm^{-1} and 2936/2886 cm^{-1}, respectively[42]. The redshifts were observed for the corresponding bands after Fe^{3+} binding, indicating the weakening of the C-H bond. The effect may be connected to the interaction between the CH group with a metal cation. For instance, it was shown that such reactions can occur between alkali metals and hexane in gas-phase, which resulted in red-shifts of corresponding bands on the FTIR spectra[43]. However, more evidently the changes in the distribution of electron densities in protein molecules after iron binding to other functional groups, e.g. carboxy, hydroxy, amino, etc. may result in such shifts. In the fingerprint region, two additional bands 1472 cm^{-1} (almost undetectable) and 1451 cm^{-1} of δ_{as}(CH$_3$) and δ(CH$_2$)vibrations can be distinguished[42,44]. The band at 1637 cm^{-1} was assigned to amide I vibrations, while the amide II band was observed at 1533 cm^{-1}[44,45]. However, the same region is characteristic to the vibrations of COO$^-$ group. The changes in peak maximum distribution from 1533 to 1518 cm^{-1} should indicate the interaction of Fe^{3+} through carboxylic groups of glutamic and aspartic acids, but also can be a reason of changes in protein tertiary structure. The data is constituent with the molecular docking analysis which indicates the highest probability for Fe^{3+} binding to glutamic acid[46]. Interestingly, the position of amide I is sensitive to the protein secondary structure and its position indicates the high impact of β-sheet structures in the bLTF.

More precisely secondary structure can be outlined on amide III modes, which mainly come from CN str. and NH bending ($\approx$30% each)[44,46]. The spectrum of native protein has bands at 1338 cm^{-1}, 1307 cm^{-1} distinctive for α-helix, and a more intense band at 1240 cm^{-1} of β-sheet, which is complementary to the observed position of the amide I band. After Fe^{3+} binding to protein, the shift from 1240to 1246 cm^{-1} was observed, indicating the changes in protein tertiary structure. Instead, the band at 1337 cm^{-1} has disappeared which may be due to the broadening and shift of adsorption band ν_s(COO$^-$) of glutamic and aspartic acids. This band can shift significantly upon cation chelation ($+60/-90$ cm^{-1})[44]. The maximum of the corresponding band shifted from
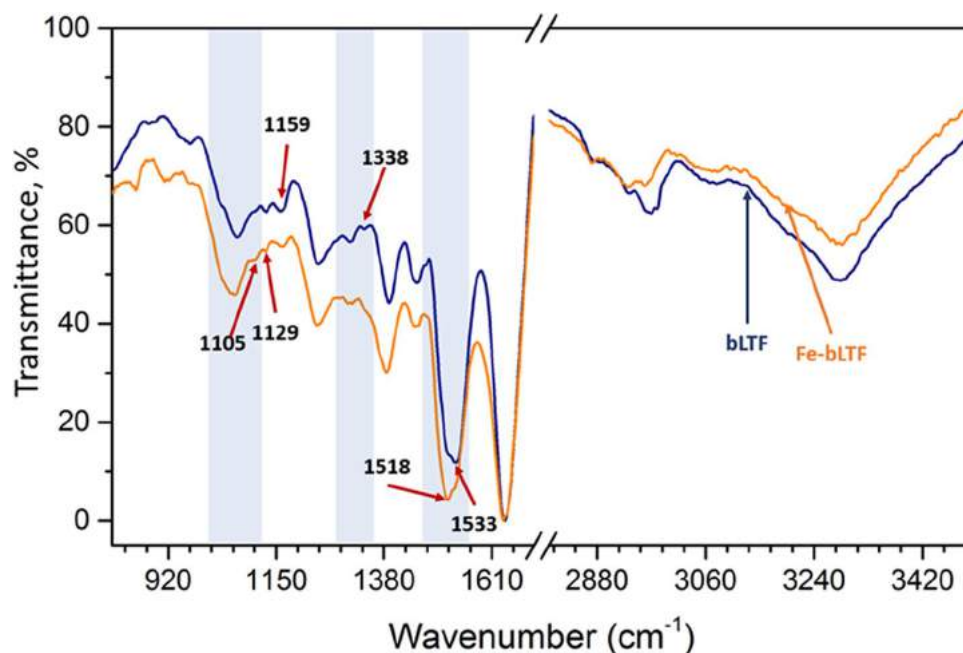
Figure 4. ATR-FTIR spectra of native bLTF (blue) and Fe-bLTF complex (orange), where the regions with the most significant changes are shadowed.
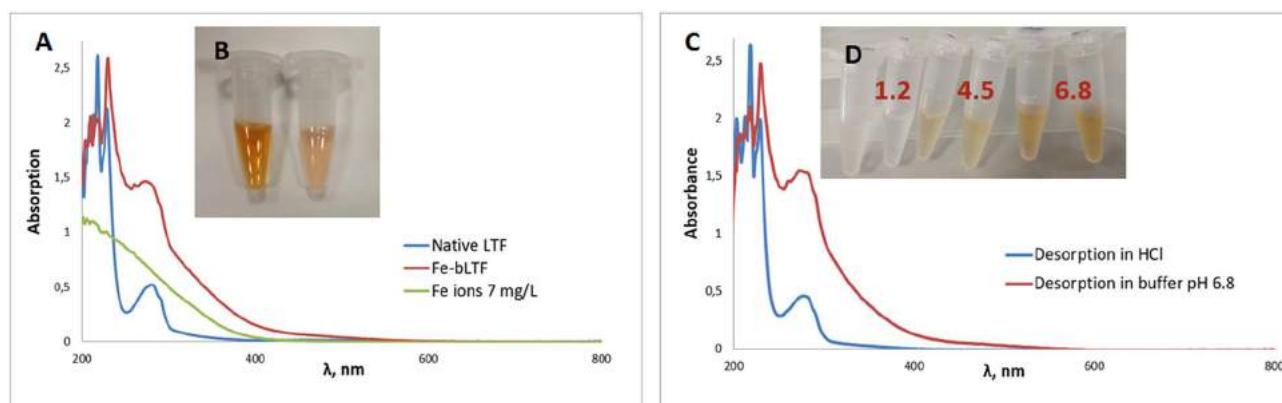

Figure 5. UV–ViS study of Fe-bLTF complexes: (**A**) spectra of native bLTF and Fe-bLTF complexes; (**B**) the solutions of Fe-bLTF complex on the right and unmodified bLTF on the left; (**C**) spectra of Fe-bLTF complexes after Fe^{3+} desorption in phosphate buffer pH 6.8 and 0.1 M hydrochloric acid; (**D**) Fe-bLTF complex solutions after 2 h desorption in 0.1 M hydrochloric acid (pH 1.2) and phosphate buffers pH 4.5, 6.8.

1391 to 1385 cm^{-1} after iron incorporation. The data indicate, that iron rather interacts with bLTF through carboxy groups. The vibrational bands ν(C–O) of serine, aspartic, and glutamic acid appeared at 1159 cm^{-1} and 1129 cm^{-1} on a spectrum of native bLTF. Moreover, band 967 cm^{-1} could also arise from the serine residue (ν(CO) or ν(CC)), while the band at 1066 cm^{-1} comes from ν(C–O) of threonine[44]. The spectrum of Fe-bLTF revealed a decrease in the 1129 cm^{-1} band, which become almost undetectable. Instead, the band at 1105 cm^{-1} has appeared, which can be assigned to ν(CN) of histidine. The shift from 1066 to 1062 cm^{-1} and broadening of the band also indicates the possible interaction of Fe^{3+} with hydroxo groups of threonine residues. However, it is noteworthy to mention that bLTF is a glycoprotein, thus in the region from 950 to 1200 cm^{-1} the bands which come from vibrations of ν(C–O), ν_{st}(C–O), ν_{st}(C–C) of carbohydrates can occur[47]. Moreover, bands at 914 cm^{-1} and 850 cm^{-1} that become visible after Fe^{3+} adsorption onto bLTF may correspond to $\nu CO + \delta CCH + \nu_{asy}$ (ring of pyranose) and $\nu CC + \delta CCH + \delta CH$($\beta$-pyranose). Generally, the appearance of the bands corresponding to more than one functional group in the same region is the main drawback of spectroscopy in the infrared range. Thus, makes it difficult to outline precisely which functional groups take part in the protein reactions.

The metal complexation also can be investigated by UV–Vis spectroscopy (Fig. 5A). The nature of the light absorbance in complexes is related to d–d and charge transfer transitions. Such transitions are the reason for the development of pink-salmon color in bLTF upon Fe^{3+} embedding to iron-binding sites. The solution of
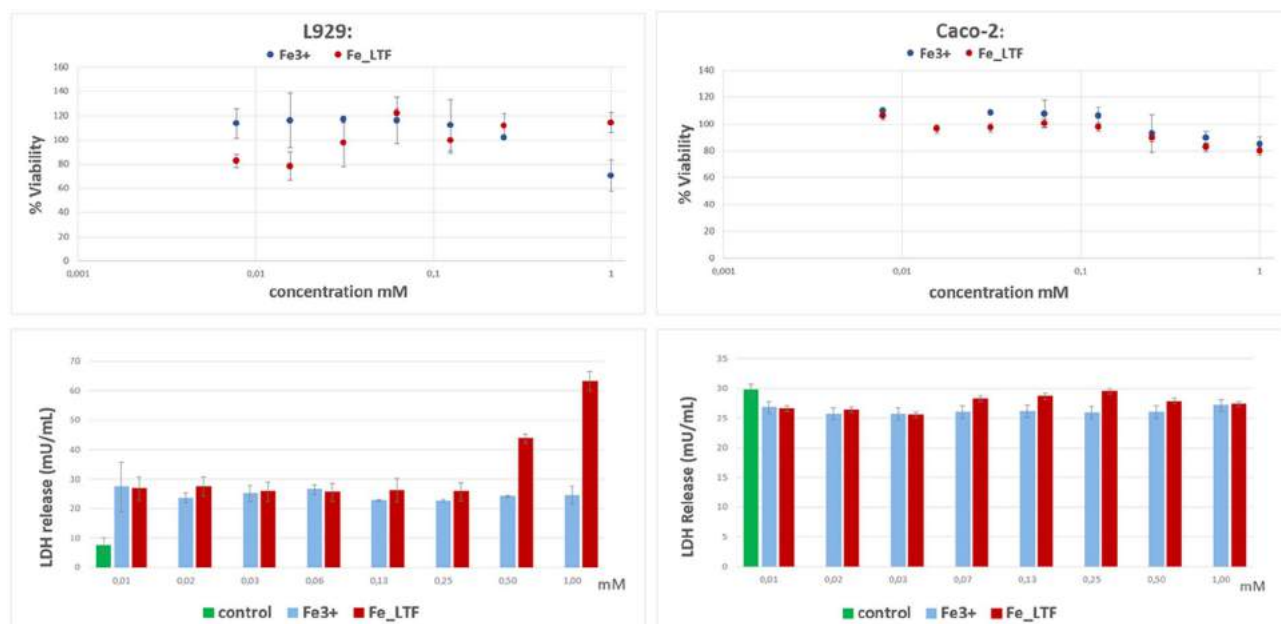
Figure 6. Cytotoxic effect of iron citrate and complex of Fe-bLTF in L929 and Caco-2 cells detected with the MTT reduction assay (values are expressed as a percentage of cell viability) and LDH release assay (values are expressed in mU/mL).

unmodified bLTF revealed the intence pink-salmon color indicating the high iron conten in the protein. Further enrichment of the bLTF with iron changes the color of the complex solution to red–brown (Fig. 5B). The d–d transitions result in a weak absorption band. In the case of Fe-bLTF, the band of d–d transition can be determined at ≈ 466 nm where after Fe^{3+} adsorption onto bLTF the slight increase of the light absorption, e.g. from 0.015 to 0.058, has been observed. More intense light absorption is connected to ligand-to-metal charge transfer and was detected at ≈ 280 nm[48]. Here, the increase of absorption from 0.52 to 1.436 has occurred after Fe^{3+} binding to bLTF which indicates the involvement of tyrosines and tryptophans in metal-protein interactions.

The UV–Vis spectroscopy is indicative of the quantity of bonded iron and thus can be utilized for the investigation of the sorption process. For instance, a methodology for the determination of bLTF saturation with iron was proposed by Majka et al.[49]. The UV-difference spectroscopy was also useful for the study of preferential binding of certain metal ions to Ova-transferrin[50]. However, it rather will not be useful for the determination of bLTF iron supersaturation, e.g. additional studies should be performed to outline the regions with linear correlation.

The changes in protein color and absorbance in UV–VIS were helpful for the control of the Fe^{3+} desorption process (Fig. 5C). Iron desorption was performed in three different buffers, namely 0.1 M hydrochloric acid (pH 1.2) and phosphate buffers with pH 4.5 and 6.8. The respective buffers usually are utilized in pharmacies for the imitation of conditions in a different part of the digestive tract. After 2 h of the desorption process, the changes in the protein color have occurred at pH 4.5 and 1.2—it becomes less intense in the first case and disappeared in the second case (Fig. 5D). We were able to observe the respective changes in the UV–Vis spectra of protein after iron desorption at pH 1.2. The absorbance intensity of protein after desorption at pH 6.8 has not changed. Instead, at pH 4.5 the formation of iron phosphate precipitate has occurred which disturbs both the UV–Vis and ICP-MS analysis of the process.

The ICP-MS quantification has revealed that at pH 6.8 Fe-bLTF released only 1.08 ± 0.26% of iron which is on the level of allowed measurement error, indicating the formation of a relatively stable complex. Instead, the acidification of the solution promotes iron release. The iron desorption at pH 1.2 was estimated as 57.97 ± 3.48%. Our previous study revealed that iron release also can be promoted by the addition of other chelating agents or competing ions. The presence of citrate and zinc ions caused the iron release from holo-lactoferrin even in the basic environment of pH 7.4 and 8.6[25]. It is worthy to mention, that the intraluminal pH of the duodenum normally is near 6 which means that majority of Fe^{3+} may remain bonded in the Fe-bLTF complex in such conditions. However, the presence of other components in the food can promote iron release from the complex. Thus, further studies should be performed for the assessment of the stability of Fe-bLTF complexes and thus iron bioavailability from such preparations.

Cytotoxicity study of bLTF. The comparison between cytotoxicity of Fe-bLTF with iron citrate was performed at the same iron concentration in mM (determined by ICP-MS). For studies, the L929 cell line and Caco-2 cell line were selected. L929 is a normal murine fibroblast-derived cell line which is recommended by ISO norms (EN ISO 10,993–5, ISO 10,993–12) for the biological evaluation of new medical devices. Caco-2 is a cell line derived from human caucasian colon adenocarcinoma and shows great similarity to enterocytes—intestinal absorptive cells. The results for cytotoxicity evaluation are presented in Fig. 6.

Our investigation has revealed that both iron forms, i.e. complexed with bLTF and iron citrate, at the concentration of up to 0.5 mM did not decrease the viability of the Caco-2 and L929 lines in MTT test (Fig. 6). On the other hand, the concentration of 1 mM caused a slight decrease in the viability of L929 cells to ca. 70%. Similar results were obtained for iron chloride on BALB/c and HepG2 cells. Line HepG2 was more sensitive to iron chloride than BALB/c and its viability at concentration 1 mM was ca. 60%. In studies of He et al.[51] viability of Caco-2 cells was not limited by the concentration of iron chloride to 1 mM. Although the lower concentrations did not show a decrease in viability of L929 cells, the LDH test has shown an increase in the permeability of cell membranes similar to BALB/c and HepG2 when treated with iron chloride[52]. This phenomenon was not observed for Caco-2 cells. Both, iron complexed with bLTF and citrate did not increase the level of released LDH what means that did not adversely affect the integrity of the membranes.

Summing up, the synthesized Fe-bLTF complex does not have more negative effects on cells than the commonly used supplement of iron. In subsequent studies, it will be necessary to analyze the bioavailability of the obtained complex across the intestinal barrier and its potential with lactoferrin receptor binding. It seems that due to the presence of LTF receptors on the surface of Caco-2 cells, even small amounts of the complex should promote the absorbance of iron from the environment and improve health indicators in iron deficiency disorders.

In conclusion, we have synthesized the iron-rich Fe-bLTF complex. The batch sorption analysis was shown to be useful for the description of metal binding processes. Moreover, the derived sorption parameters can be utilized for the selection of the synthesis conditions and the prediction of final product properties. The study also revealed that during the synthesis some amount of protein can undergo oxidation and oligomerization. Moreover, the changes in protein structure with formation of more compact arrangement was observed. The synthesized complex did not release Fe^{3+} at pH 6.8, common for the duodenum. Additionally, the cytotoxicity study has shown that obtained complex at the concentration of Fe^{3+} up to 0.5 mM did not decrease the viability of the Caco-2 and L929 lines. The toxicity of the Fe-bLTF complex was not higher than the toxicity of iron citrate. Thus, the synthesized complex potentially can be used as dietary supplement in treatment of IDA.

Materials and methods
Chemicals and materials.
Sigma-Aldrich (Steinheim, Germany) has supplied the following chemicals and materials: lactoferrin from bovine milk (bLTF), ammonium iron (III) citrate, sodium chloride, sodium hydroxide, MS-grade nitric acid, hydrochloric acid, potassium dihydrogen phosphate, Amicon® Ultra Centrifugal membrane filters, ICP multi-element standard solution IV and Scandium standard solution for ICP, trypsin, fetal bovine serum (FBS), Dulbecco's Modified Eagle's Medium (DMEM), phosphate-buffered saline (PBS), EDTA, penicillin–streptomycin solution, L929 normal mouse fibroblast cells and Caco-2 cells, MTT assay kit and LDH release assay kit. Invitrogen Bolt™ 4–12% Bis–Tris Plus polyacrylamide gel 12 wells, Simply Blue™ Safe Stain (Coomassie G$_{250}$ stain), MES running buffer, Load sample buffer, and Sample reducing agent were obtained from TermoFisher Scientific (Waltham, MA, USA). Perfect™ Color Protein Ladder was from EUR$_X$ Sp. z o.o. (Gdansk, Poland). The set of automatic pipettes and laboratory plastics were obtained from Eppendorf (Hamburg, Germany). Moreover, deionized water was obtained with Milli-Q RG system from Millipore (Millipore Intertech, Bedford, MA, USA).

Methods.
Preparation of Fe^{3+} and protein solutions for the batch sorption study and complex synthesis. To simplify the description of possible processes that may take place during interaction as the reaction medium 0.09% NaCl was utilized. The presence of salt was utilized to improve protein solubility and stability, while NaCl has shown to have no pH dependence of the preferential interaction[53]. bLTF was suspended in 0.09% NaCl solution to concentration of 5 mg/mL. For the study, bLTF standard purchased from Sigma-Aldrich (Steinheim, Germany) was utilized. Before the study, the physicochemical characterization of the bLTF was performed, among others, the iron content was determined. The results are presented in the O. Pryshchepa et al. (2022) article[1]. The bLTF from the same batch was utilized in both studies. Iron stock solution with a concentration of ≈ 6 g/L was prepared from ammonium iron (III) citrate by dissolution in deionized water. Subsequently, solutions containing appropriate Fe^{3+} concentrations were prepared from stock solution by dilution with 0.09% NaCl. The pH of all prepared solutions was adjusted to 7.4 with 0.1 M sodium hydroxide or 0.1 M hydrochloric acid.

Isotherm study of Fe^{3+} adsorption. 0.2 mL of bLTF suspension was transferred to a sample unit of Amicon® Ultra Centrifugal Filtres cut-off 3 kDa. Subsequently, 0.2 mL of Fe^{3+} solution with a concentration of ≈ 5, 10, 20, 30, 50, 100, 200, 300, 600, 800, 1100, 1400, and 1600 mg/L (the exact concentration was determined by ICP-MS) was added to the sample unit and obtained mixture was incubated at room temperature (T ≈ 23 °C) for 24 h. After the desired time has elapsed, the reaction was terminated by centrifugation (RT, 15 000 rpm, 5 min).The filtrate was subjected to ICP-MS analysis. The analyses were performed in triplicates. Here and later the dilutions for ICP-MS analyses were performed with 1% HNO$_3$ and. The analysis was performed on Shimadzu ICP-MS 2030 (Kyoto, Japan) with scandium as an internal standard. The calculations ofsorption parameters were performed as described in Pomastowski et al. and Pryshchepa et al.[22,54].

Molecular docking. 3D structure of diferric bLTF (code name 1BLF) was downloaded from https://www.rcsb.org website (accessed Apr 12, 2022). Experimental data snapshots for asmentioned structure were obtained by Moore, S.A. et al. with X-Ray diffraction method at 2.8 Å resolution[55]. Molegro Molecular Viewer 7 has been used to optimize the 3D structure of the protein. Metal Ion-Binding Site Prediction and Docking Server (MIB) was used for the analysis and visualization. Previously, the server was successfully used for the prediction of different metal ions binding to proteins, among others Fe^{3+} to desulfoferrodoxin from *Desulfovibriodesulfuricans*

(1DFX)[33]. Sites for Fe^{3+} and bLTF interactions proposed by the program were collected in the .pdb format and further visualized in the PyMol program.

Synthesis of Fe-lactoferrin complex. bLTF suspension was mixed with 600 mg/L Fe^{3+} solutions at the ratio 1:1 (v/v) and incubated with stirring for 24 h (T ≈ 23 °C). The obtained complex was separated and washed twice with deionized water to remove the electrolytes excess by utilization of membrane filters cut-off 3 kDa (Amicon® Ultra Centrifugal Filters). Subsequently, the synthesized product was lyophilized. The amount of iron in the complex was determined by ICP-MS analysis. Thus, nearly 1.5 mg of the complex was mineralized with 0.1 mL of MS-Grade nitric acid. Then, first dilution was performed with deionized water. The analyses were performed in triplicates.

Electron microscopy. Native bLTF and Fe-bLTF complex was dispersed in ethanol, placed on a carbon-coated copper grid (Lacey Carbon Support Film 400 mesh; Electron Microscopy Sciences), and dried at room temperature. Subsequently, the samples were subjected to analysis by transmission electron microscope (TEM) (FEI Tecnai F20 X- Twin, Hillsboro, OR, USA) coupled with an EDX detector.

SDS-PAGE analysis. Native bLTF and Fe-bLTF complex was suspended in deionized water to a concentration of 0.5 mg/mL. The protein solutions were analyzed with the utilization of 4–12% Bis–Tris Plus polyacrylamide gel (Thermo Scientific, Waltham, MA, USA) in reduced and non-reduced mode and applying MES Running Buffer according to the standard procedure recommended by the manufacturer. Gel staining was performed with Coomassie Blue R-350 ready-to-use stain.

Fourier transform infrared spectroscopic (FTIR) analysis. FTIR analysis was performed for both native bLTF and modified with Fe^{3+} in the MIR range (4000–400 cm^{-1}). The spectra were recorded with the utilization of attenuated total reflection (ATR) mode on Alpha FTIR spectrometer (Bruker, Billerica, Massachusetts, USA). Normalized FTIR spectra were plotted using the Origin software (v. 2015, OriginLab Corporation, Northampton, Massachusetts, USA).

UV–Vis spectroscopy. The UV–Vis spectra for native bLTF, for bLTF after Fe^{3+} sorption, as well as after desorption process were recorded with NanoDrop ND2000 UV–Vis spectrophotometer (TermoFisher Scientific, Waltham, MA, USA) in the range λ = 200 − 800. The spectra were plotted in MS Excel software.

Iron desorption study. Iron desorption tests were performed in three buffers, namely 0.1 M hydrochloric acid, phosphate buffers pH 4.5 and pH 6.8, which imitates the conditions in different parts of the digestive tract[56]. Nearly 1.5 mg of the complex was suspended in 0.5 mL of the buffer and incubated for 2 h. Subsequently, mixtures were filtrated with Amicon® Ultra Centrifugal Filtres cut-off 3 kDa. The iron content in the filtrate was determined by ICP-MS analysis. The analyses were performed in triplicates.

Fe-bLTF cytotoxicity study. L929 cell line of mouse fibroblasts and Caco-2 cell line of Caucasian colon adenocarcinoma from European Collection of Authenticated Cell Cultures operated by Public Health England (Sigma) were cultured in DMEM supplemented with 10% (v/v) fetal bovine serum, 2 mM glutamine, and 100 U/mL penicillin, and 100 µg/mL streptomycin (Sigma). These cell lines were cultured in 75 cm^2 flasks at 37 °C and 5% CO^2. The cells were harvested by trypsinization using 0.25% trypsin/EDTA every 3–4 days.

For MTT and LDH release assays, cells were cultured on 96-well plates at density 2×10^5 cells/mL and incubated for 24 h. Then, the medium was replaced with a new one containing Fe^{3+} of the appropriate concentration and incubated for 24 h. Then 10% (v/v) of Thiazolyl Blue Tetrazolium Bromide (MTT) solution (5 mg/mL in PBS) was added and incubated for 4 h at 37 °C. Next, the medium from wells was removed and the formazan crystals were dissolved in DMSO for 10 min by mixing. Absorbance was measured using a microplate reader (Multiskan, ThermoFisher) at 570 nm and 650 nm as background absorbance.

The LDH release assay was performed using a commercially available kit from Sigma Aldrich (Lactate Dehydrogenase Activity Assay Kit MAK066) under the standard procedure provided by the supplier. Results are presented in milliunits per mL of medium.

Data availability
All data generated or analyzed during this study are included in this published article.

References
1. Ortiz, Y., García-Amézquita, E., Acosta, C. H. & Sepúlveda, D. R. Functional dairy products. In *Global Food Security and Wellness* (eds Barbosa-Cánovas, G. V. *et al.*) 67–103 (Springer, New York, 2017).
2. Moughan, P. J. Milk proteins: A rich source of bioactives for developing functional foods. In *Milk Proteins* 633–649 (Elsevier, Amsterdam, 2020).
3. Takayama, Y. *Lactoferrin and its Role in Wound Healing* (Springer, Netherlands, 2012).
4. Vogel, H. J. Lactoferrin, a bird's eye view. *Biochem. Cell Biol.* **90**, 233–244 (2012).
5. Shubham, K. *et al.* Iron deficiency anemia: A comprehensive review on iron absorption, bioavailability and emerging food fortification approaches. *Trends Food Sci. Technol.* **99**, 58–75 (2020).

6. Haschka, D., Hoffmann, A. & Weiss, G. Iron in immune cell function and host defense. *Semin. Cell Dev. Biol.* **115**, 27–36 (2021).
7. Abu Hashim, H., Foda, O. & Ghayaty, E. Lactoferrin or ferrous salts for iron deficiency anemia in pregnancy: A meta-analysis of randomized trials. *Eur. J. Obstet. Gynecol. Reprod. Biol.* **219**, 45–52 (2017).
8. Shin, K., Wakabayashi, H., Yamauchi, K., Yaeshima, T. & Iwatsuki, K. Recombinant human intelectin binds bovine lactoferrin and its peptides. *Biol. Pharm. Bull.* **31**, 1605–1608 (2008).
9. Davidson, L. A. & Lonnerdal, B. Fe-saturation and proteolysis of human lactoferrin: Effect on brush-border receptor-mediated uptake of Fe and Mn. *Am. J. Physiol. Gastroint. Liver Physiol.* **257**(6), 930–934 (1989).
10. Kincaid, R. L., Blauwiekel, R. M. & Cronrath, J. D. Supplementation of copper as copper sulfate or copper proteinate for growing calves fed forages containing molybdenum. *J. Dairy Sci.* **69**, 160–163 (1986).
11. Ma, X. Y. *et al.* Relative bioavailability of iron proteinate for broilers fed a casein-dextrose diet. *Poult. Sci.* **93**, 556–563 (2014).
12. Paik, I., Lee, H. & Park, S. Effects of organic iron supplementation on the performance and iron content in the egg yolk of laying hens. *J. Poult. Sci.* **46**, 198–202 (2009).
13. Dalev, P. G. Utilization of waste whey as a protein source for production of iron proteinate: An antianaemic preparation. *Biores. Technol.* **48**, 75–77 (1994).
14. Shilpashree, B. G., Arora, S., Sharma, V. & Singh, A. K. Preparation of succinylated sodium caseinate–iron complex by adopting ultrafiltration technology: A novel food fortificant. *Innov. Food Sci. Emerg. Technol.* **32**, 165–171 (2015).
15. Shilpashree, B. G., Arora, S., Sharma, V., Bajaj, R. K. & Tomar, S. K. Preparation of iron bound succinylated milk protein concentrate and evaluation of its stability. *Food Chem.* **196**, 800–807 (2016).
16. Basak, S. & Singhal, R. S. Succinylation of food proteins- a concise review. *LWT* **154**, 112866 (2022).
17. Baker, E. N. Structure and reactivity of transferrins. *Adv. Inorg. Chem.* **41**, 389–469 (1994).
18. Kawakami, H., Dosako, S. & Nakajima, I. Effect of lactoferrin on iron solubility under neutral conditions. *Biosci. Biotechnol. Biochem.* **57**, 1376–1377 (1993).
19. Nagasako, Y., Saito, H., Tamura, Y., Shimamura, S. & Tomita, M. Iron-binding properties of bovine lactoferrin in iron-rich solution. *J. Dairy Sci.* **76**, 1876–1881 (1993).
20. Ndayisaba, A., Kaindlstorfer, C. & Wenning, G. K. Iron in neurodegeneration–cause or consequence?. *Front. Neurosci.* **13**, 180 (2019).
21. Kumar, K. V. *et al.* Characterization of the adsorption site energies and heterogeneous surfaces of porous materials. *J. Mater. Chem. A* **7**, 10104–10137 (2019).
22. Pryshchepa, O. *et al.* A new approach for spontaneous silver ions immobilization onto casein. *Int. J. Mol. Sci.* **20**, 3864 (2019).
23. Buszewski, B. *et al.* Interactions of zinc aqua complexes with ovalbumin at the forefront of the Zn2+/ZnO-OVO hybrid complex formation mechanism. *Appl. Surf. Sci.* **542**, 148641 (2021).
24. Sprynskyy, M., Kowalkowski, T., Tutu, H., Cukrowska, E. M. & Buszewski, B. Adsorption performance of talc for uranium removal from aqueous solution. *Chem. Eng. J.* **171**, 1185–1193 (2011).
25. Pryshchepa, O. *et al.* Synthesis and physicochemical characterization of zinc-lactoferrin complexes. *J. Dairy Sci.* https://doi.org/10.3168/jds.2021-20538 (2022).
26. Al-Ghouti, M. A. & Da'ana, D. A. Guidelines for the use and interpretation of adsorption isotherm models: A review. *J. Hazard. Mater.* **393**, 122383 (2020).
27. Buszewski, B., Rodzik, A., Railean-Plugaru, V., Sprynskyy, M. & Pomastowski, P. A study of zinc ions immobilization by β-lactoglobulin. *Colloids Surf. A* **591**, 124443 (2020).
28. Bou-Abdallah, F. & Giffune, T. R. The thermodynamics of protein interactions with essential first row transition metals. *Biochim. Biophys. Acta (BBA) Gen. Subj.* **1860**, 879–891 (2016).
29. Feig, A. L. & Lippard, S. J. Reactions of non-heme Iron(II) centers with dioxygen in biology and chemistry. *Chem. Rev.* **94**, 759–805 (1994).
30. Pan, Y. H. *et al.* 3D morphology of the human hepatic ferritin mineral core: New evidence for a subunit structure revealed by single particle analysis of HAADF-STEM images. *J. Struct. Biol.* **166**, 22–31 (2009).
31. Ghosh, S., Mukherjee, A., Sadler, P. J. & Verma, S. Periodic iron nanomineralization in human serum transferrin. 2217–2221 https://doi.org/10.1002/anie.200705723 (2008).
32. Booyjžsen, C. *et al.* Fibrillation of transferrin. *Biochim. Biophys. Acta (BBA) Gen. Subj.* **1820**(3), 427–436 (2012).
33. Lin, Y.-F. *et al.* MIB: Metal Ion-binding site prediction and docking server. *J. Chem. Inf. Model.* **56**, 2287–2291 (2016).
34. Gurd, F. R. N. & Wilcox, P. E. Complex formation between metallic cations and proteins, peptides, and amino acids. *Adv. Protein Chem.* **11**, 311–427 (1956).
35. Voswinkel, L., Vogel, T. & Kulozik, U. Impact of the iron saturation of bovine lactoferrin on adsorption to a strong cation exchanger membrane. *Int. Dairy J.* **56**, 134–140 (2016).
36. Marangon, M., van Sluyter, S. C., Waters, E. J. & Menz, R. I. Structure of haze forming proteins in white wines: Vitis vinifera thaumatin-like proteins. *PLoS ONE* **9**, e113757 (2014).
37. Shahnawaz Khan, M., Tabrez, S., Rehman, M. T. & Alokail, M. S. Al (III) metal augment thermal aggregation and fibrillation in protein: Role of metal toxicity in neurological diseases. *Saudi J. Biol. Sci.* **27**, 2221–2226 (2020).
38. Wang, K. *et al.* Self-assembled IR780-loaded transferrin nanoparticles as an imaging, targeting and PDT/PTT agent for cancer therapy. *Nat. Publ. Group* https://doi.org/10.1038/srep27421 (2016).
39. Evanoff, D. D. & Chumanov, G. Synthesis and optical properties of silver nanoparticles and arrays. *ChemPhysChem* **6**, 1221–1231 (2005).
40. Adam, F. I., Bounds, P. L., Kissner, R. & Koppenol, W. H. Redox properties and activity of iron – citrate complexes: Evidence for redox cycling. *Chem. Res. Toxicol.* **28**, 604–614 (2015).
41. Rose, A. L. The influence of extracellular superoxide on iron redox chemistry and bioavailability to aquatic microorganisms. *Front. Microbiol.* **3**, 124 (2012).
42. Nandiyanto, A. B. D., Oktiani, R. & Ragadhita, R. How to read and interpret FTIR spectroscope of organic material. *Indones. J. Sci. Technol.* **4**, 97 (2019).
43. Sibert, E. L. III., Tabor, D. P. & Lisy, J. M. Modeling the CH stretch vibrational spectroscopy of M+ [cyclohexane](M= Li, Na, and K) ions. *J. Phys. Chem. A* **119**(41), 10293–10299 (2015).
44. Barth, A. Infrared spectroscopy of proteins. *Biochim. Biophys. Acta (BBA) Bioenerg.* **1767**, 1073–1101 (2007).
45. Socrates, G. G. *Infrared and Raman Characteristic Group Frequencies: Tables and Charts. Infrared and Raman Characteristic Group Frequencies Contents: Tables and Charts* (John Wiley & Sons Ltd, Hoboken, 2004).
46. Singh, B. R., DeOliveira, D. B., Fu, F.-N. & Fuller, M. P. Fourier transform infrared analysis of amide III bands of proteins for the secondary structure estimation. *Biomol. Spectrosc. III* **1890**, 47–55 (1993).
47. Kozłowicz, K. *et al.* Identification of sugars and phenolic compounds in honey powders with the use of GC–MS, FTIR spectroscopy, and X-ray diffraction. *Sci. Rep. 2020* **10**, 1–10 (2020).
48. Atkins, P. W., Overton, T. L., Rourke J. P., Weller, M. T., and Armstrong, F. A. d-Metal complexes: Electronic structure and properties in *Shriver & Atkins' Inorganic chemistry*. 473–506 (Oxford University Press, 2010).
49. Majka, G. *et al.* A high-throughput method for the quantification of iron saturation in lactoferrin preparations. *Anal. Bioanal. Chem.* **405**, 5191–5200 (2013).

50. Saponja, J. A. & Vogel, H. J. Quadrupolar central transition (QCT) and 13C NMR competition studies of metal ion binding to ovotransferrin. *Can. J. Chem.* **89**, 779–788 (2011).
51. He, W., Feng, Y., Li, X., Wei, Y. & Yang, X. Availability and toxicity of Fe(II) and Fe(III) in Caco-2 cells. *J. Zhejiang Univ. Sci. B* **9**(9), 707–712 (2008).
52. Terpilowska, S. & Siwicki, A. K. Interactions between chromium (III) and iron (III), molybdenum (III) or nickel (II): Cytotoxicity, genotoxicity and mutagenicity studies. *Chemosphere* **201**, 780–789 (2018).
53. Arakawa, T. & Timasheff, S. N. Mechanism of protein salting in and salting out by divalent cation salts: Balance between hydration and salt binding. *Biochemistry* **23**, 5912–5923 (1984).
54. Pomastowski, P. *et al.* Silver-lactoferrin nanocomplexes as a potent antimicrobial agent. *J. Am. Chem. Soc.* **138**, 7899–7909 (2016).
55. Moore, S. A., Anderson, B. F., Groom, C. R., Haridas, M. & Baker, E. N. Three-dimensional structure of diferric bovine lactoferrin at 2.8 Å resolution. *J. Mol. Biol.* **274**, 222–236 (1997).
56. Recommendations on dissolution testing in *European Pharmacopoeia 7.0 volume 1*. 665–667 (European Directorate for the Quality of Medicines & HealthCare, Council of Europe Publishing, 2011), ISBN 978-9287167002.

Acknowledgements

Author contributions

O.P: conceptualization, investigation, data curation, formal analysis, methodology, validation, visualization, writing original draft preparation, writing—review & editing; K.R.: investigation, data curation, formal analysis, methodology, visualization, validation, writing original draft preparation, writing—review & editing; A.G.: investigation, data curation, formal analysis, validation, G.S.: data curation, visualization, formal analysis, writing—review & editing; P.M.: data curation, formal analysis; B.B.: resources; visualization; P.P.: conceptualization, project administration, supervision, funding acquisition, writing—review & editing.

Competing interests

The authors declare no competing interests.

Additional information

Supplementary Information The online version contains supplementary material available at https://doi.org/10.1038/s41598-022-15814-2.

Correspondence and requests for materials should be addressed to O.P.

Reprints and permissions information is available at www.nature.com/reprints.

Publisher's note Springer Nature remains neutral with regard to jurisdictional claims in published maps and institutional affiliations.

6.4 Synthesis and physicochemical characterization of zinc-lactoferrin complexes

O. Pryshchepa, G. Sagandykova, J. Rudnicka, P. Pomastowski, S. Sprynskyy, B. Buszewski

Synthesis and physicochemical characterization of zinc-lactoferrin complexes

Oleksandra Pryshchepa,[1,2] **Gulyaim Sagandykova,**[1] **Joanna Rudnicka,**[1,2] **Paweł Pomastowski,**[1]
Myroslav Sprynskyy,[2] **and Bogusław Buszewski**[1,2]*

[1]Centre for Modern Interdisciplinary Technologies, Nicolaus Copernicus University in Toruń, Wileńska 4, 87-100 Toruń, Poland
[2]Department of Environmental Chemistry and Bioanalytics, Faculty of Chemistry, Nicolaus Copernicus University in Toruń, Gagarina 7, 87-100 Toruń, Poland

ABSTRACT

One trend of the modern world is the search for new biologically active substances based on renewable resources. Milk proteins can be a solution for such purposes as they have been known for a long time as compounds that can be used for the manufacturing of multiple food and non-food products. Thus, the goal of the work was to investigate the parameters of Zn-bovine lactoferrin (bLTF) interactions, which enables the synthesis of Zn-rich protein complexes. Zinc-bLTF complexes can be used as food additives or wound-healing agents. Methodology of the study included bLTF characterization by sodium dodecyl sulfate-PAGE, MALDI-TOF, and MALDI-TOF/TOF mass spectrometry as well Zn-bLTF interactions by attenuated total reflection-Fourier-transform infrared, Raman spectroscopy, scanning and transmission microscopy, and zeta potential measurements. The obtained results revealed that the factors that affect Zn-bLTF interactions most significantly were found to be pH and ionic strength of the solution and, in particular, the concentration of Zn^{2+}. These findings imply that these factors should be considered when aiming at the synthesis of Zn-bLTF metallocomplexes.

Key words: bovine lactoferrin, zinc-lactoferrin interactions, whey proteins, metallocomplexes

INTRODUCTION

The connection between the quality of food and health has led to development of "functional foods," which implies the search and modification of naturally occurring compounds. Dairy products and their derivates are considered healthy and safe to consume, thus making them an attractive source for manufacturing new value-added goods (Ortiz et al., 2017). Proteins are the most valuable components of dairy products, and thus the production of food additives and supplements based on milk proteins is of high interest among dietitians, scientists, and food producers. Additionally, the utilization of milk proteins for the production of antibacterial agents is considered (Pomastowski et al., 2016; Buszewski et al., 2021).

Lactoferrin (**LTF**) is one of the most attractive milk proteins. Lactoferrin is a multifunctional protein belonging to the family of transferrins, which are non-heme iron-binding glycoproteins (Takayama, 2012). The transferrin family in mammals comprises serum transferrin (**TR**), LTF, and melanotransferrin (Baker, 1994). The main functions of both TR and LTF are Fe^{3+} transport and regulation. However, a more important function of the LTF is the host immune response for infection or inflammation (Lambert, 2012). The wide spectrum of biological activity of LTF also includes antimicrobial (Yoshida et al., 2000), antiviral (Waarts et al., 2005), antifungal (Andersson et al., 2000), immunoregulatory, and antiinflammatory properties (Grigorieva et al., 2019). Additionally, LTF plays a role in cell proliferation and migration; among others, topical administration of bLTF enhances wound closure (Takayama, 2012). What is interesting is that intravenously injected bovine lactoferrin (**bLTF**) was shown to be able to cross the blood-brain barrier (Takayama, 2012). Studies on adult mice have shown that bLTF given orally can absorb effectively from the intestine in an unchanged state (Fischer et al., 2007). Thus, the unique properties of LTF are the reason for the extensive investigations into LTF as a potential active drug substance (Wang, 2016; Sabra and Agwa, 2020). Lactoferrin can be used in pharmaceutical preparations with a wide spectrum of therapeutic effects: promotion of microelements absorption, boosting of the immune system, improvement of wound healing, including infected wounds, and so on. Indeed, preparations containing bLTF have already been developed. However, they usually are in the form of a mechanical

117

mixture of zinc salts and LTF, which may not be as effective as Zn-protein complexes.

Zinc is an indispensable microelement that ensures numerous functions of an organism: protein structural component (zinc fingers and related motifs), co-factor of enzymes, signaling mediator, and so on (Kambe et al., 2015; Santos et al., 2020). Zinc deficiency is an issue in both developing and developed countries and is a subject of numerous research (Santos et al., 2020). The bioavailability of microelements is highly dependent on the form in which they are provided to the organism (Kawakami et al., 1993; Ianni et al., 2019). Increased bioavailability is observed for microelements in form of proteinates (Tang and Skibsted, 2016; Ianni et al., 2019). For instance, the Zn^{2+} and Fe^{2+} complexation with whey proteins significantly increased their uptake by Caco-2 cells as compared with inorganic salts (Shilpashree et al., 2020). Moreover, Zn^{2+} ions exhibit antibacterial properties (Bong et al., 2010; McDevitt et al., 2011), and in combination with bLTF may have a synergistic effect against a wide spectrum of microorganisms. Thus, such Zn-bLTF complexes may also have potential in wound healing preparations and can be a solution in the search for value-added goods derived from milk.

The metal-binding function of the transferrins is determined by their structure (i.e., by the presence of 2 intramolecular iron-binding sites comprising 2 tyrosines, aspartic acid, and histidine; Mizutani et al., 2012; Takayama, 2012). Apart from iron, the transferrins can reversibly bind other metals, and thus are suggested to play role in the metabolism of other metals, such as aluminum, manganese, copper, and zinc (Baker, 1994). Interestingly, Ainscough et al. (1980) reported that in human milk LTF appears with loosely bonded zinc, where zinc to protein ratio has the same order as iron to protein ratio. This may indicate the similar significance of LTF for zinc absorption as for iron. It is noteworthy to mention that the meaning of "saturated" regarding metalloproteins most often implies only the state when structurally defined metal-binding sites are filled. However, it was revealed that depending on conditions LTF can bind much more Fe^{3+} than can be explained only by the presence of intramolecular binding sites (Kawakami et al., 1993). For Zn^{2+}, it was shown that at least 2 additional metal-binding sites can appear at pH 8.6 on the surface of the C-lobe separated from LTF (Jabeen et al., 2005).

The process of metal ions binding to proteins is studied intensively as it is important and required for the understanding of the mechanisms of protein activity (e.g., catalytic), structural stability, and functional regulations (Gurd and Wilcox, 1956; Bou-Abdallah and

Giffune, 2016). However, such studies mostly include only the process of the metals embedding into intramolecular binding sites. Nevertheless, the data indicate that zinc binding sites in proteins often include different combinations of histidines and cysteines. Moreover, glutamic and aspartic acid also can be involved in the chelation of the Zn^{2+} in proteins (Auld, 2013). What is interesting is that one of the action mechanisms of zinc in enzymes is the "water activation" by lowering its dissociation constant pK. Thus, zinc, while binding to protein, still can have water molecules in its coordination sphere (Auld, 2013; Bou-Abdallah and Giffune, 2016). Little information was found in the literature about the interaction of zinc with proteins through functional groups oriented to the surface of the protein. According to the existing knowledge, regardless of other conditions, stable Zn^{2+} complexes with proteins require the involvement of nitrogen-containing groups for metal chelation (Gurd and Wilcox, 1956; Yamauchi et al., 2002; Bou-Abdallah and Giffune, 2016; Alhazmi, 2019). Interestingly, the ability of Zn^{2+} to lower the pK of coordinated water molecules can lead to its dissociation and formation of ZnO. Such a feature of zinc was the reason for the formation of ZnO-protein nanocomposites, which were synthesized with the utilization of whey proteins (Shi et al., 2008) and ovalbumin (Buszewski et al., 2021). However, it should be noted that nanocomposites generally have a wider spectrum of toxic effects than other forms of metal compounds. The formation of homogeneous Zn-protein complexes was observed with the utilization of β-LG (Buszewski et al., 2020) and caseins (Pomastowski et al., 2014). The abovementioned facts indicate the need for the comprehensive study of the Zn-protein complexes formation.

Hence, the study aimed to investigate the parameters of Zn-bLTF interactions that enable the synthesis of homogeneous Zn-rich complex. One of the basic assumptions taken into account during the study was the formation of the Zn-bLTF complexes at any of the investigated conditions. The present study can be considered as an indispensable first step for the investigation of Zn-bLTF complexes as possible food additives for managing zinc deficiency or agents that promote wound healing, including infected wounds.

MATERIALS AND METHODS

Chemicals and Materials

The chemicals and materials used were of the highest available purity offered by suppliers. Standard lactoferrin from bovine milk (bLTF), ultrapure water

(liquid chromatography-MS purity >99%), acetonitrile, trifluoroacetic acid, ammonium bicarbonate, sodium bicarbonate, ammonium citrate dibasic, tri-sodium citrate dihydrate, sinapinic acid (**SA**), sodium chloride, sodium hydroxide, nitric acid, zinc nitrate hexahydrate, hydrochloric acid, dithiothreitol, iodoacetamide, Amicon Ultra Centrifugal membrane filters, ICP multielement standard solution IV, Zinc standard solution for ICP, and Scandium standard solution for ICP were purchased from Sigma-Aldrich. Invitrogen Bolt 4–12% Bis-Tris Plus polyacrylamide gel 10 and 12 wells, Simply Blue Safe Stain (Coomassie G_{250} stain), SeeBlue Plus 2 Pre-Stained Protein Standard, MES running buffer, load sample buffer, and sample reducing agent were supplied by ThermoFisher Scientific. Peptide calibration standard II, protein calibration standard II, α-cyano-4-hydroxycinnamic acid (**HCCA**), Anchor-Chip, and GroundSteel target plates were obtained from Bruker Daltonics. A set of automatic pipettes and all laboratory plastics were obtained from Eppendorf. Moreover, trypsin for protein MS from Promega was used. Deionized water was obtained with the Milli-Q RG system from Millipore (Millipore Intertech).

Characterization of LTF

Zeta Potential Measurements and Isoelectric Point Determination. Zeta (ζ) potential measurements were performed on a Malvern Zetasizer NanoZS (Malvern) using a DTS1070 cuvette (Malvern). The analysis was carried out in the automatic selection mode of voltage and number of runs. The results were obtained taking into account the Smoluchowski approximation (Oćwieja et al., 2015):

$$\zeta = \eta\mu_e/\varepsilon_r\varepsilon_0 , \qquad [1]$$

where η = solution viscosity; μ_e = electrophoretic mobility; ε_0 = electric permeability in vacuum, and ε_r = dielectric constant of the solution.

Each measurement was performed in triplicate. For isoelectric point (**pI**) determination, the zeta potential was measured as a function of pH. The potentiometric acid-base titration in the pH range from 4.0 to 9.0 was performed with the utilization of 1 mg/mL of bLTF solution obtained by protein suspension in 0.09% NaCl. The pH adjustment was performed by a dropwise addition of 0.1 *M* hydrochloric acid or 0.1 *M* sodium hydroxide solutions. Here and later, the pH of the solutions was determined using the FiveEasy Plus pH meter (Mettler Toledo) with a combined electrode with glass membrane and Ag/AgCl reference system (Mettler Toledo). Before the measurements, the pH meter

was calibrated by standard buffered solutions with pH values 4.0, 7.0, and 10.0.

Intact Protein Analysis by MALDI-TOF-MS. Sinapinic acid was used as a matrix for MALDI analysis. Intact protein was suspended in the 0.1% trifluoroacetic acid to a concentration of 10 mg/mL. The saturated solution of SA was prepared in the TA30 solvent [30:70 (vol/vol) acetonitrile:0.1% trifluoroacetic acid]. Then, 1 µL of the samples was applied on the GroundSteel target plate by dried droplet technique with utilization of 1 µL of the matrix solution. Protein calibration standard II was used for mass calibration. All the MS spectra were obtained using the MALDI-TOF/TOF mass spectrometer UltrafleXtreme (Bruker Daltonics) equipped with modified neodymium-doped yttrium aluminum garnet (Nd:YAG) laser operating at a wavelength of 355 nm and frequency of 2 kHz. The system was controlled using the Bruker Daltonics software (flexControl and flexAnalysis). The MS spectra were obtained in the linear positive mode in an m/z range of 10,000 to 100,000, applying an acceleration voltage of 25 kV and the minimum laser power of 60% and attenuation of 50%. Spectra were acquired by summing up 3 individual spectra obtained with 500 laser shots each and were plotted using the Origin software (v. 2015, OriginLab Corp.) from raw data without any modifications.

SDS-PAGE Coupled to Protein In-Gel Tryptic Digestion and MALDI-TOF/TOF-MS Analysis. The SDS-PAGE separation was carried out by the standard procedure recommended by the manufacturer. In-gel tryptic digestion was carried out by procedure described in the study by Shevchenko et al. (2006) with only one modification [i.e., the digestion step was performed by the protocol recommended by the producer of trypsin (Promega)]. For MALDI-TOF/TOF-MS analysis, the HCCA was used as a matrix. The matrix solution was prepared as follows: HCCA was dissolved in a mixture containing 85% acetonitrile, 15% ultrapure water, and 0.1% trifluoroacetic acid to a final concentration of 1.4 mg/mL. One microliter of the protein tryptic digest solutions was applied on an AnchorChip target plate by dried droplet technique with the utilization of 1 µL of the matrix solution. Peptide calibration standard II (Bruker Daltonics) was used for mass calibration. The MS spectra for protein digests (peptide fingerprints mass spectra) were recorded in a reflectron positive mode in the range of m/z 500 to 3,500. The measurements were performed with the utilization of acceleration voltage of 25 kV, minimum laser power of 80%, and attenuation of 27%. Spectra were acquired by summing up 3 individual spectra obtained with 500 laser shots each. The peptide spectra analysis was carried out using the BioTools and ProteinScape software

(Bruker Daltonics). Protein identification was carried out by applying Mascot search with nonstandard search parameters (i.e., cysteine modified by carbamidomethylation) and mass tolerance was set to 0.1 Da.

Preparation of Samples for the Study of Zn-Lactoferrin Interactions

The Zn-bLTF interaction study was performed in 3 different buffers, namely 0.09% sodium chloride solution pH 6.0; 0.1 M ammonium bicarbonate/ammonium citrate buffer, pH 7.4; and 0.1 M sodium citrate/sodium, bicarbonate buffer, pH 8.6. Each of the buffers was prepared as follows: sodium chloride was dissolved in deionized water and adjusted to pH 6.0 with 0.1 M sodium hydroxide or 0.1 M hydrochloric acid; 0.1 M ammonium bicarbonate was prepared in deionized water and adjusted to pH 7.4 with 0.1 M ammonium citrate solution; and 0.1 M sodium bicarbonate and 0.1 M trisodium citrate were prepared in deionized water, mixed (1:1, vol/vol), and adjusted to pH 8.6 with 0.1 M sodium hydroxide solution. The bLTF was suspended in the buffers to gain the concentration of 5 mg/mL (by weight). The Zn^{2+} solutions were obtained from stock (6 g/L prepared from $ZnNO_3$ in deionized water) by dilution in the buffers to obtain solutions with a metal concentration of 6, 60, and 600 mg/L (the exact Zn^{2+} concentrations were measured by ICP-MS). The bLTF and Zn^{2+} solutions were mixed at the ratio 1:1 (vol/vol) and incubated with stirring for 24 h at room temperature ($\approx$23°C). The protein after interaction with Zn^{2+} (product of interaction) was separated and washed twice with ultrapure water to remove the electrolytes excess by utilization of membrane filters cut-off 3 kDa (Amicon Ultra Centrifugal Filters). The obtained products were lyophilized and subjected to analysis. Moreover, the obtained first supernatant was analyzed for the determination of the Zn^{2+} adsorption capacity of protein.

Characterization of Prepared Samples

ICP-MS Analysis. Metal quantification in the solutions was performed on a Shimadzu ICP-MS 2030 with scandium as an internal standard. Determination of the metal content in bLTF and the products of Zn-bLTF interactions were carried out on mineralized samples. Nearly 2 mg of the samples was placed in Eppendorf tubes and mixed with 100 μL of nitric acid. Then, the Eppendorf tubes were closed tightly and heated at 80°C for 3 h. The mineralized samples were quantitatively transferred to polypropylene tubes and diluted with

ultrapure water. Subsequent dilutions were performed with 1% HNO_3. The obtained solutions were subjected to inductively coupled plasma (**ICP**)-MS analysis.

For the determination of the metal adsorption capacity of protein, the equilibrium concentration of Zn^{2+} in the supernatant was determined. The supernatant dilutions were performed with 1% HNO_3 in polypropylene tubes. The adsorption capacity was calculated according to

$$q = \frac{(C_0 - C) \times V}{m}, \qquad [2]$$

where q is the amount of adsorbed Zn^{2+}, m is the mass of the protein dispersed in the reaction mixture (g), C_0 is the initial concentration of Zn^{2+} in the reaction mixture (mg/L), C is the equilibrium concentration of Zn^{2+} in the reaction mixture (mg/L), and V is the volume of the reaction mixture (L).

Fourier Transform Infrared Spectroscopy. Fourier transform infrared spectroscopy (**FTIR**) analysis was performed for verification of the changes as a result of bLTF interactions with Zn^{2+}. Infrared spectra for both native bLTF and after incubation with Zn^{2+} in different conditions were recorded in the mid-infrared range (4,000–400 cm^{-1}). The spectra were collected with the utilization of attenuated total reflection (**ATR**) mode on Alpha FTIR spectrometer (Bruker). The FTIR spectra were plotted using the Origin software (v. 2015, OriginLab Corp.).

Raman Spectroscopy. Raman spectroscopy as a complementary technique for FTIR was performed to distinguish more precisely the functional groups that may be involved in the interactions between bLTF and Zn^{2+}. The bLTF and the products of Zn-bLTF interactions were placed on borosilicate microscope slides. The Raman spectra were recorded on Senterra II Dispersive Raman Microscope (Bruker) in the range of 4,000 to 400 cm^{-1}. The excitation wavelength at λ = 532 nm was used with a power of 20 mW. Raman spectra were plotted using the Origin software (v. 2015, OriginLab Corp.) and were normalized by a signal of the amide I band.

Electron Microscopy. The products of Zn-bLTF interaction dispersed in ethanol were placed on a carbon-coated copper grid (Lacey Carbon Support Film 400 mesh, Electron Microscopy Sciences), dried at room temperature, and subjected to analysis by transmission electron microscopy coupled with an energy-dispersive X-ray spectrometer (TEM-EDX-FEI Tecnai F20 X-Twin) and scanning electron microscopy (LEO 1430 VP, LEO Electron Microscopy Ltd.).

RESULTS AND DISCUSSION

Interactions Between BLTF and Zinc

The bLTF was analyzed using gel electrophoresis with a 4 to 12% gradient. Numerous bands of proteins were observed in the range of 14 to 198 kDa (Figure 1). The obtained results indicated the presence of multiple impurities in the product as well as bLTF dimer. The supplier declared the purity of the standard to be not less than 85% by SDS-PAGE assay. This emphasizes the need to perform characterization of the target protein before the study of the interactions with metal ions. The presence of other proteins in the sample may affect the binding of the studied metal ions to the target protein. Interactions of the proteins from impurities can be assigned as interactions of the target protein with metal ions and lead to distorted interpretation of the results.

Ion-exchange chromatography is one of the most common techniques for the isolation and purification of bLTF (Ye et al., 2000; Yoshida et al., 2000). The high isoelectric point of bLTF (higher than 8; Takayama,

2012) enables its selective isolation from other whey proteins. Lactoperoxidase is another whey protein that has a pI value (9.2–9.9) and molecular weight close to bLTF (89 kDa), which makes it the major impurity of bLTF. However, the concentrations of lactoperoxidase in the bLTF isolates usually are at a very low level and can be neglected (Du et al., 2013). Another source of the bLTF impurities may arise from the degradation as a result of the cleavage of the protein chain during isolation or storage. Proteins can undergo multiple reactions that affect their biological activity; among others, peptide bond hydrolysis and protein oxidation may be a reason for their fragmentation. Peptide bond cleavage occurs in the presence of water and is promoted even under mildly acidic conditions (Simpson, 2010). Whey acidification is usually used for casein separation and is one of the major steps in whey protein fractionation (Yoshida et al., 2000; Pomastowski et al., 2016). Moreover, acidification as well as other technological processes such as spray-drying, high-pressure treatment, and so on can lead to partial protein denaturation and therefore to higher susceptibility to the protein primary structure degradation. It should be noted that metal
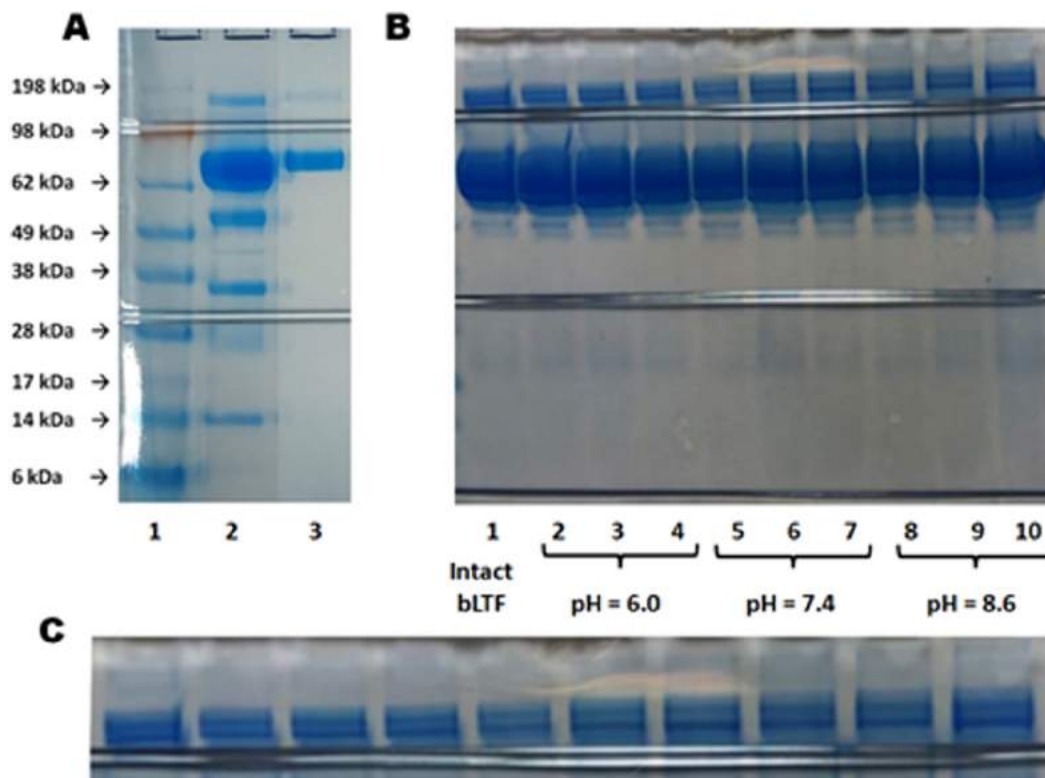
Figure 1. Sodium dodecyl sulfate-PAGE electropherogram of (A) protein markers (lane 1), intact bovine lactoferrin (bLTF; lane 2), and bLTF after membrane ultrafiltration (lane 3) with cut-off 50 kDa; (B) intact bLTF (lane 1); from left to right products of bLTF interaction with Zn^{2+} at pH 6.0, 7.4, and 8.6 with metal concentration of 6 mg/L (lanes 2, 5, and 8), 60 mg/L (lanes 3, 6, and 9), and 600 mg/L (lanes 4, 7, and 10), respectively; and (C) enlarged fragment of the electropherogram B corresponding to dimer bands.

ions are important factors that stabilize the proteins against degradation by tertiary structure stabilization (Kambe et al., 2015; Franco et al., 2018). Considering the bLTF structure, the peptide bridge connecting the 2 protein lobes is the most compliant place for degradation and enzymatic digestion (Takayama, 2012). The SDS-PAGE analysis showed the band between 38 and 49 kDa, which can correspond to the parts of bLTF molecule such as the N-lobe and C-lobe. The smaller proteins, with bands present on the electropherogram, can be derivatives of bLTF further cleavage. From Figure 1A, it can be observed that it was possible to obtain the pure bLTF by membrane ultrafiltration with a 50 kDa cut-off value. Thus, it can be suggested that all impurities were introduced during the LTF isolation and storage. Moreover, bLTF ordered from another lot revealed almost no evidence of impurities (Figure 1B.1).

The SDS-PAGE analysis of the protein after interaction with Zn^{2+} did not show significant changes in the intensity and position of the main band of bLTF. However, slight changes in the electrophoretic mobility of the bLTF dimer band can be observed (Figure 1C). The changes in the protein mobility were observed for all samples obtained at pH 8.6 and pH 7.4, where the highest changes were for samples synthesized at pH 8.6 and with the utilization of higher Zn^{2+} concentration. In the previous study of bLTF by PAGE-IEF, such slight changes in electrophoretic mobility were observed for the protein with different iron saturation levels, which influences the pI value (Voswinkel et al., 2016). Thus, it can be deduced that changes in the electrophoretic mobility may be due to the Zn^{2+} binding to the protein. However, it should be noted that such drift of the protein band position can also be due to interference of the excess of ions in the sample, which comes from the buffer used. Still, it was shown that NaCl up to a concentration of 0.4 M has little effect on the migration of the protein bands (See et al., 1985). In the study, the buffers used had a concentration of 0.1 M and the samples were washed twice with ultrapure water after synthesis.

By utilization of MALDI-TOF-MS in linear positive mode, it was possible to estimate the molecular weight of bLTF ($[M+H]^+$) (Figure 2). Average masses of bLTF were in the range of 82 to 84 kDa with a maximum of nearly 83,200 Da. In the previous study of our group, the average masses of isolated bLTF were in the range of 77 to 81 kDa with a maximum of 77,700 Da (Pomastowski et al., 2016). Bovine lactoferrin is the glycoprotein and the differences in masses are related to its glycosylation degree. Bovine lactoferrin has 5 possible glycosylation sites and 4 of them are always glycosylated (Asn233, 368, 476, and 545), whereas the fifth (Asn281) is glyco-

sylated in about 15 to 30% depending on the stage of lactation (van Veen et al., 2004). Moreover, the level of bLTF glycosylation is also dependent on other factors such as inflammation, environmental, and stress conditions (Wei et al., 2000). Yoshida et al. revealed that 2 different forms such as bLTF-a (molecular mass, M_r, $\approx 84{,}000$) and bLTF-b ($M_r \approx 80{,}000$) can be isolated both from colostrum and mature milk (Yoshida and Ye-Xiuyun, 1991; Yoshida et al., 2000). Moreover, it was shown that bLTF-a is more resistant to proteolytic degradation than bLTF-b. Additionally, a previous study has shown that bLTF-a displays a higher bacteriostatic activity against *Escherichia coli* than bLTF-b (Yoshida et al., 2000). The studies indicated the significance of the degree of glycosylation of proteins on their biological activity, which should be taken into account during the investigation. Other signals were suggested to correspond to multiple-charged bLTF ($[M+2H]^{2+}$) ions and the impurities in the sample, namely $[M_1+H]^+$, signals marked by F, and other smaller proteins. On the spectrum of the protein after filtration with 50 kDa cut-off, only the signals from multiple-charged ions of bLTF can be seen and additional small signals of some impurity near 22.5 ($[M_2+H]^+$) and 14 kDa. Still, it should be noted that even though protein degradation is an unwanted process, the peptides derived from whey proteins have numerous useful properties. For instance, lactoferricin of bLTF reveals even higher bactericidal ability than bLTF itself (Takayama, 2012; Dullius et al., 2018).

Further bLTF samples were subjected to SDS-PAGE separation and in-gel tryptic digestion coupled to MALDI-TOF/TOF-MS analysis, which enabled the identification of 6 proteins that were found to be the most abundant in the mixture. Almost all studied proteins were identified as bLTF as well as its dimer and fragments, but the protein with a mass of nearly 14 kDa was shown to be bovine keratin. The obtained results may serve as additional evidence of the bLTF degradation during isolation and storage as the main source of impurities as was suggested from SDS-PAGE analysis (Figure 1). All subsequent analyses, including the studies of bLTF-Zn interactions, were performed using the bLTF standard with higher purity with no additional purification.

Zeta potential measurement is usually used for the characterization of electrochemical properties of biomolecules. The knowledge about proteins' net charge is important for the prediction of their behavior in the solutions (e.g., their dispersion stability, interaction with sorbents or membranes during separation and purification). One of the applications of ζ-potential measurements is the protein pI determination, at which
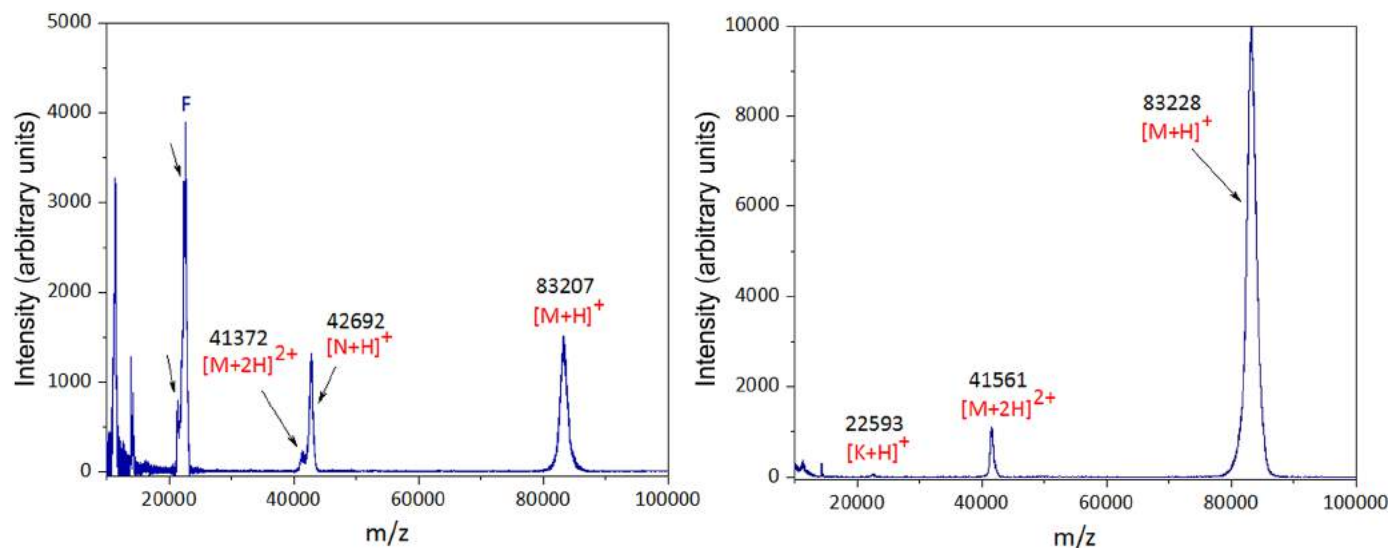
Figure 2. The MALDI-TOF-MS spectra of native bovine lactoferrin (bLTF; on the left) and bLTF after membrane filtration with cut-off value 50 kDa; signals $[M_1+H]^+$, $[M_2+H]^+$, and F correspond to signals of impurities.

the net charge of the protein equals zero. At pI proteins become more hydrophobic, compact, and less stable, and hence can easily aggregate and precipitate (Salgın et al., 2012). What is important is that the protein net charge may affect the process of metal-protein interaction (Gurd and Wilcox, 1956; Roosen-Runge et al., 2013). Thus, the pI value is an important parameter for the description of the mechanisms of metal binding to protein.

In our study, the protein acid-base potentiometric titration has shown that, as a function of pH (Figure 3), ζ-potential values of bLTF vary from +20 to −6 mV at the pH values of 4 to 9. The ζ-potential changes in the specified pH range fit a linear model. This allows determining the pI value of bLTF, which was established at pH = 7.4 ± 0.2. The utilization of other models did not show significant changes. The majority of literature sources indicate a bLTF pI value in a range between 8.0 and 9.0 (Lambert, 2012; Takayama, 2012). The differences in the pI values are related to differences in the measurement technique used. For instance, for A-type lipase of *Candida antarctica* pI value at 4 was determined by electrophoretic mobility, whereas the isoelectric focusing technique showed the pI value as 7.5 (Salgın et al., 2012). Moreover, the studies performed in our group have shown that depending on the ions present in the solution the determined pI values for β-LG were from 5.3 to 7.6 within the same technique (Gołębiowski et al., 2020). The study indicates the high importance of the effect of specific protein-ion interactions on the obtained results. Moreover, the ionic strength of the dispersion medium also can result

in differences in pI values (Salgın et al., 2012). What is interesting is that the previous investigation performed in our group for bLTF with molecular weight ≈78 kDa has revealed a pI value of 6.0 ± 0.3 (Pomastowski et al., 2016). Both in the present study and in the one performed by Pomastowski et al. the conditions for pI determination of bLTF were the same, namely the protein was titrated in 0.09% NaCl, indicating the influence of the glycosylation level on the electrochemical features of proteins.

The spectra obtained within ATR-FTIR analysis of native bLTF have revealed a typical pattern of absorption bands (Figure 4). The bands that occurred in the region from 2,800 to 3,700 cm^{-1} represent stretching (str.) vibrations related to hydrogen-containing groups.
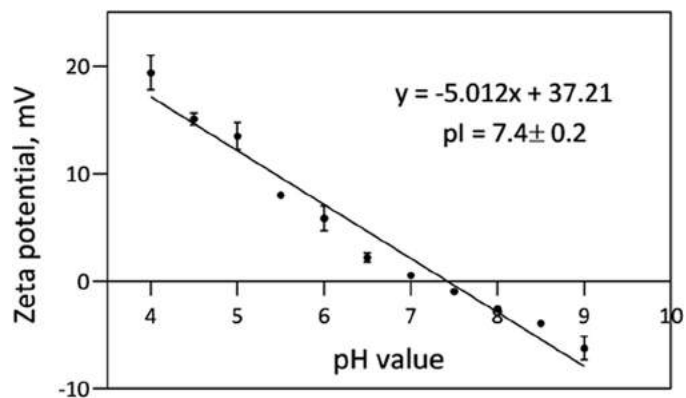

Figure 3. Zeta potential of bovine lactoferrin as a function of pH. pI = isoelectric point.

The absorption band with a maximum at 3,280 cm^{-1} corresponds to O–H and N–H str. vibrations. The broad shape of the band indicates the involvement of amino and hydroxyl groups in the hydrogen bond. The bands at 3,078, 2,980, 2,936, and 2,886 cm^{-1} come from C-H asymmetric and symmetric stretching vibrations of CH$_3$ and CH$_2$ groups as well as aromatic rings (Nandiyanto et al., 2019). Additional band for δ_{as}(CH$_3$) (1,472 cm^{-1}) is almost undetectable on the spectrum of native bLTF due to signals overlay. Instead, the band for δ(CH$_2$) was visible at 1,451 cm^{-1} (Barth, 2007; Nandiyanto et al., 2019). After interaction with Zn^{2+} in all of the samples, the new band at 3,653 cm^{-1} has appeared. The band might appear due to the unbounded O–H group vibrations, which are more often connected to the presence of water in the sample, but also may be due to the hydrogen bonds destruction in the protein (Socrates, 2004). The results may indicate that the samples were not dried completely after the synthesis. However, the signals were even more intense in samples obtained at pH values 7.4 and 8.6. As Zn^{2+} appears in the solution as aqua complex (Kręžel and Maret, 2016), the results may indicate the metal adsorption on the protein surface with a coordination sphere partially filled with water molecules, thus enhancing the water signal in the spectrum. It should be noted, that water always accompanies the protein molecules. Some scientists claim that water molecules are the indispensable part of the protein that take part not only in the tertiary structure formation but also participate actively in the protein reactions, for instance in the directed proton transfer (Kotting and Gerwert, 2007). More interestingly, the unusual enhancement of the signals of the methyl and methylene groups was observed, especially in the samples formed at pH 7.4 and 8.6, which may be due to the changes in the protein crystal structure rearrangement. For instance, similar but less significant effects were observed in the case of the study of solid to liquid transitions in long-chain alkanes (Corsetti et al., 2017). In the fingerprint region, the signal 1,637 cm^{-1} was assigned to the characteristic band for the peptide bond of amide I. The absorbance of the band in ≈80% is due to CO str. vibrations (Socrates, 2004). However, the out-of-phase C-N str. vibration and NH in-plane bending (≈10% each) also contribute to the amide I band (Socrates, 2004; Barth, 2007). The position of the band is dependent on the protein secondary structure and indicates the presence of a large number of β-sheet structures in the bLTF molecule. The data derived from crystallography studies also indicate a high amount of β-sheet in the proteins from the transferrin family (Baker, 1994; Mizutani et al., 2012; Takayama, 2012). The amide II band, which comes from out-of-phase NH in-plane bending and the CN str. vibration with a small contribution from CO in-plane bending and CC/NC str. vibrations, was observed at 1,533 cm^{-1} (Socrates, 2004; Barth, 2007). The bands appeared at 1,338 cm^{-1}, 1,309 cm^{-1} (α-helix), and 1,240 cm^{-1} (β-sheet) can be assigned to amide III modes, which mainly comes from CN str. and NH bending (≈30% each; Singh et al., 1993; Barth, 2007). The more intense band at 1,240 cm^{-1} also indicates the prevalence of β-sheet structures in the protein molecule. The enhancement and shifts of the amide III bands after protein interaction with Zn^{2+} may indicate the metal complexation through NH and CN groups and changes in protein secondary structure (Socrates, 2004). The relatively strong absorption band at 1,391 cm^{-1} can be attributed to ν_s(COO$^-$) of glutamic and aspartic acids (Nandiyanto et al., 2019). The band may shift significantly upon cation chelation (+60/−90 cm^{-1}). Bovine lactoferrin has 40 glutamic and 36 aspartic acid residues in a single molecule, which makes up 11% of the total number of residues and may indicate the high potential in metal ion chelation (Pomastowski et al., 2016). The bands at 1,159 cm^{-1} and 1,129 cm^{-1} can be assigned to ν(C–O) of serine, aspartic, and glutamic acid, whereas the band at 1,067 cm^{-1} comes from ν(C–O) of threonine. The band that occurred at 967 cm^{-1} could also arise from the serine residue (Barth, 2007). The significant enhancement of the bands after protein interaction with Zn^{2+} indicates the changes in the composition of the accompanying metal ions in the protein and the involvement of all of the assigned AA, namely serine, aspartic, and glutamic acids. The bands below the 800 cm^{-1} come from amide IV–VII, the interpretation of which is hard to perform due to a lack of information for protein in the literature (Socrates, 2004). Detailed changes in FTIR bands and their intensities can be found in Table 1, where an increase or decrease in intensities was assigned by arrows.

Raman spectroscopy can be considered as complementary to FTIR vibrational spectroscopic technique, which can provide more structural details on chromophores as they are saturated in π-electrons and thus can be polarized more easily (Wen, 2007). Obtained Raman spectra of native bLTF have several absorption bands, characteristic for proteins (Figure 5). The broad band with a maximum at 3,325 cm^{-1} can be assigned to O–H and N–H str. vibrations involved in hydrogen bonding (Socrates, 2004). The band at 3,055 cm^{-1} could also be due to N–H str. vibrations, whereas intensive bands at 2,931 and 2,873 cm^{-1} come from aliphatic C–H str. vibrations. The band of amide I appeared at 1,669 cm^{-1}. Similar to FTIR, the position of the amide I band indicates the high impact of β-sheet structures
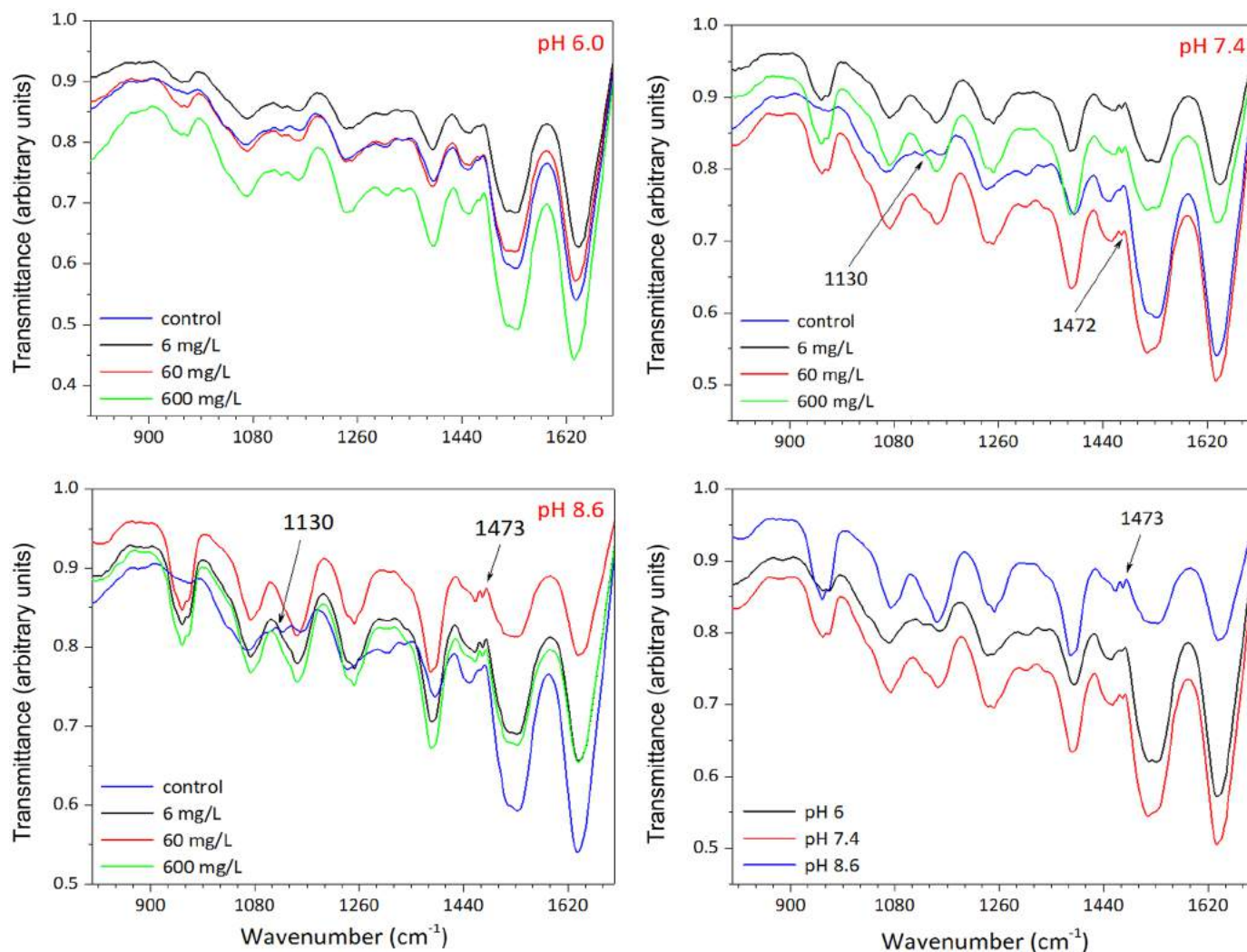
Figure 4. Attenuated total reflection-Fourier-transform infrared spectra of native bovine lactoferrin (bLTF) and bLTF after interactions with Zn^{2+} (fingerprint region).

in the molecule. However, in the amide III region, the intensive band at 1,284 cm^{-1} and the less intensive one at nearly 1,329 cm^{-1} should indicate the presence of all structures, namely α-helix, β-sheet, and random coils (Wen, 2007). The changes in the signal distribution of the amide III bands after bLTF interaction with Zn^{2+}, the same as in the FTIR spectra, may indicate the changes in the secondary structure of the protein as well as the significant role of CN and NH groups in metal ion binding. What is interesting is that according to literature data the amide II band should have low intensity in Raman spectra (Socrates, 2004; Jacob et al., 2009). However, in our study, the vibrational band at 1,503 cm^{-1}, which may be related to amide II, has rather medium intensity. The band at 1,602 cm^{-1} was assigned to ring modes of aromatic residues, namely

phenylalanine, tyrosine, and tryptophan. The additional bands for each of the residues can be found at 1,206, 1,168, and 835 cm^{-1} for tyrosine, 1,035 and 1,003 cm^{-1} for phenylalanine as well as 1,550 (indole ring modes), and 874 and 757 cm^{-1} for tryptophan (Wen, 2007; Rygula et al., 2013).

What is important is that the bands of these AA are sensitive to the local environment. Moreover, the π-cation interactions affect some of the bands such as 757 and 1,550 cm^{-1} of tryptophan, which should be helpful for the study of metal-protein interactions (Wen, 2007). Thus, the changes in relative intensities of the bands indicate the changes in the cation content in the protein. The bands at 1,450 and 1,096 cm^{-1} correspond to C–H and C–N deformation vibrations (Rygula et al., 2013). The bands that occurred in region 500 to

Table 1. The assigned bands derived from attenuated total reflection–Fourier-transform infrared spectra of native bovine lactoferrin (bLTF) and after interaction with Zn^{2+}[1]

Assignment	Native bLTF	Products of Zn-bLTF interaction								
		pH 6.0			pH 7.4			pH 8.6		
		6 mg/L	60 mg/L	600 mg/L	6 mg/L	60 mg/L	600 mg/L	6 mg/L	60 mg/L	600 mg/L
Nonbonded O–H str., OH str. of water molecules	—	3,653↑	3,646↑	3,647↑	3,656↑↑	3,655↑↑	3,655↑↑	3,657↑↑	3,658↑↑	3,655↑↑
N–H str.; bonded O–H, aliphatic and aromatic	3,283	3,292	3,283	3,275	3,292	3,283	3,283	3,284	3,294	3,293
	3,078	3,079↑↑	3,078	3,082	3,076	3,068	3,068	3,086	3,079	3,078
C–H sym/asym. str.	2,970	2,980↑↑	2,980↑↑	2,980↑↑	2,980↑↑	2,980↑↑	2,980↑↑	2,980↑↑	2,980↑↑	2,980↑↑
	2,934	2,936	2,932↑	2,934↑	—	2,932↑	2,932↑	2,932↑↑	2,932↑↑	2,933↑↑
	2,876	2,886	2,885↑	2,885↑	2,888	2,889↑	2,889↑↑	2,888↑↑	2,888↑↑	2,889↑↑
Amide I band	1,637	1,642	1,636	1,633	1,643	1,635	1,636	1,639	1,638	1,638
Amide II	1,533	1,532	1,531	1,537	1,537	1,516	1,516	1,532	1,528	1,533
δas.(CH_3)	1,468	1,471	1,471↑	1,470	1,472↑	1,472↑	1,473↑	1,473↑	1,473↑	1,473↑
δ(CH_2)	1,451	1,454	1,454↑	1,453	1,456↑	1,455↑	1,456↑	1,460↑	1,460↑	1,460↑
Asp, Glu ν_s(COO^-)	1,391	1,390↑	1,390↑	1,391↑	1,384↑↑	1,386↑↑	1,384↑↑	1,385↑↑	1,383↑↑	1,384↑↑
Amide III	1,338	1,337	1,338↑	1,339↑	—	—	—	—	—	—
	1,309	1,306	1,307↑	1,312↑	1,304	1,307	1,314	1,306	1,314	1,311
Asp,Glu, ν(C–O)/Ser, ν(CO), δ(CO_2H)	1,240	1,250/1,241↑	1,250/1,240↑	1,249/1,241↑	1,241/1,251↑↑	1,241/1,250↑↑	1,251↑↑	1,251↑↑	1,251↑↑	1,251↑↑
	1,159	1,159↑	1,158↑	1,158↑	1,153↑↑	1,155↑↑	1,153↑↑	1,153↑↑	1,151↑↑	1,153↑↑
	1,129	1,130↑	1,129↑	1,128↑	—	—	—	—	—	—
Thr ν(C–O)	1,067	1,071↑	1,070↑	1,071↑	1,072↑↑	1,072↑↑	1,071↑↑	1,072↑↑	1,072↑↑	1,072↑↑
Ser, ν(CO), δ(CO_2H)	967	966/957↑↑	967/957↑↑	967/956↑↑	965/955↑↑	966/956↑↑	965/955↑↑	965/955↑↑	965/955↑↑	965/955↑↑

[1]sym. = symmetric; asym. and as. = asymmetric; str. = stretching vibrations; def. = deformation vibrations; ↑ indicates small changes (relative to amide I band) in band intensities; ↑↑ indicates significant changes (relative to amide I band) in band intensities.
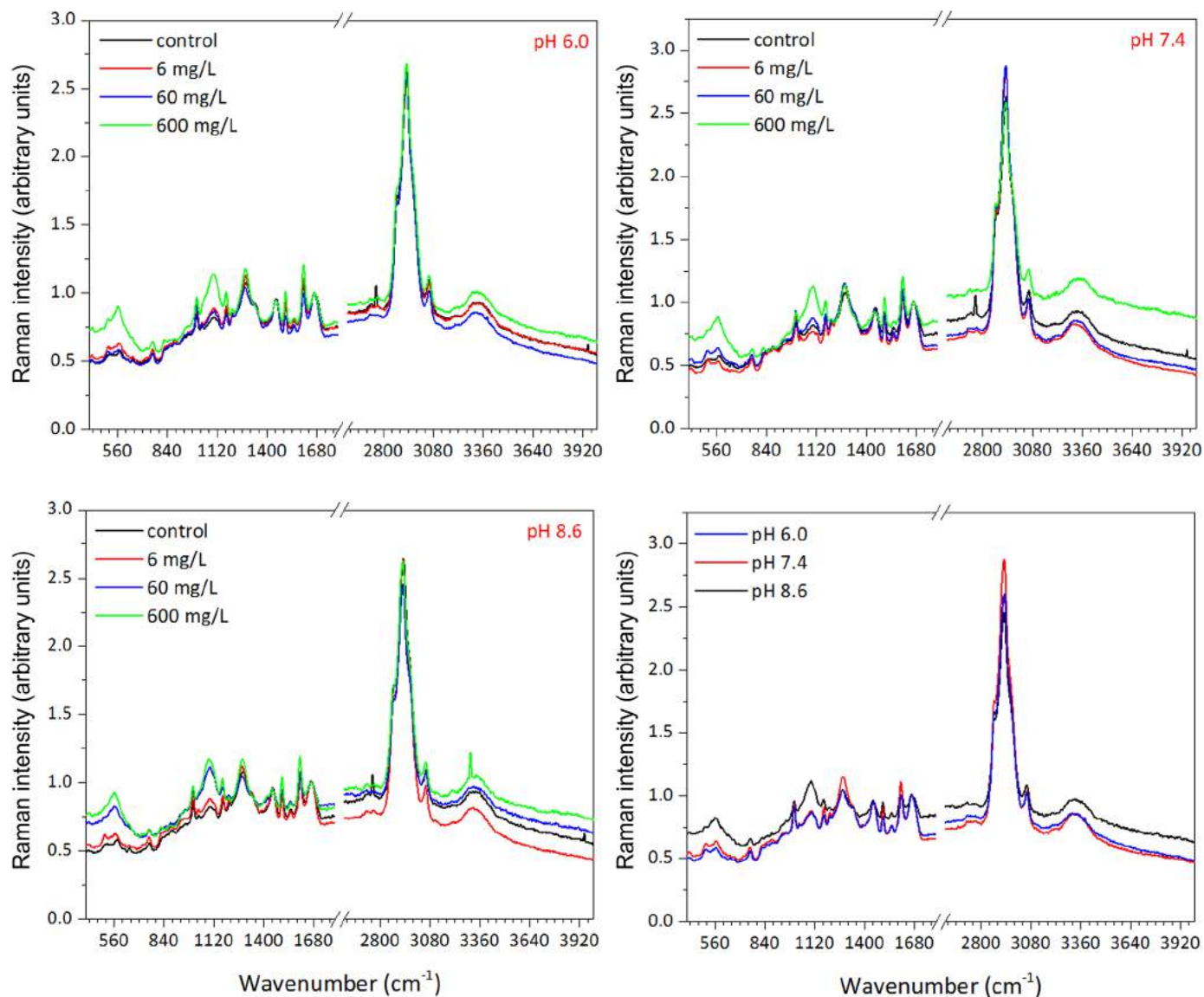
Figure 5. Raman spectra of native bovine lactoferrin (bLTF) and bLTF after interactions with Zn^{2+}.

600 cm^{-1} could arise due to the S–S stretching vibrations (Wen, 2007), whereas 417 cm^{-1} can be assigned to the Fe–O or Fe–NO complexes in iron-binding proteins (Ashton et al., 2017). The changes in intensities of some of the bands that correspond to S–S stretching vibration indicate the changes in the protein secondary and tertiary structure. Detailed changes in the bands and their intensities after the Zn-LTF interactions can be found in Table 2, where an increase or decrease in intensity was assigned by arrows.

Table 3 presents the results of ICP-MS determination of the 6 most common for proteins metal ions. According to obtained results, it is visible that Zn^{2+} binding occurred only at pH 7.4 and 8.6, but not at pH 6.0. The

changes in the FTIR and Raman spectra observed for samples obtained at pH 6.0 may be due to the decrease of all metal contents in the sample as a result of the washing steps after the synthesis. Further discussion of the observed phenomena will be provided in the next section, which presents the proposed mechanisms of the metal-protein interaction.

Scanning electron microscopy images revealed minor changes in the protein surface structure. However, reasonable conclusions could not be derived because the main drawback of the method is a spatial resolution, which limits detailed characterization of the changes in protein structure after the interaction. In addition, observation of the protein structure is one

Table 2. The assigned bands derived from Raman spectra of native bovine lactoferrin (bLTF) and after interaction with Zn^{2+}[1]

Assignment	Native bLTF	Products of Zn–bLTF interaction								
		pH 6.0			pH 7.4			pH 8.6		
		6 mg/L	60 mg/L	600 mg/L	6 mg/L	60 mg/L	600 mg/L	6 mg/L	60 mg/L	600 mg/L
Hydrogen bonded O–H/N–H	3,335	3,342	3,315	3,335	3,315	3,312	3,312	3,323	3,327	3,308
N–H stretching vibration	3,060	3,057	3,057	3,060	3,058	3,057	3,058	3,057	3,058	3,057
Aliphatic and aromatic C–H sym/asym. str.	2,931	2,931	2,930	2,931	2,930	2,930	2,931	2,930	2,930	2,929
	2,878	2,876	2,875	2,879	2,876	2,875	2,876	2,876	2,875	2,874
	2,760	2,769	2,769	—	2,767	2,767	—	2,764	—	—
	2,736	2,735	2,724	—	2,726	2,726	—	2,724	—	—
Amide I	1,664	1,665	1,665	1,662	1,664	1,663	1,662	1,661	1,661	1,662
Tyr, Trp, Phe (ring modes)	1,604	1,603	1,602↑	1,603↑	1,603	1,602↑	1,602↑	1,602	1,602	1,601↑
Trp (indol ring)	1,550	1,552	1,550↓	1,551↓	1,551↓	1,549↓	1,556/1,548↑	1,549	1,549	1,549↑
Amide II	1,503	1,502	1,501↓	1,502	1,502	1,501	1,501↑	1,501	1,501	1,500↑
C–H def.	1,451	1,450	1,448	1,448	1,448	1,445↓	1,443↓	1,446	1,447	1,442
Glu, Asp ν(CO)	—	—	—	—	—	—	1,414	—	1,414	1,417
Trp (C_a–H) def., amide III	1,329	—	—	1,326↓	—	—	1,329	1,331	1,329	1,342
Amide III	1,284	1,280↑	1,277↓	1,276↑	1,278↑	1,278↑	1,281↑	1,276	1,275	1,277↑
Tyr (α-helix)	1,206	1,207	1,205	1,206↑	1,205	1,204	1,203	1,204	1,200↑	1,203↑
Tyr (CH_3)	1,172	1,170	1,169	1,169↑↑	1,170	1,169	1,168↑	1,169	1,168↑↑	1,168↑↑
C–N	1,101	1,099↑	1,101↑	1,098↑↑	1,102↓	1,097↑	1,101↑↑	1,094↑	1,098↑↑	1,090↑↑
Phe	1,033	1,034	1,032	—	1,031↓	1,030↑	—	1,031	—	—
Phe	1,005/960	1,004↑	1,003↑	1,004↑	1,003	1,002	1,003	1,002	1,003	1,003
Tyr (H-bonding)	881	881	878	876	878	880	883↑	877	876	875↓
	836	831	835↑	823↑	832	827	820↑	827↑	826↑	820↑
Trp (indol ring)	758	758↑	757	762↑	757↓	756↑	758↑	756↑	758↑	755↑
S–S TGT conformer	576	567↑	566	564↑↑	569↓	568↑	569↑↑	567	561↑↑	561↑↑
S–S GGG conformer	519	510↑	508	508↑	510	510	513	506↑	505	510
Fe–O, Fe–NO	414	416	415	420	417	418	420	411	415	420

[1]sym. = symmetric; asym. and as. = asymmetric; str. = stretching vibrations; def. = deformation vibrations; ↑ indicates small changes (relative to amide I band) in band intensities; ↑↑ indicates significant changes (relative to amide I band) in band intensities.

Table 3. Results ($\pm$ SD) for the inductively coupled plasma MS measurements of the metals content in the native bovine lactoferrin (bLTF) and after interaction with the Zn^{2+} solution of 6, 60, and 600 mg/L at pH 6.0, 7.4, and 8.6

Sample	Metal					
	Zn, mg/g	Fe, mg/g	Mg, µg/g	Na, mg/g	K, mg/g	Ca, mg/g
Native bLTF	0.017 ± 0.003	1.45 ± 0.06	9.5 ± 2.3	0.96 ± 0.16	0.11 ± 0.02	<LOQ[1]
pH 6.0						
6 mg/L	0.007 ± 0.005	1.24 ± 0.19	20.9 ± 0.6	0.28 ± 0.05	0.08 ± 0.02	<LOQ
60 mg/L	0.036 ± 0.002	1.17 ± 0.02	7.0 ± 3.6	<LOQ	<LOQ	<LOQ
600 mg/L	0.034 ± 0.003	0.80 ± 0.14	18.1 ± 1.0	<LOQ	<LOQ	<LOQ
pH 7.4						
6 mg/L	0.037 ± 0.005	1.22 ± 0.05	6.1 ± 0.9	<LOQ	<LOQ	<LOQ
60 mg/L	0.621 ± 0.022	1.25 ± 0.04	7.2 ± 1.4	<LOQ	<LOQ	<LOQ
600 mg/L	12.392 ± 0.720	1.14 ± 0.08	6.0 ± 0.6	<LOQ	<LOQ	<LOQ
pH 8.6						
6 mg/L	0.056 ± 0.005	1.18 ± 0.07	5.6 ± 0.4	—	<LOQ	<LOQ
60 mg/L	1.687 ± 0.080	1.11 ± 0.05	5.9 ± 1.0	—	<LOQ	<LOQ
600 mg/L	16.885 ± 1.426	1.02 ± 0.01	5.3 ± 6.7	—	<LOQ	<LOQ

[1]Limit of quantification.

of the main challenges in protein science (i.e., due to its low stability under exposure to high energies). The previous study with ovalbumin revealed that the Zn^{2+} interaction with proteins can lead to the formation of ZnO nanoparticles (Buszewski et al., 2021). Hence, the transmission electron microscopy (**TEM**)-energy-dispersive X-ray spectrometry analysis of the samples was performed. It was possible to detect Zn only in the samples prepared with the utilization of Zn^{2+} solution of 600 mg/L at pH 7.4 and 8.6. However, the formation of ZnO nanoparticles was not observed even for these samples. Thus, it could be deduced the formation of homogeneous metal-protein complexes at pH 7.4 and 8.6 (Figure 6).

Mechanisms of Zn-bLTF Interactions

The ICP-MS analysis revealed that after bLTF interaction with Zn^{2+} the changes in the quantity of all 6 of the most common metals that usually accompany proteins have occurred. What is interesting is that among all metals the Fe^{3+} has the highest affinity to bLTF (Takayama, 2012), but after interaction with zinc solutions in all utilized conditions, the iron content has decreased. The most dramatic decrease (i.e., $\approx$45%) was observed when Zn^{2+} solution with the concentration of 600 mg/L at pH 6.0 was used. The effect may be connected with 2 factors, and the first one is the acidic conditions that weaken the bond between Fe^{3+} and bLTF. The second factor is the competition of Zn^{2+} for metal-binding sites, which become more evident with a higher concentration of metal in the solution (Gurd and Wilcox, 1956). In all other cases, the decrease of iron content was in the range from 13 to 30 %. For pH 7.4 and 8.6, the main factor that should affect iron content

is the presence of citrate ions in the solution. Citrate ions compete with bLTF for the metal ion. Generally, the native bLTF had 1.45 ± 0.06 mg/g of iron, which equals the ratio of metal:protein = 2.1:1, and thus means that both metal-binding sites were filled with iron. After the reaction, the portion of the iron was released from the protein, which enables the embedding of the Zn^{2+} into bLTF. However, at pH 6.0 the utilization of zinc solution of 6 mg/L also decreased the Zn^{2+} content. When solutions of 60 and 600 mg/L were used, a slight increase in Zn^{2+} content was observed. However, such small changes can be neglected because even they cannot compensate for the amount of vanished Fe^{3+}, leaving the bLTF unsaturated. Almost the same was the case when a solution of 6 mg/L at pH 7.4 and 8.6 was used. In turn, with the usage of zinc solution of 60 mg/L for both 7.4 and 8.6 the amount of bonded Zn^{2+} was already higher than vanished Fe^{3+}. Thus, it can be suggested that some portion of Zn^{2+} was bonded to surface functional groups of bLTF. The usage of the solution with a zinc concentration of 600 mg/L enables to bond $\approx$16 and 22 of Zn^{2+} at pH 7.4 and 8.6, respectively, which implies the formation of new metal-binding sites on the protein surface.

The deep chemistry of reactants should be considered for the proper description of the processes on the surface of the protein. Consideration of the participation of AA and peptides as building blocks of the protein can simplify the description. Subsequently, the extrapolation of obtained data for peptides and AA can be used for the description of interactions of more sophisticated molecules such as proteins. Such an approach was used by Sych et al. (2018) for the prediction of place(s) of formation of Ag clusters in protein. Tang and Skibsted (2016) reported the discussion of the bioavailability of
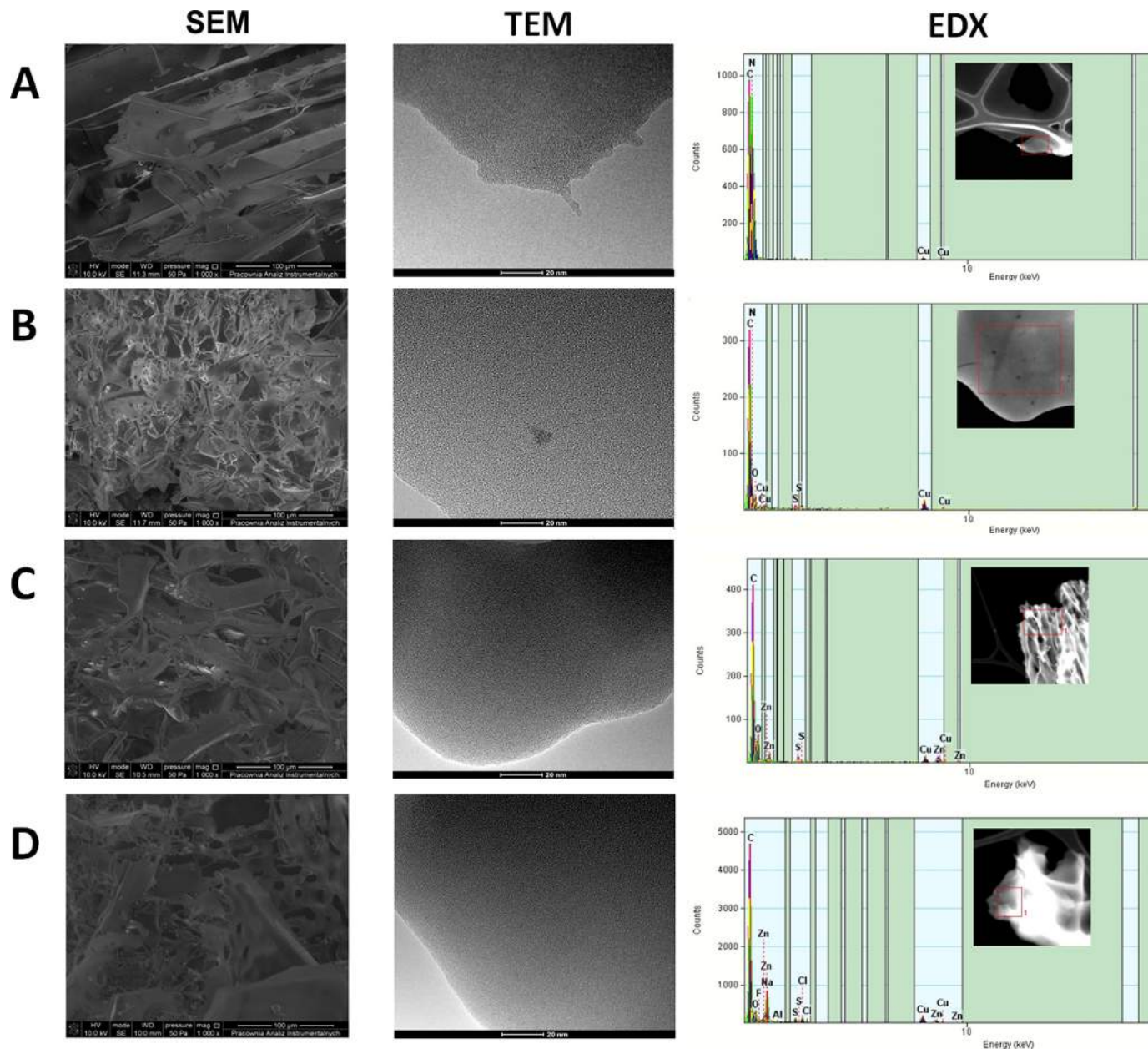
Figure 6. Results of scanning electron microscopy (SEM) and transmission electron microscopy (TEM)-energy-dispersive X-ray spectrometry (EDX) analysis of (A) native bovine lactoferrin (bLTF) and samples obtained with the utilization of Zn^{2+} solution of 600 mg/L at pH (B) 6.0, (C) 7.4, and (D) 8.6.

Zn^{2+} from whey. On the other hand, the authors reported the obtained data in an attempt to explain the role of individual AA in Zn^{2+} binding to the protein and therefore in Zn^{2+} homeostasis. Generally, this approach is well known from the first research on formation of metal ammine complexes (Gurd and Wilcox, 1956). However, such an approach should be applied carefully with consideration of the whole spectrum of intra- and supramolecular effects that can affect the interactions between the species. For instance, although Zn^{2+} ions form relatively stable complexes with glycine, this interaction is not significant for the binding of metal ions to protein. In this case, side chains of AA comprising the protein are of higher importance. However, for small peptides, it was shown that nitrogen from peptide bonds participates in metal complexation (Gurd and Wilcox, 1956). Thus, such molecules as glycine may also participate in the metal complexation.

Sulfhydryl (thiol) groups of side chains of the AA comprising the protein can form the strongest bonds with metals, particularly Zn^{2+} (Gurd and Wilcox, 1956; Tang and Skibsted, 2016). Cysteine is of high importance in proteins containing zinc finger structures, where metal-binding sites comprise different combinations of histidine and cysteine residues (Bou-Abdallah and Giffune, 2016). Bovine lactoferrin has 34 cysteines in its structure, which provides the respective amount of thiol groups (Pomastowski et al., 2016). However, free thiol groups are very reactive and undergo oxidation reaction with the formation of sulfenic (R-S–OH), sulfinic (R–SO_2H), and sulfonic (R–SO_3H) derivatives as well as the disulfide bond. In general, the presence of free thiol groups is distinctive for proteins located in the cytoplasm, whereas proteins in other compartments comprise oxidized thiol groups predominantly in form of disulfide bridges (Trivedi et al., 2009). In the bLTF, not only the number but also the position of cysteines predict 17 disulfide bonds (Schanbacher et al., 1993). The disulfide bridges are essential elements of the protein tertiary structure and are responsible for protein thermal stability (Trivedi et al., 2009). It was shown that Ag^+ and Hg^+ can easily break the disulfide bridges and form a highly stable bond with the thiol group (Gurd and Wilcox, 1956). For instance, Pomastowski et al. (2016) worked with both the experimental data as well as molecular dynamic analysis that have shown the involvement of disulfide bonds in Ag^+ binding to bLTF. However, a vast number of other metals are supposed to react with cystine (oxidized form of cysteine, containing disulfide bond) in a way similar to simple AA (Gurd and Wilcox, 1956). Still, the disulfide bond can undergo degradation in a basic environment by direct attack of hydroxyl anion on the sulfur atom with the formation of sulfenic acid and thiolate anion (Trivedi et al., 2009). Thus, although Zn^{2+} has a strong binding affinity to disulfides and cystine was thought to participate in intracellular Zn^{2+} homeostasis (Tang and Skibsted, 2016), the Zn^{2+} interactions with protein disulfide bonds are highly dependent on the reaction environment (Gurd and Wilcox, 1956). In our investigation, according to the Raman spectra, it can be observed that the changes in the signals corresponding to the disulfide bonds have occurred. The obtained data indicate the changes in the bLTF molecule conformation: the increase of signal near 560 cm^{-1} with an increase of Zn^{2+} in the complexes may indicate the prevalence of less stable TGT conformer of S-S bond in the molecule, whereas the signal near 510 cm^{-1} from more stable GGG conformer disappears (Wen, 2007). Such changes may not be connected to metal binding through a disulfide bond, but show the effect of Zn^{2+} on bLTF structure.

Numerous studies, including the one carried out by Buszewski et al., indicated that glutamic and aspartic acids play an important role in Zn^{2+} coordination by proteins (Jabeen et al., 2005; Pomastowski et al., 2014; Buszewski et al., 2020). Moreover, Zn^{2+} appears in water in form of aqua complex, which is considered as acid according to Brønsted-Lowry theory. The central ion in the complex causes the polarization of water molecules, resulting in a more labile proton. The dissociation of the proton leads to the formation of the aqua-hydroxo complex (Krężel and Maret, 2016). Similarly, the labile proton can interact with carboxylic groups of AA, leading to the formation of the hydroxo complex with subsequent transformation to ZnO, which can lead to the formation of ZnO-protein nanocomposites (Shi et al., 2008; Buszewski et al., 2021). The TEM analysis of synthesized Zn-bLTF complexes showed that zinc oxide nanoparticles did not form at any of the utilized conditions. Regarding the interactions between Zn^{2+} and carboxylic groups, it should be noted that they have an electrostatic character. In addition, it was shown that glutamic and aspartic acids have low zinc binding affinity, which implies the involvement of other nitrogen-containing residues to form stable complexes (Gurd and Wilcox, 1956; Yamauchi et al., 2002; Tang and Skibsted, 2016). The Lewis acid-base theory also indicates that because the Zn^{2+} belongs to borderline metal ions it has the highest affinity to ligands with nitrogen atoms such as nitrogen of peptide bond, imidazole ring, and guanidine (Alhazmi, 2019). In the present study, according to the results of ICP-MS measurements (Table 3), the binding of Zn^{2+} was not observed at pH 6.0. The effect can be explained by the chemistry of the bLTF. Apart from cysteine, histidine can bind metal most strongly. However, the imidazole group of free histidine has $pK_a \approx 5.99$ (Belitz et al., 2009), whereas the inclusion of histidine to the protein chain shift the pK_a to higher values (Gurd and Wilcox, 1956), which implies that at pH 6.0 the availability of imidazole group for Zn^{2+} is limited. Thus, the binding of Zn^{2+} to imidazole groups may not appear. Instead, the interactions with carboxylic groups are weak, so it cannot hold the Zn^{2+} on the protein surface. By changing the pH to the higher values (7.4 and 8.6), the imidazole groups become more available, resulting in Zn^{2+} binding to protein. The evidence of Zn^{2+} interaction through carboxylic and imidazole groups can be observed from Raman and FTIR spectra from the changes in vibration intensity and shifts of appropriate bands, which appear in complexes synthesized in pH 7.4 and 8.6. Still, bLTF has only 9 histidines in its structure and 2 of them are the part of clefts in metal-binding sites. According to obtained results, both binding sites are filled with Fe ions (the bLTF:Fe^{3+} molar

ratio is nearly 1:2). Thus, the effect of histidine on the Zn^{2+} binding ability of bLTF is not dominant, whereas other nitrogen-containing functional groups have much higher pK_a, which indicates that a much more complex mechanism is involved in the process. Additionally, the FTIR spectra have revealed that serine and threonine may also be involved in the coordination of Zn^{2+}. Instead, the changes in the signals of aromatic AA, which are sensitive to cation-π interactions, may indicate the changes in the cation content in the complexes.

However, it should be noted that in the previous study on β-lactoglobulin interaction with zinc, the Zn^{2+} binding to protein was studied at pH 4.6, which is much lower than the pK_a of imidazole groups (Buszewski et al., 2020). The majority of publications indicate the pI for β-LG at pH 5.1 to 5.3 (e.g., by free-flow electrophoresis; Łapińska et al., 2017), but determined within the study of its interaction with Zn^{2+} was at pH 4.6 (by ζ-potential measurements; Buszewski et al., 2020). Thus, it may indicate the significant effect of the net charge of the protein on the effectiveness of the metal binding to protein. Bovine lactoferrin is a protein with high content of cationic residues. The presence of positively charged functional groups in AA has been shown to decrease the metal-binding constant, which was assumed due to electrostatic repulsion (Gurd and Wilcox, 1956). Similarly, the electrostatic repulsion may decrease Zn^{2+} binding ability to protein. Thus, in discussion of the protein as a charged macromolecule, it is reasonable to consider the pH value of the system as compared with pI. The pI value for bLTF in the present study was defined at pH ≈ 7.4 ± 0.2. However, the accuracy of this method still may not exclude the presence of the slight positive charge on the protein surface at this pH value, especially after binding of a small portion of Zn^{2+}. In addition, it implies that at pH 8.6 the charge of the protein is negative, whereas at pH 6.0 it is positive.

The effect of the protein charge can be observed on differences in metal binding in the solution at different pH. As it can be seen, the Zn^{2+} content in complexes obtained in pH 8.6 is 3 and 1.5 times higher than for pH 7.4 for the systems containing 60 and 600 mg/L of Zn^{2+}. Moreover, it is important to notice that the effect of concentration on the metal-protein binding can be observed. The results of measurements of metal adsorption on the protein from solution with 60 and 600 mg/L of Zn^{2+} and pH 8.6 was determined as 6.16 ± 0.28 and 64.60 ± 2.25 mg/g, respectively, whereas the Zn^{2+} content in the corresponding complexes was 1.69 ± 0.08 and 16.88 ± 1.42 mg/g, respectively. The protein can be considered a biocolloid, which according to the DLVO (Derjaguin–Landau–Verwey–Overbeek) theory implies

the presence of a double electric layer and solvation shell on the surface of protein particles. Thus, the high metal concentration in the solution by affecting the solvation shell probably makes it possible for Zn^{2+} ions to interact with several functional groups, resulting in much higher stability of the complex. Therefore, the amount of Zn^{2+} that remains bounded to the protein after washing steps is higher. The effect also can be seen for Zn^{2+} adsorption from solutions at pH 7.4, but with less difference with the corresponding Zn^{2+} content in the complex. The adsorption was determined as 2.8 ± 0.22 and 19.0 ± 1.24 mg/g, whereas metal content in the corresponding complexes was 0.62 ± 0.2 and 12.39 ± 0.72 mg/g for 60 and 600 mg/L of Zn^{2+} concentration, respectively. However, while considering the interactions between Zn^{2+} and bLTF at pH 7.4 and 8.6, the presence of citrate and bicarbonate ions also should not be avoided. The Zn^{2+} binding constants to bicarbonate and citrate indicate that in both systems Zn^{2+} ions appear predominantly in the form of citrate complex (Fouillac and Criaud, 1984; Krężel and Maret, 2016), which implies the competition of citrate anion with protein for Zn^{2+}. Thus, the higher adsorption of Zn^{2+} in the system with higher metal concentration may not indicate the changes in the shielding effect of the double electric layer, but the higher availability of metal ions, as the concentration of citrate remains stable. Still, the buffer with pH 8.6 comprises a higher concentration of citrate anion and the binding capability of protein in pH 8.6 is higher, which may indicate the higher influence of protein net charge on its metal-binding efficiency.

However, the tertiary structure of the protein also affects the metal-binding properties. The formation of stable metal-protein complexes involves the coordination of several functional groups by a metal ion. Thus, an appropriate number of functional groups is not sufficient because their location is also important. Additionally, this may affect the thermodynamics of the process (Gurd and Wilcox, 1956). It is well known that the changes in free Gibbs energy must have a negative value for the occurrence of spontaneous reaction. The chelation of Zn^{2+} ions by proteins implies an enthalpy effect, which according to Tang and Skibsted (2016) for bLTF was determined as $\Delta H = -100$ kJ/mol. However, the entropy for the reaction was determined as $\Delta S = -250.5$ J/mol K (measured in pH 7.4). The Zn^{2+} chelation by bLTF implies the release of water molecules from the aqua complex, which leads to the increase in entropy of the system. The determined negative value of the entropy may indicate the changes in the flexibility of the protein molecule. It is even more interesting to investigate how the pH difference may affect the

thermodynamics of the process, which is the aim of our future study. The pH and ionic strength of the system affect the conformation of the protein molecule and therefore the bLTF metal-binding properties as well as the thermodynamics of the process (Gurd and Wilcox, 1956).

CONCLUSIONS

This study presents the results for the bLTF interaction with Zn^{2+} at 3 different pH and 3 different metal concentrations. Study revealed that the Zn^{2+} immobilization onto protein has occurred in the solution at pH 7.4 and 8.6, but not at pH 6.0. Obtained data indicate that the availability of nitrogen-containing functional groups and protein net charge (which can be manipulated by pH changes) have a significant impact on the ability of protein to bind Zn^{2+}. Moreover, the higher ionic strength of the solution, in particular the Zn^{2+} concentration, increases the probability of metal ion chelation through several functional groups of the protein and thus formation of stable metallocomplexes. Finally, the pH and the ionic strength should affect the conformation of the protein, which also may result in the formation of structures favorable for Zn^{2+} binding. However, it is noteworthy to mention that changes in protein tertiary structure also change the thermodynamics of the process.

ACKNOWLEDGMENTS

REFERENCES

Ainscough, E. W., A. M. Brodie, and J. E. Plowman. 1980. Zinc transport by lactoferrin in human milk. Am. J. Clin. Nutr. 33:1314–1315. https://doi.org/10.1093/ajcn/33.6.1314.

Alhazmi, H. 2019. FT-IR spectroscopy for the identification of binding sites and measurements of the binding interactions of important metal ions with bovine serum albumin. Sci. Pharm. 87:5. https://doi.org/10.3390/scipharm87010005.

Andersson, Y., S. Lindquist, C. Lagerqvist, and O. Hernell. 2000. Lactoferrin is responsible for the fungistatic effect of human milk. Early Hum. Dev. 59:95–105. https://doi.org/10.1016/S0378-3782(00)00086-4.

Ashton, L., V. L. Brewster, E. Correa, and R. Goodacre. 2017. Detection of glycosylation and iron-binding protein modifications using Raman spectroscopy. Analyst (Lond.) 142:808–814. https://doi.org/10.1039/C6AN02516A.

Auld, D. S. 2013. Zinc-Binding Sites in Proteins. Springer.

Baker, E. N. 1994. Structure and reactivity of transferrins. Adv. Inorg. Chem. 41:389–469. https://doi.org/10.1016/S0898-8838(08)60176-2.

Barth, A. 2007. Infrared spectroscopy of proteins. Biochim. Biophys. Acta 1767:1073–1101. https://doi.org/10.1016/j.bbabio.2007.06.004.

Belitz, H. D., W. Grosch, and P. Schieberle. 2009. Food Chemistry. Springer.

Bong, C. W., F. M. Alfatti, F. A. Zam, Y. Obayashi, and S. Suzuki. 2010. The effect of zinc exposure on the bacteria abundance and proteolytic activity in seawater. Pages 57–63 in 57 Interdisciplinary Studies on Environmental Chemistry—Biological Responses to Contaminants. Terrapub.

Bou-Abdallah, F., and T. R. Giffune. 2016. The thermodynamics of protein interactions with essential first row transition metals. Biochim. Biophys. Acta 1860:879–891. https://doi.org/10.1016/j.bbagen.2015.11.005.

Buszewski, B., A. Rodzik, V. Railean-Plugaru, M. Sprynskyy, and P. Pomastowski. 2020. A study of zinc ions immobilization by β-lactoglobulin. Colloids Surf. A Physicochem. Eng. Asp. 591:124443. https://doi.org/10.1016/j.colsurfa.2020.124443.

Buszewski, B., P. Žuvela, A. Król-Górniak, V. Railean-Plugaru, A. Rogowska, M. W. Wong, M. Yi, A. Rodzik, M. Sprynskyy, and P. Pomastowski. 2021. Interactions of zinc aqua complexes with ovalbumin at the forefront of the Zn2+/ZnO-OVO hybrid complex formation mechanism. Appl. Surf. Sci. 542:148641. https://doi.org/10.1016/j.apsusc.2020.148641.

Corsetti, S., T. Rabl, D. McGloin, and J. Kiefer. 2017. Intermediate phases during solid to liquid transitions in long-chain n-alkanes. Phys. Chem. Chem. Phys. 19:13941–13950. https://doi.org/10.1039/C7CP01468F.

Du, Q.-Y., D.-Q. Lin, Z.-S. Xiong, and S.-J. Yao. 2013. One-step purification of lactoferrin from crude sweet whey using cation-exchange expanded bed adsorption. Ind. Eng. Chem. Res. 52:2693–2699. https://doi.org/10.1021/ie302606z.

Dullius, A., M. I. Goettert, and C. F. V. de Souza. 2018. Whey protein hydrolysates as a source of bioactive peptides for functional foods – Biotechnological facilitation of industrial scale-up. J. Funct. Foods 42:58–74. https://doi.org/10.1016/j.jff.2017.12.063.

Fischer, R., H. Debbabi, A. Blais, M. Dubarry, M. Rautureau, P. N. Boyaka, and D. Tome. 2007. Uptake of ingested bovine lactoferrin and its accumulation in adult mouse tissues. Int. Immunopharmacol. 7:1387–1393. https://doi.org/10.1016/j.intimp.2007.05.019.

Fouillac, C., and A. Criaud. 1984. Carbonate and bicarbonate trace metal complexes: Critical reevaluation of stability constants. Geochem. J. 18:297–303. https://doi.org/10.2343/geochemj.18.297.

Franco, I., M. D. Pérez, C. Conesa, M. Calvo, and L. Sánchez. 2018. Effect of technological treatments on bovine lactoferrin: An overview. Food Res. Int. 106:173–182. https://doi.org/10.1016/j.foodres.2017.12.016.

Gołębiowski, A., P. Pomastowski, A. Rodzik, A. Król-Górniak, T. Kowalkowski, M. Górecki, and B. Buszewski. 2020. Isolation and self-association studies of beta-lactoglobulin. Int. J. Mol. Sci. 21:9711. https://doi.org/10.3390/ijms21249711.

Grigorieva, D. V., I. V. Gorudko, E. V. Shamova, M. S. Terekhova, E. V. Maliushkova, I. V. Semak, S. N. Cherenkevich, A. V. Sokolov, and A. V. Timoshenko. 2019. Effects of recombinant human lactoferrin on calcium signaling and functional responses of human

neutrophils. Arch. Biochem. Biophys. 675:108122. https://doi.org/10.1016/j.abb.2019.108122.

Gurd, F. R. N., and P. E. Wilcox. 1956. Complex formation between metallic cations and proteins, peptides, and amino acids. Adv. Protein Chem. 11:311–427. https://doi.org/10.1016/s0065-3233(08)60424-6.

Ianni, A., M. Iannaccone, C. Martino, D. Innosa, L. Grotta, F. Bennato, and G. Martino. 2019. Zinc supplementation of dairy cows: Effects on chemical composition, nutritional quality and volatile profile of Giuncata cheese. Int. Dairy J. 94:65–71. https://doi.org/10.1016/j.idairyj.2019.02.014.

Jabeen, T., S. Sharma, N. Singh, A. Bhushan, and T. P. Singh. 2005. Structure of the zinc-saturated C-terminal lobe of bovine lactoferrin at 2.0 Å resolution. Acta Crystallogr. D Biol. Crystallogr. 61:1107–1115. https://doi.org/10.1107/S0907444905016069.

Jacob, C. R., S. Luber, and M. Reiher. 2009. Analysis of secondary structure effects on the IR and Raman spectra of polypeptides in terms of localized vibrations. J. Phys. Chem. B 113:6558–6573. https://doi.org/10.1021/jp900354g.

Kambe, T., T. Tsuji, A. Hashimoto, and N. Itsumura. 2015. The physiological, biochemical, and molecular roles of zinc transporters in zinc homeostasis and metabolism. Physiol. Rev. 95:749–784. https://doi.org/10.1152/physrev.00035.2014.

Kawakami, H., S. Dosako, and I. Nakajima. 1993. Effect of lactoferrin on iron solubility under neutral conditions. Biosci. Biotechnol. Biochem. 57:1376–1377. https://doi.org/10.1271/bbb.57.1376.

Kotting, C., and K. Gerwert. 2007. Protein reactions: Resolved with tr-FT-IR. Spectrosc. Eur. 19:19–23.

Krężel, A., and W. Maret. 2016. The biological inorganic chemistry of zinc ions. Arch. Biochem. Biophys. 611:3–19. https://doi.org/10.1016/j.abb.2016.04.010.

Lambert, L. A. 2012. Molecular evolution of the transferrin family and associated receptors. Biochim. Biophys. Acta 1820:244–255. https://doi.org/10.1016/j.bbagen.2011.06.002.

Łapińska, U., K. L. Saar, E. V. Yates, T. W. Herling, T. Müller, P. K. Challa, C. M. Dobson, and T. P. J. Knowles. 2017. Gradient-free determination of isoelectric points of proteins on chip. Phys. Chem. Chem. Phys. 19:23060–23067. https://doi.org/10.1039/C7CP01503H.

McDevitt, C. A., A. D. Ogunniyi, E. Valkov, M. C. Lawrence, B. Kobe, A. G. McEwan, and J. C. Paton. 2011. A Molecular Mechanism for Bacterial Susceptibility to Zinc. PLoS Pathog. 7:e1002357. https://doi.org/10.1371/journal.ppat.1002357.

Mizutani, K., M. Toyoda, and B. Mikami. 2012. X-ray structures of transferrins and related proteins. Biochim. Biophys. Acta 1820:203–211. https://doi.org/10.1016/j.bbagen.2011.08.003.

Nandiyanto, A. B. D., R. Oktiani, and R. Ragadhita. 2019. How to read and interpret FTIR spectroscope of organic material. Indones. J. Sci. Technol. 4:97. https://doi.org/10.17509/ijost.v4i1.15806.

Oćwieja, M., Z. Adamczyk, M. Morga, and K. Kubiak. 2015. Silver particle monolayers — Formation, stability, applications. Adv. Colloid Interface Sci. 222:530–563. https://doi.org/10.1016/j.cis.2014.07.001.

Ortiz, Y., E. García-Amézquita, C. H. Acosta, and D. R. Sepúlveda. 2017. Functional Dairy Products. Pages 67–103 in Global Food Security and Wellness. G. V. Barbosa-Cánovas, G. M. Pastore, K. Candoğan, I. G. M. Meza, S. Caetano da Silva Lannes, K. Buckle, R. Y. Yada, and A. Rosenthal, ed. Springer.

Pomastowski, P., M. Sprynskyy, and B. Buszewski. 2014. The study of zinc ions binding to casein. Colloids Surf. B Biointerfaces 120:21–27. https://doi.org/10.1016/j.colsurfb.2014.03.009.

Pomastowski, P., M. Sprynskyy, P. Žuvela, K. Rafińska, M. Milanowski, J. J. Liu, M. Yi, and B. Buszewski. 2016. Silver-lactoferrin nanocomplexes as a potent antimicrobial agent. J. Am. Chem. Soc. 138:7899–7909. https://doi.org/10.1021/jacs.6b02699.

Roosen-Runge, F., B. S. Heck, F. Zhang, O. Kohlbacher, and F. Schreiber. 2013. Interplay of pH and binding of multivalent metal ions: Charge inversion and reentrant condensation in protein solutions. J. Phys. Chem. B 117:5777–5787. https://doi.org/10.1021/jp401874t.

Rygula, A., K. Majzner, K. M. Marzec, A. Kaczor, M. Pilarczyk, and M. Baranska. 2013. Raman spectroscopy of proteins: A review. J. Raman Spectrosc. 44:1061–1076. https://doi.org/10.1002/jrs.4335.

Sabra, S., and M. M. Agwa. 2020. Lactoferrin, a unique molecule with diverse therapeutical and nanotechnological applications. Int. J. Biol. Macromol. 164:1046–1060. https://doi.org/10.1016/j.ijbiomac.2020.07.167.

Salgın, S., U. Salgın, and S. Bahadır. 2012. Zeta potentials and isoelectric points of biomolecules: The effects of ion types and ionic strengths. Int. J. Electrochem. Sci. 7:12404–12414.

Santos, H. O., F. J. Teixeira, and B. J. Schoenfeld. 2020. Dietary vs. pharmacological doses of zinc: A clinical review. Clin. Nutr. 39:1345–1353. https://doi.org/10.1016/j.clnu.2019.06.024.

Schanbacher, F. L., R. E. Goodman, and R. S. Talhouk. 1993. Bovine mammary lactoferrin: Implications from messenger ribonucleic acid (mRNA) sequence and regulation contrary to other milk proteins. J. Dairy Sci. 76:3812–3831. https://doi.org/10.3168/jds.S0022-0302(93)77725-5.

See, Y. P., P. M. Olley, and G. Jackowski. 1985. The effects of high salt concentrations in the samples on molecular weight determination in sodium dodecyl sulfate polyacrylamide gel electrophoresis. Electrophoresis 6:382–387. https://doi.org/10.1002/elps.1150060806.

Shevchenko, A., H. Tomas, J. Havli, J. V. Olsen, and M. Mann. 2006. In-gel digestion for mass spectrometric characterization of proteins and proteomes. Nat. Protoc. 1:2856–2860. https://doi.org/10.1038/nprot.2006.468.

Shi, L., J. Zhou, and S. Gunasekaran. 2008. Low temperature fabrication of ZnO–whey protein isolate nanocomposite. Mater. Lett. 62:4383–4385. https://doi.org/10.1016/j.matlet.2008.07.038.

Shilpashree, B. G., S. Arora, S. Kapila, and V. Sharma. 2020. Whey protein-iron or zinc complexation decreases pro-oxidant activity of iron and increases iron and zinc bioavailability. Lebensm. Wiss. Technol. 126:109287. https://doi.org/10.1016/j.lwt.2020.109287.

Simpson, R. J. 2010. Stabilization of Proteins for Storage. Cold Spring Harbor Protocols. https://doi.org/10.1101/pdb.top79.

Singh, B. R., D. B. DeOliveira, F.-N. Fu, and M. P. Fuller. 1993. Fourier transform infrared analysis of amide III bands of proteins for the secondary structure estimation. Pages 47–55 in Biomolecular Spectroscopy III. SPIE.

Socrates, G. G. 2004. Infrared and Raman Characteristic Group Frequencies: Tables and Charts. 3rd ed. John Wiley & Sons, Ltd.

Sych, T. S., A. A. Buglak, Z. V. Reveguk, V. A. Pomogaev, R. R. Ramazanov, and A. I. Kononov. 2018. Which amino acids are capable of nucleating fluorescent silver clusters in proteins? J. Phys. Chem. C 122:26275–26280. https://doi.org/10.1021/acs.jpcc.8b08979.

Takayama, Y. 2012. Lactoferrin and Its Role in Wound Healing. Springer.

Tang, N., and L. H. Skibsted. 2016. Zinc bioavailability from whey. Enthalpy-entropy compensation in protein binding. Food Res. Int. 89:749–755. https://doi.org/10.1016/j.foodres.2016.10.002.

Trivedi, M., J. Laurence, and T. Siahaan. 2009. The role of thiols and disulfides on protein stability. Curr. Protein Pept. Sci. 10:614–625. https://doi.org/10.2174/138920309789630534.

van Veen, H. A., M. E. J. Geerts, P. H. C. Van Berkel, and J. H. Nuijens. 2004. The role of N-linked glycosylation in the protection of human and bovine lactoferrin against tryptic proteolysis. Eur. J. Biochem. 271:678–684. https://doi.org/10.1111/j.1432-1033.2003.03965.x.

Voswinkel, L., T. Vogel, and U. Kulozik. 2016. Impact of the iron saturation of bovine lactoferrin on adsorption to a strong cation exchanger membrane. Int. Dairy J. 56:134–140. https://doi.org/10.1016/j.idairyj.2016.01.008.

Waarts, B.-L., O. J. C. Aneke, J. M. Smit, K. Kimata, R. Bittman, D. K. F. Meijer, and J. Wilschut. 2005. Antiviral activity of human lactoferrin: Inhibition of alphavirus interaction with heparan sulfate. Virology 333:284–292. https://doi.org/10.1016/j.virol.2005.01.010.

Wang, B. 2016. Molecular determinants of milk lactoferrin as a bioactive compound in early neurodevelopment and cognition. J. Pediatr. 173:S29–S36. https://doi.org/10.1016/j.jpeds.2016.02.073.

Wei, Z., T. Nishimura, and S. Yoshida. 2000. Presence of a glycan at a potential N-glycosylation site, Asn-281, of bovine lactoferrin. J. Dairy Sci. 83:683–689. https://doi.org/10.3168/jds.S0022-0302(00)74929-0.

Wen, Z. 2007. Raman spectroscopy of protein pharmaceuticals. J. Pharm. Sci. 96:2861–2878. https://doi.org/10.1002/jps.20895.

Yamauchi, O., A. Odani, and M. Takani. 2002. Metal–amino acid chemistry. Weak interactions and related functions of side chain groups. J. Chem. Soc. Dalt. Trans. 18:3411–3421. https://doi.org/10.1039/B202385G.

Ye, X., S. Yoshida, and T. B. Ng. 2000. Isolation of lactoperoxidase, lactoferrin, α-lactalbumin, β-lactoglobulin B and β-lactoglobulin A from bovine rennet whey using ion exchange chromatography. Int. J. Biochem. Cell Biol. 32:1143–1150. https://doi.org/10.1016/S1357-2725(00)00063-7.

Yoshida, S., Z. Wei, Y. Shinmura, and N. Fukunaga. 2000. Separation of lactoferrin-a and -b from bovine colostrum. J. Dairy Sci. 83:2211–2215. https://doi.org/10.3168/jds.S0022-0302(00)75104-6.

Yoshida, S., and Ye-Xiuyun.. 1991. Isolation of lactoperoxidase and lactoferrins from bovine milk acid whey by carboxymethyl cation exchange chromatography. J. Dairy Sci. 74:1439–1444. https://doi.org/10.3168/jds.S0022-0302(91)78301-X.

ORCIDS

Oleksandra Pryshchepa ● https://orcid.org/0000-0001-9586-7069
Gulyaim Sagandykova ● https://orcid.org/0000-0001-6778-4653
Joanna Rudnicka ● https://orcid.org/0000-0001-5550-4001
Paweł Pomastowski ● https://orcid.org/0000-0002-1594-0623
Bogusław Buszewski ● https://orcid.org/0000-0002-5482-7500

6.5 Study on the zinc ions binding to human lactoferrin

A. Rogowska, **O. Pryshchepa**, Som N. Narayan, P. Śpiewak, A. Gołębiowski, K. Rafińska, K. Kurzydłowscki, B. Buszewski, P. Pomastowski, *"Study on the zinc ions binding to human lactoferrin"*, Journal of Molecular Structure, 1282, 2023: 135149, https://doi.org/10.1016/j.molstruc.2023.135149
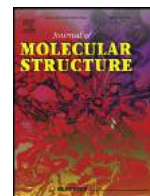
Study on the zinc ions binding to human lactoferrin

Agnieszka Rogowska [a,b], Oleksandra Pryshchepa [a,*], Narayan N. Som [c], Piotr Śpiewak [c],
Adrian Gołębiowski [a,b], Katarzyna Rafińska [b], Renata Dobrucka [c,d], Krzysztof Kurzydłowski [e],
Bogusław Buszewski [a,b], Paweł Pomastowski [a]

[a] Centre for Modern Interdisciplinary Technologies, Nicolaus Copernicus University in Torun, Wileńska 4, 87-100 Torun, Poland
[b] Department of Environmental Chemistry and Bioanalytics, Faculty of Chemistry, Nicolaus Copernicus University in Torun, Gagarina 7, 87-100 Torun, Poland
[c] Faculty of Materials Science and Engineering, Warsaw University of Technology, Wołoska 141, 02-507 Warsaw, Poland
[d] Department of Non-Food Products Quality and Packaging Development, Institute of Quality Science, Poznań University of Economics and Business, Al.
Niepodległości 10, 61-875 Poznań, Poland
[e] Faculty of Mechanical Engineering, Białystok University of Technology, Wiejska 45C, 15-351 Białystok, Poland

A B S T R A C T

The article presents the results of the study of Zn^{2+} binding to recombinant human lactoferrin. Isotherm studies were utilized with subsequent fit to Langmuir, Freundlich, and Henry models. Moreover, the kinetics of the process was investigated with the use of pseudo-first, pseudo-second, and Weber-Morris models for the process description. The study results revealed the complex nature of Zn^{2+} binding to lactoferrin, where based on isotherm three different sorption steps can be distinguished. Based on isotherm three different concentrations of Zn^{2+} solution (60, 300, and 600 mg/L) were chosen for Zn-lactoferrin complexes synthesis for further investigations. Sodium dodecyl sulfate-polyacrylamide gel electrophoresis, transmission electron microscopy, inductively coupled plasma mass spectrometry, Fourier-transform infrared and Raman spectroscopies were utilized which enabled the description of the Zn-binding process in a more accurate way. As a result, the highest Zn^{2+} content (7.92 mg/g) was observed for the complex synthesized with 600 mg/L Zn^{2+} solution. Spectroscopic studies reveal that the zinc ions binding may occur through the deprotonated carboxylic groups of aspartic and glutamic acids, imidazole ring of a histidine, or –CN and –OH groups of other amino acids as well as through weak noncovalent cation–π interactions. According to obtained results, it is also can be suggested that high Zn^{2+} concentration can lead to changes in protein structure and partial loss of Fe^{3+} from the metal-binding clefts. The obtained lab results were also complemented with Molecular Dynamics and Density Functional Theory simulations that support the conclusions outlined from lab experiments.

1. Introduction

In the 60 s of the last century, it was discovered that zinc is an essential micronutrient for the proper functioning of the human body [1–3]. Zinc is ubiquitous in cells of living organisms and has catalytic, regulatory as well as structural functions [1,4]. Currently, the deficiency of this essential element is considered to be a serious worldwide problem. The increased demand for zinc, and thus a greater risk of its deficiency, occurs mainly in pregnant and lactating women, infants, children, and teenagers. Too low supply of zinc in children may lead to abnormalities in the structure and functioning of the digestive, skeletal, reproductive, immune, and central nervous systems [1,4,5]. Low zinc content in foods is associated with growth in zinc deficiency soils. Moreover, food processing can lead to significant zinc loses and thus decrease its amount in the final product [6]. Finally, food rich in phytic acid prevents zinc absorption due to the formation of insoluble phytates. All these can be a reason for inadequate zinc admission from food and the occurrence of zinc deficiency in organisms. It is suggested that more than 25% of the world's population is at risk of zinc deficiency which indicates the necessity of additional zinc supplementation, especially in the zinc deficiency risk group [7].

Zinc supplements usually are based on soluble zinc salts (gluconate, sulfate, citrate, acetate) [8]. However, high doses of pharmacological zinc often cause unwanted side effects. It was shown that up to 18% of healthy males and even 84% of females were sus-

* Corresponding author.

ceptible to side effects when 50 mg of inorganic zinc was provided. They suffered from headaches, abdominal cramps, nausea, loss of appetite, and vomiting [9]. In turn, the presence of protein in the diet has been shown to have a beneficial effect on zinc absorption [2]. Besides, it was revealed that microelements in form of proteinates have higher bioavailability and lower gastrointestinal side effects, in particular zinc and iron complexes with whey proteins [10,11]. The production of such complexes may include the processes of heat denaturation, enzymatic hydrolysis, or succinylation aiming for the higher efficiency of metal binding and yield of the final product [12,13]. However, the such procedure leads to the loss of the biological activity of the proteins. Instead, the utilization of lactoferrin enables the synthesis of iron- and zinc-rich complexes based on the unmodified protein which may preserve its biological properties [14,15].

The utilization of LTF as a basis for the production of metal-protein complexes is beneficial due to its biological properties. LTF is abundant in human milk, accounting for 1-10 mg/mL depending on the lactation stage and general physiological condition. LTF is a high molecular weight glycoprotein (approx. 80 kDa) that binds iron and shows a multifunctional action, including prebiotic, anti-bacterial, anti-inflammatory, anti-cancer, anti-oxidant, and immunoregulatory properties [16]. The high concentration of LTF in the colostrum (up to 10 mg/mL) helps to protect newborns and infants from being susceptible to parasitic, fungal, bacterial, and viral infections [16,17]. Moreover, this protein also can modulate iron and zinc absorption in the intestine [18,19]. Thus, complexes based on LTF should have several beneficial effects on the organism and seems to be promising strategy in the treatment of zinc and iron deficiency.

Thus, the study aimed to obtain the complexes of recombinant human lactoferrin (hLTF) and zinc, which could be used as a food additive, including infant formulas. In the study recombinant hLTF saturated with iron, expressed in rice was used for the determination of the hLTF ability to bind Zn^{2+}. Recent biophysical and biochemical studies have shown that recombinant hLTF has very similar properties to natural hLTF. Recombinant hLTF has the same iron-binding capacity, antibacterial properties as well as thermal and pH stability [20,21]. It was shown that it can be efficiently bound and absorbed by human intestinal cells. Furthermore, the rice expression system allows for large-scale use of LTF in the food and pharmaceutical industries, which is difficult with natural hLTF isolated from human milk. In addition, the use of rice for recombinant hLTF expression carries a low risk of allergenicity, and at the same time has good nutritional properties [20,21].

To assess the nature of Zn^{2+} binding to hLTF, adsorption isotherm and kinetics studies were applied. Additionally, to confirm the immobilization process and to identify changes that occurred in the protein as a result of the sorption process the transmission electron microscope (TEM-EDX), inductively coupled plasma mass spectrometry (ICP-MS), Fourier transformed infrared spectroscopy (FTIR), RAMAN spectroscopy, and sodium dodecylsulfate polyacrylamide gel electrophoresis (SDS-PAGE) as well as capillary electrophoresis coupled with ICP-MS techniques were used. Finally, the molecular dynamics and quantum mechanical calculations were performed to complement the laboratory findings regarding the mechanism of Zn-lactoferrin complex formation.

2. Materials and methods

2.1. Chemicals and reagents

Expressed in rice, recombinant hLTF saturated with iron ($\geq$90% SDS-PAGE) and zinc nitrate hexahydrate as well as other chemicals (i. e. solvents and ICP-MS standards) were supplied by Merck Life Science Sp.z.o.o. (Poznań, Poland) from Sigma-Aldrich. Calibra-

tion standard, matrix, and target plates for MALDI analysis were provided by Bruker Daltonics (Bremen, Germany). Polyacrylamide gel, stain, protein standard, running buffer, load sample buffer, and sample reducing agent for gel electrophoresis analysis were purchased from ThermoFisher Scientific (Waltham, MA, USA). Ultrapure water was provided by the Milli-Q RG system (Millipore Intertech, Bedford, MA, USA).

2.2. Isoelectric point determination

For isoelectric point (pI) determination zeta potential value was measured at different pH conditions (pH from 4 to 9). The protein was suspended in 0.09% NaCl solution to the final concentration of 1 mg/mL. Then, the pH of the sample for each measurement point was adjusted by applying 0.1 M sodium hydroxide or 0.1 hydrochloric acid solutions. The pH of the sample was measured using FiveEasy Plus pH meter (Mettler Toledo, Columbus, Ohio) equipped with a combined electrode with glass membrane and Ag/AgCl reference system (Mettler Toledo, Columbus, Ohio). Measurement of zeta potential in each pH point was performed in triplicate using Malvern Zetasizer Nano ZS (Malvern, Worcestershire, UK) and disposable folded capillary cells (Malvern, Worcestershire, UK).

2.3. MALDI-TOF MS analysis

Recombinant hLTF was dissolved in 0.1% trifluoroacetic acid to the final concentration of 1 mg/mL. Saturated solutions of sinapic acid (SA) or 2,5-dihydroxybenzoic acid (DHB) at a concentration of 10 mg/mL were prepared in TA30 solvent (30:70 (v/v) of acetonitrile to 0.1% trifluoroacetic acid). 1 μL of the sample was spotted on the GroundSteel target plate. After evaporation of the solvent, the sample was covered with 1 μL of the matrix (SA or DHB solutions) and air-dried. The calibration was performed using protein calibration standard II provided by Bruker Daltonics (Bremen, Germany). The mass spectra were registered in a mass range of $10\,000-100\,000$ *m/z* using MALDI-TOF/TOF mass spectrometer UltrafleXtreme (Bruker Daltonics, Bremen, Germany) working in the linear positive mode. The data were analyzed with Bruker Daltonics software (flexControl and flexAnalysis).

2.4. Isotherm study

All samples were prepared in 0.1 M ammonium citrate-bicarbonate buffer adjusted to a pH of 7.4 as described earlier [14]. The isotherm study was conducted by applying ten different Zn^{2+} solutions (6, 15, 30, 45, 60, 120, 300, 450, 600, and 900 mg/L). The recombinant hLTF solution at a concentration of 5 mg/mL was mixed with zinc nitrate solution at each of the concentrations listed above in a volumetric ratio 1:1 (obtaining the initial Zn^{2+} concentrations in the reaction mixture of 3, 7.5, 15, 22.5, 30, 60, 150, 225, 300, and 450 mg/L). Namely, 0.2 mL of zinc solution was mixed with 0.2 mL of recombinant hLTF in the Eppendorf tube. The prepared in triplicate samples were incubated at 20 °C with mixing (900 rpm) using Termomixer from Eppendorf (Germany, Hamburg). The reaction was stopped after 24 h of incubation. Next, samples were transferred to Amicon®Ultra-0.5 Centrifugal membrane filters with 3 kDa cut-off (Sigma-Aldrich, Steinheim, Germany) and centrifuged (RT, 10 min, 15 000 rpm). The obtained filtrates were diluted using 1% nitric acid to an expected Zn^{2+} concentration not greater than 100 ppb and then measured by ICP-MS 2030 (Shimadzu, Kyoto, Japan). The concentration of zinc in the sample was estimated based on a calibration curve made with the use of ICP multi-element standard solution IV (Sigma-Aldrich, Steinheim, Germany). Experimental data were fitted to the Freundlich and Langmuir models as well as presented as a function of C_e/C_0 by appro-

priate equations described in previous work [22]. The initial linear fragment of the isotherm curve was also fitted to the Henry isotherm model. The isotherm constant was determined according to Sieczka et al. [23].

2.5. Kinetics study

All samples were prepared in 0.1 M ammonium citrate-bicarbonate buffer adjusted to a pH of 7.4 [14]. The kinetic study was performed using three Zn^{2+} solutions (60, 300, and 600 mg/L). The recombinant hLTF solution (5 mg/mL) and appropriate zinc nitrate solution were mixed in a volumetric ratio 1:1 (i.e., 0.2 mL of each solution), so the initial Zn^{2+} concentration in the reaction was 30, 150, and 300 mg/L, respectively. The prepared in triplicate samples were incubated at 20 °C with mixing (900 rpm) using Termomixer from Eppendorf (Germany, Hamburg). The reaction was conducted for 2, 5, 10, 20, 30, 60, 120, 300, 540, and 1440 min. Then, samples were treated as in the case of the isotherm study. The determination of zinc concentration also was conducted as it was described in Section 2.4. The content of adsorbed Zn^{2+} onto hLTF molecule, the efficiency of the process, kinetics models parameters as well as distribution coefficient (K_d), and the change of Gibbs free energy (ΔG^0) were calculated, according to Rogowska et al. [24].

2.6. Preparation of the recombinant human lactoferrin with immobilized zinc

The samples were prepared in 0.1 M ammonium citrate-bicarbonate buffer pH 7.4 [14] using three different Zn^{2+} solutions (60, 300, and 600 mg/L). Preparative synthesis was performed in 15 mL centrifugal tubes, where 7.5 mL of protein suspension and 7.5 mL of Zn^{2+} solution were added. The prepared samples were next incubated at 20 °C with mixing (900 rpm) for 24 h. Then, the synthesized complexes were collected by centrifugation (RT, 10 min, 15 000 rpm) on the Amicon® Ultra-4 Centrifugal membrane filters. The remaining protein concentrate was washed three times to flush away any unbound Zn^{2+} by adjusting the sample volume to 4.0 mL with ultra-pure water. Each time the samples were concentrated 16-fold on the filters (from an initial volume of 4 mL to a final volume of 250 μL). The purified protein concentrate was transferred to a new Eppendorf tube and frozen (−20 °C). The obtained sample was lyophilized using FeeZone Freeze Dryer (Labconco, Kansas City, MO, USA) to obtain the powder which was then subjected to further analysis.

2.7. Determination of zinc and iron content in the lactoferrin-Zn complexes

The hLTF-Zn complexes of exact mass (nearly 1.5 mg) were digested for 3 h at 80 °C using 100 μL of concentrated nitric acid. Then mineralized protein was diluted to 10 mL with ultra-pure water. Further dilution was performed with 1% nitric acid to an expected Zn^{2+} concentration not greater than 100 ppb. Obtained samples were subjected to ICP-MS analysis (ICP-MS 2030, Shimadzu, Kyoto, Japan). Zinc and iron content was estimated based on a calibration curve prepared with the use of ICP multi-element standard solution IV (Sigma-Aldrich, Steinheim, Germany).

2.8. Gel electrophoresis analysis

Recombinant hLTF and hLTF-Zn complexes were suspended in ultrapure deionized water to a final concentration of 1 mg/mL. The SDS-PAGE analysis was performed according to the manufacturer procedure in reduced mode (ThermoFisher Scientific, Waltham, MA, USA). For this purpose, 6.5 μL of the sample was mixed with

1 μL of 10X Bolt™ Sample Reducing Agent and 2.5 μL of 4X Bolt™ LDS Sample Buffer. The obtained mixture was incubated for 10 min at 70 °C and then applied on the well of Bolt™ 4 to 12%, Bis-Tris Plus, Mini Protein Gel, and MES running buffer. Coomassie Blue R-350 ready-to-use stain (Thermo Scientific, Waltham, MA, USA) was used for gel staining.

2.9. The study by capillary electrophoresis coupled with ICP-MS

Capillary electrophoresis was performed for both hLTF and hLTF-Zn complex. The lyophilized samples were suspended in borate buffer (30.183 g of Na-Borat in 0.5 L of water; pH = 7.8) to obtain solutions with a final concentration of 1 mg/mL. The analysis was conducted on PrinCe capillary electrophoresis (CE) system (Prince Technologies B.V.) with the utilization of non-coated fused silica capillary 90 cm × 75 μm ID. The conditioning of the capillary was performed by rinsing it for 1 min with 0.1 M NaOH, Milli-Q water, and then 1 min with borate running buffer. Sample injection was performed by applying the pressure of 250 mbar for 20 s. The analysis conditions were: +20 kV voltage and 250 mbar pressure.

The CE-capillary was connected to the NexIon 300D ICP-mass spectrometer (Perkin Elmer) using an in-house interface [55] which enabled monitoring of element-selective electropherograms on-line by ICP-MS using dynamic reaction cell (DRC) mode for ions/isotopes ^{48}[SO], ^{56}Fe, and ^{66}Zn. Each sample was analyzed using two DRC gas: ammonia (0.6 ml/min, RPq = 0.45) for ^{56}Fe and ^{66}Zn as well as oxygen for sulfur ^{48}[SO] and ^{66}Zn. Both DRC gasses allowed the detection of silver isotopes. The RF power was 1250 W and the plasma gas was set at 16 L Ar/min. Nebulizers' gas flow rate was established at 0.98 Ar/min.

2.10. Transmission electron microscope analysis

Recombinant hLTF and hLTF-Zn complexes were suspended in ultrapure deionized water and placed on a carbon-coated copper grid (Lacey Carbon Support Film 400 mesh, Electron Microscopy Sciences). After drying at room temperature samples were analyzed by transmission electron microscopy coupled with an energy-dispersive X-ray spectrometer (TEM-EDX - FEI Tecnai F20 X- Twin, Hillsboro, OR, USA).

2.11. Fourier-transform infrared spectroscopy analysis

The FT-IR analysis was performed using a transmission spectroscope and a spectroscope equipped with an attenuated total reflectance (ATR) adapter. In the first case, recombinant hLTF and hLTF-Zn complexes were suspended in ultrapure deionized water and placed on a CaF$_2$ plate. After drying at 30 °C samples were analyzed by SPECTRUM 200 Perkin ELMER spectrophotometer (Perkin Elmer, Waltham, MA, USA) in the range of 400 - 4000 cm^{-1}. In the case of ATR FT-IR analysis, the lyophilized powder of recombinant hLTF and hLTF-Zn complexes were directly analyzed using an Alpha FTIR spectrometer in ATR mode (Bruker, Billerica, Massachusetts, USA) at the same wavelength range. The spectra were plotted using the OPUS 7.5 software (Bruker Daltonics, Hamburg, Germany).

2.12. RAMAN spectroscopy analysis

Recombinant hLTF and hLTF-Zn complexes were suspended in ultrapure deionized water and placed on a microscopic slide. The RAMAN analysis was conducted using Senterra II Dispersive Raman Microscope (Bruker). The spectra were registered in the range of 4000 to 400 cm^{-1}. The applied excitation wavelength was $\lambda = 532$ nm with a power of 20 mW. The spectra were plotted using the OPUS 7.5 software (Bruker Daltonics, Hamburg, Germany).

2.13. Molecular dynamics calculations

The structure of hLTF was obtained from the RSCB protein database (ID - 1LFG) with a resolution of 0.202 nm. The missing heavy atoms and protonation state of the protein have been fixed with PDB fixer software [25]. Thereafter, the MD simulations were performed using the GROMACS-2020 version with the GROMOS force field [26,27]. The parameters for protein residues were obtained with the gromos43a1 force field. Instead, the nonbonded parameters were obtained from the paper of W. Lin et al. [28]. Finally, the force field of CO_3^{-2} and other non-residue components was obtained from the PRODGR server [29]. We have considered the physiological pH condition, i.e., pH=7.4. The whole protein was solvated in a cubic box by considering the SPC (simple point charge) explicit water mode with a side length of 10 nm. Thereafter, ten Cl^- were added randomly to the box to neutralize the positive charge of the protein. To avoid the clash during the simulation, energy minimization has been performed. Throughout the calculations, the periodic boundary conditions were applied. The temperature of the whole system, including protein, was set at 300 K using the velocity rescaling algorithm and Berendsen thermostat under NVT ensemble for 50 ps. In the NPT ensemble, the Parrinello-Rahman barostat was used to equilibrate the system for 100 ps at a normal pressure of 1 bar. The cut-off for nonbonded interactions was set to 1.2 nm with a 1 nm switching distance and using the Particle mesh Ewald (PME) method for long-ranged electrostatic interaction [30]. The Molecular Dynamics (MD) simulation was run for 30 ns with an integration time step of 2 fs. Chimera software was used for statistical analysis of the binding affinity of the Zinc aqua complex $[Zn(H_2O)_x]^{2+}$(ZAC) to protein [31]. Moreover, the potential binding sites in protein were estimated using the pyrx (Auto-dock vina) package [32]. We have considered different numbers of Zn^{2+}(i.e., 1, 5, 10, 15, 20, 40, and 45 atoms per 1 protein molecule) to evaluate the effect of the metal ion concentration on the system. The preliminary results for binding energy and potential binding sites of Zn^{2+} binding to 1LFG (40 zinc atoms per protein molecule) were theoretically obtained within Auto-dock vina and accounts for -5.86 kJ/mol for eight turns of docking.

2.14. Quantum mechanics simulations

Density functional theory (DFT) calculations were performed to analyze ZAC interaction with bare amino acids and their peptides at pH = 7.4. We have calculated the binding energy (ΔE_{BE}), interactional Gibbs free energy (ΔG), and Gibbs free energy (ΔG_r) of the reaction for the proton transfer.

The binding energy was calculated using the below equation [33]:

$$\Delta E_{BE} = E\left(AA + ZAC/Zn^{2+}\right) - E(AA) - E\left(ZAC/Zn^{2+}\right)$$

where $E(AA+ZAC/Zn^{+2})$ is the total energy of the ZAC interacting with Amino acid (AA), E(AA) is the total energy of corresponding free amino acid, and $E(ZAC/Zn^{2+})$ is the total energy of the ZAC.

The interactional Gibbs free energy changes (ΔG) were calculated according to the:

$$\Delta G = G(AA + ZAC) - G(AA) - G(ZAC)$$

where ΔG is the change of interactional Gibbs free energy, G(AA+ZAC), G(AA), and G(ZAC) are the Gibbs free energy of amino acid interacting with ZAC, corresponding free amino acid, and free ZAC, respectively.

The possibility of the proton transfer from ZAC with six coordinated water molecules (ZAC6) to deprotonated carboxyl groups of glutamic and aspartic acids was evaluated (reported previously

[34]). The Gibbs free energy of the reaction was determined as follows:

$$\Delta G_r = \text{Gibbs free energy of product}$$
$$- \text{Gibbs free energy of reactant} = [G(AspH/GluH) + G(PZAC)]$$
$$- [G(Asp-/Glu-) + G(ZAC)]$$

where G(AspH/GluH) is the Gibbs free energy of protonated aspartic/glutamic acid, G(PZAC) is the Gibbs free energy of aqua hydroxy zinc complex $[Zn(OH)(H_2O)_5]^+$, G(Asp-/Glu-) represents the Gibbs free energy of deprotonated aspartic/glutamic acid and G(ZAC) is a Gibbs free energy of ZAC ($[Zn(H_2O)_6]^{2+}$).

Finally, we performed calculations of harmonic vibrational frequencies to compute the IR and Raman spectra and thus validate the experimentally obtained data. Both techniques can provide information about the interaction mechanism of ZAC with proteins [14,34]. The M06–2X functional was employed for the DFT calculations. Geometry optimizations were performed at M06–2X/6–311++(d,p) level with the implicit SDM solvation method at a solvent dielectric constant of 78.4 using the Gaussian 16 software package [35–37].

3. Results and discussion

3.1. Characterization of expressed in rice recombinant human lactoferrin

3.1.1. Matrix-assisted laser desorption/ionization analysis

Literature data indicate that the biological properties of LTF are dependent on its physicochemical features, e. g. glycosylation level, iron saturation status, etc. [16]. Thus, before modifying recombinant hLTF with Zn^{2+}, its basic characterization was performed. To determine the exact mass of the used protein the MALDI-TOF-MS approach was applied. Regardless of the used matrix, the protein mass was set at 78.5 kDa (Fig. 1). Depending on the degree of glycosylation, the mass of hLTF may range from 77 to 82 kDa [38]. In the Y. A. Suzuki work the mass of recombinant hLTF from the rice was determined as 78.9 kDa which is close to our results [20]. The small differences may be connected with the differences in the glycans' structure and measurement error [39].

3.1.2. Isoelectric point determination

Another important biochemical parameter for proteins' characterization is their isoelectric point (pI) which was determined as 6.6 for recombinant hLTF. In general, the pI for LTF is considered to be in the range of 8.5 – 9 [16]. Thus, it is significantly higher than for other whey proteins [40]. However, some studies indicate that depending on the utilized method isoelectric point for hLTF can be much lower (5.2 – 8.7), which is in agreement with the obtained result [41]. Moreover, based on the research performed for transferrin, it can be assumed that the degree of iron saturation and the differences in the N-glycans may affect the pI [42,43] (Fig. 2).

3.2. Batch sorption study of zinc ions sorption onto recombinant human lactoferrin

3.2.1. Isotherm studies

To evaluate the mechanism of Zn^{2+} binding by recombinant hLTF, isotherm studies were performed. Fig. 3 presents the plot of protein sorption capacity as a function of Zn^{2+} concentration in the reaction mixture as well as the fitting of experimental data to the Henry, Langmuir, and Freundlich models. In addition, Table 1 presents the calculated constants and parameters for the applied models. As can be seen, the process of Zn^{2+} binding by recombinant hLTF is complex, which requires the use of different models to describe the individual sections of the obtained curve.
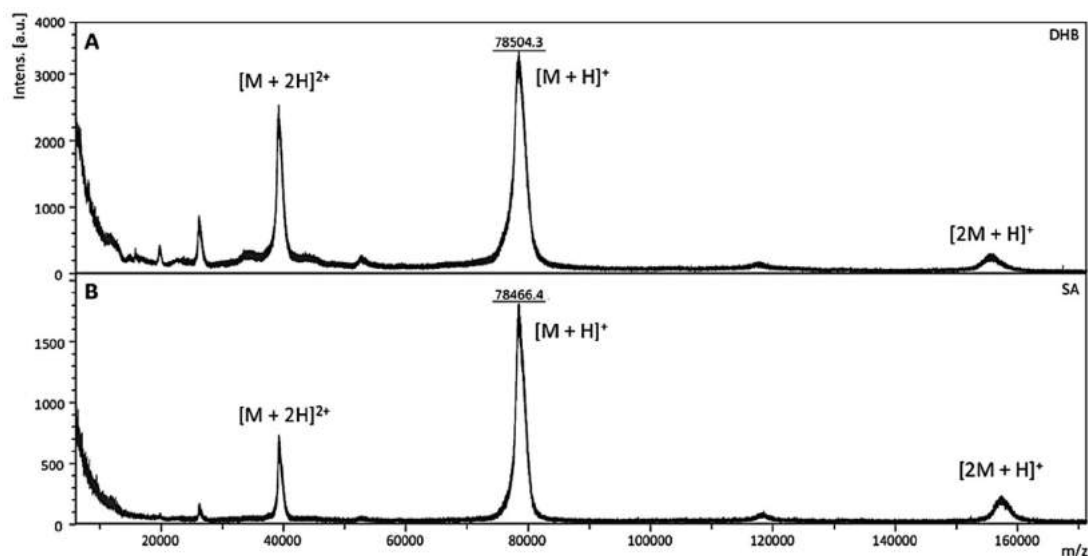
Fig. 1. MALDI-TOF MS spectra of recombinant hLTF obtained by applying: A. DHB and B. SA matrix.

Table 1
Parameters calculated for Henry, Freundlich, and Langmuir mathematical models of sorption isotherms.

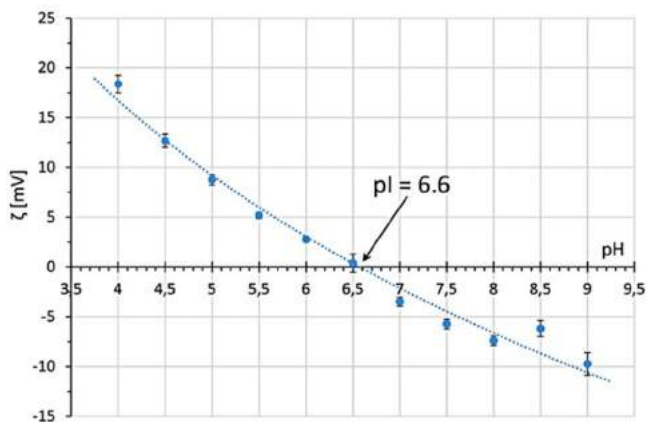| Henry Model		Freundlich Model				Langmuir Model			
K_H [L/g]	R^2	K_F [L/g]	n	S	R^2	K_L [L/g]	q_m [mg/g]	S	R^2
0.079	1.000	0.080	1.367	32.053	0.993	0.040	11,745.948	30.377	0.960

Fig. 2. Measured zeta potential dependence on pH for recombinant hLTF.

The first step observed on the isotherm curve shows linear nature. This step includes initial concentrations in the reaction mixture of Zn^{2+} from 3 to 30 mg/L. The Henry isotherm model is shown to be the most appropriate to describe this fragment. The obtained Henry constant (K_H) was 0.0786 L/g and the determination coefficient (R^2) was 1. When Zn^{2+} concentrations in the reaction mixture were above 30 mg/L the nature of the process changed and the Henry model did not fit well with the experimental data. For this reason, the Freundlich and Langmuir models were used. As can be seen, the Freundlich model provides a better fit to the experimental data, while the Langmuir model does not work for the description of the Zn^{2+} sorption process by recombinant hLTF. Finally, the modified BET model which shows the data as a function of C_e/C_0 was applied (Fig. 3B) [34,44]. The approach revealed the presence of three process steps. The first step is related to the formation of a monolayer of Zn^{2+} on the protein surface and corresponds to the initial Zn^{2+} concentrations of 3 – 30 mg/L. The

second step occurred when initial Zn^{2+} concentrations were from 30 to 150 mg/L. The presence of this step indicates the changes in recombinant hLTF structure as a result of the gradual penetration of Zn^{2+} into the protein structure. The last step can be associated with the further intake of Zn^{2+} inside the protein structure.

3.2.2. Kinetics studies

Fig. 4**A,B,C** present the plots of Zn^{2+} concentrations change as a function of sorption time. It can be assumed that regardless of the initial Zn^{2+} content, the overall nature of the process was similar.

During about the first 10 min, rapid sorption of Zn^{2+} took place, and after this time the system reached an equilibrium state. However, as the initial Zn^{2+} increased the higher sorption efficiency (28.36 ± 0.96, 51.07 ± 0.11, $59.02 \pm 0.26\%$) and sorption capacity of the protein (3.47 ± 0.12, 36.20 ± 0.08, 82.56 ± 0.36 mg/g) was observed. The application of the zero-order kinetic model for the description of the initial linear section allowed to determine the speed of the process, which turned out to be dependent on the initial Zn^{2+} content in the solution. The calculated rate constants were 1.24, 15.13, and 17.55 mg/(L•min) for initial Zn^{2+} concentration in the solution of 30, 150, and 300 mg/L respectively. Therefore, the application of the zero-order kinetic model indicates an increase in the speed of the process when higher concentrations of Zn^{2+} were used for immobilization.

For a more detailed process description pseudo-first-order (PFO) and pseudo-second-order (PSO) kinetic models were employed. Fig. 4**D,E,F** show curves resulting from the fitting of experimentally obtained data to selected kinetic models. The calculated kinetic parameters were summarized in Table 2. Based on the obtained values of the relative approximate error it can be concluded that for all Zn^{2+} initial concentrations, the PSO model provides the best correlation with the experimental results. Furthermore, for both PFO and PSO models, the most appropriate data description was in the case when starting Zn^{2+} concentration was 150 mg/L. According to current reports, it is believed that the sorption pro-
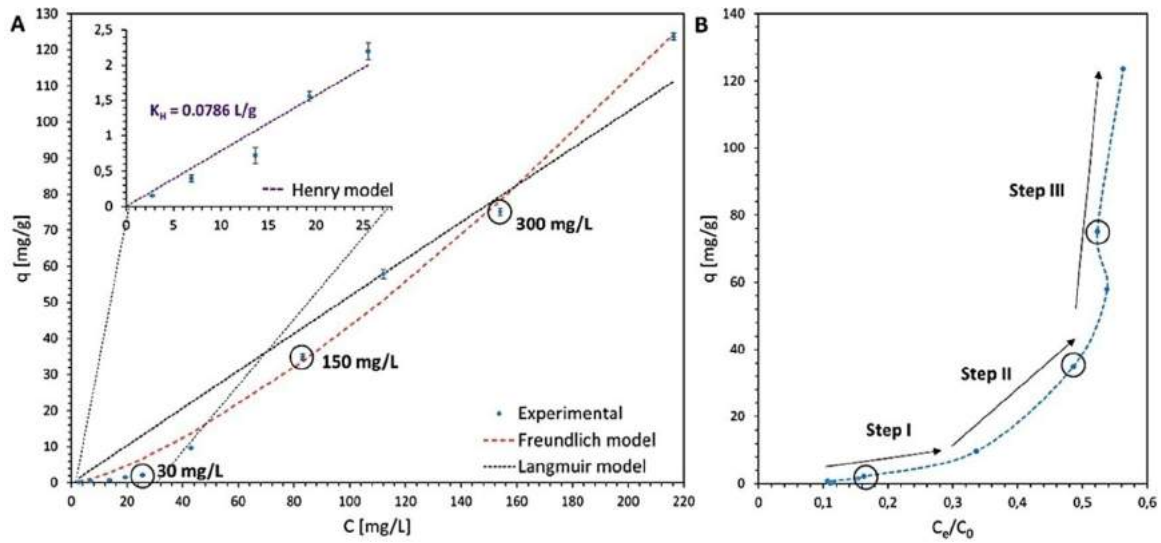
Fig. 3. Isotherm of Zn^{2+} ions sorption onto recombinant hLTF and matching of experimental data to the Henry, Freundlich, and Langmuir isotherms models (A). K_H is a calculated constant for the Henry model. Sorption isotherm of Zn^{2+} ions as a function of C_e/C_0 (B).
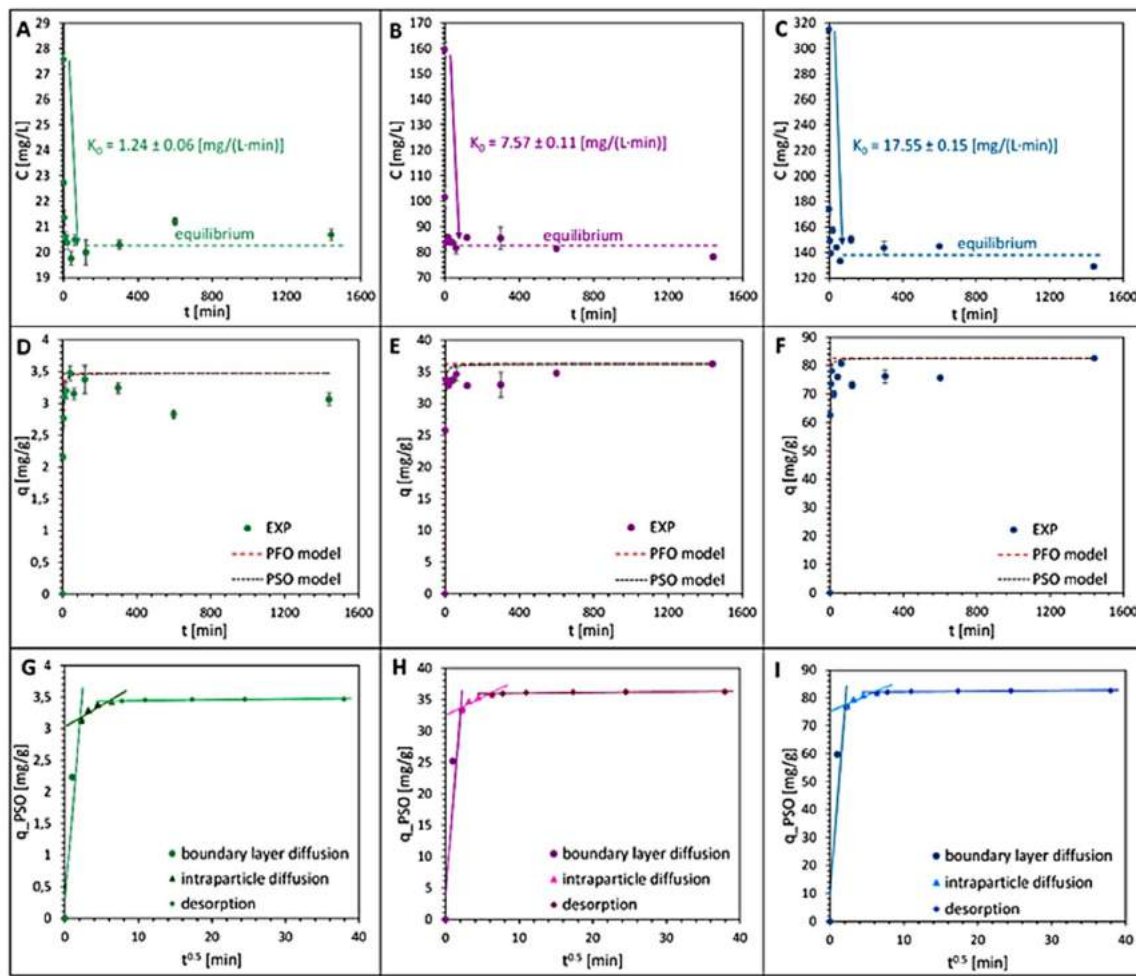
Fig. 4. The plot of the Zn^{2+} concentration change as a function of time and data fitting to zero-order kinetic model for initial Zn^{2+} concentrations in the solution of: A. 30, B. 150, and C. 300 mg/L. Fitting of experimental data to PFO and PSO kinetic models for Zn^{2+} concentration in the reaction mixture of D. 30, E. 150, and F. 300 mg/L. The fitting plot of PSO data to intra-particle diffusion model for Zn^{2+} concentration of G. 30, H. 150, and I. 300 mg/L.

Table 2
The kinetics parameters of PFO and PSO models.

C_0 Zn^{2+} [mg/L]	PFO			PSO		
	k_1 [min^{-1}]	$A_{approx.}$ [%]	q_e [mg/g]	k_2 [min^{-1}]	$A_{approx.}$ [%]	q_e [mg/g]
30	0.897	8.279	3.474	0.518	7.261	3.473
150	1.234	5.648	36.200	0.063	3.831	36.189
300	1.410	6.952	82.556	0.032	5.103	82.534

k_1 - rate constant of the PFO model; k_2 - rate constant of the PSO model; q_e – ions amount sorbed in equilibrium; $A_{approx.}$ - relative approximate error.

cesses occurring in biological systems mostly follow the PSO kinetics, which is consistent with the results obtained in this study [45].

Finally, the intra-particle Weber-Morris (WM) model was utilized for the description of data fitted to the PSO kinetic model (Fig. 4**G,H,I**). This model takes into account the diffusion nature of sorbate mass transfer. There are three stages of diffusion that control the course of the adsorption kinetics: diffusion of sorbate from the depth of the solution to the surface, diffusion in the boundary layer, and diffusion deep into the sorbent structure [46]. Regardless of the Zn^{2+} initial concentration in the reaction mixture the presence of all three steps was observed. The fact indicates that no only surface Zn^{2+} binding occurs. Other limiting processes may take place, such as ions transport to the interior of the protein molecule or changes in the protein structure induced by Zn^{2+}. The constant related to the impact of sorbate diffusion in the boundary layer was calculated from the y-axis intercept. Obtained values account for 3.030, 32.481, and 75.064 mg/g for initial Zn^{2+} concentration in the solution of 30, 150, and 300 mg/L, respectively. The corresponding constants are related to the thickness of the layer. Instead, the constants of intra-particle diffusion rate were calculated as 0.068, 0.573, and 1.156 mg/g•min$^{0.5}$, respectively.

The change in Gibbs free energy (ΔG^0) of the system was calculated based on the value of the distribution coefficient (K_d). The K_d values were 175.90, 463.81, and 639.97 for the initial Zn^{2+} concentration in the solution of 30, 150, and 300 mg/L, respectively. Thus, the ΔG^0 values were calculated as −12.68, −15.06, and −15.85 kJ/mol. The negative value of ΔG^0 indicates the spontaneous nature of the sorption process [34,47]. The literature data revealed that for metals binding to structurally-defined metal-binding sites, such as zinc fingers or active sites of the enzymes, the binding energy ranges from -33 kJ/mol and up to even – 200 kJ/mol, where the highest values are on the level comparable to covalent bonds [48]. Instead, the obtained in the study values of energy change are characteristic of noncovalent weak interactions which are typical for reversible physical adsorption. It is noteworthy to mention that Zn^{2+} has the highest affinity to the imidazole group of histidine [49] where the binding energy accounts ≈ 20 kJ/mol per one bond [52]. Thus, it can be suggested that the majority of the bonded Zn^{2+} interacts with the protein through one bond. However, it is also can be noticed that an increase in the Zn^{2+} concentration in the solution leads to a more significant change in Gibbs free energy. It can be related to the changes in protein structure induced by metal that leads to the possibility to form several bonds with protein.

3.3. Characterization of recombinant human lactoferrin-Zn complexes

3.3.1. Sodium dodecyl sulfate-polyacrylamide gel electrophoresis (SDS-PAGE)

Fig. 5 presents the picture of obtained SDS-PAGE gel for unmodified protein and protein modified with Zn^{2+} solutions of different concentrations. For all samples, there is an intense band of about 80 kDa which corresponds to lactoferrin molecule mass, and a small, bright band of about twice the time higher mass from
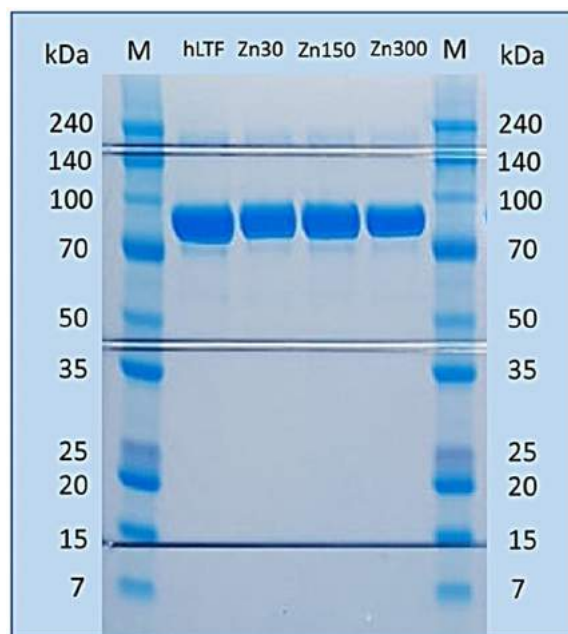

Fig. 5. SDS-PAGE of native recombinant hLTF and hLTF-Zn complexes obtained after application of initial Zn^{2+} concentration of 30 (Zn30), 150 (Zn150), and 300 (Zn300) mg/L as well as protein marker (M).

lactoferrin dimer. The absence of other bands indicates the high purity of the used protein [14]. The obtained bands for the modified protein, even after the application of the highest concentration of Zn^{2+}, do not change significantly compared to the native protein. The results indicate that Zn^{2+} sorption did not lead to protein degradation and obtained complex is stable. Moreover, the protein modification did not affect its dimerization level.

3.3.2. Capillary electrophoresis coupled with ICP-MS

Fig. 6 summarizes the obtained electropherograms for the species ^{48}[SO], ^{56}Fe, and ^{66}Zn. As can be seen, the signal from the protein had a migration time of ≈ 220 s. The same migration time was observed for iron indicating the strong binding of this element in the protein. No zinc was detected in the native protein. Instead, on the electropherogram of the hLTF-Zn complex strong signal from ^{66}Zn was detected. The signal of zinc has a different migration time (≈280 s) in comparison to protein and protein-bound iron. It can be concluded that due to the low binding energy of the Zn^{2+} under applied voltage during the analysis, it can be easily separated. Moreover, it can be expected the change in protein charge upon metal binding [50]. However, no change in migration time was observed which should indicate that all of the absorbed zinc was separated from protein during the analysis. It is also noteworthy to mention that on the electropherogram of zinc-modified protein, the presence of an additional signal derived from an iron can be detected. In our previous work regarding silver complexes based on bLTF, completely different results were obtained
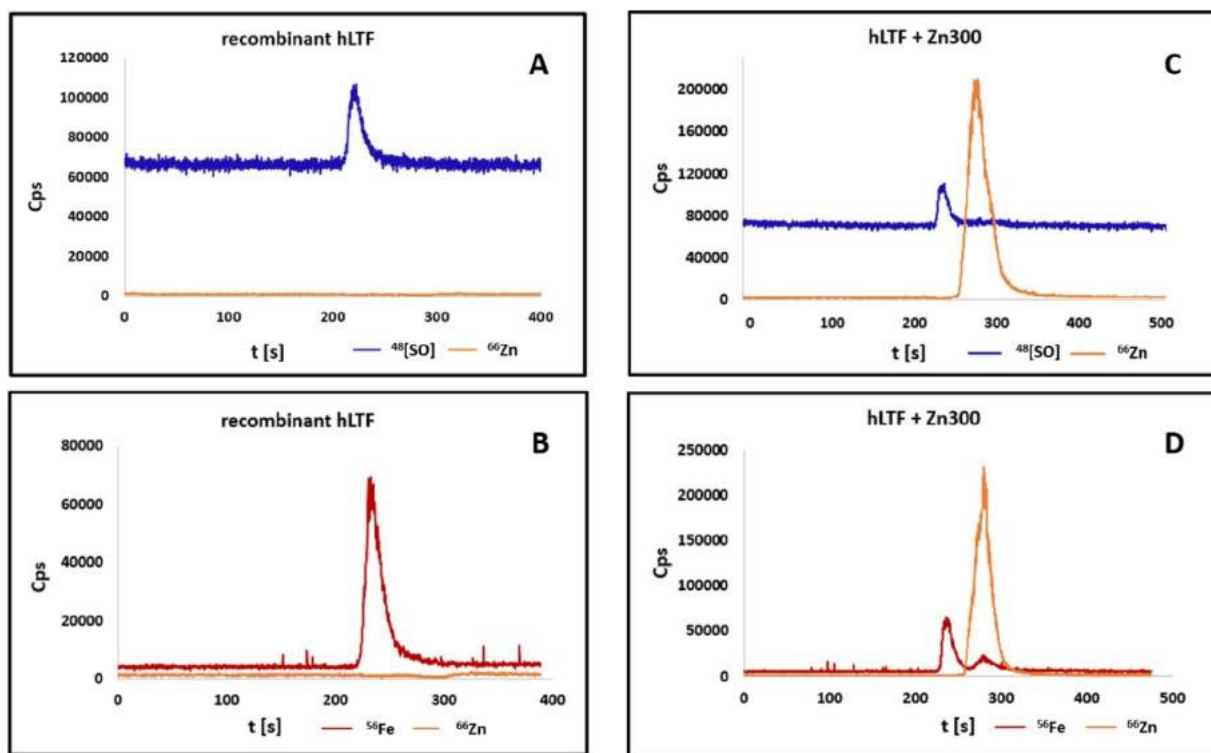
Fig. 6. Electropherograms obtained by CE-ICP-MS for native recombinant hLTF with A. oxygen in DRC and B. ammonia in DRC as well as hLTF-Zn complex synthesized by application of initial Zn^{2+} concentration of 300 (Zn300) mg/L with C. oxygen in DRC and D. ammonia in DRC.
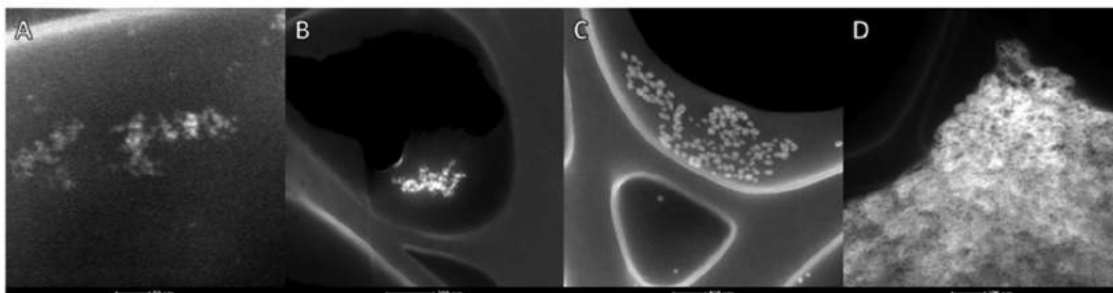

Fig. 7. Transmission Electron Microscope (TEM) images of A. recombinant hLTF and hLTF-Zn complexes obtained after application of initial Zn^{2+} concentration of B. 30, C. 150, and D. 300 mg/L.

[51]. Firstly, two signals from ^{107}Ag were detected and one of them had the same migration time as the protein. The results revealed that in the case of silver much stronger bonds can form with lactoferrins. Secondly, there was no split of the peak that comes from iron. Thus, it can be suggested that Zn^{2+} induced the changes in the recombinant hLTF which led to the weakening of the iron-protein bond.

3.3.3. Transmission electron microscopy

Fig. 7 shows the images of recombinant hLTF before and after its functionalization with Zn^{2+}. Earlier studies have shown that the interaction of Zn^{2+} with certain proteins, e.g. ovalbumin, can lead to the formation of zinc oxide nanoparticles (ZnONPs) [34]. However, in the case of recombinant hLTF, this effect was not observed regardless of the used initial Zn^{2+} concentration. The EDX analysis allowed for the determination of changes in the zinc content in the samples. Zinc was not detected in the native protein, whereas it was detected in the remaining samples. Therefore, it can be assumed that in this case, homogeneous metal-protein complexes are formed as a result of Zn^{2+} interaction with recombinant hLTF.

3.3.4. Inductively coupled plasma mass spectrometry

The exact content of zinc in the obtained complexes was determined by the ICP-MS technique. Table 3 summarizes the amount of zinc and iron in each tested sample. As expected, the zinc content in the complex increases when higher initial concentrations of this element were used. At the highest concentration of Zn^{2+}, the content of this metal was almost 8 mg per gram of LTF. Obtained values are lower than those from the kinetic data. After hLTF-Zn complex washing, the remaining Zn^{2+} accounted for about 16, 14, and 10% of the initially bound ions when the Zn^{2+} solutions of 60, 300, and 600 mg/L were utilized for the synthesis. This effect is due to the complexes' purification procedure carried out after immobilization by washing it three times with deionized water. Thus, only the most strongly bonded Zn^{2+} remains in the complex. It can be assumed that during the washing process, the weak hydrogen bonds between Zn^{2+} and amino acid residues were broken [52,53]. Previous studies on Zn^{2+} binding to bLTF revealed that the pH of the solution also affects the process [14]. Higher absorption capacity against Zn^{2+} was observed at pH 8.6 in comparison with pH 7.4. Instead, at the pH equal to 6.0 no Zn^{2+} binding occurs which should be connected both with the availability of deproto-

Table 3

The content of zinc and iron per gram of native human lactoferrin or its zinc complexes.

	hLTF	hLTF + Zn30	hLTF + Zn150	hLTF + Zn300
Zn [mg/g]	0.429 ± 0.153	0.570 ± 0.100	5.106 ± 0.594	7.919 ± 0.074
Fe [mg/g]	1.075 ± 0.056	0.905 ± 0.070	0.945 ± 0.097	0.901 ± 0.004

nated functional groups as well as with the net charge of the protein. Instead, the presence of other chelating agents, such as citrate, decreases the sorption ability of bLTF.

It is noteworthy to mention, that Zn^{2+} sorption by recombinant hLTF does not affect significantly the iron content in protein. Only a slight decrease in the content (12–17%) of this element can be observed after interaction with Zn^{2+}. This suggests a different primary binding site for both of these elements in the lactoferrin molecule in applied experimental conditions. Due to the high affinity of Zn^{2+} to protein functional groups, it can replace other metal ions which show lower affinity [54]. Still, a previous study has shown that in the case of bovine lactoferrin (bLTF), the increase in the Zn^{2+} and citrate ion in the solution led to iron elimination from protein structure up to 30% [14]. Instead, the study of Jabeen et al. has shown that in the case when the apo-C-lobe of bLTF was mixed with Zn^{2+} it took place in the metal-binding cleft. Moreover, two more Zn^{2+} were additionally bound on the protein surface [55].

3.3.5. Fourier transform infrared spectroscopy

Fig. 8**A** presents the Fourier transform infrared (FT-IR) transmission spectra and Fig. 8**B** presents the attenuated total reflectance Fourier transform infrared (ATR FT-IR) spectra for recombinant hLTF before and after modification with Zn^{2+}.

Both techniques reveal the significant changes in the sample as a result of Zn^{2+} binding and the number of these changes increases with the increase of applied initial Zn^{2+} concentration. Changes are practically invisible on the spectrum obtained for the sample after the application of 30 mg/L zinc. It is related to the slight difference in the zinc content in the complex compared to the native protein, which was confirmed by ICP-MS (Table 3). However, already after the application of the initial Zn^{2+} concentration of 150 mg/L, significant changes in the spectrum were observed, and the use of the initial concentration of 300 mg/L led to even more visible changes. On the spectra obtained by both FTIR and ATR-FTIR techniques, it was observed changes in the range of 1470 to 1570 and 1250 to 1350 cm^{-1} correspond to amide II and III [14,56]. Thus, it indicates the structural changes in the protein due to the binding of Zn^{2+}. Additionally, both techniques enabled us to observe the gradual disappearance of the signal at 1449 and 1048 cm^{-1} which probably are related to the stretching and bending vibrations of the phenyl ring in phenylalanine [57]. This change may imply weak noncovalent cation–π interactions between the phenyl ring and metal ions [58,59]. The energy of such interactions is usually in the range of -8.4 to -16.7 kJ/mol [58]. The changes of $\Delta G°$ calculated based on kinetic data are within this range. Thus, this type of interaction may participate in Zn^{2+} binding by recombinant hLTF. Additionally, both techniques enabled to detection of signal loss at 1246 and 1110 cm^{-1} after zinc binding. Those signals can be attributed to the vibrations of tryptophan (δCH, νCC) as well as histidine (νCN, δCH) or glutamic acid(νCN,δOH) [57]. However, the use of FTIR in the ATR mode allowed for a more precise analysis of changes occurring in the protein. For example, changes in the range of 2960–2875 cm^{-1} can be observed after applying only ATR mode. The vibrations in this range probably come from the asymmetric and symmetric stretching vibrations of the C–H group [60]. In addition, only using ATR FT-IR was possible to detect the appearance of signals at 1069, 970, 910, 890, and 845 cm^{-1} coming

probably from functional groups of tryptophan (νCN,δCH, νCC), aspartic acid (νCN,νCC), threonine (δCO^2H), glutamic acid (νCO,νCC), and alanine (νCN,νCC), respectively [57,61,62] (Fig. 8**B**). Considering the pH of the immobilization process which was established as 7.4 it can be determined that the dominant deprotonated functional groups in applied conditions were carboxyl groups (pKa = 2 – 6) [63]. Therefore, changes in the spectrum from aspartic and glutamic acid may confirm a significant share of the deprotonated carboxyl groups of these amino acids in the binding of Zn^{2+}. The classical FT-IR technique revealed two other changes related to the fading of signals at 1170 and 1078 cm^{-1} related to the wagging vibrations of the CH_2 group in lactoferrin molecule and the stretching vibration of the CH group in aspartic acid [57,61,62] (Fig. 8**A**).

Bioinformatic research carried out for the genome of human have shown that about 10% of all encoded proteins participate in Zn^{2+} binding [54,64]. The N-, O-, and S-donors of the side chains of different amino acids participate in Zn^{2+} binding by proteins [54]. It was shown that in psoriasin the zinc is coordinated by one aspartic acid and three histidine residues [65]. Histidine groups are also involved in the coordination of Zn^{2+}in the "zinc fingers" (ZF) [64,66]. In the case of ZF, except for histidine, cysteine groups are also involved in zinc binding [54,64]. However, it was noted that sometimes other amino acids such as glutamic or aspartic acids may participate in creating binding sites in the ZF [54,64]. Nevertheless, the bonding stability depends on many factors e.g. hydrophobic and electrostatic interactions as well as hydrogen bonds [64]. As the changes at the FT-IR spectra of hLTF-Zn complexes indicated the participation of those amino acids in zinc binding it can be postulated that also in lactoferrin similar binding sites may be present. It was also demonstrated that –OH and –CN groups as Lewis bases can participate in the coordination of Zn^{2+} [67]. The changes in the FT-IR bands' position related to these groups were also observed in the current study. Therefore, it can be assumed that those groups may create the zinc-binding site in human lactoferrin.

3.3.6. Raman spectroscopy

Fig. 9 presents the registered RAMAN spectra for protein before and after Zn^{2+} binding. As in the case of the FT-IR technique, the process of Zn^{2+} sorption led to changes in the spectra, and these changes were the most intense after using the highest of the tested initial Zn^{2+} concentrations. The decrease in the intensity of bands at 1547 and 751 cm^{-1} after protein immobilization with Zn^{2+} is related probably to the vibrations of the indole ring of tryptophan [68]. In addition, the increase in the intensity of the signal at 1413 cm^{-1} may be attributed to the νCO group of glutamic or aspartic acid residues. The participation of functional groups of these amino acids in Zn^{2+} binding was also confirmed by FT-IR techniques. Moreover, the changes in the bands at 1197 and the range of 870–815 cm^{-1} revealed the possible participation of tyrosine residues in Zn^{2+} binding which was not detected using only the FT-IR approach [14]. In turn, the signal at 1443 cm^{-1} is probably derived from $\delta_{as}CH_3$ vibrations [61]. Moreover, interesting changes were observed in the range of 415–410 cm^{-1}, not detected previously by the FT-IR method. These changes may be attributed to the Fe–NO or Fe–O complexes present in iron-binding proteins [69]. As demonstrated by ICP-MS studies, the sorption of zinc ions only slightly reduced the iron content in the sample, which suggests
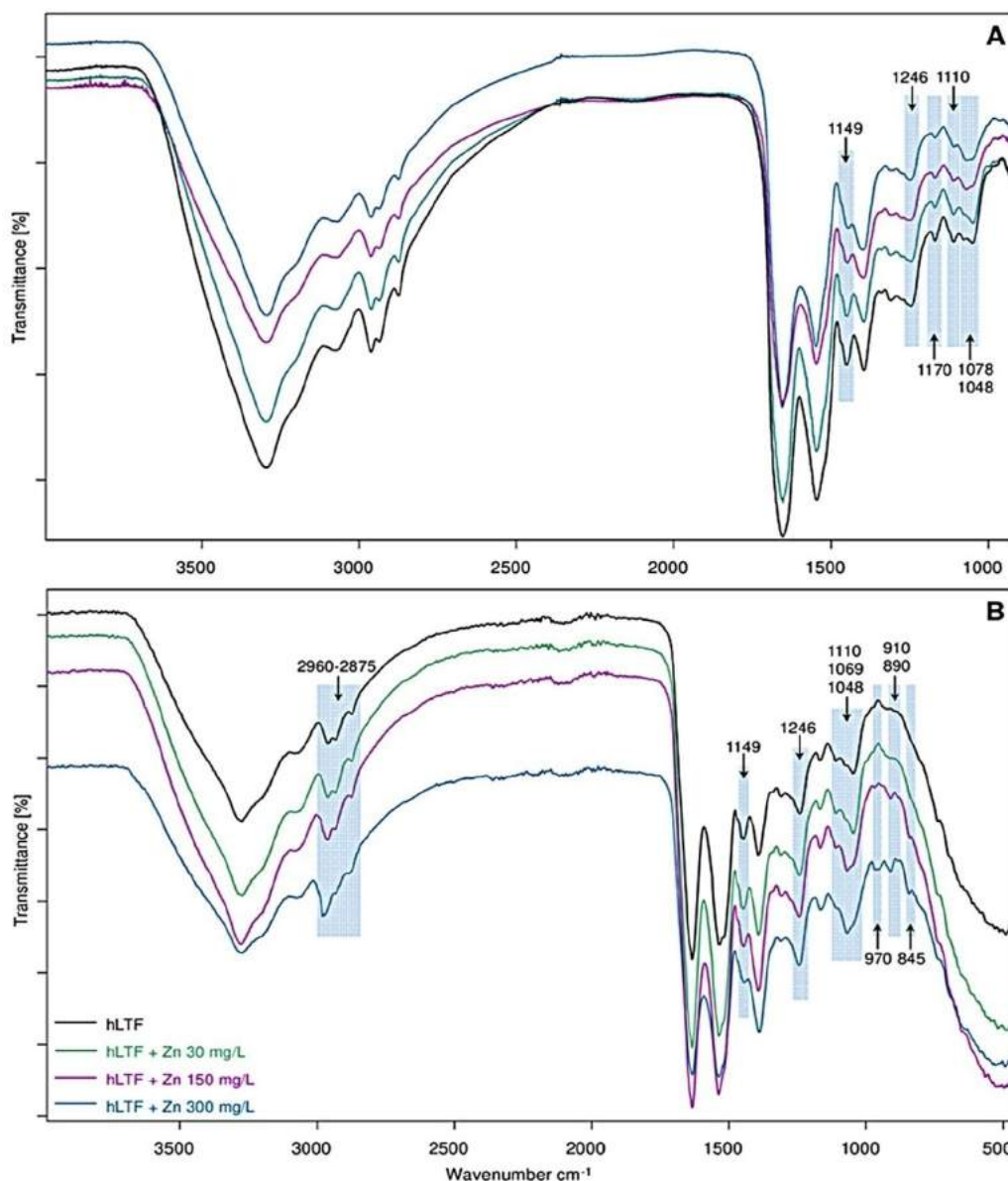
Fig. 8. A. Fourier transform infrared (FT-IR) spectra and B. attenuated total reflectance Fourier transform infrared (ATR FT-IR) spectra of recombinant hLTF and hLTF-Zn complexes obtained after application of initial Zn^{2+} concentration of 30, 150, and 300 mg/L.

that there are other major zinc-binding sites in recombinant hLTF. Since the changes in the RAMAN spectra for the iron-binding complexes are also insignificant, it can be confirmed that the zinc immobilization process has a low influence on the iron-binding ability of the protein.

3.4. Interaction between the 1LFG protein and zinc aqua complex by computational modeling

3.4.1. Molecular dynamics calculations

MD simulations aimed at the evaluation of the structural stability of hLTF and the elimination of Fe^{3+} upon the increase in the concentration of Zn^{2+}. Moreover, it was possible to outline the parameters of ZAC interaction with proteins' amino acids, including the changes in the structure of the ZAC coordination sphere. At low concentrations, for one Zn^{2+}, after 30 ns, we observed ZAC with six coordinated water molecules (H_2O) (ZAC6). ZAC6 did not interact with protein side chains and resided outside the protein. The data is consistent with the results obtained

from the isotherm study, where the adsorption for the lowest utilized Zn^{2+} concentrations was negligible and accounts for less than 0.15 mg/g.

In the case of 5 Zn^{2+} already three ZAC interacted with protein through glutamic acids (Glu523 and Glu80) as well as aspartic acid (Asp541). The corresponding ZAC comprised five, three, and four H_2O, respectively. At the same time, two ZAC with five and six coordinated H_2O resided outside the protein. More details on obtained interaction parameters can be found in Table S1. For 10 Zn^{2+} the ZAC interacting with protein had a maximum of four coordinated H_2O and were bonded to protein through Asp 205 and 541. Four out of 38 aspartic acids (Asp 55, 205, 424, and 541) take part in the ZAC chelating. Mostly, the interaction appears with the outermost aspartic acids of the protein. The lower number of H_2O in the coordination sphere was related to the formation of polydentate binding with the ZAC that resides inside the protein. Other amino acids that were interacting with ZAC are as follows: Tyr319, Glu80, and His253. The non-interacting ZAC had one, two, three, and five H_2O in their coordination sphere.
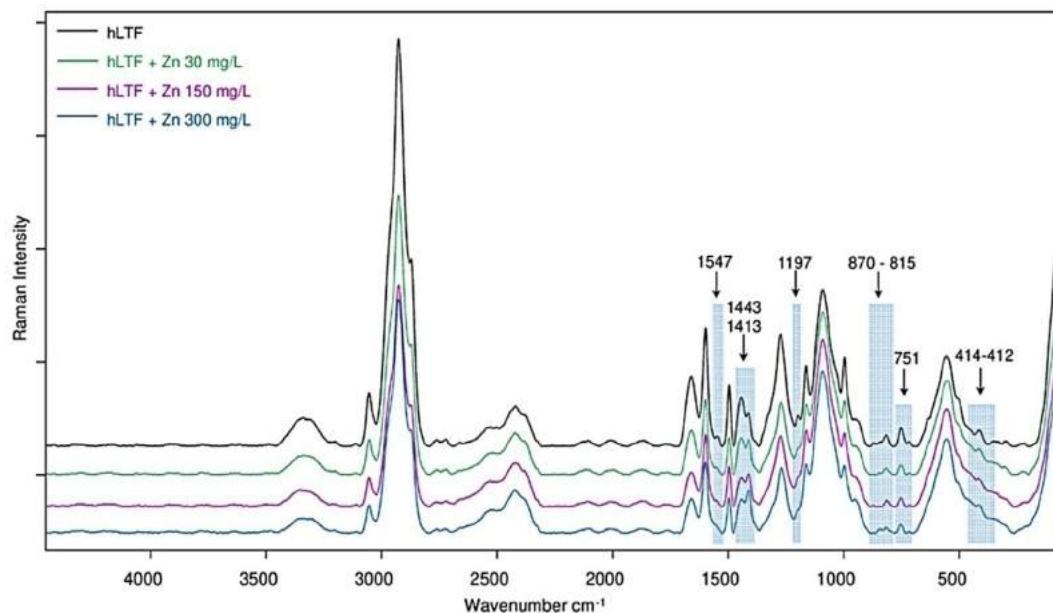
Fig. 9. RAMAN spectra of recombinant hLTF and hLTF-Zn complexes obtained after application of initial Zn^{2+} concentration of 30, 150, and 300 mg/L.
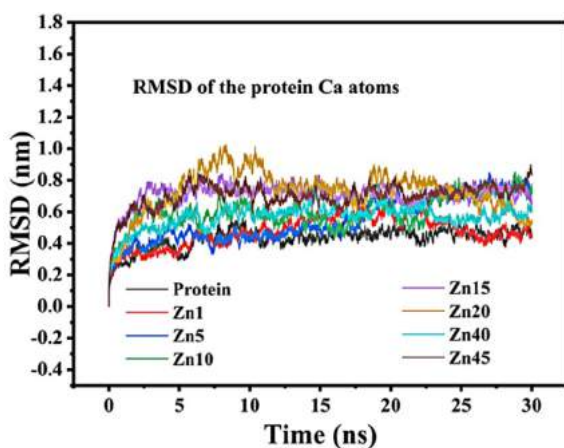

Fig. 10. RSMD of the $C\alpha$ of 1LFG at different concentrations of Zn^{2+}.

When 15 and 20 Zn^{2+} were added to the box, the structure of a protein was found to be affected due to the presence of the ZAC6 within the protein. We also can confirm it with the RMSD plot (see Fig. 10). At these Zn^{2+} concentrations, all ZAC of the system comprised from two to six coordinated H_2O, but interacting ones had a maximum of five. Zinc interaction with protein appeared through multiple amino acids, such as aspartic acid (Asp), glutamic acid (Glu), histidine (His), tyrosine (Tyr), threonine (Thr), asparagine (Asn), and serine (Ser). On average, the calculated distances between the ZAC and amino acids were 2.11 Å. Moreover, the drifting of Fe^{3+} has been observed, leading to the opening of the protein. Released from protein Fe^{3+} formed the ferric hexaaqua complex $[Fe(H_2O)_6]^{3+}$. More polydentate complexes were observed in the case of 20 Zn^{2+} leading to the slight bending between the C and N lobe, whereas the C lobe gets expanded due to the presence of ZAC6 within it. The results of FTIR analysis also indicated the changes in the protein structure upon zinc chelation. Furthermore, from FTIR and Raman analyses, it was predicted that all the above-mentioned amino acids could take part in the Zn^{2+} chelation. Finally, the ICP-MS and CE-ICP-MS investigations showed that

recombinant hLTF interaction with Zn^{2+} leads to the weakening of the iron-protein bond and thus partial Fe^{3+} elimination from protein. All the same was also observed for bLTF in our previous work [14].

Interestingly, with the increase of Zn^{2+} in the system, the interaction of ZAC with several amino acids simultaneously occurred. For 10 Zn^{2+} the interaction with two amino acids was observed, while for 15 and 20 Zn^{2+} it was noticed that ZAC can interact even through three amino acids Asn644, His597, and Glu413. Again, in our previous work, we predicted that the high amount of zinc in the solution can induce changes in the protein structure which should enable the formation of a polydentate complex [14]. Moreover, we have suggested that high metal concentration should squeeze the double electric layer, promoting Zn^{2+} chelation with several amino acid residues. The assumption was also supported by the MD simulations performed for 40 Zn^{2+} where the minimum distance between the hydrogen of ZAC and Asp-(Asp541)/Glu-(Glu80) was observed and accounted for about 1.73 and 1.71 Å, respectively, which also indicates the strong interaction. In **Figure S1.** can be seen some snapshots of interaction between ZAC and hLTF. Still, for 45 Zn^{2+} the distance of nearby hydrogen of ZAC is found to be increased and for Asp541/Glu80 accounted about 2.7 Å and 3.64 Å respectively. The effect may be connected with the increase of repulsion forces between ZAC.

It is noteworthy to mention, that it was not observed the replacement of Fe^{3+} by Zn^{2+} in protein metal-binding clefts, but zinc bonded to other binding sites. A previous DFT study on human serum transferrin showed that the binding energy of Zn^{2+} in the Fe-binding sites is found to be lower compared to the Fe^{3+}. Thus, the replacement of Fe^{3+} by zinc in hLTF at low metal concentrations also seems complicated [70]. The same was deduced from experimentally obtained results. Moreover, a previous study of our group performed for bLTF also confirm the observed findings. In the case when in the synthesis of Zn-bLTF complex low metal concentration was utilized (i.e., zinc concentration in solution was 3 mg/L), the amount of bonded Zn^{2+} was almost fifteen and eight times lower at pH 7.4 and 8.6, respectively, in comparison to the eliminated Fe^{3+} [14].

The analysis of structural deviation in protein with the root means square deviations (RMSD) of the position of the $C\alpha$ atoms

Table 4

Calculated binding energy, the distance between the functional groups of Amino acids and Hydrogen of ZAC6, and interactional Gibbs free energy.

Amino acids	ZAC6 interacting with AA			Zn^{2+} interaction with AA		
	ΔE_b (kJ/mol)	Distance between AA and Hydrogen of ZAC6 H_{dis} (Å)	Change in interactional Gibbs free energy ΔG (kJ/mol)	ΔE_b (kJ/mol)	Zn_{dis} (Å)	Change in interactional Gibbs free energy ΔG (kJ/mol)
Aspartic acid (bare)	−132.08	1.42	−124.63	−98.70	1.95	−88.83
Aspartic acid (in peptide bond)	−90.29	1.52	−183.10	−95.90	1.96	−89.93
Glutamic acid (bare)	−168.87	1.42	−159.88	−105.65	1.97	−88.00
Glutamic acid (in peptide bond)	−137.48	1.42	−125.66	−98.78	1.97	−92.56
Alanine	−1.55	2.59	6.81	17.95	2.48	24.12
Histidine	−77.91	1.82	−70.68	8.58	2.60	6.75
Threonine	−68.37	1.73	−64.89	−71.46	2.07	−62.43
Tyrosine	−78.49	1.82	−65.62	38.28	2.18	43.39
Glutamine	−53.51	1.77	−40.00	−0.27	2.64	3.79
Phenylalanine	−55.60	1.84	−45.23	−1.13	2.58	1.60
Tryptophan	−141.62	1.72	−127.14	−3.45	2.51	0.82
Serine	−56.52	1.74	−46.90	7.37	2.22	35.97

revealed that no significant changes occurred in the system containing 1 and 5 Zn^{2+} compared to pristine protein. The RMSD plot also confirmed the opening of protein structure due to the presence of ZAC6 at 20 Zn^{2+} for about 5 to 10 ns. Thermal stabilization was achieved after 20 ns for all the cases (Fig. 10). Moreover, it was reported early that with the absence of Fe^{3+}, the RMSD increases [71]. Thus, the observed in our study increased RSMD before thermal stabilization can be related to the drifting of Fe^{+3} ions from the protein structure. Even higher deviations were observed in the case of 45 Zn^{2+}. Whereas, in the presence of 40 Zn^{2+} lesser deviations were detected, confirming that the protein structure is highly altered after a specific concentration. Thus, we have not analyzed the concentrations beyond 45 Zn^{2+}.

3.4.2. Density functional theory calculations

Initially, we examined the amino acid conformation at pH=7.4 and called them bare amino acids. The formation of the peptide bond by amino acids affects the interaction with ZAC6. According to our MD calculations, we observed that protein interacts through Asp, Glu, Tyr, Gln, His, Ser, and Thr. Thus, we have calculated the binding energy and interactional Gibbs free energy change for ZAC6 interaction with these amino acids. Moreover, we have calculated the binding energies for alanine (Ala), phenylalanine (Phe), and tryptophan (Trp) which did not show any interactions within MD simulations. Finally, MD calculations showed that ZAC interacts predominantly through OE2/OD1 of Glu/Asp-and -OH groups of Tyr, Thr, and Ser. Therefore, to evaluate the influence of amino acid incorporation into a peptide, we have examined the peptides containing acidic (Glu, Asp) with the basic (Lys, Arg)/(Gln, Asn) amino acids as reported in previous studies [34,72]. The results presenting the minimum energy configurations are listed in Table 4.

The highest calculated binding energy and the change in the Gibbs free energy were observed for Asp/Glu. The respective values were found to be −132.08 kJ/mol and −168.87 kJ/mol, respectively. Moreover, it was noticed the lowest distance between these residues COO− and H of ZAC6 which accounts for 1.42 Å and 1.48 Å, respectively. In general, according to the calculated binding energies the zinc interaction strength with amino acids decreases in the row Glu>Asp> His>Thr> Tyr>Phe> Ala.

In the case of Ala, it was a considerably high affinity of ZAC6 toward the amino group where binding energy accounted for −41.34 kJ/mol. However, there is no free amino side of Ala-available in protein as it takes part in peptide bonds with other amino acids such as aspartic acid. While, the binding energy of

the ZAC6 to CH_3 group of Ala-accounted for only −1.55 kJ/mol, and the calculated change in Gibbs free energy was positive, confirming that no interaction can occur. In the case of Phe-and Tyr, ZAC6 resides near the phenyl ring, which confirms the weak noncovalent cation-π interactions. The findings validate our prediction from IR and Raman spectra obtained experimentally. Still, we observed a higher value of change in Gibbs free energy compared to experimental results. These overestimations of the Gibbs free energy may come from the negligence of peptide bonds and nearby amino acids. The respective analysis of Asp/Glu-containing peptides indicates that the binding energy is highly affected with consideration of the peptide bond. It also can be observed the differences in the values of change in free Gibbs energy obtained for Asp/Glu-acids that take part in peptide bonds compared to the bare Asp/Glu.

Finally, we have calculated the Gibbs free energy of the reaction (ΔG_r) for proton transfer from ZAC6 to Asp-(Dp)/Glu-(Ep) with the formation of AspH(Dp)/GluH(Ep) which was about −31.57/−32.86 kJ/mol. The total energy of the product is lower than the reactant, and the negative value of ΔG_r confirms the spontaneous character of reactions. In the work of B. Buszewski et al., similar results were obtained [34]. The respective water molecule dissociation was considered as the reason for the ZAC hydrolysis with the formation of ZnO nanoparticles after interaction with ovalbumin. Still, ZAC interaction with recombinant hLTF did not lead to the formation of nanoparticles which can be connected with the significant differences in the physicochemical properties of both proteins.

In the previous work of our group [15], the molecular docking of Fe^{3+} binding to bLTF was performed. The analysis enabled an estimation of possible binding sites on the protein surface. However, the performed molecular docking did not consider the H_2O molecules that always accompany metal ions in solutions as part of the coordination sphere. Thus, to evaluate the difference in binding capabilities, we have analyzed the interaction of amino acids with bare Zn^{2+} compared to ZAC6. We found that bare Zn^{2+} shows a lower affinity toward amino acids [33] than ZAC6. The change in Gibbs free energy obtained for Zn^{2+}interaction was positive for almost all analyzed amino acids except for Asp, Glu, and Thr. Instead, the positive value of change in Gibbs free energy for ZAC6 was observed only for one analyzed amino acid, Ala. It may be connected with alanine being an amino acid with no electron donor functional group in its side chain. The drastic difference observed in our calculations indicated the importance of the utilization of proper specie for all theoretical approaches. In general, the previ-
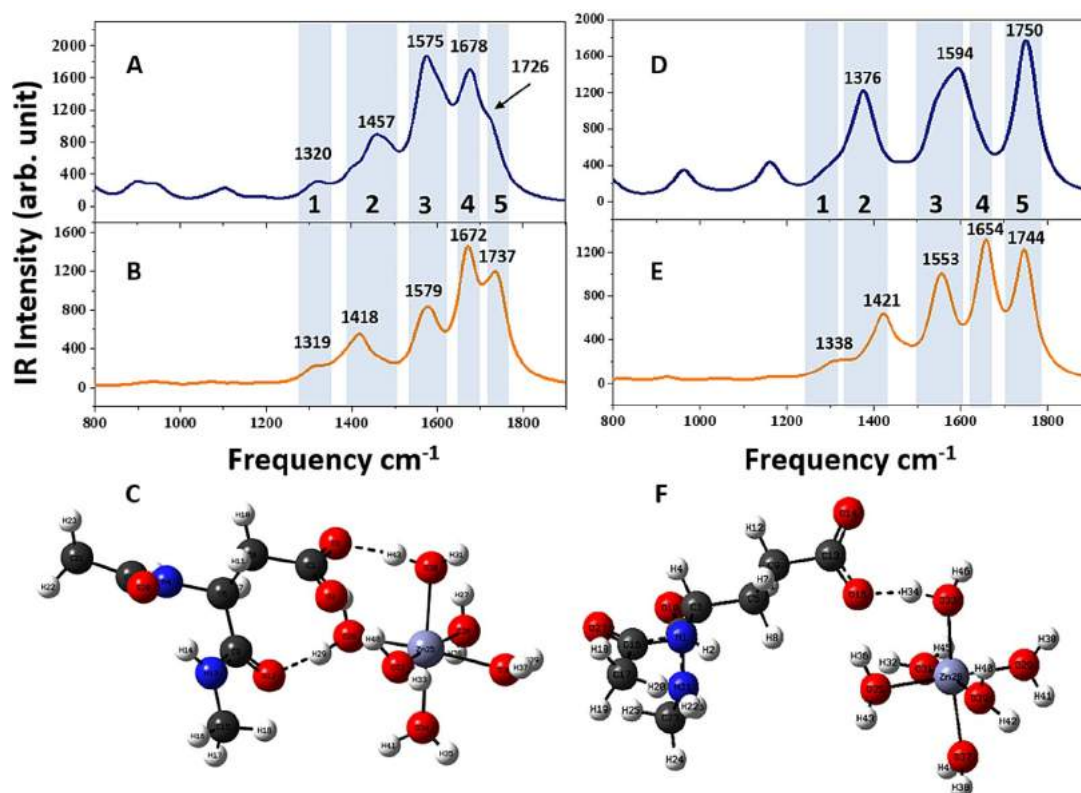
Fig. 11. The calculated IR spectra for dipeptide of A. Asp-interacting with ZAC6; B. bare Asp; D. Glu-interacting with ZAC6; E. bare Glu-where bands: 1 comes from COO$^-$; 2 δ_{as}(CH$_3$); 3 Amide II; 4 Amide I; 5 C = O str. vibration of COOH group. 3D ball-and-stick models are presented on: C. Asp-interacting with ZAC6; F. Glu-interacting with ZAC6.

ous works note that the utilization of bare Zn^{2+} is suitable for predicting the reactions in a gaseous phase. While utilization of ZAC in MD and DFT calculations more precisely describes the processes that may take in solutions [73].

3.4.3. Results for calculated IR and Raman spectra

To support our experimental results, we have calculated IR spectra for bare amino acids (in dipeptide) and corresponding amino acids bonded with ZAC6 Fig. 11. In the case of the Glu-(Ep), we have analyzed IR shifts of the amide II (1553 cm^{-1}), amide I (1654 cm^{-1}), δ_{as}(CH$_3$) (1421 cm^{-1}), and COO$^-$(1338 cm^{-1}) bands which are well-matched with the experimental and previous reports [14]. The possible overestimations in the calculations are due to the choice of the basis set (6–311++(d,p)). After Glu-(Ep) interaction with ZAC6, we observed the blue shift in the modes of amide bands. We observed the shift of the Amide II band from 1553 cm^{-1} to 1594 cm^{-1}, as shown in Fig.. 11**C,D**. Similarly, the corresponding changes also occurred in the vibrational modes of Asp-(Dp) after interacting with ZAC6, which is visible in the range 1400–1600 cm^{-1} (Fig. 11**A.B**). These shifts in IR modes can be directly attributed to the metal-protein interactions [74]. The results are consistent with the ATR-FTIR analysis findings, which indicated the changes in the amide II and amide III bands.

Previously it is reported that the presence/appearance of the band at ~1725 cm^{-1} comes from C = O stretching vibrations of the COOH group. By the changes in these vibrations, the protonated state of the carboxyl group can be tracked [75]. In our study of both amino acids (Asp/Glu), we observed the changes in intensity and shift of the corresponding bands. In the case of Glu-amino acid, the band at 1744 cm^{-1} has shifted to 1750 cm^{-1} after interaction with ZAC6. Moreover, the increase in the corresponding band's intensity confirmed the carboxyl groups' higher protonation state. Whereas, in the case of Asp-decrease in the band intensity can

be explained by not strong enough interaction with hydrogen to form protonated COOH. The estimated distance was 1.52 Å which is greater as compared to the Glu. Finally, the protonation of the carboxyl group in Glu-was also confirmed by the disappearance of COO$^-$ stretching band at 1338 cm^{-1}. Instead, in Asp-it remained intact. Still, it can be observed the band shift indicating the interaction between the hydrogen of H$_2$O of ZAC and COO- of Asp-(Dp) (see Fig. 11). The observed changes are in excellent agreement with our experimental results.

Furthermore, we analyzed the IR spectra of other free amino acids such as Ala, His, Thr, Gln, Phe, and Trp. DFT calculations indicated that ZAC6 has comparatively high affinity towards the NH$_3$ group but not to the CH$_3$ groups. However, as NH$_3$ groups of alanine participate in the peptide bond formation, the changes in vibrational bands that come from Ala-should not be due to direct participation in the ZAC6 binding. The respective changes should come from ZAC6 interaction with the neighboring Ala-amino acids. For instance, it can come from ZAC6 interaction with Asp55/Glu80, which forms peptide bonds with Ala-on both amino- and carboxy-sides. Fig. 12**.** shows the calculated IR spectra for the bare and interacting amino acids.

As can be seen, the prominent band at 893 cm^{-1} disappeared when ZAC6 is near NH$_3$, which may be explained by its strong interaction (1.52 Å) compared to CH$_3$ (2.59 Å). To confirm our presumption, we calculated the IR spectra of tripeptide comprised of Glu-with Ala-and Val-from MD simulation and observed an IR peak at 842.95 cm^{-1} corresponding to the vibrations of Ala (nCC, nCN). Instead, the nature of the IR spectrum of Glu80 is like for Glu-in peptide, a slight shift is observed due to the presence of peptide bonds with Ala-and Val (see Fig. 13). The corresponding band is present on the spectrum obtained within ATR-FTIR analysis which confirms that Ala-does not interact with ZAC6.
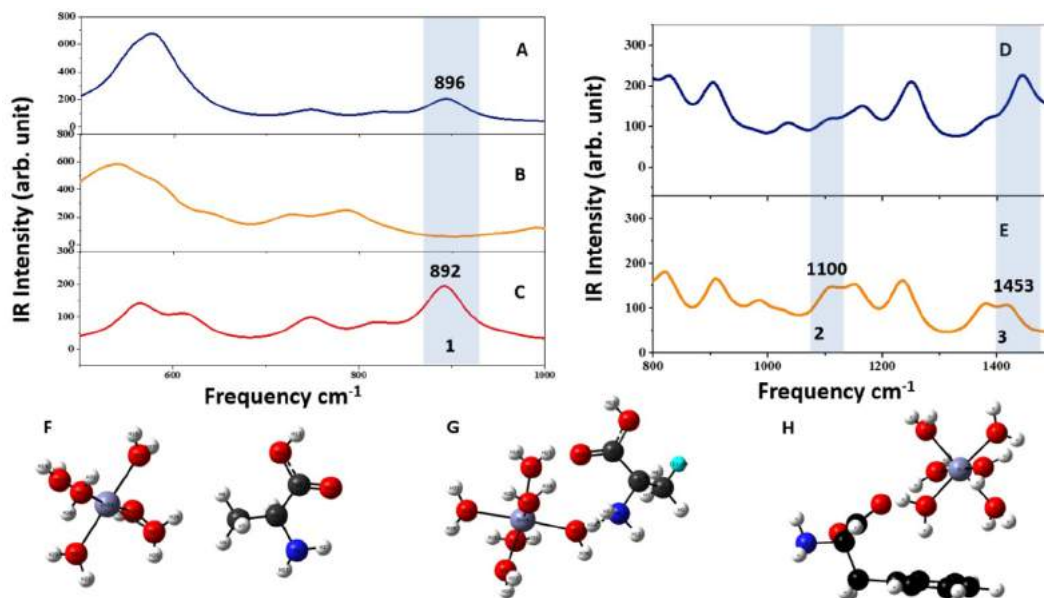
Fig. 12. The calculated IR spectra for free amino acids of A. ZAC6 with Ala-towards CH_3 and B. NH_3 groups; C. bare Ala; D. bare Phe; E. ZAC6 interacting with Phe, where bands: 1 comes from C = O str. of COOH group, 2, and 3 comes from the aromatic ring of phenylalanine. 3D ball-and-stick models are presented on: F. ZAC6 with Ala-towards CH_3; G. ZAC6 with Ala-towards NH_3; H. ZAC6 interacting with Phe.
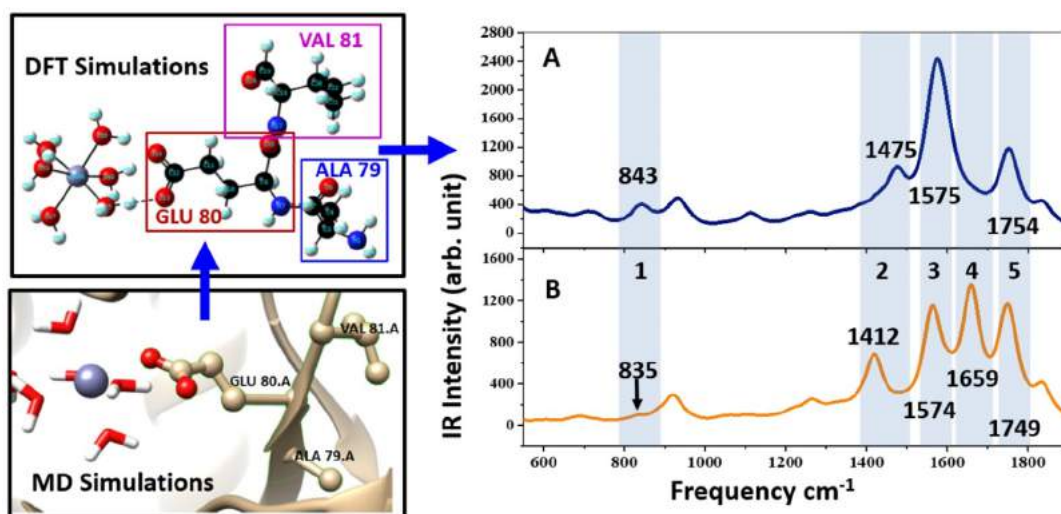

Fig. 13. Represents the results of MD and DFT simulations for tripeptide Ala79-Glu80-Val881 (left) as well as calculated IR spectra for respective tripeptide A. after and B. before interaction with ZAC6 (right), where bands: 1 comes from Alanine (νCN, νCC); 2 $\delta_{as}(CH_3)$; 3 Amide II; 4 Amide I; 5 C = O str. of COOH group.

We have also investigated the direct interaction of ZAC6 with free Phe. It was shown that the ZAC6 prefers to bind near the phenyl ring. Therefore, we have analyzed the bending and stretching vibrations of phenylalanine's phenyl ring, which is about 1453 and 1100 cm^{-1}. We found that after interaction with ZAC6, its band shifts to higher bending frequencies, whereas the intensity of bending vibration decreases. The ZAC6 is expected to interact with the C = O of bare phenylalanine as the distance is 1.69 Å from ZAC. However, in LTF, this group contributes to peptide bond formation. In the case of interaction with the phenyl ring, the calculated distance is about 2.26 Å, which may indicate a very weak interaction. Therefore, we observe the decreased intensity but not the disappearance of a peak as observed in the results obtained experimentally. Still, it is noteworthy to mention that the change in Gibbs free energy and binding energy confirms the weak noncovalent cation–π interactions. In the case of Tyr, we observed the same situation as with Ala. However, the distance between C = O

and ZAC6 (2.06 Å) is higher than for Ala. While the distance between the OH and ZAC6 is 1.82 Å, and with the phenyl ring, it is about 3.37 Å. It can be concluded that ZAC shows affinity towards the OH group and may exhibit weak noncovalent cation–π interactions with the phenyl ring.

Previously, three IR signals of Tyr-were reported for hLTF that is 1516 cm^{-1}, 1236 cm^{-1}, and 1166 cm^{-1} [74], and with DFT calculations, we observed these peaks at 1558 cm^{-1}, 1199 cm^{-1}, and 1125 cm^{-1} respectively, which is in good agreement. The difference may be due to the basic set choice and ignorance of the peptide bond with other amino acids. After the interaction with the ZAC6, we observed the disappearance of the band at 1125 cm^{-1} and a shift in the other two bands which are 1199 cm^{-1} to 1204 cm^{-1} and 1558 to 1601 cm^{-1}, which confirms the interaction. We analyzed the change in respective vibration modes of νCN, and δCH within our calculations and it was found to be at 1099 cm^{-1} and 1243 cm^{-1}, respectively. These peaks disappear with the interac-
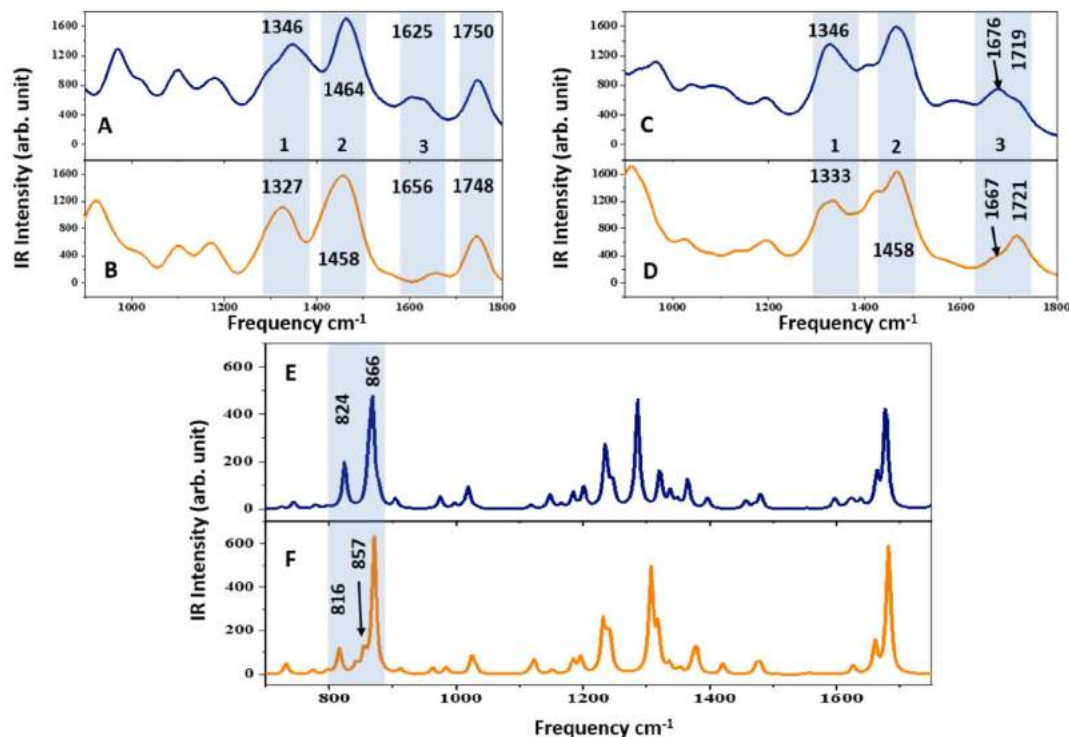
Fig. 14. The calculated Raman spectra of A Glu-interacting with ZAC; B pristine Glu; C Asp-interacting with ZAC; D pristine Asp; E Tyr-interacting with ZAC; F pristine Tyr.

tion with ZAC6, which is in good agreement with our experimental observations. From our theoretical findings, we have observed the band at 911 cm^{-1} which has shifted after interaction with ZAC6 to 919 cm^{-1}. The respective band within ATR-FTIR analysis was observed at 910 cm^{-1}. We can have a depth scenario while considering the peptide bond of amino acids to have a reasonable change in Gibbs free energy compared to the experimental. However, it is computationally costly to take a large protein sequence for DFT calculations to achieve an accurate Gibbs free energy change while interacting with ZAC6. The DFT-based IR analysis confirms the interaction between the amino acids and ZAC6. The protonation of the carboxyl group is confirmed with both IR analysis and with reaction Gibbs energy which is negative, showing that the reaction is spontaneous.

A more precise analysis of the interaction between the amino acids and ZAC6 can be obtained from the Raman spectroscopy for the process of protonation of the carboxyl group of Glu-and Asp (Fig. 14). We observed the change in Amide I (1656 and 1667 cm^{-1}), Amide II (1458), and Amide III (1326 and 1333) bands. The appearance of a peak at 1748 cm^{-1} is previously attributed to the protonation of a carboxyl group (1710 cm^{-1} [76]) in Glu-while interacting with ZAC6. A similar change can be observed for Asp (1721 cm^{-1}). These changes confirm their interaction and protonation of the carboxyl group. The interaction between the Tyr-and ZAC6 can be confirmed by the change in the in-plane C–C stretching and out-of-plane wagging, which is previously reported at 857 cm^{-1} and 826 cm^{-1}, respectively [77]. The observed shift in peaks to 866 cm^{-1} and 824 cm^{-1} confirms the participation of ZAC6. There is a good agreement between the IR and Raman spectra with experimentally observed values and convincingly confirms the strong interaction of ZAC with 1LFG protein.

4. Conclusions

The results obtained in this study shed new light on the nature of Zn^{2+} binding by hLTF. The use of three initial concentrations of

Zn^{2+} (distinctive for each different isotherm step) made it possible to track the gradual changes in the protein upon Zn^{2+} binding. Although the general course of the process, regardless of the concentration used, was similar, the increase in the initial concentrations contributed to the increase in the sorption velocity, efficiency, and protein sorption capacity. It was also revealed that the change in Gibbs free energy increased with the use of higher Zn^{2+} initial concentrations. The determined zinc content in the complexes obtained after the application of initial Zn^{2+} concentrations of 30, 150, and 300 mg/L was about 0.57, 5.11, and 7.92 mg/g, respectively. The applied metal concentration causes partial elimination of iron from protein structure. Additionally, the results from CE-ICP-MS indicated the weakening of the iron-protein bond. The formation of zinc oxide nanoparticles was not observed. The FT-IR and RAMAN study allowed determining the potential functional groups of hLTF amino acids that can participate in Zn^{2+} binding which were carboxyl groups of Glu-and Asp, the imidazole ring of His, and –CN, –OH of other amino acids. Weak noncovalent cation–π interactions also contribute to the Zn^{2+} binding. Finally, we analyzed the interaction between amino acids and ZAC/Zn^{2+} using DFT and MD. The calculations confirmed the possibility of proton transfer from ZAC6 to the carboxyl group of Glu-and Asp-reported before. The results also confirmed the experimental findings regarding ZAC6 interactions with functional groups of amino acids, changes in the protein structure, and Fe^{3+} drifting.

All these allowed us to conclude that mechanisms of zinc binding to hLTF comprise several steps. The proposed mechanism includes the initial interaction of ZAC with the outermost functional groups of the proteins, such as carboxylic groups of Asp/Glu-residues or hydroxy groups of Ser/Thr/Tyr. Such interactions induce changes in the protein structure, which enables the formation of polydentate bonds with the ZAC (formation of new metal-binding sites). Moreover, the migration of ZAC inside the protein molecule occurs. Thus, a higher ZAC amount can be bonded to the protein. The process intensifies with the increase of Zn^{2+} concentration.

Declaration of Competing Interest

The authors declare that they have no known competing financial interests or personal relationships that could have appeared to influence the work reported in this paper.

CRediT authorship contribution statement

Agnieszka Rogowska: Investigation, Data curation, Formal analysis, Validation, Visualization, Writing – original draft. **Oleksandra Pryshchepa:** Conceptualization, Methodology, Visualization, Writing – original draft, Writing – review & editing. **Narayan N. Som:** Methodology, Investigation, Data curation, Formal analysis, Validation, Visualization, Writing – original draft. **Piotr Śpiewak:** Methodology, Investigation, Data curation, Formal analysis, Validation, Visualization, Writing – original draft. **Adrian Gołębiowski:** Methodology, Investigation, Data curation, Validation. **Katarzyna Rafińska:** Methodology, Investigation, Data curation, Validation. **Renata Dobrucka:** Resources. **Krzysztof Kurzydłowski:** Resources. **Bogusław Buszewski:** Resources. **Paweł Pomastowski:** Conceptualization, Project administration, Supervision, Funding acquisition, Writing – review & editing.

Data availability

Data will be made available on request.

Acknowledgments

Supplementary materials

Supplementary material associated with this article can be found, in the online version, at doi:10.1016/j.molstruc.2023.135149.

References

[1] N. Roohani, R. Hurrell, R. Kelishadi, R. Schulin, Zinc and its importance for human health: an integrative review, J. Res. Med. Sci. 18 (2013) 144–157 http://www.ncbi.nlm.nih.gov/pubmed/23914218.

[2] B. Lönnerdal, Dietary Factors Influencing Zinc Absorption, J. Nutr. 130 (2000) 1378S–1383S, doi:10.1093/jn/130.5.1378S.

[3] B.G. Gomez, M.T. Perez-Corona, Y. Madrid, Availability of zinc from infant formula by in vitro methods (solubility and dialyzability) and size-exclusion chromatography coupled to inductively coupled plasma-mass spectrometry, J. Dairy Sci. 99 (2016) 9405–9414, doi:10.3168/jds.2016-11405.

[4] M.L. Ackland, A.A. Michalczyk, Zinc and infant nutrition, Arch. Biochem. Biophys. 611 (2016) 51–57, doi:10.1016/j.abb.2016.06.011.

[5] L.M. Plum, L. Rink, H. Haase, The Essential Toxin: impact of Zinc on Human Health, Int. J. Environ. Res. Public Health 7 (2010) 1342–1365, doi:10.3390/ijerph7041342.

[6] M.B. Reddy, M. Love, The Impact of Food Processing on the Nutritional Quality of Vitamins and Minerals, in: 1999: pp. 99–106. https://doi.org/10.1007/978-1-4615-4853-9_7.

[7] W. Maret, H.H. Sandstead, Zinc requirements and the risks and benefits of zinc supplementation, J. Trace Elem. Med. Biol. 20 (2006) 3–18, doi:10.1016/j.jtemb.2006.01.006.

[8] R. Wegmüller, F. Tay, C. Zeder, M. Brnić, R.F. Hurrell, Zinc absorption by young adults from supplemental zinc citrate is comparable with that from zinc gluconate and higher than from zinc oxide, J. Nutr. 144 (2014) 132–136, doi:10.3945/jn.113.181487.

[9] H.O. Santos, F.J. Teixeira, B.J. Schoenfeld, Dietary vs. pharmacological doses of zinc: a clinical review, Clin. Nutri. 39 (2020) 1345–1353, doi:10.1016/j.clnu.2019.06.024.

[10] N. Tang, L.H. Skibsted, Zinc bioavailability from whey. Enthalpy-entropy compensation in protein binding, Food Res. Int. 89 (2016) 749–755, doi:10.1016/j.foodres.2016.10.002.

[11] B.G. Shilpashree, S. Arora, S. Kapila, V. Sharma, Whey protein-iron or zinc complexation decreases pro-oxidant activity of iron and increases iron and zinc bioavailability, LWT 126 (2020) 109287, doi:10.1016/j.lwt.2020.109287.

[12] N.L. Jensen, L. Utah, Enzymatically prepared metal proteinates, United States Patent US3969540A, 1975.

[13] P.G. Dalev, Utilization of waste whey as a protein source for production of iron proteinate: an antianaemic preparation, Bioresour. Technol. 48 (1994) 75–77, doi:10.1016/0960-8524(94)90140-6.

[14] O. Pryshchepa, G. Sagandykova, J. Rudnicka, P. Pomastowski, M. Sprynskyy, B. Buszewski, Synthesis and physicochemical characterization of zinc-lactoferrin complexes, J. Dairy Sci. 105 (2022) 1940–1958, doi:10.3168/jds.2021-20538.

[15] O. Pryshchepa, K. Rafińska, A. Gołębiowski, M. Sugajski, G. Sagandykova, P. Madajski, B. Buszewski, P. Pomastowski, Synthesis and physicochemical characterization of bovine lactoferrin supersaturated complex with iron (III) ions, Sci. Rep. 12 (2022) 12695, doi:10.1038/s41598-022-15814-2.

[16] Y. Takayama, Lactoferrin Structure Function and Genetics, in, in: Lactoferrin and Its Role in Wound Healing, Springer Netherlands, Dordrecht, 2012, pp. 43–66, doi:10.1007/978-94-007-2467-9_3.

[17] M. Czosnykowska-Łukacka, M. Orczyk-Pawiłowicz, B. Broers, B. Królak-Olejnik, Lactoferrin in human milk of prolonged lactation, Nutrients 11 (2019) 2350, doi:10.3390/nu11102350.

[18] S. Fernández-Menéndez, M.L. Fernández-Sánchez, H. González-Iglesias, B. Fernández-Colomer, J. López-Sastre, A. Sanz-Medel, Iron bioavailability from supplemented formula milk: effect of lactoferrin addition, Eur. J. Nutr. 56 (2017) 2611–2620, doi:10.1007/s00394-016-1325-7.

[19] P. Blakeborough, D.N. Salter, M.I. Gurr, Zinc binding in cow's milk and human milk, Biochem. J. 209 (1983) 505–512, doi:10.1042/bj2090505.

[20] Y.A. Suzuki, S.L. Kelleher, D. Yalda, L. Wu, J. Huang, N. Huang, B. Lönnerdal, Expression, characterization, and biologic activity of recombinant human lactoferrin in rice, J. Pediatr. Gastroenterol. Nutr. 36 (2003) 190–199, doi:10.1097/00005176-200302000-00007.

[21] N. Huang, D. Bethell, C. Card, J. Cornish, T. Marchbank, D. Wyatt, K. Mabery, R. Playford, Bioactive recombinant human lactoferrin, derived from rice, stimulates mammalian cell growth, In Vitro Cell. Dev. Biol. Anim. 44 (2008) 464–471, doi:10.1007/s11626-008-9136-7.

[22] O. Pryshchepa, G.N. Sagandykova, P. Pomastowski, V. Railean-Plugaru, A. Król, A. Rogowska, A. Rodzik, M. Sprynskyy, B. Buszewski, A New Approach for Spontaneous Silver Ions Immobilization onto Casein, Int. J. Mol. Sci. 20 (2019) 3864, doi:10.3390/ijms20163864.

[23] A. Sieczka, E. Koda, A. Miszkowska, P. Osiński, Identification of Processes and Migration Parameters for Conservative and Reactive Contaminants in the Soil-Water Environment, in: 2019: pp. 551–559. https://doi.org/10.1007/978-981-13-2221-1_60.

[24] A. Rogowska, V. Railean-Plugaru, P. Pomastowski, J. Walczak-Skierska, A. Król-Górniak, A. Gołębiowski, B. Buszewski, The study on molecular profile changes of pathogens via zinc nanocomposites immobilization approach, Int. J. Mol. Sci. 22 (2021) 5395, doi:10.3390/ijms22105395.

[25] P. Eastman, J. Swails, J.D. Chodera, R.T. McGibbon, Y. Zhao, K.A. Beauchamp, L.-.P. Wang, A.C. Simmonett, M.P. Harrigan, C.D. Stern, R.P. Wiewiora, B.R. Brooks, V.S. Pande, OpenMM 7: rapid development of high performance algorithms for molecular dynamics, PLoS Comput. Biol. 13 (2017) e1005659, doi:10.1371/journal.pcbi.1005659.

[26] M.J. Abraham, T. Murtola, R. Schulz, S. Páll, J.C. Smith, B. Hess, E. Lindahl, GROMACS: high performance molecular simulations through multi-level parallelism from laptops to supercomputers, SoftwareX 1 (2015) 19–25 –2, doi:10.1016/j.softx.2015.06.001.

[27] R.D. Lins, P.H. Hünenberger, A new GROMOS force field for hexopyranose-based carbohydrates, J. Comput. Chem. 26 (2005) 1400–1412, doi:10.1002/jcc.20275.

[28] W. Lin, W.J. Welsh, W.R. Harris, Molecular mechanics studies of model Iron(III) transferrin complexes in vacuo and in aqueous solution, Inorg. Chem. 33 (1994) 884–890, doi:10.1021/ic00083a010.

[29] A.W. Schüttelkopf, D.M.F. van Aalten, PRODRG: a tool for high-throughput crystallography of protein–ligand complexes, Acta. Crystallogr. D Biol. Crystallogr. 60 (2004) 1355–1363, doi:10.1107/S0907444904011679.

[30] T. Darden, L. Perera, L. Li, L. Pedersen, New tricks for modelers from the crystallography toolkit: the particle mesh Ewald algorithm and its use in nucleic acid simulations, Structure 7 (1999) R55–R60, doi:10.1016/S0969-2126(99)80033-1.

[31] E.F. Pettersen, T.D. Goddard, C.C. Huang, G.S. Couch, D.M. Greenblatt, E.C. Meng, T.E. Ferrin, UCSF Chimera - A visualization system for exploratory research and analysis, J. Comput. Chem. 25 (2004) 1605–1612, doi:10.1002/jcc.20084.

[32] O. Trott, A.J. Olson, AutoDock Vina: improving the speed and accuracy of docking with a new scoring function, efficient optimization, and multithreading, J. Comput. Chem. 31 (2010) 455–461, doi:10.1002/jcc.21334.

[33] X. Liu, M. Wu, C. Li, P. Yu, S. Feng, Y. Li, Q. Zhang, Interaction structure and affinity of zwitterionic amino acids with important metal cations (Cd2+, Cu2+, Fe3+, Hg2+, Mn2+, Ni2+ and Zn2+) in aqueous solution: a theoretical study, Molecules 27 (2022) 2407, doi:10.3390/molecules27082407.

[34] B. Buszewski, P. Žuvela, A. Król-Górniak, V. Railean-Plugaru, A. Rogowska,

M.W. Wong, M. Yi, A. Rodzik, M. Sprynskyy, P. Pomastowski, Interactions of zinc aqua complexes with ovalbumin at the forefront of the Zn2+/ZnO-OVO hybrid complex formation mechanism, Appl. Surf. Sci. 542 (2021) 148641, doi:10.1016/j.apsusc.2020.148641.

[35] Y. Zhao, D.G. Truhlar, The M06 suite of density functionals for main group thermochemistry, thermochemical kinetics, noncovalent interactions, excited states, and transition elements: two new functionals and systematic testing of four M06-class functionals and 12 other functionals, Theor. Chem. Acc. 120 (2008) 215–241, doi:10.1007/s00214-007-0310-x.

[36] M.J. Frisch, G.W. Trucks, H.B. Schlegel, G.E. Scuseria, M.A. Robb, J.R. Cheeseman, G. Scalmani, V. Barone, G.A. Petersson, H. Nakatsuji, X. Li, M. Caricato, A.V. Manerich, J. Bloino, B.G. Janesko, R. Gomperts, B. Mennucci, H.P. Hratchian, J.V. Ortiz, A.F. Izmaylov, J.L. Sonnenberg, D. Williams-Young, F. Ding, F. Lipparini, F. Egidi, J. Goings, B. Peng, A. Petrone, T. Henderson, D. Ranasinghe, V.G. Zakrzewski, J. Gao, N. Rega, G. Zheng, W. Liang, M. Hada, M. Ehara, K. Toyota, R. Fukuda, J. Hasewaga, M. Ishida, T. Nakajima, Y. Honda, O. Kitao, H. Nakai, T. Vreven, K. Throssel, J.A. Montgomery Jr., F. Peralta, R. Ogliaro, M.J. Bearpack, J.J. Heyd, E.N. Brothers, K.N. Kudin, V.N. Staroverov, T.A. Keith, R. Kobayashi, J. Normand, K. Raghavachari, A.P. Rendell, J.C. Burant, S.S. Iyengar, J. Tomasi, M. Cossi, J.M. Millam, M. Klene, C. Adamo, R. Cammi, J.W. Ochterski, R.L. Martin, K. Morokuma, O. Farkas, J.B. Foresman, D.j. Fox, Gaussian 16, Revision C.01, (2016).

[37] A.v. Marenich, C.J. Cramer, D.G. Truhlar, Universal solvation model based on solute electron density and on a continuum model of the solvent defined by the bulk dielectric constant and atomic surface tensions, J. Phys. Chem. B 113 (2009) 6378–6396, doi:10.1021/jp810292n.

[38] P. Marnila, H.J. Korhonen, Lactoferrin for human health, in: dairy-derived ingredients, Elsevier (2009) 290–307, doi:10.1533/9781845697198.2.290.

[39] K. Zlatina, S.P. Galuska, The N -glycans of lactoferrin: more than just a sweet decoration, Biochem. Cell Biol. 99 (2021) 117–127, doi:10.1139/bcb-2020-0106.

[40] R. Sharma, Whey Proteins in Functional Foods, in: Whey Proteins, Elsevier, 2019, pp. 637–663, doi:10.1016/B978-0-12-812124-5.00018-7.

[41] K.-I. Shimazaki, A. Kawaguchi, T. Sato, Y. Ueda, T. Tomimura, S. Shimamura, Analysis of human and bovine milk lactoferrins by rotofor and chromatofocusing, Int. J. Biochem. 25 (1993) 1653–1658, doi:10.1016/0020-711X(93)90524-I.

[42] A.G. Hovanessian, Z.L. Awdeh, Gel isoelectric focusing of human-serum transferrin, Eur. J. Biochem. 68 (1976) 333–338, doi:10.1111/j.1432-1033.1976.tb10819.x.

[43] G. Majka, K. Śpiewak, K. Kurpiewska, P. Heczko, G. Stochel, M. Strus, M. Brindell, A high-throughput method for the quantification of iron saturation in lactoferrin preparations, Anal. Bioanal. Chem. 405 (2013) 5191–5200, doi:10.1007/s00216-013-6943-9.

[44] M. Sprynskyy, T. Kowalkowski, H. Tutu, E.M. Cukrowska, B. Buszewski, Adsorption performance of talc for uranium removal from aqueous solution, Chem. Eng. J. 171 (2011) 1185–1193, doi:10.1016/j.cej.2011.05.022.

[45] I. Michalak, K. Chojnacka, A. Witek-Krowiak, State of the art for the biosorption process—a review, Appl. Biochem. Biotechnol. 170 (2013) 1389–1416, doi:10.1007/s12010-013-0269-0.

[46] B. An, Cu(II) and As(V) adsorption kinetic characteristic of the multifunctional amino groups in chitosan, Processes 8 (2020) 1194, doi:10.3390/pr8091194.

[47] X. Du, Y. Li, Y.-.L. Xia, S.-.M. Ai, J. Liang, P. Sang, X.-.L. Ji, S.-.Q. Liu, Insights into protein–ligand interactions: mechanisms, models, and methods, Int. J. Mol. Sci. 17 (2016) 144, doi:10.3390/ijms17020144.

[48] F. Bou-Abdallah, T.R. Giffune, The thermodynamics of protein interactions with essential first row transition metals, Biochimica et Biophysica Acta (BBA) - General Subjects 1860 (2016) 879–891, doi:10.1016/j.bbagen.2015.11.005.

[49] F.R.N. Gurd, P.E. Wilcox, Complex formation between metallic cations and proteins, peptides, and amino acids, Adv. Protein Chem. (1956) 311–427, doi:10.1016/S0065-3233(08)60424-6.

[50] F. Roosen-Runge, B.S. Heck, F. Zhang, O. Kohlbacher, F. Schreiber, Interplay of pH and binding of multivalent metal ions: charge inversion and reentrant condensation in protein solutions, J. Phys. Chem. B 117 (2013) 5777–5787, doi:10.1021/jp401874t.

[51] O. Pryshchepa, P. Pomastowski, K. Rafińska, A. Gołębiowski, A. Rogowska, M. Monedeiro-Milanowski, G. Sagandykova, B. Michalke, P. Schmitt-Kopplin, M. Gloc, R. Dobrucka, B. Buszewski, Synthesis, physicochemical characterization, and antibacterial performance of silver—Lactoferrin complexes, Int. J. Mol. Sci. 23 (2022) 7112, doi:10.3390/ijms23137112.

[52] S.-.J. Park, M.-.K. Seo, Solid-solid interfaces, Interface Sci. Technol. (2011) 253–331, doi:10.1016/B978-0-12-375049-5.00004-9.

[53] G.W. Gokel, Introduction and overview of supramolecular receptor types, in: Comprehensive Supramolecular Chemistry II, Elsevier, 2017, pp. 1–10, doi:10.1016/B978-0-12-409547-2.12472-2.

[54] A. Krężel, W. Maret, The biological inorganic chemistry of zinc ions, Arch. Biochem. Biophys. 611 (2016) 3–19, doi:10.1016/j.abb.2016.04.010.

[55] T. Jabeen, S. Sharma, N. Singh, A. Bhushan, T.P. Singh, Structure of the zinc-saturated C-terminal lobe of bovine lactoferrin at 2.0 A resolution, Acta. Crystallogr. D Biol. Crystallogr. 61 (2005) 1107–1115, doi:10.1107/S0907444905016069.

[56] Y. Ji, X. Yang, Z. Ji, L. Zhu, N. Ma, D. Chen, X. Jia, J. Tang, Y. Cao, DFT-calculated IR spectrum amide I, II, and III band contributions of N -Methylacetamide fine components, ACS Omega 5 (2020) 8572–8578, doi:10.1021/acsomega.9b04421.

[57] M.E. Mohamed, A.M.A. Mohammed, Experimental and computational vibration study of amino acids, international letters of chemistry, Phys. Astron. 15 (2013) 1–17, doi:10.18052/www.scipress.com/ILCPA.15.1.

[58] B.P. Dimitrijević, S.Z. Borozan, S.Ð. Stojanović, π−π and cation−π interactions in protein–porphyrin complex crystal structures, RSC Adv. 2 (2012) 12963, doi:10.1039/c2ra21937a.

[59] R. Wu, T.B. McMahon, Investigation of cation-π interactions in biological systems, J. Am. Chem. Soc. 130 (2008) 12554–12555, doi:10.1021/ja802117s.

[60] M.E. Mohamed, A.M.A. Mohammed, Experimental and computational vibration study of amino acids, international letters of chemistry, Phys. Astron. 15 (2013) 1–17, doi:10.18052/WWW.SCIPRESS.COM/ILCPA.15.1.

[61] A. Barth, Infrared spectroscopy of proteins, Biochimica et Biophysica Acta (BBA) - Bioenergetics 1767 (2007) 1073–1101, doi:10.1016/j.bbabio.2007.06.004.

[62] A. Barth, The infrared absorption of amino acid side chains, Prog. Biophys. Mol. Biol. 74 (2000) 141–173, doi:10.1016/S0079-6107(00)00021-3.

[63] A. Rogowska, P. Pomastowski, M. Złoch, V. Railean-Plugaru, A. Król, K. Rafińska, M. Szultka-Młyńska, B. Buszewski, The influence of different pH on the electrophoretic behaviour of Saccharomyces cerevisiae modified by calcium ions, Sci. Rep. 8 (2018) 7261, doi:10.1038/s41598-018-25024-4.

[64] K. Kluska, J. Adamczyk, A. Krężel, Metal binding properties, stability and reactivity of zinc fingers, Coord. Chem. Rev. 367 (2018) 18–64, doi:10.1016/j.ccr.2018.04.009.

[65] D.E. Brodersen, M. Kjeldgaard, Structural investigations of calcium and zinc binding in proteins, Sci. Prog. 82 (1999) 295–312, doi:10.1177/003685049908200402.

[66] A.M. Smith, CHAPTER 1. Interaction of metal ions with proteins as a source of inspiration for biomimetic materials, Funct. Metallosupramol. Mater. (2015) 1–31, doi:10.1039/9781782622673-00001.

[67] M. Giustiniano, P. Tortorella, M. Agamennone, A. di Pizio, A. Rossello, E. Nuti, I. Gomez-Monterrey, E. Novellino, P. Campiglia, E. Vernieri, M. Sala, A. Bertamino, A. Carotenuto, Amino acid derivatives as new zinc binding groups for the design of selective matrix metalloproteinase inhibitors, J. Amino Acid. 2013 (2013) 1–12, doi:10.1155/2013/178381.

[68] Z. Wen, Raman spectroscopy of protein pharmaceuticals, J. Pharm. Sci. 96 (2007) 2861–2878, doi:10.1002/jps.20895.

[69] L. Ashton, V.L. Brewster, E. Correa, R. Goodacre, Detection of glycosylation and iron-binding protein modifications using Raman spectroscopy, Analyst 142 (2017) 808–814, doi:10.1039/C6AN02516A.

[70] T. Sakajiri, H. Yajima, T. Yamamura, Density functional theory study on metal-binding energies for human serum transferrin-metal complexes, ISRN Biophys. 2012 (2012) 1–5, doi:10.5402/2012/124803.

[71] L. Anghel, A. Radulescu, R.V. Erhan, Structural aspects of human lactoferrin in the iron-binding process studied by molecular dynamics and small-angle neutron scattering, Eur. Phys. J. E 41 (2018) 109, doi:10.1140/epje/i2018-11720-x.

[72] J. Uranga, J.I. Mujika, R. Grande-Aztatzi, J.M. Matxain, Oxidation of acid, base, and amide side-chain amino acid derivatives via hydroxyl radical, J. Phys. Chem. B 122 (2018) 4956–4971, doi:10.1021/acs.jpcb.7b12450.

[73] L. Rulíšek, Z. Havlas, Theoretical studies of metal ion selectivity. 1. DFT calculations of interaction energies of amino acid side chains with selected transition metal ions (Co 2+, Ni2+, Cu 2+, Zn2+, Cd2+, and Hg2+), J. Am. Chem. Soc. 122 (2000) 10428–10439, doi:10.1021/ja001265g.

[74] G. Duca, L. Anghel, R.V. Erhan, Structural aspects of lactoferrin and serum transferrin observed by ftir spectroscopy, Chem. J. Mold. 13 (2018) 111–116, doi:10.19261/cjm.2018.482.

[75] M.T. Hasan, B.J. Senger, C. Ryan, M. Culp, R. Gonzalez-Rodriguez, J.L. Coffer, A.v. Naumov, Optical band gap alteration of graphene oxide via ozone treatment, Sci. Rep. 7 (2017) 6411, doi:10.1038/s41598-017-06107-0.

[76] A. Capocefalo, D. Mammucari, F. Brasili, C. Fasolato, F. Bordi, P. Postorino, F. Domenici, Exploring the potentiality of a SERS-active pH Nano-Biosensor, Front. Chem. 7 (2019), doi:10.3389/fchem.2019.00413.

[77] G. Pezzotti, Raman spectroscopy in cell biology and microbiology, J. Raman Spectrosc. 52 (2021) 2348–2443, doi:10.1002/jrs.6204.

7. Podsumowanie i wnioski

Przedstawione w pracy badania pozwoliły na sformułowanie następujących postulatów:

1. Wiązanie jonów metali z aktywnymi grupami funkcyjnymi ma charakter heterogenny oraz odbywa się poprzez wieloetapowe procesy oddziaływania jonów z białkami;

2. Interakcje jonów metali z białkami może skutkować redukcją jonów metali oraz zmianami w strukturze białka. Procesy te zachodzą w sposób spontaniczny w warunkach optymalnych znaczeń deskryptorów fizyko-chemicznych, takich jak pH czy też stężenia jonów metali;

3. Zachodzące procesy wiązania jonów cynku są podobne dla wszystkich laktoferyn niezależnie od źródła ich pozyskiwania.

Po raz pierwszy otrzymano kompleksy laktoferyny bogate w jony żelaza(III) i cynku. Otrzymano nanokompozyt srebra na bazie laktoferyny bydlęcej w środowisku kwaśnym. Kompleksy zostały scharakteryzowane pod względem właściwości fizyko-chemicznych i biologicznych. Przed przystąpieniem do badań stanowiących część doświadczalną niniejszej rozprawy doktorskiej dokonano przeglądu literaturowego, który umożliwił sformułowanie problemu badawczego oraz sposoby jego rozwiązania i weryfikacji. Otrzymane wyniki przedstawiono w pięciu publikacjach stanowiących całość przedłożonej rozprawy doktorskiej, ich krótkie podsumowanie opisano poniżej.

1. Praca pt. „*Silver nanoparticles: synthesis, investigation techniques, and properties*", stanowi przegląd literaturowy w której przedstawiono wyniki metaanalizy dotyczącej syntezy i właściwości nanocząstek i nanokompozytów srebra. Wykazano, że właściwości materiałów i substancji złożonych można kontrolować poprzez dobór odpowiednich warunków syntezy poprzez zmianę stężenia prekursora, pH, temperatury, itp. Ponadto w artykule opisano podstawy i możliwości technik instrumentalnych używanych w badaniach nanoukładów: nanocząstek, nanokompozytów oraz kompleksów metali i innych materiałów o złożonej strukturze. Wykazano możliwe błędy oraz ograniczenia tych metod, które warto brać pod uwagę w celu minimalizacji błędnej interpretacji wyników. Na koniec przedyskutowano skutki oddziaływania nanocząstek srebra z komórkami organizmów żywych, co pozwoliło na określenie trzech możliwych mechanizmów ich toksycznego działania – (1) uwalnianie Ag^+ inaczej też mechanizm *"Konia Trojańskiego"*, (2) działanie kwantowo-mechaniczne oraz (3) działanie indukcyjne.

2. W pracy pt. „*Synthesis, physicochemical characterization and antibacterial performance of silver-lactoferrin complexes*" przedstawiono wyniki badań procesu sorpcji Ag^+ na laktoferynie bydlęcej. Kształt izotermy adsorpcji oraz parametry uzyskane po zastosowaniu

modeli adsorpcji Freundlicha oraz Langmuira wskazują na złożony oraz heterogenny charakter oddziaływania Ag^+ z laktoferyną. Analiza za pomocą mikroskopii elektronowej wykazała obecność nanocząstek w materiale, zaś łączenie elektroforezy kapilarnej z oznaczaniem zawartości srebra za pomocą ICP-MS w trybie *on-line* wskazało także na obecność Ag^+. Za pomocą technik spektroskopowych określono możliwe miejsca wiązania srebra z białkami. Mogą to być grupy funkcyjne aminokwasów takich jak kwas glutaminowy i asparaginowy, czy też tryptofanu i metioniny. Kinetyka trawienia pepsyną wskazała na spowolnione trawienie kompleksu na początku, co może być związane zinhibicją enzymu przez Ag^+. Jednak fragmenty częściowo strawionego białka ulegały szybszej lizie, co wskazuje na zachodzące zmiany w strukturze białka odsłaniające miejsca cięcia dla enzymu. Kompleks wykazywał się skutecznością działania przeciwbakteryjnego wobec wybranych bakterii. Oznaczone minimalne stężenie hamujące wzrost (MIC) bakterii było dużo niższe w porównaniu do stężenia wolnych jonów Ag^+. Zarówno kompleks Ag-LTF jak i Ag^+ wykazywały podobne działanie cytotoksyczne na komórki fibroblastów mysich L929. Ciekawym jednak okazała się różnica w kształcie komórek. Po oddziaływaniu Ag^+ z fibroblastami linii L929 zaobserwowano zmianę ich kształtu na okrągły charakterystyczny dla komórek apoptotycznych. Z kolei, po działaniu Ag-bLTF namnażanie się komórek zostało zahamowane, przy zachowaniu natywnego kształtu. Wskazuje to na różne mechanizmy działania toksycznego obu czynników.

3. W pracy pt. *,,Synthesis and physicochemical characterization of bovine lactoferrin supersaturated complex with iron (III) ions''* opisano wyniki badań sorpcji jonów Fe^{3+} na laktoferynie bydlęcej. Użyte do opisu sorpcyjne modele również wykazały heterogenny charakter wiązania się jonów żelaza(III) na laktoferynie. Dalsze badanie produktu reakcji metodami instrumentalnymi wykazały, że w wyniku interakcji otrzymany został homogenny kompleks Fe-bLTF zawierający ok. 50 atomów żelaza na jedną cząsteczkę białka. Za pomocą rozdzielania w żelu poliakryloamidowym (SDS-PAGE) w trybie redukcyjnym oraz nie-redukcyjnym zaobserwowano zwiększenie frakcji dimeru białka oraz częściową degradację białka wskutek odwracalnej redukcji żelaza. Technika ta wskazała także na tworzenie się bardziej szczelnej (zwartej) struktury białka. Metody spektroskopowe ujawniły udział grup karboksylowych kwasów glutaminowego i asparaginowego oraz hydroksylowych tyrozyny i seryny w wiązaniu się jonów żelaza. Kolejno zbadano cytotoksyczność otrzymanych kompleksów na liniach komórkowych gruczolaka jelita grubego Caco-2 oraz fibroblastów mysich L929. Otrzymany kompleks nie wykazywał większej toksyczności niż odpowiednie stężenia jonów żelaza(III) w formie cytrynianu.

4. W pracy pt. *,,Synthesis and physicochemical characterization of zinc-lactoferrin complexes"* opisano wyniki badań związanych z wpływem warunków reakcji na skuteczność wiązania jonów Zn^{2+} do cząsteczki laktoferyny bydlęcej. Zaobserwowano, że w pH 6,0 nie zachodziło wiązanie cynku na białku, z kolei przy pH 7,4 oraz 8,6 udało się otrzymać stabilne kompleksy Zn-bLTF, przy czym sorpcja była bardziej skuteczna przy użyciu wyższych stężeń jonów metali oraz wyższym pH. Uzyskane dane wskazują, że dostępność grup funkcyjnych zawierających azot oraz ładunek białka mają znaczący wpływ na zdolność wiązania Zn^{2+} przez LTF. Wyższa siła jonowa roztworu, w szczególności stężenie Zn^{2+} zwiększa prawdopodobieństwo chelatowania jonów grupami funkcyjnymi białek, a tym samym tworzenie się stabilnych metalokompleksów, co może być skutkiem zmian w trzeciorzędowej strukturze białka.

5. Dalsze badania mechanizmów wiązania cynku na laktoferynie przedstawiono w artykule pt. *,,Study on the zinc ions binding to human lactoferrin"*. Kinetyka oraz izoterma adsorpcji wykazała heterogenny charakter wiązania się Zn^{2+} oraz wieloetapowość zachodzących procesów. Spektroskopia w podczerwieni (FTIR) oraz Ramana wskazały na oddziaływanie Zn^{2+} poprzez grupy funkcyjne kwasów asparaginowego i glutaminowego, seryny, treoniny, histydyny oraz tryptofanu. Potwierdzenie udziału tych reszt aminokwasów zostało dokonane przez zastosowanie teorii funkcjonału gęstości oraz dynamiki molekularnej. Zarówno metody instrumentalne jak i metody chemii obliczeniowej wskazały na zmiany w strukturze białka oraz osłabienia wiązania Fe-LTF, co skutkowało częściową eliminacją jonów żelaza(III) ze struktury białka. Proces zmian strukturalnych nasilał się przy zwiększeniu stężenia jonów Zn^{2+} w mieszaninie reakcyjnej. Zwiększenie stężenia jonów metalu także spowodowało zwiększenie szybkości zachodzących zmian. Na podstawie uzyskanych wyników udało się określić poszczególne etapy zachodzące w czasie interakcji jonów cynku z laktoferyną.

8. Streszczenie

W niniejszej pracy przeprowadzono dobór warunków syntezy kompleksów i nanokompozytów laktoferyny z jonami d-metali o znaczeniu biologicznym, mianowicie jonami srebra, żelaza(III) oraz cynku. Zbadano wpływ różnych czynników na skuteczność adsorpcji jonów metali na białku. Między innymi, określono wpływ pH oraz stężenia jonów metali na właściwości uzyskanych biologicznie aktywnych substancji. Otrzymane układy scharakteryzowano pod względem właściwości fizykochemicznych oraz biologicznych. Do tych celów użyto metody mikroskopii elektronowej, spektrometrii mas, spektroskopii oraz sprzężone metody rozdzielania. Określona została także stabilność kompleksów w buforach imitujących warunki układu pokarmowego. Możliwość wykorzystania kompleksów jako aktywnych substancji w preparatach leczniczych lub suplementów diety została również przebadana za pomocą metod mikrobiologicznych oraz cytotoksyczności *in vitro*. Stwierdzono wysoki potencjał aplikacyjny zaproponowanych metod syntezy kompleksów metal-LTF. Na koniec została podjęta próba określenia rzeczywistego mechanizmu oddziaływania metali z białkami na przykładzie wiązania się Zn^{2+} na laktoferynie ludzkiej poprzez zastosowanie metod obliczeniowych dynamiki molekularnej oraz teorii funkcjonału gęstości.

Wstępny etap badań obejmował charakteryzację modelowych białek, tzn. laktoferyny bydlęcej oraz rekombinowanej laktoferyny ludzkiej. Określona została masa molekularna, punkt izoelektryczny oraz zawartość jonów żelaza(III) oraz cynku, co jest niezmiernie ważne do określenia procesów zachodzących podczas oddziaływania jonów metali z białkami oraz stechiometrii reakcji. W kolejnym etapie dokonano opisu natury procesu z wykorzystaniem klasycznych badań adsorpcji. Kolejny ważny etap pracy stanowił uzupełnienie danych adsorpcji o wyniki metod spektroskopowych oraz mikroskopii elektronowej. Wyniki mikroskopii elektronowej wskazały na powstanie homogennych kompleksów żelaza i cynku oraz nanokompozytu srebra z laktoferyną. Dla ostatniego wykazano zależność rozmiaru nanocząstek od stężenia jonów srebra w roztworze. Ponadto, wykazano korelację pomiędzy kształtem izotermy adsorpcji oraz rozmiarem i ilością inkluzji metalicznych w nanokompozycie. Badania spektroskopowe wykazały udział poszczególnych grup funkcyjnych w wiązaniu jonów metali, gdzie największy udział dla wszystkich przebadanych metali miały grupy karboksylowe kwasów glutaminowego i asparaginowego. Wykazano także udział grup funkcyjnych innych aminokwasów - histydyny, tryptofanu, seryny, tyrozyny oraz treoniny. Stwierdzono także, że wiązanie jonów metali do białka indukuje zmiany w jego strukturze i pojawienie się nowych miejsc wiążących z jednoczesną zmianą w zdolności wiązania jonów żelaza. Dobra zgodność

wyników eksperymentalnych i teoretycznych pozwoliła na zaproponowanie mechanizmu oddziaływania cynku z laktoferyną. Dodatkowo, udało się określić każdy poszczególny etap zachodzących w czasie oddziaływania zmian.

9. Abstract

In the work, the selection of conditions for the synthesis of complexes and nanocomposites based on lactoferrin and ions of d-metals of biological importance, namely silver, iron(III), and zinc ions, was carried out. The influence of various factors on the efficiency of metal binding to the protein was investigated. Among others, the influence of pH and concentration of metal ions on the properties of the obtained biologically active substances were examined. The obtained nanocomposites and metal-rich protein complexes were characterized in terms of physicochemical and biological properties. Electron microscopy, spectrometric, spectroscopic, and coupled separation techniques were used for these purposes. The stability of the complexes in buffers imitating the conditions of various parts of the digestive system was also determined. The possibility for the utilization of as-synthesized complexes as active substances in pharmaceutical preparations or dietary supplements was also assessed based on the *in vitro* methods for antibacterial properties and cytotoxicity study. A high potential for the use of the proposed synthesis methods in the pharmaceutical, cosmetics, and food processing industries was found. Finally, an attempt was made to determine the actual mechanism of interaction of metals with proteins on the example of Zn^{2+} binding to human lactoferrin by applying computational methods of molecular dynamics and density functional theory.

The initial stage of the research included the characterization of model proteins, i.e. bovine lactoferrin and recombinant human lactoferrin. The molecular weight, isoelectric point, and the content of iron and zinc ions were determined, which is extremely important for the determination of the processes that take part during the interaction of metals with proteins and the stoichiometry of the reaction. In the next stage, the nature of the process was described using the classical sorption approach. Another important stage of the work was to complement the sorption data with data from spectroscopic methods and electron microscopy. The results of electron microscopy revealed the formation of homogeneous complexes of iron and zinc and a nanocomposite of silver with lactoferrin. Moreover, the dependence of the size of silver nanoparticles on the concentration of silver in the solution was demonstrated. In addition, a correlation was found between the shape of the adsorption isotherm and the size and number of metallic inclusions in the nanocomposite. Spectroscopic studies showed the participation of functional groups in the binding of metals, where the largest share for all the tested metals had the carboxylic groups of glutamic and aspartic acids. Additionally, the participation of functional groups of other amino acids – histidine, tryptophan, serine, tyrosine, and threonine has also been demonstrated. It was also found that the binding of metals to the protein induces changes in its structure and the emergence of new metal-binding sites with a simultaneous change in the iron-

binding capacity. The good agreement between experimental and theoretical results allowed us to propose a mechanism of interaction of zinc with lactoferrin. Finally, it was possible to identify each individual stage of the changes that take place during the metal binding.

10. Dorobek naukowy

Pozostałe publikacji naukowe:

1. **O. Pryshchepa,** G. N. Sagandykova, P. Pomastowski, V. Railean-Plugaru, A. Król, A. Rogowska, A. Rodzik, M. Sprynskyy, and B. Buszewski, "*A New Approach for Spontaneous Silver Ions Immobilization onto Casein*", International Journal of Molecular Sciences, 2019, 20 (16): 3864; https://doi.org/10.3390/ijms20163864; (**IF = 6.208, MP =140**);

2. M. Złoch, A. Rodzik, **O. Pryshchepa**, K. Pauter, M. Szultka-Młyńska, A. Rogowska, W. Kupczyk, P. Pomastowski, and B. Buszewski, "*Problems with identifying and distinguishing salivary streptococci: a multi-instrumental approach*", Future Microbiology, 2020, 15 (12): 1157-1171; https://doi.org/10.2217/fmb-2020-0036; (**IF = 3.553, MP =100**);

3. T. Dyrda-Terniuk, M. Sugajski, **O. Pryshchepa**, J. Śliwiak, M. Buszewska-Forajta, P. Pomastowski, and B. Buszewski, "*The study of protein-cyclitol interactions*", International Journal of Molecular Sciences, 2022, 23 (6): 2940; https://doi.org/10.3390/ijms23062940; (**IF = 6.208, MP =140**);

4. A. Arendowski, G. Sagandykova, R. Mametov, K. Rafińska, **O. Pryshchepa**, and P. Pomastowski, "*Nanostructured layer of silver for detection of small biomolecules in surface-assisted laser desorption ionization mass spectrometry*", Materials, 2022, 15(12): 4076; https://doi.org/10.3390/ma15124076; (**IF = 3.748, MP =140**);

5. G. Sagandykova, P. Piszczek, A. Radtke, R. Mametov, O. Pryshchepa, D. Gabryś, M. Kolankowski, and P. Pomastowki, "*Silver nanostructured substrates in LDI-MS of low molecular weight compounds*", Materials, 2022, 15 (13): 4660; https://doi.org/10.3390/ma15134660; (**IF = 3.748, MP =140**);

6. P. Roychoudhury, A. Golubeva, P. Dąbek, **O. Pryshchepa**, G. Sagandykova, P. Pomastowski, M. Głoc, R. Dobrucka, K. Kurzydłowski, B. Buszewski, and A. Witkowski, "*Study on biogenic spindle-shaped iron-oxide nanoparticles by Pseudostaurosira trainorii in field of Laser Desorption/Ionization Applications*", International Journal of Molecular Sciences, 2022, 23(19): 11713; https://doi.org/10.3390/ijms231911713; (**IF = 6.208, MP = 140**);

7. G. Sagandykova, O. Pryshchepa, K. Rafińska, R. Mametov, P. Madajski, and P. Pomastowski, "LDI-MS performance of gold nanostars as an inorganic matrix for low molecular weight analytes", International Journal of Mass Spectrometry, 2022, 478: 116872; https://doi.org/10.1016/j.ijms.2022.116872; (**IF = 1.934, MP = 70**);

8. A. Gołębiowski, P. Pomastowski, K. Rafińska, P. Zuvela, M. W. Wong, **O. Pryshchepa**, P. Madajski, and B. Buszewski, *"Functionalization of alpha-lactalbumin by zinc ions"*, ACS Omega, 2022, 7 (43): 38459-38474; https://doi.org/10.1021/acsomega.2c03674; (**IF = 4.132, MP = 70**);

9. **O. Pryshchepa**, M. Złoch, P. Pomastowski, V. Railean-Plugaru, A. Rodzik, M. Szultka-Młyńska, and B. Buszewski, *"Modern Approaches for Microorganisms' Identification"*, In: B. Buszewski, I. Baranowska (Eds.) Handbook of Bioanalytics. Springer, Cham., 2022, https://doi.org/10.1007/978-3-030-63957-0_40-1

10. **O. Pryshchepa**, M. Złoch, P. Pomastowski, V. Railean-Plugaru, A. Rodzik, M. Szultka-Młyńska, B. Buszewski, "Nowoczesne metody identyfikacji mikroorganizmów", W: I. Staneczko-Baranowska, B. Buszewski (Eds.) Bioanalityka w nauce i życiu Tom 1, Wydawnictwo Naukowe PWN, Warszawa, 2020: 589-611.

Konferencje naukowe:

1. M. Złoch, **O. Pryshchepa**, P. Pomastowski, M. Szultka-Młyńska, B. Buszewski, *"Application of MALDI-TOF MS technique for examination of clinical specimens on example of salivary bacteria analysis"*, V Science Conference "Metabolomics Circle", 26-28.10.2018, Przysiek koło Torunia, Poland (wykład);

2. **O. Pryshchepa**, M. Złoch, K. Pauter, M. Szultka-Młyńska, P. Pomastowski, B. Buszewski *"Selection of experimental conditions for the identification of bacteria by MALDI-TOF MS"*, 15th ISC 'Modern Analytical Chemistry, 19-20.09.2019, Prague, Czech Republic (wykład);

3. **O. Pryshchepa**, G. Sagandykova, K. Rafińska, J. Rudnicka, P. Pomastowski, M. Sprynskyy, B. Buszewski, *"The influence of different conditions on the formation of Zn-Lactoferrin complexes"*, 15th International Scientific Conference "The Vital Nature Sign", 20-21 May 2021, Kaunas, Lithuania, (wykład, on-line);

4. B. Buszewski, **O. Pryshchepa**, A. Rodzik, P. Pomastowski, *"Metal-protein nanocomposites – their biosynthesis, characterisation and application"*, ECOpole'20, 7-10.10.2020, Kraków, Poland (wykład);

5. **O. Pryshchepa,** G. Sagandykova, J. Rudnicka, P. Pomastowski, M.Sprynskyy, B. Buszewski *"The Study on Bovine Lactoferrin Interactions With Zinc Ions By Coupled Analytical Techniques"*, "Quo Vadis Life Science", 23-27.06.2021, Opole, Poland, (krótki komunikat, on-line);

6. R. Mametov, A. Arendowski, **O. Pryshchepa**, K. Rafińska, P. Pomastowski, G. Sagandykova, *"Novel SALDI Plate Based on Electrodeposition o Silver for Analysis of Low Molecular Weight*

Compounds", International Conference on Innovative and Smart Material, 11-13.12.2021, Kraków, Polska (krótki komunikat, on-line);

7. G. Sagandykova, **O. Pryshchepa**, K. Rafińska, R. Mametov, P. Madajski, P. Pomastowski, *"Perfomance of Gold Anisotropic Nanoparticles in LDI-MS of Low Molecular Weight Compounds"*, International Conference on Innovative and Smart Material, 11-13.12.2021, Kraków, Polska (wykład, on-line);

8. **O. Pryshchepa**, K. Rafińska, A. Gołębiowski, M. Sugajski, A. Rogowska, G. Sagandykova, P. Pomastowski, B. Buszewski, *"The Study on the Formation of Supersaturated Complex of Iron with Bovine Lactoferrin"*, 16th International Scientific Conference "The Vital Nature Sign", 12-13.05.2022, Kaunas, Litwa (wykład, on-line);

9. G. Sagandykova, P. Piszczek, A. Radtke, R. Mametov, **O. Pryshchepa**, D. Gabryś, M. Kolankowski, P. Pomastowski, *"Silver Nanostructures in LDI-MS of Low Molecular Weight Compounds"*, 16th International Scientific Conference "The Vital Nature Sign", 12-13.05.2022, Kaunas, Litwa (wykład, on-line);

10. K. Rafińska, **O. Pryshchepa**, A. Gołębiowski, P. Pomastowski, B. Buszewski, *"Lactoferrin as a carrier of iron ions"*, 16th International Scientific Conference "The Vital Nature Sign" 12-13.05.2022, Kaunas, Litwa (wykład, on-line)

11. **O. Pryshchepa**, K. Rafińska, A. Gołębiowski, A. Rogowska, P. Schmitt-Kopplin, B. Michalke, B. Buszewski, P. Pomastowski, "Utilization of ICP-MS technique for investigation of bovine lactoferrin interactions with metals and characterization of respective metal-rich protein complexes", 10th Nordic Conference on Plasma Spectrochemistry, 12-15.06.2022, Loen, Norwegia (wykład);

12. T. Dyrda-Terniuk, A. Gołębiowski, **O. Pryshchepa**, K. Rafińska, M. Buszewska-Forajta, P. Pomastowski, B. Buszewski, *"Studying the mechanism of silver ions binding to casein"*, 10th Nordic Conference on Plasma Spectrochemistry, 12-15.06.2022, Loen, Norwegia (poster);

13. T. Dyrda-Terniuk, M. Sugajski, **O. Pryshchepa**, J. Śliwiak, M. Buszewska-Forajta, P. Pomastowski, B. Buszewski *"Investigation of D-sorbitol and D-(−)-quinic acid interactions with Bovine Serum Albumin"*, XI Polska Konferencja Chemii Analitycznej, PoKoChA 2022, 19-23.06.2022, Łódź, Polska (poster);

14. **O. Pryshchepa**, P. Pomastowski, *"New aspects in lactoferrin study"*, 31st Annual conference Biomaterials in Medicine and Veterinary Medicine, 13-16.10.2022, Rytro, Poland (krótki komunikat);

15. G. Sagandykova, P. Piszczek, A. Radtke, R. Mametov, **O. Pryshchepa**, D. Gabryś, M. Kolankowski, and P. Pomastowski "LDI process with the use of silver nanostructured

substrates in analysis of low molecular weight compounds" 31st Annual conference Biomaterials in Medicine and Veterinary Medicine, 13-16.10.2022, Rytro, Poland (poster).

Granty:

1. Grant Wydziału Chemii nr 2092/2019, pt. *"Badanie molekularnych mechanizmów wiązania metali z białkami"*; Kierownik: mgr Oleksandra Pryshchepa (18.10.2019-14.01.2020);

2. Grant Wydziału Chemii nr 492/2020, pt. *"Badanie aktywności biologicznej bionanokompozytów cynku i srebra z laktoferyną"*; Kierownik: mgr Oleksandra Pryshchepa (03.03.2020-30.11.2020);

3. Grant Wydziału Chemii nr 492/2020, pt. *" Badanie biologicznej aktywności kompleksów laktoferyny z metalami"*; Kierownik: mgr Oleksandra Pryshchepa (05.05.2021-30.11.2021);

4. Grant BIOG-NET z Fundacji na rzecz Nauki Polskiej nr FNP 4.4 PO IR 2014-2020, program TEAM-NET, *"Zaawansowane biokompozyty dla gospodarki jutra BIOG-NET"*, Lider zespołu UMK: dr hab. Paweł Pomastowski, prof. UMK, Wykonawca projektu: mgr Oleksandra Pryshchepa (01.01.2020-30.06.2022);

5. Grant Preludium 20 z Narodowego Centrum Nauki nr NCN 2021/41/N/ST4/01666, pt. *"Wykorzystanie spektrometrii mass z laserową desorpcją/jonizacją próbki wspomaganą matrycą i technik separacyjnych w badaniach wpływu mikrobiomu gruczołów mlekowych na ilość i potranslacyjne modyfikacje laktoferyny w mleku krowim"*; Kierownik: mgr Oleksandra Pryshchepa (02.02.2022-01.02.2024);

6. Grant Bekker NAWA 2022 z Narodowej Agencji Wymiany Akademickiej nr BPN/BEK/2022/1/00315 pt. *"Badanie antybiotykooporności wybranych patogenów bakterii izolowanych z mleka krów z zapaleniem wymienia"*, Kierownik: mgr Oleksandra Pryshchepa (01.06.2023-1.09.2023).

Staże:

Odbyłam trzy staże przemysłowe w zakładzie mleczarskim Polmlek Grudziądz Sp. z o. o. z zakresu stosowania metod mikrofiltracji do procesów dekontaminacji mikrobiologicznej mleka, ultrafiltracji do procesów frakcjonowania i zagęszczania białek mleka a także nanofiltracji w procesach odsalania oraz standaryzacji peptydowej i laktozowej układów mleczarskich. Staże w odbywały się w terminach: 03-13.08.2023; 05-13.09.2023; 14-18.11.2022.

Szkolenia:

14-18.02.2022 – szkoła cytometrii „*Cytometria przepływowa - podstawowe narzędzie badawcze*", Collegium Medicum UMK, Bydgoszcz

11. Oświadczenia

MSc. Oleksandra Pryshchepa
Centre for Modern Interdisciplinary Technologies,
Nicolaus Copernicus University in Toruń,
4 Wileńska Str., 87-100 Torun, Poland

STATEMENT

I hereby declare that, as a co-author of the following articles were:

1. O. Pryshchepa, P. Pomastowski, B. Buszewski, "Silver nanoparticles: Synthesis, investigation techniques, and properties", Advances in Colloid and Interface Science, 284, 2020: 102246, https://doi.org/10.1016/j.cis.2020.102246;

my contribution in the preparation of the article was on the design of general concept of the manuscript, literature review, preparation of original draft, editing and correction of manuscript.

2. O. Pryshchepa, G. Sagandykova, J. Rudnicka, P. Pomastowski, S. Sprynskyy, B. Buszewski "Synthesis and physicochemical characterization of zinc-lactoferrin complexes", Journal of Dairy Science, 3 (105), 2022: 1940-1958, https://doi.org/10.3168/jds.2021-20538;

my contribution in the preparation of the article was on the design of general concept of the performed study, planning and performing of the majority of the experiments, data interpretation, preparation of original draft, editing and correction of manuscript.

3. O. Pryshchepa, P. Pomastowski, K. Rafińska, A. Gołębiowski, A. Rogowska, M Monedeiro-Milanowski, G. Sagandykova, B. Michalke, P. Schmitt-Kopplin, M. Gloc, R. Dobrucka, K. Kurzydłowski, B. Buszewski, "Synthesis, physicochemical characterization and antibacterial performance of silver-lactoferrin complexes", International Journal of Molecular Sciences, 23 (13), 2022: 7112, https://doi.org/10.3390/ijms23137112;

my contribution in the preparation of the article was on the design of general concept of the performed study, planning and performing of the majority of the experiments, data interpretation, preparation of original draft, editing and correction of manuscript, correspondence with the journal editorial board during the revision.

4. O. Pryshchepa, K. Rafińska, A. Gołębiowski, M. Sugajski, G. Sagandykova, P. Madajski, B. Buszewski, P. Pomastowski, "Synthesis and physicochemical characterization of bovine lactoferrin supersaturated complex with iron (III) ions", Scientific Reports, 12 (1), 2022: 12695, https://doi.org/10.1038/s41598-022-15814-2

my contribution in the preparation of the article was on the design of general concept of the performed study, planning and performing of the majority of the experiments, data interpretation, preparation of original draft, editing and correction of manuscript, correspondence with the journal editorial board during the revision.

5. A. Rogowska, O. Pryshchepa, N.N. Som, P. Śpiewak, A. Gołębiowski, K. Rafińska, R. Dobrucka, K. Kurzydłowski, B. Buszewski, P. Pomastowski, „Study on the Zinc Ions Binding To Human Lactoferrin", Journal of Molecular Structure, 2023: 135149, https://doi.org/10.1016/j.molstruc.2023.135149

my contribution in the preparation of the article was on the design of general concept of the performed study, data interpretation, preparation of original draft, editing and correction of manuscript, correspondence with the journal editorial board during the revision.

Oleksandra Pryshchepa.

Torun, 16 February 2023

Dr Paweł Pomastowski, Dsc.
Centre for Modern Interdisciplinary Technologies,
Nicolaus Copernicus University in Toruń,
4 Wileńska Str., 87-100 Torun, Poland

STATEMENT

I hereby declare that, as a co-author of the following articles, being a part of the PhD thesis of Ms. Oleksandra Pryshchepa, MSc:

1. O. Pryshchepa, P. Pomastowski, B. Buszewski, "Silver nanoparticles: Synthesis, investigation techniques, and properties", Advances in Colloid and Interface Science, 284, 2020: 102246, https://doi.org/10.1016/j.cis.2020.102246;

2. O. Pryshchepa, G. Sagandykova, J. Rudnicka, P. Pomastowski, S. Sprynskyy, B. Buszewski "Synthesis and physicochemical characterization of zinc-lactoferrin complexes", Journal of Dairy Science, 3 (105), 2022: 1940-1958, https://doi.org/10.3168/jds.2021-20538;

3. O. Pryshchepa, P. Pomastowski, K. Rafińska, A. Gołębiowski, A. Rogowska, M Monedeiro-Milanowski, G. Sagandykova, B. Michalke, P. Schmitt-Kopplin, M. Gloc, R. Dobrucka, K. Kurzydłowski, B. Buszewski, "Synthesis, physicochemical characterization and antibacterial performance of silver-lactoferrin complexes", International Journal of Molecular Sciences, 23 (13), 2022: 7112, https://doi.org/10.3390/ijms23137112;

4. O. Pryshchepa, K. Rafińska, A. Gołębiowski, M. Sugajski, G. Sagandykova, P. Madajski, B. Buszewski, P. Pomastowski, "Synthesis and physicochemical characterization of bovine lactoferrin supersaturated complex with iron (III) ions", Scientific Reports, 12 (1), 2022: 12695, https://doi.org/10.1038/s41598-022-15814-2

5. A. Rogowska, O. Pryshchepa, N. N. Som, P. Śpiewak, A. Gołębiowski, K. Rafińska, R. Dobrucka, K. Kurzydłowski, B. Buszewski, P. Pomastowski, „Study on the Zinc Ions Binding To Human Lactoferrin", Journal of Molecular Structure, 2023: 135149, https://doi.org/10.1016/j.molstruc.2023.135149

that my contribution was on co-supervision, assistance in the experiments planning and data interpretation, editing and correction of the manuscripts.

Prof. Dr. Boguslaw Buszewski, D.Sc, dr h.c. mult.
Jan Czochralski Kuyavian-Pomeranian Research & Development Centre
1.Parkowa Str. 87-134 Przysiek, Poland

STATEMENT

I hereby declare that, as a co-author of the following papers, being a part of the PhD thesis of Ms. Oleksandra Pryshchepa, MSc:

(D1) O. Pryshchepa, P. Pomastowski, B. Buszewski, "Silver nanoparticles: Synthesis, investigation techniques, and properties", Advances in Colloid and Interface Science, 284, 2020: 102246, https://doi.org/10.1016/j.cis.2020.102246;

(D2) O. Pryshchepa, G. Sagandykova, J. Rudnicka, P. Pomastowski, S. Sprynskyy, B. Buszewski "Synthesis and physicochemical characterization of zinc-lactoferrin complexes", Journal of Dairy Science, 3 (105), 2022: 1940-1958, https://doi.org/10.3168/jds.2021-20538;

(D3) O. Pryshchepa, P. Pomastowski, K. Rafińska, A. Gołębiowski, A. Rogowska, M Monedeiro-Milanowski, G. Sagandykova, B. Michalke, P. Schmitt-Kopplin, M. Gloc, R. Dobrucka, K. Kurzydłowski, B. Buszewski, "Synthesis, physicochemical characterization and antibacterial performance of silver-lactoferrin complexes", International Journal of Molecular Sciences, 23 (13), 2022: 7112, https://doi.org/10.3390/ijms23137112;

(D4) O. Pryshchepa, K. Rafińska, A. Gołębiowski, M. Sugajski, G. Sagandykova, P. Madajski,B. Buszewski, P. Pomastowski, "Synthesis and physicochemical characterization of bovine lactoferrin supersaturated complex with iron (III) ions", Scientific Reports, 12 (1), 2022: 12695, https://doi.org/10.1038/s41598-022-15814-2

(D5) A. Rogowska, O. Pryshchepa, Som N. Narayan, P. Śpiewak, A. Gołębiowski, K. Rafińska, K. Kurzydłowski, B. Buszewski, P. Pomastowski, „Study on the Zinc Ions Binding To Human Lactoferrin", Journal of Molecular Structure, 2023: 135149, https://doi.org/10.1016/j.molstruc.2023.135149

that my contribution was partially on co-supervising of experiments, controlling and some interpretation of data, and editing and correcting of manuscripts.

prof. zw. dr hab. Bogusław Buszewski, dr h.c. mult.

Torun, 20 February 2023

Dr. Gulyaim Sagandykova
Centre for Modern Interdisciplinary Technologies,
Nicolaus Copernicus University in Toruń,
4 Wileńska Str., 87-100 Torun, Poland

STATEMENT

I hereby declare that, as a co-author of the following articles, being a part of the PhD thesis of Ms. Oleksandra Pryshchepa, MSc:

1. O. Pryshchepa, G. Sagandykova, J. Rudnicka, P. Pomastowski, S. Sprynskyy, B. Buszewski "Synthesis and physicochemical characterization of zinc-lactoferrin complexes", Journal of Dairy Science, 3 (105), 2022: 1940-1958, https://doi.org/10.3168/jds.2021-20538;

2. O. Pryshchepa, P. Pomastowski, K. Rafińska, A. Gołębiowski, A. Rogowska, M Monedeiro-Milanowski, G. Sagandykova, B. Michalke, P. Schmitt-Kopplin, M. Gloc, R. Dobrucka, K. Kurzydłowski, B. Buszewski, "Synthesis, physicochemical characterization and antibacterial performance of silver-lactoferrin complexes", International Journal of Molecular Sciences, 23 (13), 2022: 7112, https://doi.org/10.3390/ijms23137112;

3. O. Pryshchepa, K. Rafińska, A. Gołębiowski, M. Sugajski, G. Sagandykova, P. Madajski, B. Buszewski, P. Pomastowski, "Synthesis and physicochemical characterization of bovine lactoferrin supersaturated complex with iron (III) ions", Scientific Reports, 12 (1), 2022: 12695, https://doi.org/10.1038/s41598-022-15814-2

that my contribution was on assistance in the performing of some experiments, the visual design of the figures, and the correction of the manuscripts.

MSc. Adrian Gołębiowski
Chair of Environmental Chemistry and Bioanalytics,
Faculty of Chemistry, Nicolaus Copernicus University,
7 Gagarina Str., 87-100 Torun, Poland

STATEMENT

I hereby declare that, as a co-author of the following articles, being a part of the PhD thesis of Ms. Oleksandra Pryshchepa, MSc:

1. O. Pryshchepa, P. Pomastowski, K. Rafińska, A. Gołębiowski, A. Rogowska, M Monedeiro-Milanowski, G. Sagandykova, B. Michalke, P. Schmitt-Kopplin, M. Gloc, R. Dobrucka, K. Kurzydłowski, B. Buszewski, "Synthesis, physicochemical characterization and antibacterial performance of silver-lactoferrin complexes", International Journal of Molecular Sciences, 23 (13), 2022: 7112, https://doi.org/10.3390/ijms23137112;

2. O. Pryshchepa, K. Rafińska, A. Gołębiowski, M. Sugajski, G. Sagandykova, P. Madajski, B. Buszewski, P. Pomastowski, "Synthesis and physicochemical characterization of bovine lactoferrin supersaturated complex with iron (III) ions", Scientific Reports, 12 (1), 2022: 12695, https://doi.org/10.1038/s41598-022-15814-2;

3. A. Rogowska, O. Pryshchepa, N.N. Som, P. Śpiewak, A. Gołębiowski, K. Rafińska, R. Dobrucka, K. Kurzydłowski, B. Buszewski, P. Pomastowski, „Study on the Zinc Ions Binding To Human Lactoferrin", Journal of Molecular Structure, 2023: 135149, https://doi.org/10.1016/j.molstruc.2023.135149

that my contribution was on the performance of all ICP-MS measurements.

Dr. eng. Maciej Monedeiro-Milanowski
ul. Mierosławskiego 2/4, 85-654 Bydgoszcz

STATEMENT

I hereby declare that, as a co-author of the following article, being a part of the PhD thesis of Ms. Oleksandra Pryshchepa, MSc:

1. O. Pryshchepa, P. Pomastowski, K. Rafińska, A. Gołębiowski, A. Rogowska, M Monedeiro-Milanowski, G. Sagandykova, B. Michalke, P. Schmitt-Kopplin, M. Gloc, R. Dobrucka, K. Kurzydłowski, B. Buszewski, "Synthesis, physicochemical characterization and antibacterial performance of silver-lactoferrin complexes", International Journal of Molecular Sciences, 23 (13), 2022: 7112, https://doi.org/10.3390/ijms23137112;

that my contribution was on the assistance in the performing of microbiological tests.

Dr. Katarzyna Rafińska, DSc.
Chair of Environmental Chemistry and Bioanalytics,
Faculty of Chemistry, Nicolaus Copernicus University,
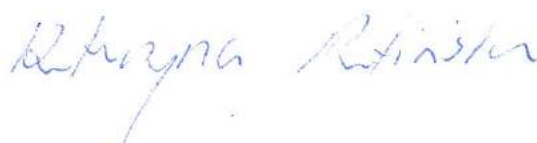7 Gagarina Str., 87-100 Torun, Poland

STATEMENT

I hereby declare that, as a co-author of the following articles, being a part of the PhD thesis of Ms. Oleksandra Pryshchepa, MSc:

1. O. Pryshchepa, P. Pomastowski, K. Rafińska, A. Gołębiowski, A. Rogowska, M Monedeiro-Milanowski, G. Sagandykova, B. Michalke, P. Schmitt-Kopplin, M. Gloc, R. Dobrucka, K. Kurzydłowski, B. Buszewski, "Synthesis, physicochemical characterization and antibacterial performance of silver-lactoferrin complexes", International Journal of Molecular Sciences, 23 (13), 2022: 7112, https://doi.org/10.3390/ijms23137112;

2. O. Pryshchepa, K. Rafińska, A. Gołębiowski, M. Sugajski, G. Sagandykova, P. Madajski, B. Buszewski, P. Pomastowski, "Synthesis and physicochemical characterization of bovine lactoferrin supersaturated complex with iron (III) ions", Scientific Reports, 12 (1), 2022: 12695, https://doi.org/10.1038/s41598-022-15814-2

3. A. Rogowska, O. Pryshchepa, N.N Som, P. Śpiewak, A. Gołębiowski, K. Rafińska, R. Dobrucka, K. Kurzydłowski, B. Buszewski, P. Pomastowski, „Study on the Zinc Ions Binding To Human Lactoferrin", Journal of Molecular Structure, 2023: 135149, https://doi.org/10.1016/j.molstruc.2023.135149

that my contribution was on the planning, performing, and data interpretation for cytotoxicity tests. Moreover, I performed the interpretation of the data acquired during the TEM-EDX analysis and took part in the writing and correction of the manuscripts.

Toruń, 24 February 2023

MSc. Piotr Madajski
Department of Chemistry of Materials Adsorption and Catalysis,
Faculty of Chemistry, Nicolaus Copernicus University in Torun,
Gagarina 7, 87-100 Torun, Poland

STATEMENT

I hereby declare that, as a co-author of the following article, being a part of the PhD thesis of Ms. Oleksandra Pryshchepa, MSc:

1. O. Pryshchepa, K. Rafińska, A. Gołębiowski, M. Sugajski, G. Sagandykova, P. Madajski, B. Buszewski, P. Pomastowski, "Synthesis and physicochemical characterization of bovine lactoferrin supersaturated complex with iron (III) ions", Scientific Reports, 12 (1), 2022: 12695, https://doi.org/10.1038/s41598-022-15814-2

that my contribution was on the planning and performing of the TEM imaging with EDX analysis.

Torun, 15 February 2023

Dr. Joanna Rudnicka
Chair of Environmental Chemistry and Bioanalytics,
Faculty of Chemistry, Nicolaus Copernicus University,
7 Gagarina Str., 87-100 Torun, Poland

STATEMENT

I hereby declare that, as a co-author of the following article, being a part of the PhD thesis of Ms. Oleksandra Pryshchepa, MSc:

1. O. Pryshchepa, G. Sagandykova, J. Rudnicka, P. Pomastowski, S. Sprynskyy, B. Buszewski "Synthesis and physicochemical characterization of zinc-lactoferrin complexes", Journal of Dairy Science, 3 (105), 2022: 1940-1958, https://doi.org/10.3168/jds.2021-20538.

that my contribution was on the assistance in samples preparation for the instrumental analysis.

Dr ing. Myroslav Sprynskyy, DSc.
Chair of Environmental Chemistry and Bioanalytics,
Faculty of Chemistry, Nicolaus Copernicus University,
7 Gagarina Str., 87-100 Torun, Poland

STATEMENT

I hereby declare that, as a co-author of the following article, being a part of the PhD thesis of Ms. Oleksandra Pryshchepa, MSc:

1. O. Pryshchepa, G. Sagandykova, J. Rudnicka, P. Pomastowski, S. Sprynskyy, B. Buszewski "Synthesis and physicochemical characterization of zinc-lactoferrin complexes", Journal of Dairy Science, 3 (105), 2022: 1940-1958, https://doi.org/10.3168/jds.2021-20538;

that my contribution was on manuscript correction.

MSc. Mateusz Sugajski
Chair of Environmental Chemistry and Bioanalytics,
Faculty of Chemistry, Nicolaus Copernicus University,
7 Gagarina Str., 87-100 Torun, Poland

STATEMENT

I hereby declare that, as a co-author of the following article, being a part of the PhD thesis of Ms. Oleksandra Pryshchepa, MSc:

1. O. Pryshchepa, K. Rafińska, A. Gołębiowski, M. Sugajski, G. Sagandykova, P. Madajski, B. Buszewski, P. Pomastowski, "Synthesis and physicochemical characterization of bovine lactoferrin supersaturated complex with iron (III) ions", Scientific Reports, 12 (1), 2022: 12695, https://doi.org/10.1038/s41598-022-15814-2

that my contribution was on the performing of molecular docking analysis, data interpretation writing original draft.

15.02.2023
Sugajski Mateusz

HELMHOLTZ
MUNICH

Helmholtz Zentrum München Deutsches Forschungszentrum für
Gesundheit und Umwelt (GmbH), Postfach 11 29, 85758 Neuherberg

Prof. Dr. Ph. Schmitt-Kopplin
Director Research Unit Analytical
Biogeochemistry (BGC)
Ingolstädter Landstraße 1
D-85764 Neuherberg/Germany

Tel. +49(o)89 3187 3246
Fax +49(0)89 3187-3358

schmitt-kopplin@helmholtz-munich.de

15. Februar 2023

To Whom it may concern

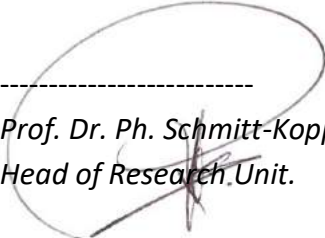**Subject:** *Statement on paper in PhD-thesis of Ms. Oleksandra Pryshchepa, MSc*

Dear Sir,

I hereby declare that, as a co-author of the following article, being a part of the PhD thesis of Ms. Oleksandra Pryshchepa, MSc:

O. Pryshchepa, P. Pomastowski, K. Rafińska, A. Gołębiowski, A. Rogowska, M Monedeiro-Milanowski, G. Sagandykova, B. Michalke, P. Schmitt-Kopplin, M. Gloc, R. Dobrucka, K. Kurzydłowski, B. Buszewski, "Synthesis, physicochemical characterization and antibacterial performance of silver-lactoferrin complexes", International Journal of Molecular Sciences, 23 (13), 2022: 7112, https://doi.org/10.3390/ijms23137112.

that my contribution was to provide the access to the equipment for CE-ICP-MS analysis, co-supervision and manuscript correction.

Sincerely,

Prof. Dr. Ph. Schmitt-Kopplin
Head of Research Unit.

Prof. Dr ing. Krzysztof Kurzydłowski, D.Sc,
Faculty of Mechanical Engineering,
Białystok University of Technology,
Wiejska 45C, 15-351 Białystok, Poland

STATEMENT

I hereby declare that, as a co-author of the following article, being a part of the PhD thesis of Ms. Oleksandra Pryshchepa, MSc:

1. O. Pryshchepa, P. Pomastowski, K. Rafińska, A. Gołębiowski, A. Rogowska, M Monedeiro-Milanowski, G. Sagandykova, B. Michalke, P. Schmitt-Kopplin, M. Gloc, R. Dobrucka, K. Kurzydłowski, B. Buszewski, "Synthesis, physicochemical characterization and antibacterial performance of silver-lactoferrin complexes", International Journal of Molecular Sciences, 23 (13), 2022: 7112, https://doi.org/10.3390/ijms23137112;

2. A. Rogowska, O. Pryshchepa, N. N. Som, P. Śpiewak, A. Gołębiowski, K. Rafińska, R. Dobrucka, K. Kurzydłowski, B. Buszewski, P. Pomastowski, „Study on the Zinc Ions Binding To Human Lactoferrin", Journal of Molecular Structure, 2023: 135149, https://doi.org/10.1016/j.molstruc.2023.135149

that my contribution was in the form of advice provided in discussion of the research program and interpretation of the results of microscopic investigations.

K. Kurzydłowski.

Neuherberg, 15 February 2023

Prof. Dr. Bernhard Michalke
Research Unit Analytical BioGeoChemistry,
Helmholtz Zentrum Muenchen-German Research Center for Environmental Health GmbH
85764 Neuherberg, Germany

STATEMENT

I hereby declare that, as a co-author of the following article, being a part of the PhD thesis of Ms. Oleksandra Pryshchepa, MSc:

1. O. Pryshchepa, P. Pomastowski, K. Rafińska, A. Gołębiowski, A. Rogowska, M Monedeiro-Milanowski, G. Sagandykova, B. Michalke, P. Schmitt-Kopplin, M. Gloc, R. Dobrucka, K. Kurzydłowski, B. Buszewski, "Synthesis, physicochemical characterization and antibacterial performance of silver-lactoferrin complexes", International Journal of Molecular Sciences, 23 (13), 2022: 7112, https://doi.org/10.3390/ijms23137112.

that my contribution was to provide the methodology for the CE-ICP-MS analysis, guidance, co-supervision and manuscript correction.

Bernhard Michalke

Dr. Narayn N. Som,
Laboratory Nanostructures
Institute of High Pressure Physics, Polish Academy of Sciences
Sokolowska 29/37, 01-142 Warsaw, Poland

STATEMENT

I hereby declare that, as a co-author of the following article, being a part of the PhD thesis of Ms. Oleksandra Pryshchepa, MSc:

1. A. Rogowska, O. Pryshchepa, N. N. Som, P. Śpiewak, A. Gołębiowski, K. Rafińska, R. Dobrucka, K. Kurzydłowski, B. Buszewski, P. Pomastowski, „Study on the Zinc Ions Binding To Human Lactoferrin", Journal of Molecular Structure, 2023: 135149, https://doi.org/10.1016/j.molstruc.2023.135149

that my contribution was on the performing of computational calculations and running the simulations with the utilization of the models and methods of Molecular Dynamics and Density Functional Theory. The interpretation of the obtained data, preparation of materials for the article, i.e., visual design of the figures, tables and the writing of manuscript draft.

Dr. Narayan Som

Narayan 15/02/2023

Dr. Renata Dobrucka, D.Sc,
Faculty of Materials Science and Engineering,
Warsaw University of Technology,
Wołoska 141, 02-507 Warsaw, Poland

STATEMENT

I hereby declare that, as a co-author of the following article, being a part of the PhD thesis of Ms. Oleksandra Pryshchepa, MSc:

1. O. Pryshchepa, P. Pomastowski, K. Rafińska, A. Gołębiowski, A. Rogowska, M Monedeiro-Milanowski, G. Sagandykova, B. Michalke, P. Schmitt-Kopplin, M. Gloc, R. Dobrucka, K. Kurzydłowski, B. Buszewski, "Synthesis, physicochemical characterization and antibacterial performance of silver-lactoferrin complexes", International Journal of Molecular Sciences, 23 (13), 2022: 7112, https://doi.org/10.3390/ijms23137112;

2. A. Rogowska, O. Pryshchepa, N. N. Som, P. Śpiewak, A. Gołębiowski, K. Rafińska, R. Dobrucka, K. Kurzydłowski, B. Buszewski, P. Pomastowski, „Study on the Zinc Ions Binding To Human Lactoferrin", Journal of Molecular Structure, 2023: 135149, https://doi.org/10.1016/j.molstruc.2023.135149

that my contribution was on mentoring and controlling during experiments, interpretation and writing of the results of microscopic investigations, correction of manuscripts.

Piotr Śpiewak, PhD. Eng.
Faculty of Materials Science and Engineering,
Warsaw University of Technology,
Wołoska 141, 02-507 Warsaw, Poland

STATEMENT

I hereby declare that, as a co-author of the following article, being a part of the PhD thesis of Ms. Oleksandra Pryshchepa, MSc:

1. A. Rogowska, O. Pryshchepa, N. N. Som, P. Śpiewak, A. Gołębiowski, K. Rafińska, R. Dobrucka, K. Kurzydłowski, B. Buszewski, P. Pomastowski, „Study on the Zinc Ions Binding To Human Lactoferrin", Journal of Molecular Structure, 2023: 135149, https://doi.org/10.1016/j.molstruc.2023.135149

that my contribution was on the planning, assistance, and supervision of computational calculations with the utilization of the models and methods of Molecular Dynamics and Density Functional Theory. The assistance in the interpretation of the obtained data and correction of the manuscript.

Ph.D. Michał Gloc
Faculty of Materials Science and Engineering
Warsaw University of Technology
Wołoska 141, 02-507 Warsaw, Poland

STATEMENT

I hereby declare that, as a co-author of the following article, being a part of the Ph.D. thesis of Ms. Oleksandra Pryshchepa, MSc:

1. O. Pryshchepa, P. Pomastowski, K. Rafińska, A. Gołębiowski, A. Rogowska, M Monedeiro-Milanowski, G. Sagandykova, B. Michalke, P. Schmitt-Kopplin, M. Gloc, R. Dobrucka, K. Kurzydłowski, B. Buszewski, "Synthesis, physicochemical characterization and antibacterial performance of silver-lactoferrin complexes", International Journal of Molecular Sciences, 23 (13), 2022: 7112, https://doi.org/10.3390/ijms23137112;

that my contribution was on the performing of SEM and STEM-EDX analysis, corresponding data interpretation and writing of original draft.

Agnieszka Rogowska
Błonie, 23.02.2023

STATEMENT

I hereby declare that, as a co-author of the following publication, being a part of the doctoral dissertation of MSc Oleksandra Pryshchepa:

1. O. Pryshchepa, P. Pomastowski, K. Rafińska, A. Gołębiowski, A. Rogowska, M Monedeiro-Milanowski, G. Sagandykova, B. Michalke, P. Schmitt-Kopplin, M. Gloc, R. Dobrucka, K. Kurzydłowski, B. Buszewski, "Synthesis, physicochemical characterization and antibacterial performance of silver-lactoferrin complexes", International Journal of Molecular Sciences, 23 (13), 2022: 7112, https://doi.org/10.3390/ijms23137112;

2. A. Rogowska, O. Pryshchepa, N. N. Som, P. Śpiewak, A. Gołębiowski, K. Rafińska, R. Dobrucka, K. Kurzydłowski, B. Buszewski, P. Pomastowski, „Study on the Zinc Ions Binding To Human Lactoferrin", Journal of Molecular Structure, 2023: 135149, https://doi.org/10.1016/j.molstruc.2023.135149

that my contribution was sample preparation and performing the instrumental analysis of FTIR, CE-ICP-MS, RAMAN, SDS-PAGE as well as sample preparation for TEM and ICP-MS analysis; synthesis of hLTF-Zn complexes; conducting kinetics and isotherm studies; interpretation of the obtained data; figures and tables preparation and writing original draft.

Rogowska Agnieszka